

LIFETIME MEASUREMENTS AND THE FEASIBILITY OF VIBRATIONAL
PHONON CONFIGURATIONS IN DEFORMED RARE-EARTH NUCLEI

A Dissertation

Submitted to the Graduate School
of the University of Notre Dame
in Partial Fulfillment of the Requirements
for the Degree of

Doctor of Philosophy

by

Clark R. Casarella

Ani Aprahamian, Director

Graduate Program in Physics

Notre Dame, Indiana

October 2016

LIFETIME MEASUREMENTS AND THE FEASIBILITY OF VIBRATIONAL PHONON CONFIGURATIONS IN DEFORMED RARE-EARTH NUCLEI

Abstract

by

Clark R. Casarella

One of the many paradigms of nuclear structure involves the coupling of dynamic quadrupole, octupole & hexadecapole vibrations superimposed on top of a well-deformed ground state. Historically, the nature and feasibility of collective vibrational degrees of freedom in deformed nuclei have garnered significant skepticism and experimental/theoretical interest, yet the entire rare-earth region lacked the completeness and richness of data to fully understand the systematic behavior of these low-lying excitations. Successful interpretation of quadrupole and octupole vibrational phonon states hinges upon measurement of E0 transition strengths, two-nucleon transfer reaction cross sections, and absolute transition probabilities, the latter equating to precision lifetime measurements of excited states. We have measured 29 new lifetimes in ^{160}Gd and 47 new lifetimes in ^{162}Dy below 3.1 MeV excitation energy, including many potentially key vibrational phonon states at the University of Kentucky Accelerator Laboratory using the Doppler Shift Attenuation Method via Inelastic Neutron Scattering (DSAM-INS). This work discusses our experimental observations in terms of the various collective multiphonon configurations in two rare-earth nuclei, ^{160}Gd and ^{162}Dy , with a first-of-its-kind measurement of 3 distinct modes of a two-phonon vibration, a $K^\pi=0^+$ $\gamma\gamma$ -type and 2 $K^\pi=4^+$ $\gamma\gamma$ -type vibrations in ^{162}Dy . This work is funded by the National Science Foundation (NSF) under grant

numbers PHY-1068192, PHY-1205412, and PHY-0956310.

DEDICATION

To Ani Aprahamian, my academic advisor and mentor, for giving me the swift kick I needed at periodic times to push me through the revolving door that is graduate school, and for frequently reminding me that “If what you were doing was easy, someone would have already done it long ago”.

To below-freezing temperatures, without you, I would have stuck around the South Bend/Notre Dame area for a few more years.

To Jacee Rohlck, for reminding me on numerous occasions that she will eternally love me (read: put up with me), no matter the circumstances.

To Starbucks, for supplying me with a near limitless amount of coffee (a necessary tool for good work) throughout graduate school.

To the best friends I have ever made in my entire life (my fellow graduate students), for keeping me sane and sufficiently distracted throughout my career here at Notre Dame.

To Dr. Richard Prior, for convincing me it was a good idea to come to TUNL with him in 2010, effectively bringing me to the event horizon of the black hole that is experimental nuclear physics research.

To Shelly Leshner, for providing me with the answers to numerous questions about the analysis process and for her gracious use of publication data for part of the results presented in this work (^{160}Gd excitation functions and level lifetimes below 2.0 MeV excitation energy).

To Ben Crider, Erin Peters, and the entire cadre of nuclear scientists at the

University of Kentucky, for answering my inane, incessant, and frankly, unintelligent questions about nuclear physics and the analysis methods I would need to implement to complete the Herculean task of understanding nuclear structure.

Lastly, to my father, the late Anthony “Tony” Casarella, for *everything*.

CONTENTS

FIGURES	vii
TABLES	xiv
CHAPTER 1: INTRODUCTION	1
1.1 Nuclei as a Many-body Quantum System	1
1.2 Deformation in Nuclei	3
1.3 Excited States in Deformed Nuclei	9
1.4 Historical Impetus in Experimental Nuclear Structure	13
1.5 Assessing Nuclear Structure from Decay Radiation	18
1.5.1 Why Measure Lifetimes?	18
1.5.2 Importance of Transition Probabilities	21
1.6 Decay and Structure Systematics in the $150 < A < 180$ Region	23
CHAPTER 2: EXPERIMENTS AND DATA ACQUISITION	38
2.1 Lifetime Measurements of Excited States	38
2.2 DSAM-INS Formalism	39
2.3 (n,n' γ) Experiments at the University of Kentucky	42
2.3.1 Excitation Function Measurements	46
2.3.2 Angular Distribution Measurements	49
2.4 Experimental Campaigns	52
2.4.1 The ^{160}Gd Campaign	52
2.4.2 The ^{162}Dy Campaign	53
CHAPTER 3: DATA ANALYSIS	57
3.1 Calibrations and Corrections	57
3.1.1 Energy Calibrations	57
3.1.2 Nonlinearity Calibrations	58
3.1.3 Efficiency Calibrations	61
3.1.4 Self-Absorption Corrections	62
3.2 Statistical Analysis	65
3.2.1 Fitting Procedures	65
3.2.2 Observable Extraction	67
3.2.2.1 Excitation Functions	67
3.2.2.2 Angular Distributions	70

CHAPTER 4: RESULTS	77
4.1 ^{160}Gd Results	77
4.1.1 Lifetimes of 0^+ States	79
4.1.2 Lifetimes of 2^+_{γ} Band	82
4.1.3 Lifetimes of Negative Parity Bands	82
4.1.4 Lifetimes of Positive Parity Bands	83
4.1.5 Lifetimes of States with No K^{π} Assignment	85
4.2 ^{162}Dy Results	88
4.2.1 Lifetimes of 0^+ States	90
4.2.2 Lifetimes of $K^{\pi}=2^+$ and 4^+ Bands	92
4.2.3 Lifetimes of Negative Parity Bands ($K^{\pi}=2^-$, 0^- , and 2^-_2)	93
4.2.4 Lifetimes of Other Negative Parity Bands ($K^{\pi}=5^-$, 3^- , 1^- and 3^-_2)	95
4.2.5 Lifetimes of $K^{\pi}=1^+$ Band and Members of M1 Scissors	98
4.2.6 Lifetimes of States with No K^{π} Assignment	99
4.2.7 All Decays Observed (Intensities)	99
CHAPTER 5: DISCUSSION AND INTERPRETATION	125
5.1 ^{160}Gd Discussion	125
5.1.1 Excited 0^+ States and the $K^{\pi}=2^+_{\gamma}$ Band	125
5.1.2 Negative Parity States	130
5.1.3 Other Lifetime Measurements in ^{160}Gd	132
5.1.3.1 $K^{\pi}=4^+$ band as a Hexadecapole Vibration?	132
5.1.3.2 $K^{\pi}=1^+$ band	134
5.1.4 Implications & Further Discussion	137
5.2 ^{162}Dy Lifetimes	140
5.2.1 0^+ Excitations Not Observed in $(n,n'\gamma)$	140
5.2.2 A Lack of Strong β Vibrations in ^{162}Dy	142
5.2.3 On the Two-Phonon Characteristics	143
5.2.3.1 2^+_{γ} band	144
5.2.3.2 0^+_2 band $\gamma\gamma$ -vibration	144
5.2.3.3 $K^{\pi}=4^+_{1,2}$ bands at 1535,2181 keV as $\gamma\gamma$ -vibrations	146
5.2.3.4 $(2,3,4)^+$ state at 2230 keV	147
5.2.4 Negative Parity States	155
5.2.4.1 $K^{\pi}=2^-$ Band at 1148 keV	155
5.2.4.2 $K^{\pi}=0^-$ Band at 1275 keV	155
5.2.4.3 $K^{\pi}=2^-_2$ Band at 1863 keV	156
5.2.5 Other Negative Parity Bands	160
5.2.5.1 $K^{\pi}=5^-$ band	160
5.2.5.2 $K^{\pi}=3^-$ band	160
5.2.5.3 $K^{\pi}=1^-$ band	161
5.2.5.4 $K^{\pi}=3^-_2$ band	161
5.2.6 $K^{\pi}=1^+$ band	161

5.2.7	States above 2.2 MeV excitation energy	162
5.2.8	Implications & Discussion	163
CHAPTER 6: FINAL REMARKS AND FUTURE OUTLOOK		169
6.1	Impact of Presented Lifetime Measurements	169
6.1.1	^{160}Gd	169
6.1.2	^{162}Dy	170
6.2	What Lies Ahead for Rare-Earth Nuclei?	170
BIBLIOGRAPHY		176

FIGURES

1.1	Chart of nuclides showing the varying degrees of deformation ($R_{\frac{4}{2}}$ values for even-even nuclei). Orange colored squares mark a well-deformed ground state, with green representing spherical nuclei. . . .	2
1.2	Measured $B(E2)$ transition probabilities in single-particle units as a function of A , highlighting the region of deformation (as well as heavier actinide region) where strong nuclear rotations exist [19].	4
1.3	Schematic of the β quadrupole vibration about a deformed equilibrium shape.	8
1.4	Schematic of the γ quadrupole vibration about a deformed equilibrium shape.	9
1.5	Level scheme of the various phonon vibrations in deformed nuclei [57].	10
1.6	Schematic of the Q3D magnetic spectrograph at Munich used for precision (p,t)/(t,p) spectroscopy [54].	14
1.7	Angular distribution data for all 0^+ states in ^{158}Gd observed in the (p,t) reaction in [55]. A DWBA calculation for an $L=2$ transition is shown as a dotted line in the $E=1452$ keV plot to show the unique nature of the $L=0$ transitions (in solid black).	15
1.8	Number of 0^+ states in rare earth isotopes of Sm, Gd, Dy, Er, Yb, and Hf. ^{162}Dy is highlighted with a blue circle.	16
1.9	Systematics for the energies of excited 0^+ states, the first excited 2^+ bandhead, and low-lying ground state band members for even-even Samarium nuclei. Proton and neutron pairing gaps ($2\Delta_\pi$ and $2\Delta_\nu$, respectively) are drawn in green and blue and are calculated from Equations 1.4 and 1.5. Transition arrows represent known experimental $B(E2)$ measurements for 0^+ bandheads and 2^+ bandheads (in W.u. where known).	27
1.10	Systematics for the energies of excited 0^+ states, the first excited 2^+ bandhead, and low-lying ground state band members for even-even Gadolinium nuclei. Proton and neutron pairing gaps ($2\Delta_\pi$ and $2\Delta_\nu$, respectively) are drawn in green and blue and are calculated from Equations 1.4 and 1.5. Transition arrows represent known experimental $B(E2)$ measurements for 0^+ bandheads and 2^+ bandheads (in W.u. where known).	28

1.11	Systematics for the energies of excited 0^+ states, the first excited 2^+ bandhead, and low-lying ground state band members for even-even Dysprosium nuclei. New transition probabilities are presented in ^{162}Dy , with the widths proportional to $B(E2)$ values (in W.u.); also shown are the proton and neutron pairing gap ($2\Delta_\pi$ and $2\Delta_\nu$, respectively) for each isotope.	29
1.12	Systematics for the energies of excited 0^+ states, the first excited 2^+ bandhead, and low-lying ground state band members for even-even Erbium nuclei. Proton and neutron pairing gaps ($2\Delta_\pi$ and $2\Delta_\nu$, respectively) are drawn in green and blue and are calculated from Equations 1.4 and 1.5. Transition arrows represent known experimental $B(E2)$ measurements for 0^+ bandheads and 2^+ bandheads (in W.u. where known).	30
1.13	Systematics for the energies of excited 0^+ states, the first excited 2^+ bandhead, and low-lying ground state band members for even-even Ytterbium nuclei. Proton and neutron pairing gaps ($2\Delta_\pi$ and $2\Delta_\nu$, respectively) are drawn in green and blue and are calculated from Equations 1.4 and 1.5. Transition arrows represent known experimental $B(E2)$ measurements for 0^+ bandheads and 2^+ bandheads (in W.u. where known).	31
1.14	Systematics for the energies of excited 0^+ states, the first excited 2^+ bandhead, and low-lying ground state band members for even-even Hafnium nuclei. Proton and neutron pairing gaps ($2\Delta_\pi$ and $2\Delta_\nu$, respectively) are drawn in green and blue and are calculated from Equations 1.4 and 1.5. Transition arrows represent known experimental $B(E2)$ measurements for 0^+ bandheads and 2^+ bandheads (in W.u. where known).	32
1.15	Systematics for the energies of excited negative parity states, the first excited 2^+ bandhead, and low-lying excited 0^+ states below the pairing gap ($2\Delta_\pi$ and $2\Delta_\nu$) for even-even Gadolinium nuclei.	33
1.16	Systematics for the energies of excited negative parity states, the first excited 2^+ bandhead, and low-lying excited 0^+ states below the pairing gap ($2\Delta_\pi$ and $2\Delta_\nu$) for even-even Dysprosium nuclei. States with a ' \oplus ' marker indicate where a literature lifetime measurement exists.	34
1.17	Absolute $B(E2; 2_\gamma^+ \rightarrow 0_{gs}^+)$ (in Weisskopf units) measurements for rare-earth nuclei, showing the uniformity of the γ -vibration in a deformed nucleus. The bottom plot shows the energy of the 2^+ bandheads as a function of N , highlighting the smoothly varying energies.	35

1.18	Absolute $B(E2; 0_2^+ \rightarrow 2_{gs}^+)$ (in Weisskopf units) measurements for rare-earth nuclei, showing the scattered experimental data that spans an order of magnitude variance. The bottom plot shows the energy of the 0_2^+ bandheads as a function of N , which shows a slightly more variant energy systematic than the 2^+ bandheads.	36
1.19	Summary of all known multiphonon ($\gamma\gamma$, $\beta\gamma$, or $\beta\beta$) configurations in rare-earth nuclei, absolute $B(E2)$ from literature are shown in Weisskopf units to signify collective decays to γ -vibrational and/or potential β -vibrational states.	37
2.1	Techniques available to nuclear physicists to measure lifetimes as short as a few attoseconds (10^{-18} s) to the more long-lived lifetimes on the order of microseconds (10^{-6} s). (Adapted from [64], courtesy of M. K. Smith)	38
2.2	Doppler shift of an $E_\gamma=1902.055$ keV de-excitation from the $\theta_{lab}=40, 90$, and 150 degrees in red, blue, and green, respectively. The vertical lines mark the centroid of each peak of corresponding color.	41
2.3	Sample Experimental Setup at UKAL for γ -singles measurements (Made in M. Caprio's SciDraw software for Mathematica [18])	45
2.4	Typical TOF spectrum with labeled regions for corresponding γ , neutron, and background events. Note the passage of time to the left, starting at the prompt γ -ray peak, followed by a neutron bump, and wrapping back around the x-axis.	47
2.5	Superimposed excitation functions for two gamma rays ($E_\gamma=969$ & 1252 keV) leaving the same level ($E_{lev}=1518$ keV), and a single 1195 keV γ -ray leaving a separate $E_{lev}=1275$ keV level in ^{162}Dy . The different thresholds and shape of the 1195 keV and 969 keV de-excitations imply that these decays are from two different levels, clearly showing their placement in the level scheme.	49
2.6	Angular distributions for two different multipolarity γ -rays in ^{162}Dy , an E2 transition of $E_\gamma=282$ keV (the $6_{gs}^+ \rightarrow 4_{gs}^+$ transition) & an E1 transition of $E_\gamma=334$ keV (a $3^- \rightarrow 2_\gamma^+$ transition), showing distinct, inverted shapes.	51
2.7	Angles used in $^{162}\text{Dy}(n, n'\gamma)$ angular distributions. Angles in black are used in all measurements, while angles in red (137° and 145°) are used for the $E_n=1.6$ MeV measurements and angles in blue are used for both $E_n=2.2$ and 3.1 MeV datasets.	55
3.1	Spectrum from a ^{226}Ra calibration run during the ^{162}Dy experiments. Sampled, higher intensity peaks are labeled by their energy in keV (refer to Table 3.1).	60

3.2	Linear energy calibration, taken from the three $^{162}\text{Dy}(n,n'\gamma)$ angular distributions and single excitation function (ExF in the legend). . . .	62
3.3	Order-5 polynomial nonlinearity correction, taken from the $^{162}\text{Dy}(n,n'\gamma)$ angular distribution with $E_n=3.1$ MeV	63
3.4	Fifth-order relative efficiency curve taken from the $^{162}\text{Dy}(n,n'\gamma)$ angular distribution with $E_n=3.1$ MeV	64
3.5	Multiplicative factor calculated by GAMBIT to correct for the angular dependent γ -ray self-absorption by a finite-size target.	65
3.6	Example of an energy-calibrated spectrum from the ^{162}Dy angular distribution at $E_n=1.6$ MeV and $\theta_{lab}=90^\circ$, outlining typical background levels and miscellaneous γ -ray transitions.	66
3.7	A set of plots from a typical excitation function for a single γ -ray transition, in 'a)', E_γ vs. E_n , and in 'b)', the peak area vs E_n . Note the dip in γ -ray energy at 2.6 MeV, and corresponding bump in peak area (shown as a blue ellipse to guide the eye), indicating a second transition of a similar (slightly lower) energy being populated.	68
3.8	Spectra from four bombarding neutron energies ($E_n=1.4, 1.7, 1.775$, and 2.3 MeV datasets) to show the typical increase of statistics for a single peak, a 1647 keV decay from the 1728 keV state in ^{162}Dy . Note the peak area emerge just above the level energy threshold (1.775 MeV neutron dataset), with optimal statistics in the $E_n=2.3$ MeV set. . .	69
3.9	Calculated Winterbon curves ($F(\tau)$ as a function of τ) for $E_n=1.6, 2.2$, and 3.1 MeV ^{162}Dy angular distributions. Sensitive lifetime ranges from DSAM are shown as vertical black lines, with the corresponding $F(\tau)$ values as horizontal lines.	71
3.10	Example Doppler Shift for a 1149 keV γ -ray populated in the 1.5 MeV $^{160}\text{Gd}(n,n'\gamma)$ experiment. Here, the $F(\tau)$ value of 0.665 ± 0.010 corresponds to a lifetime of 21 ± 1 fs.	73
3.11	Example extraction of multipole mixing fraction (δ) for a $4^+ \rightarrow 4^+$ transition in ^{162}Dy . Top-left plot: angular distribution of the 1308 keV γ ray. Top-right plot: CINDY comparison for a range of initial spins (color online) decaying to the final spin of 4; intersections with the black ellipse mark local/global minima of χ^2 vs δ . Bottom plot: projection of CINDY comparison as χ^2 as a function of δ minimization (note the lowest χ value corresponds to the $\delta \approx 1$ for the cyan-colored $4^+ \rightarrow 4^+$ transition). (color online)	76
4.1	Lifetime inflation of the measured lifetimes for two levels ($E_{lev}=1275$ keV and $E_{lev}=1358$ keV) in ^{162}Dy caused by effects due to a higher bombarding neutron energy and unknown level-feeding from higher-lying states.	78

4.2	Level scheme for all level lifetimes measured in the ^{160}Gd experiments, with confirmed band and spin assignments shown. Previously measured lifetimes are in blue, with newly presented lifetimes in red. Individual levels and bands will be discussed in following sections. . . .	79
4.3	Visual representation of all measured lifetimes with respect to literature values (in blue). Each separate color outlines the specific regimes (<1.5 MeV, $1.5 - 2.0$ MeV, and >2.0 MeV excitation energy) of energies studied in the ^{160}Gd angular distributions.	80
4.4	Singles spectra from the $\theta_{lab}=90^\circ$ and $E_n=2.0$ MeV angular distributions of ^{160}Gd	80
4.5	Level scheme for all level lifetimes measured in the ^{162}Dy experiments, with confirmed band and spin assignments shown. Previously measured lifetimes are in blue, with newly presented lifetimes in red, levels in green constitute an unreliable lifetime measurement from our data, where $F(\tau)<0$ or is consistent with zero.	109
4.6	All measured lifetimes in ^{162}Dy (in femtoseconds) plotted as a function of excitation energy in keV. Data points in red are extracted from the $E_n=1.6$ MeV angular distributions, points in green correspond to lifetimes extracted from the 2.2 MeV angular distributions, and blue points are lifetimes from the 3.1 MeV dataset. (color online)	110
4.7	Singles spectra from the $\theta_{lab}=90^\circ$ and $E_n=2.2$ MeV angular distributions of ^{162}Dy	110
4.8	Angular distributions of $0_i^+ \rightarrow 2_{g.s.}^+$ γ -rays, highlighting their isotropic nature (color online).	111
4.9	Doppler energy shifts of $0_i^+ \rightarrow 2_{g.s.}^+$ γ -rays (color online).	112
4.10	Lowest-lying negative parity bands in ^{162}Dy with reliable lifetimes measured in our experiments in red, existing literature values in blue, and unreliable lifetimes measured in green (color online).	115
4.11	$E_\gamma=260$ keV γ ray (from the $E_x=1148$ keV level) Doppler shift and excitation functions for decays from the first 2^- band (color online). The vertical black lines highlight our justification for using a slightly higher bombarding neutron energy, for the sake of better statistics, without the potential for contaminant decay channels from other states. . . .	117
4.12	$E_\gamma=912$ & 1010 keV (de-excitations from the $E_x=1974$ keV level) Doppler shifts and excitation functions (color online). The excitation function (in blue) for the 1010 keV γ ray is scaled by a factor of 0.33 to normalize to the branching ratio of the level.	118
4.13	$E_\gamma=937$ & 1220 keV (de-excitations from the $E_x=1485$ keV level) Doppler shifts and overlaid excitation functions (color online). The excitation function (in blue) for the 1220 keV γ ray is scaled by a factor of 0.291	119

4.14	Excitation functions for the decays leaving the $E_x=1637$ keV state. Note the differing population threshold energies for each γ -ray. (color online)	120
5.1	Non-isotropic decay from the tentative 0^+ state in ^{160}Gd at $E_x=1325$ keV. 126	
5.2	Excitation function measurement from the tentative 0^+ state in ^{160}Gd at $E_x=2236$ keV.	127
5.3	Level scheme showing the calculated $B(E2)$ in W.u. and $B(E1)$ in mW.u. for the confirmed 0^+ excitations in ^{160}Gd	128
5.4	Level scheme showing the decays with calculated reduced transition probabilities for the $K^\pi=2_\gamma^+$ band and low-lying negative parity states in ^{160}Gd	131
5.5	Level scheme showing the decays with calculated reduced transition probabilities for the $K^\pi=4^+$ and 1^+ bands in ^{160}Gd	133
5.6	Level scheme showing the decays with calculated reduced transition probabilities for the levels that are not assigned to rotational bands in ^{160}Gd . Note the neutron and proton pairing gaps drawn as dotted lines ($2\Delta_\nu \sim 1625$ keV and $2\Delta_\pi \sim 1810$ keV).	135
5.7	Singles spectra cuts where remaining 0^+ excitations should be observed. Spectra for $0_{4,5}^+$ placements are from the $E_n=1.925$ MeV excitation function measurements, with $0_{8,10}^+$ from the $E_n=2.9$ MeV dataset. 142	
5.8	Level scheme outlining all measured lifetimes for $K^\pi=0^+$ bands in ^{162}Dy . New lifetime measurements are shown in red (color online), and new $B(E2;0_i^+ \rightarrow \text{g.s.})$ calculations are expressed in Weisskopf units (W.u.).	152
5.9	Measured angular distribution of 1342 keV γ ray leaving the 2230 keV level, $W(\theta)$ fit is shown with a_2 and a_4 coefficients from the $E_n=3.1$ MeV angular distribution.	153
5.10	Level scheme showing all observed transitions from the lowest-lying 2_γ^+ , 0_2^+ , and 4_1^+ band with all interband ($K^\pi=J_i^+ \rightarrow K^\pi=2_\gamma^+$) decays. Intensities for transitions to the γ -band are taken from [3]. Also shown is a tentative (2^+) state at 2230 keV with a strong decay to the 2_γ^+ band.	154
5.11	$E_\gamma=1195$ & 1275 keV (de-excitations from the $E_x=1275$ keV level) Doppler shifts and excitation functions (color online). The excitation function (in blue) for the 1275 keV γ ray is scaled by a factor of 1.53 to normalize to the branching ratio of the level.	157

5.12	Observed γ -decays from negative parity, $K^\pi=2^-, 0^-, 2_2^-$ bands in ^{162}Dy . Transition strengths are drawn proportional in width to their deduced $B(E1)$, with E1 transitions ($B(E1)$ in milli-Weksskopf units) in violet (color online). Literature $B(E3)$ values are drawn in green, expressed in W.u., and are from Refs. [53, 56]	158
5.13	Observed γ -decays from higher lying $K^\pi=5^-, 3^-, 1^-, 3_2^-$ bands in ^{162}Dy . Transition strengths are proportional in width, with E2 transitions in red and E1 transitions in violet (color online). Hollow (white with colored border) transition arrows indicate that the resulting transition probability is tentatively from an unreliable lifetime measurement.	164
5.14	$K^\pi=1^+$ band and the 1^\pm -spin levels part of the isovector M1 scissors mode in ^{162}Dy . $B(E1)$ in violet and in mW.u., $B(M1)$ in green and W.u., and $B(E2)$ in red in W.u.	165
5.15	Levels in ^{162}Dy with no rotational band assignment above the pairing gap ($2\Delta_n=1720$ keV & $2\Delta_p=1914$ keV). $B(E2)$ strenghts drawn in red and in W.u.	166
5.16	Levels in ^{162}Dy with no rotational band assignment above the pairing gap ($2\Delta_n=1720$ keV & $2\Delta_p=1914$ keV) (continued). $B(E1)$ in violet and in mW.u., and $B(E2)$ in red in W.u.	167
5.17	Levels in ^{162}Dy with no rotational band assignment above the pairing gap ($2\Delta_n=1720$ keV & $2\Delta_p=1914$ keV) (continued). $B(E1)$ in violet and in mW.u., and $B(E2)$ in red in W.u.	168
6.1	Energies of the lowest-lying 0^+ state as a function of A (top) and N (bottom) for rare earth Sm, Gd, Dy, Er, Yb and Hf isotopes.	174
6.2	Known experimental $B(E2)$ strengths of the lowest-lying 0^+ state as a function of A for rare earth Sm, Gd, Dy, Er, Yb and Hf isotopes.	175

TABLES

1.1	Selection rules used to determine J^π values of rotational members of a specific K^π band.	11
1.2	Unit conversion for transition probabilities from Weisskopf units to e^2b^λ (μ_N^2 for M1s) for ^{160}Gd and ^{162}Dy	22
2.1	Bombarding energy of neutrons used to populate the excitation functions for the ^{160}Gd experiment.	52
2.2	Angles used for lifetime measurements for the suite of ^{160}Gd experiments at 1.5, 2.0, and 2.8 MeV bombarding neutron energies.	53
2.3	Bombarding energies of neutrons used to populate the excitation functions for the ^{162}Dy experiment. ~ 75 keV steps were used at the lower energies (≤ 2 MeV) to enhance the resolution of the threshold and population shape for low-lying excitations.	54
2.4	Angles used for lifetime measurements for the suite of ^{162}Dy experiments at 1.6, 2.2, and 3.1 MeV bombarding neutron energy. Angles in bold are to emphasize differences in measurements.	56
3.1	Energies (in keV) and relative intensities (in arbitrary units) for γ -ray emissions from the ^{226}Ra decay chain used in data calibrations for this work.	59
3.2	Calibration points used for all ^{160}Gd and ^{162}Dy spectra energy calibrations.	61
4.1	Lifetimes of excited 0^+ bands in ^{160}Gd , with experimentally determined $B(E2)$ in W.u and $B(E1)$ in mW.u. (1 mW.u. = 1.90 e^2b). . .	81
4.2	Lifetimes of $K^\pi=2_\gamma^+$ band in ^{160}Gd , with experimentally determined $B(E2)$ in W.u. and multipole mixing fractions δ taken from the $E_n=1.5$ MeV angular distributions.	83
4.3	Lifetimes of excited negative parity bands in ^{160}Gd , with experimentally determined $B(E1)$ in mW.u. (1 mW.u. = 1.90 e^2b).	84
4.4	Lifetimes of excited positive parity bands in ^{160}Gd , with experimentally determined $B(E2)$ in W.u and $B(E1)$ in mW.u. (1 mW.u. = 1.90 e^2b). .	85

4.5	Lifetimes of excited states in ^{160}Gd that have no band assignment, with experimentally determined $B(E2)$ in W.u and $B(E1)$ in mW.u. (1 mW.u. = 1.90 e ² b).	87
4.6	Comparison of lifetimes measured in the campaign of (n,n' γ) experiments with literature lifetimes	90
4.14	All γ rays observed in ^{162}Dy experimental campaign, with approximate energy threshold where first observed, the absolute intensity of the observed decay (taken from the $E_n=3.1$ MeV dataset), the origin and/or placement of the de-excitation in the level scheme (whether it is a prompt ^{162}Dy decay or a background), and any notes for the reader. [†]: γ -ray excitation function is flat (definitive background) [⊗]: γ -ray does not belong to ^{162}Dy (not populated by inelastic neutron scattering or energetically between any level in ^{162}Dy) [★]: γ -ray does not fit energetically inbetween levels in ^{162}Dy , or with favored spin for (n,n' γ) reactions. [A^2]: γ -ray observed, but not placed in [3]. [‡]: Origin of γ ray unknown (presumed to <i>not</i> be ^{162}Dy from energetics considerations)	108
4.7	Lifetimes of excited 0^+ bands in ^{162}Dy , with calculated $B(E2)$ in W.u., from our measured multipole mixing fractions, branching ratios, γ -ray energies, and lifetimes, all extracted from the angular distributions. $B(E2)$ strengths in parentheses are calculated using literature intensities.	113
4.8	Lifetimes of excited 2^+ band, both 4^+ bands, and tentative 2^+ state at 2230 keV in ^{162}Dy , with calculated $B(E2)$ in W.u., from our measured multipole mixing fractions, branching ratios, γ -ray energies, and lifetimes, all extracted from the angular distributions. $B(E2)$ strengths in parentheses are calculated using literature intensities.	114
4.9	Lifetimes of negative parity bands (2^- , 0^- , 2_2^-) in ^{162}Dy , with experimentally deduced $B(E1)$ in mW.u.	116
4.10	Lifetimes of 5^- , 3^- , 1^- , and second 3^- bands in ^{162}Dy , with experimentally deduced $B(E1)$ in mW.u. and $B(E2)$ in W.u.	121
4.11	Lifetimes of 1^+ band and 1^\pm members of the isovector M1 scissors mode ($[\Omega]$ marker) in ^{162}Dy , with experimentally deduced $B(E1)$ in mW.u., $B(M1)$ in μ_N^2 and $B(E2)$ in W.u.	122
4.12	Lifetimes of states with no rotational K^π band assignment in ^{162}Dy , with experimentally deduced $B(E1)$ in mW.u., $B(M1)$ in μ_N^2 and $B(E2)$ in W.u.	123
4.13	Lifetimes of states with no rotational K^π band assignment (cont'd) in ^{162}Dy , with experimentally deduced $B(E1)$ in mW.u., $B(M1)$ in μ_N^2 and $B(E2)$ in W.u.	124
5.1	Alaga comparisons of reduced transition probabilities in ^{160}Gd	139

5.2	Observed 0^+ states in our $(n,n'\gamma)$ experiments compared with (p,t) experiments from [55], with $[\dagger]$ as the labeled ‘contaminant’ at $E_x=774.2$ keV.	141
5.3	Absolute intensities for γ -decays observed in $(n,n'\gamma)$ experiments. $[\dagger]$: γ ray not observed, reporting literature intensity ([3, 32] gives absolute intensities, while [78, 81] report relative intensities).	149
5.4	Alaga rule comparisons of measured $B(E2)$ strengths for the $K^\pi=2_\gamma^+$, 0_2^+ , and 4_1^+ band in ^{162}Dy . $[\ast]$: Alaga comparison shown in parentheses uses literature intensities to calculate $B(E2)$ strengths.	150
5.5	Ratios of $B(E2)$ probabilities of the transitions to the γ -band over the ground state band transitions, highlighting an enhancement or preference of decay to the $K^\pi=2^+\gamma$ -band.	151
5.6	Absolute intensities for γ -decays from the $K^\pi=2^-$, 0^- , and 2_2^- bands observed in $(n,n'\gamma)$ experiments, taken from the $E_n=3.1$ MeV angular distributions.	159

CHAPTER 1

INTRODUCTION

Henri Bequerel and Marie Curie's discovery of natural, spontaneous radiation in 1896 fueled the scientific tinder that erupted into modern physics. This breakthrough in scientific impetus, coupled with the formulation of quantum mechanics and the discovery of the nucleus (the incredibly dense and miniscule core of the atom) in the early 20th Century, led to this brand new field of nuclear science. Initially, the nucleus was modeled as a homogenous core of positive charge, but with continued study, the nucleus was found to be comprised of discrete, ~ 1 femtometer large (or small, depending on perspective) particles, the positively charged proton and the inert neutron, all held together with a very attractive and short-range force, the aptly named the strong interaction.

1.1 Nuclei as a Many-body Quantum System

Knowing that the atomic nucleus is comprised of protons and neutrons, we can study it as a many-body quantum system. Figure 1.1 shows the Chart of Nuclides, which displays every isotope of observed nuclei with the number of protons (Z) on the y-axis and the number of neutrons (N) on the x-axis. In this plot, the $R_{\frac{4}{2}}$ values (the ratio of the energies of the first 4^+ state to the 2^+ state) for even- Z /even- N nuclei are shown on as a color gradient; this $R_{\frac{4}{2}}$ is a classical measure of static deformation in the nucleus, with shades of orange (>3) representing well-deformed nuclei and shades of green (<2) representing spherical or near-spherical shape. Throughout the region of deformation (and the entire Nuclear Chart), experimental physicists have observed

various emergent nuclear phenomena that drive theories and further experiments to describe the nucleus in many ways.

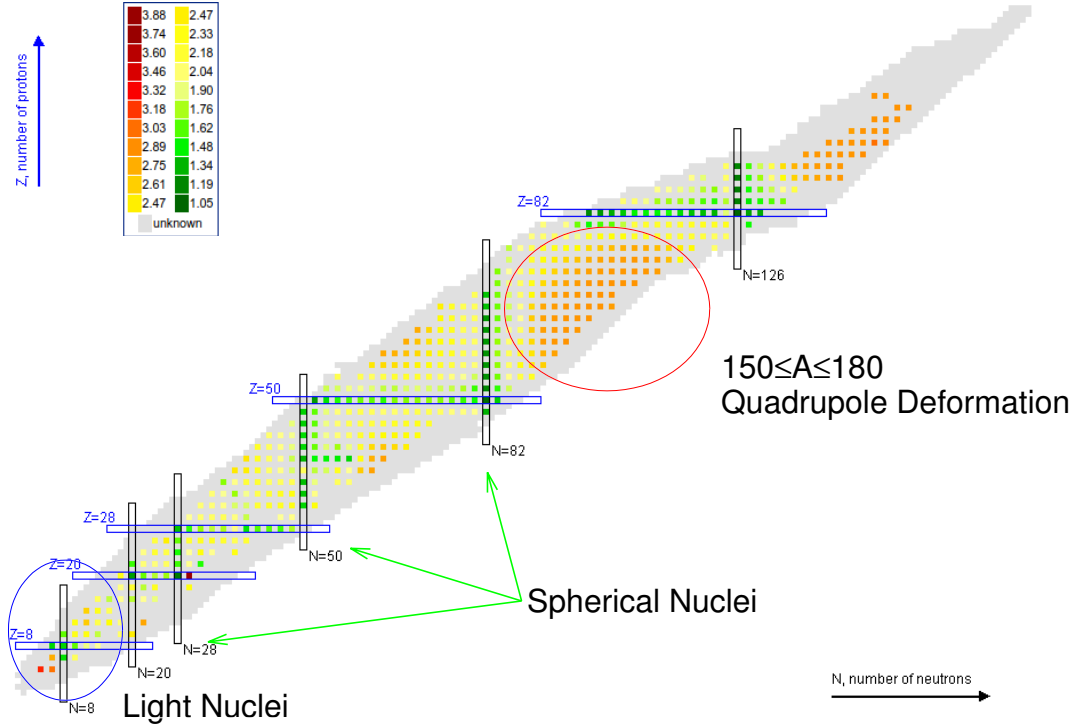


Figure 1.1. Chart of nuclides showing the varying degrees of deformation ($R_4/2$ values for even-even nuclei). Orange colored squares mark a well-deformed ground state, with green representing spherical nuclei.

One such phenomenon is the existence of surface oscillations of spherical nuclei, in which the nucleus can exhibit a macroscopic, collective motion of nucleons about the spherical equilibrium shape. These vibrations are well-documented and studied throughout the spherical mass ranges of the Chart of Nuclides as a posterchild of

collective degrees of freedom in the nucleus [4, 19]. These vibrational quanta, or phonons, also manifest in higher-order excitations (a two-phonon vibration, a three-phonon vibration, etc) as superimposed vibrations built on top of other vibrations.

Vibrations, however, are not the only collective degree of freedom afforded to the nucleons in the nucleus; collective rotations of nucleons about an axis of symmetry are abundant in nuclei [19, 77]. For spherical nuclei, a nuclear rotation is degenerate, as there is no defined axis of symmetry, but in deformed nuclei, we find strong experimental evidence of collective rotations about the axis of symmetry. We observe this strong rotational motion in the transition probabilities between nuclear states (B(E2) measurements quantized with a single-particle estimate) in Figure 1.2, where the entire region of deformation exhibits strong (>50 Weisskopf unit strength) transitions.

1.2 Deformation in Nuclei

Description of collective motion for a deformed nucleus begins by treating the nuclear radius as the static, deformed shape shown in Equation 1.1.

$$R = R_{sp} \left[1 + \sum_{\lambda\mu} \alpha_{\lambda\mu} Y_{\lambda\mu}(\theta, \phi) \right] \quad (1.1)$$

Here, R_{sp} is the average *spherical* nuclear radius, often given by $R_{sp} = R_0 A^{\frac{1}{3}} \approx 1.2 A^{\frac{1}{3}}$ fm. $Y_{\lambda\mu}(\theta, \phi)$ represent the spherical harmonics of order λ , with corresponding expansion coefficients $\alpha_{\lambda\mu}$. These static, permanent geometric deformations can be characterized by an expansion of their multipole order, λ , with $\lambda=2$ being a quadrupole deformation, $\lambda=3$ as an octupole, and so on. The lowest-order (and most common) static deformation in nuclei, the quadrupole deformation ($\lambda=2$), can be reparameterized into the Euler angles, β and γ , (Equations 1.2 & 1.3), which provides measures of the quadrupole deformation and axial asymmetry, respectively. Doing this also

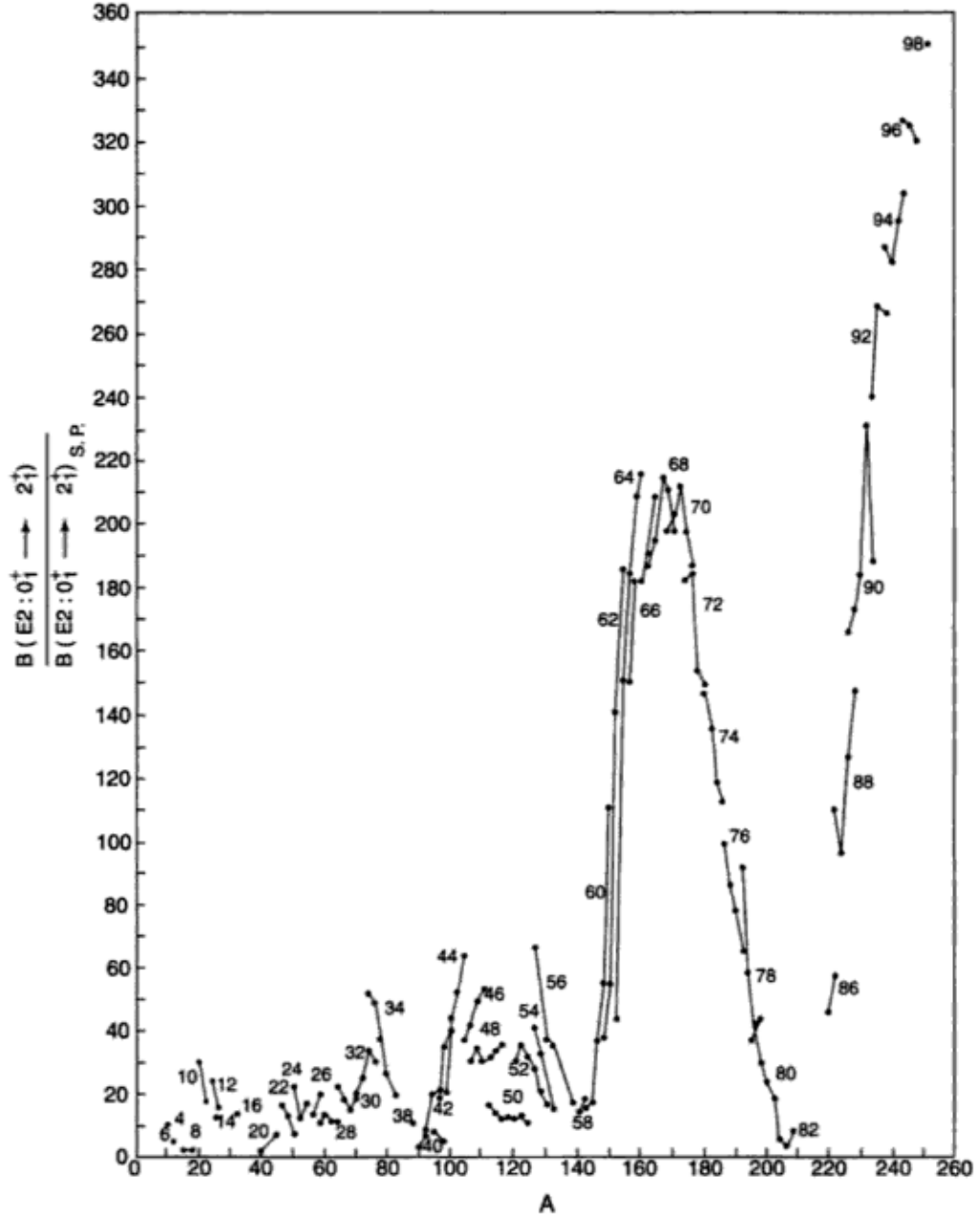


Figure 1.2. Measured B(E2) transition probabilities in single-particle units as a function of A, highlighting the region of deformation (as well as heavier actinide region) where strong nuclear rotations exist [19].

allows us to make a convenient convention of dynamic deformation ‘directions’ later on, as well as a categorization of the nuclear shape.

$$\alpha_{2,\pm 2} = \beta \sin \gamma \quad (1.2)$$

$$\alpha_{2,0} = \beta \cos \gamma \quad (1.3)$$

This work is strictly concerned with static, prolately deformed nuclei, or where $\beta > 0$ and $\gamma = 0^\circ$, although other nuclear shapes exist (oblate, axially asymmetric, etc). It is also convenient and prudent to recast the angular momentum of states in the deformed nucleus as a projection of the total angular momentum along the axis of symmetry (K^π); this is beneficial, as it helps us easily identify and distinguish the different types of collective motion in deformed nuclei. K^π can further be distinguished by the parity of states, as is typical by a $\pi = (-1)^K$ rule, where this is also a clue to the asymmetry of nuclear wave functions.

The Pauli Exclusion principle, or effects due to pairing, has a profound effect on the structure of states in the deformed nucleus. In one of the most important pairing effects, the pairing of fermions forbids particles from occupying the same space, so when two protons or neutrons pair together to create an excitation (or as the even-even nucleus resides in the ground state), they preferentially couple to $J^\pi = 0^+$. However, there is an energy intrinsic to the nucleus at which two nucleons will break their tendency to couple together as pairs; this pairing gap for protons and neutrons ($2\Delta_\pi$ & $2\Delta_\nu$ respectively) is taken from [50], and is a measure of the odd-even staggering of energies caused by the pairing interaction in the nuclear binding energy. Pairing effects also bring rise to the idea of nuclear excitations being created via quasiparticle pairs; this is stated in stark contrast to the rigid rules of the shell model where fermions (in the case of particle-hole states) will have defined occupancy of shells, and instead can exhibit partial occupancies. The energies of quasiparticle excitations simplifies the picture of the shell model immensely, in that these energies

are expressed relative to the absolute Fermi energy, which condenses the entire occupancy of the shell model down to a few excitations relative to this Fermi surface [19]. Since the quasiparticle energies are constructed with respect to the pairing gap 2Δ , we can see experimental evidence of this pairing gap, which affects the level density, the sphericity of surface shape, and the microscopic character of states [19]. In the rare-earth region of nuclei, this pairing gap is experimentally observed near ~ 1.5 - 2.0 MeV, where the states below this energy are the signatures of macroscopic collective motion of nucleons (or in terms of pairing, quasiparticle pairs in the form of vibrational phonons) as a whole, in a dramatic shift away from independent/single particle excitations [12]. With this key distinction between collective and single particle interactions in mind, the collectivity of states, not only below the pairing gap, but across the entire continuum of nuclear states is of paramount importance.

The pairing gap for a particular nuclei A_ZX_N can be calculated with Equations 1.4 and 1.5, where $E(N,Z)$ is the binding energy of the nucleus X for the particular neutron number N and proton number Z combination, and $E(N,Z+1)$ is the binding energy of a nucleus that has an added proton, $E(N,Z+3)$ is the nuclear binding energy of the nucleus with three added protons, and so on. For example, the proton pairing gap for ${}^{162}\text{Dy}$ would involve the binding energies of ${}^{162}\text{Dy}$, ${}^{163}\text{Ho}$, ${}^{165}\text{Tm}$, ${}^{161}\text{Tb}$, and ${}^{159}\text{Eu}$, for the respective entries in Equation 1.4.

$$2\Delta_\pi = \frac{1}{8}[16E(N, Z) + 9E(N, Z + 1) + E(N, Z + 3) + 9E(N, Z - 1) + E(N, Z - 3)] \quad (1.4)$$

$$2\Delta_\nu = \frac{1}{8}[16E(N, Z) + 9E(N + 1, Z) + E(N + 3, Z) + 9E(N - 1, Z) + E(N - 3, Z)] \quad (1.5)$$

Given some excitation energy, the nucleus will not remain in its stable ground

state; the deformed nucleus' excitations are not necessarily treated as single particle excitations, but instead as a movement of multiple nucleons *collectively* (as a whole) throughout the nuclear shape as it rotates. In the mid-20th Century, theoretical treatments to describe a deformed nucleus emerged as the geometric collective model of Bohr and Mottelson [11], and one of the beauties of of this descriptive model was the near-immediate appearance of low-lying surface oscillations (in this case, nuclear vibrations) about the deformed ground shape [11], as well as the prevalence of fundamental nuclear rotations. These two modes of collective motion, vibration and rotation, make up the basic degrees of freedom available to a deformed nucleus, where, in stark contrast to the degenerate vibrations of a spherical nucleus, a vibration in a deformed nucleus can be along any of the axes of symmetry according to a time-dependent multipole expansion of the deformed shape (Equation 1.1). In its lowest order ($\lambda=2$ expansion), the nucleus will exhibit quadrupole oscillations around its equilibrium shape in one of two possible types, a γ -vibration or a β -vibration. The notation and phenomenology behind these vibrations alludes to the 'direction' of oscillation with respect to the Euler parameterization. For example, the γ -vibration is a dynamic oscillation that breaks axial symmetry (the parameter γ) to maintain a $K^\pi=2^+$ projection of angular momentum, while the β -vibration maintains both axial symmetry, as well as a $K^\pi=0^+$ projection of angular momentum (an oscillation of quadrupole deformation β). Note the positive parity, which indicates a reflection symmetry for the nuclear shape and corresponding wave functions. Crude cartoon visualizations of these quadrupole vibrations can be seen in Figures 1.3 and 1.4. In these pictures, the schematic on the left looks down the axis of symmetry (represented by bold, black lines), with the side view on the right. Thin black lines outline the deformed equilibrium shape, with dashed red lines showing the extent of the dynamic, quadrupole oscillations; blue arrows are meant to guide the eye as to how the nucleus changes shape.

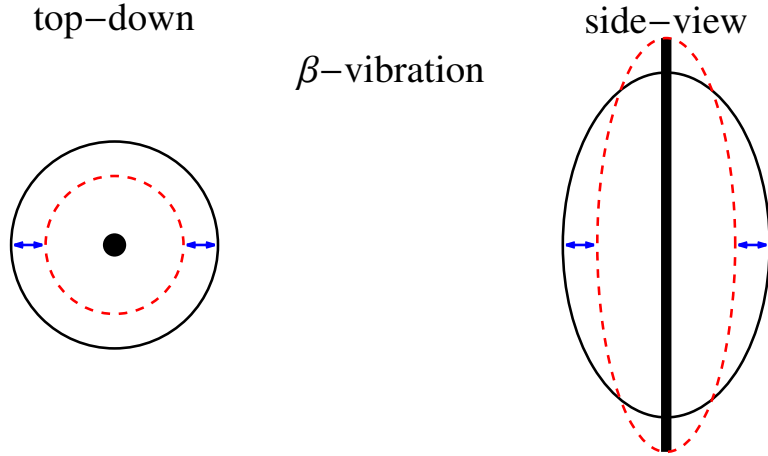


Figure 1.3. Schematic of the β quadrupole vibration about a deformed equilibrium shape.

If a single vibrational phonon can be superimposed on the rotational ground state, how feasible is the two-phonon case for deformed nuclei? Linear combinations of the quadrupole phonon structure would involve the $\gamma\gamma$ (with either a 0^+ or 4^+ K^π projection), $\beta\gamma$ ($K^\pi=2^+$), & $\beta\beta$ vibrations (again, $K^\pi=0^+$). As an analogue to the classical harmonic oscillator problem, the addition of multiple phonon quanta will increase the energy of the system by some proportional amount, so we would expect a 2 phonon vibration to be double the energy of the 1 phonon vibration, or that $E_{\text{phonon}} \propto N_{\text{phonon}}$. *In theory*, all modes of vibration should be obvious and abundant, but we will see that this is not immediately the case for deformed rare-earth nuclei given the current state of experimental data, especially with varying degrees of anharmonicity at play.

A further study in deformed nuclei is on the higher order octupole ($\lambda=3$) vibrations and if they can also exist, but the motions of the nuclear surface are significantly more difficult to envision as a drawing, especially on a 2-dimensional piece of paper.

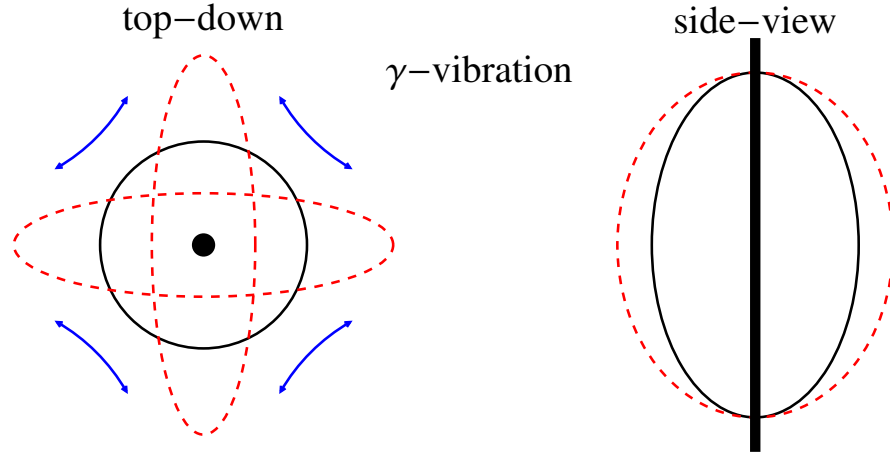


Figure 1.4. Schematic of the γ quadrupole vibration about a deformed equilibrium shape.

The octupole vibration (in spherical nuclei) manifests as a $K^\pi=3^-$ projection on the axis of symmetry, with asymmetric wave functions (and shape) due to the negative parity. However, in contrast to the degenerate quadrupole modes of $K=0,2$ in deformed nuclei, we expect a split-degeneracy of this $K^\pi=3^-$ projection into a quartet of possible projections, $K^\pi=0^-, 1^-, 2^-,$ and 3^- [11].

1.3 Excited States in Deformed Nuclei

The question then arises: what would these quadrupole and octupole vibrations look like represented as excited states in the well-deformed rotational nucleus? A mock level scheme representing the lowest lying quadrupole and octupole vibrations is given in Figure 1.5, where we can immediately see the ensemble of states corresponding to each vibration, and each vertical ‘band’ lines up with rotational members a particular vibrational state. The single-phonon vibrations of γ and β type have

their corresponding two-phonon counterparts and combinations drawn at twice the excitation energy that assumes a completely harmonic vibration.

Phonon states in deformed nuclei

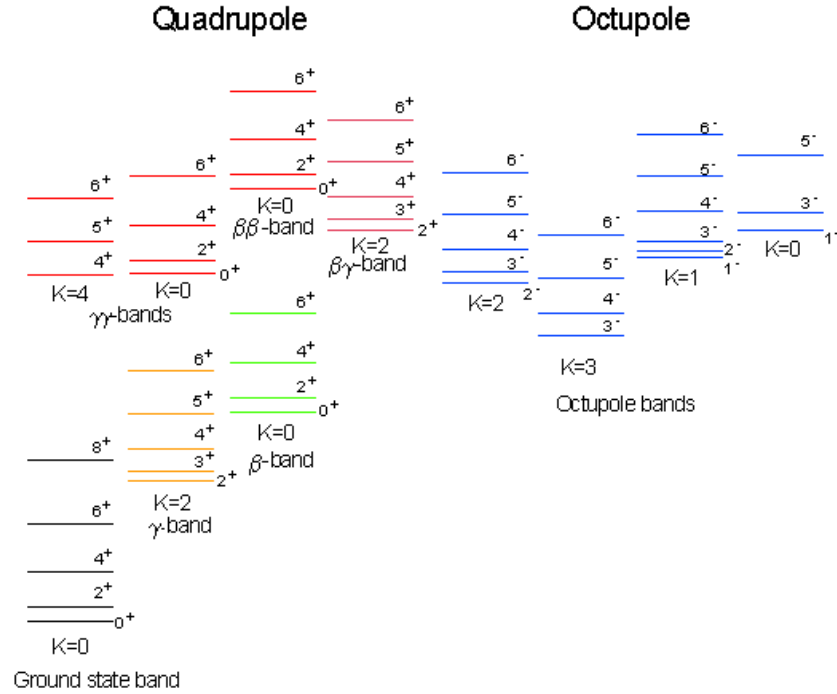


Figure 1.5. Level scheme of the various phonon vibrations in deformed nuclei [57].

Nuclear rotations are superimposed on the base vibration expected for each type of phonon as band excitations, (single quadrupole/octupole and double quadrupole) according to the $J(J+1)$ rule set out in Equation 1.6. These additions of rotational energy directly correlate to higher-lying members of a band, with \mathcal{I} being the moment

of inertia for the nucleus.

$$E_{rot} = \frac{\hbar}{2\mathcal{I}}[J(J+1) - K(K+1)] \quad (1.6)$$

The lowest lying state of a particular band will (with the exception of a $K^\pi=0^-$ band) always have $J^\pi=K^\pi$ (*e.g.* the bandhead of the $K^\pi=0^+$ band will be a $J^\pi=0^+$ excitation), where the spins and parities of other members (the superimposed rotations) of the band are selected by the selection rules outlined in Table 1.1. In short, $K^\pi=0^\pm$ will contain *every other* spin-parity, while any other projection of K simply counts up J^π from the bandhead value. For example, a $K^\pi=0^+$ band will have $J^\pi=0^+$, 2^+ , 4^+ (and so on) members, a $K^\pi=0^-$ band will contain similarly structured 1^- , 3^- , 5^- (*ad infinitum*) members, where a $K^\pi=7^+$ band has 7^+ , 8^+ , and so on.

	$K^\pi=0^+$	$K^\pi=0^-$	$K^\pi \neq 0^\pm$
$J_0^\pi=$	K^+	$(K+1)^-$	K^\pm
$J_1^\pi=$	$(K+2)^+$	$(K+3)^-$	$(K+1)^\pm$
$J_2^\pi=$	$(K+4)^+$	$(K+5)^-$	$(K+2)^\pm$
\vdots	\vdots	\vdots	\vdots

TABLE 1.1

Selection rules used to determine J^π values of rotational members of a specific K^π band.

In Figure 1.5, we immediately see a key (and long-lived) question in nuclear

structure physics: What are the nature of 0^+ excitations? From this ideal, toy picture, we already see three possible ways to make a 0^+ excitation. Understanding the nature of these common, low-lying excitations in nuclei has been a cornerstone of nuclear structure in the rare-earth region for decades. Experimentally, the searches for the nature of 0^+ have been cloudy from the evidence of double-phonon states across the entire rare-earth region such as the $\gamma\gamma$ -type vibration in several nuclei ([30], [46], [2]) that exhibit strongly collective, anti-aligned doublets of the γ -vibrational phonon.

By a similar merit, in Figure 1.5 we see the split quartet of low-lying negative parity states, as expected, yet these $\lambda=3$ excitations are not as well studied as their quadrupole counterparts [19]. Several different phenomena occur in the low-lying negative parity states of deformed nuclei, including an inversion in the energy ordering of states as N increases, irregularities among the transition probabilities (as a function of ΔK) throughout the rare-earth region of nuclei, among others [15, 19]. Continue the multipole expansion to higher-order terms, and the hexadecapole ($\lambda=4$) vibrations appear. Again, we state here that these negative parity states and higher-order vibrational phonons have not seen the same order of experimental rigor and study as their $\lambda=2$ counterparts have; this work hopes to aid in the lack of vital lifetime information on low-lying negative parity states in the deformed region of nuclei. Systematic behavior of negative parity states (as well as the strength of quadrupole vibrations) varies wildly across the entire rare-earth region of nuclei and have been caught in the epicenter of experimental focus in nuclear structure in the past several decades.

Much like the quadrupole counterparts, we can also picture a structure of coupled quadrupole-octupole-type phonons to either octupole or quadrupole phonons, further increasing the possible K -projections available to study [58]. For example, a $2^+ \otimes 3^-$ coupling can produce projections of 1^- , 2^- , 3^- , 4^- & 5^- , if we follow the same parity and triangle selection rules inherent to quantum systems.

1.4 Historical Impetus in Experimental Nuclear Structure

Experimentally, how have these low-lying excitations in deformed nuclei been studied in the past? In one of the pioneering (and one of the most-cited) works in the field, Leshner *et. al* found a surprising, completely unprecedented number of excited 0^+ states in deformed ^{158}Gd [47]. This work utilized the Q3D magnetic spectrograph at Munich with two-nucleon transfer reactions, a particularly adept way to find $J^\pi=0^+$ excitations, where seven new 0^+ excitations (of thirteen total) were discovered. The Q3D was to later be used by D. Meyer in 2006 to continue this newly sparked renaissance of nuclear structure studies on the nature of 0^+ excitations in deformed nuclei [55].

Recall the Pauli principle that governs nucleon pairing; in a two nucleon transfer reaction, (p,t) or (t,p), the paired neutrons entering or exiting the nucleus will preferentially couple to $J^\pi=0^+$ states. For an even-even nucleus with a 0^+ ground state, transfer reactions have a high overlap to this mode of excitation to $J^\pi=0^+$, giving the Q3D spectrograph its sensitivity. In the two nucleon transfer reactions angular distributions of outgoing tritons (or protons) are collected at various angles with respect to the beam direction by the opening of the spectrometer and bent through a series of 3 dipole magnets to a focal-plane detector (see Figure 1.6). Differing energies of ejectiles are bent by various amounts to the focal-plane detector, where positional dependence in the detector is directly related to the energy of the excited state populated (E_x), according to Equation 1.7. The remarkable resolution produced by the setup of quadrupole and dipole magnets propelled the Q3D above previously unattainable levels of discrimination, and has forever changed the field of nuclear structure.

$$E_{ejectile} = E_{projectile} - Q - E_x - E_{C.O.M.} \quad (1.7)$$

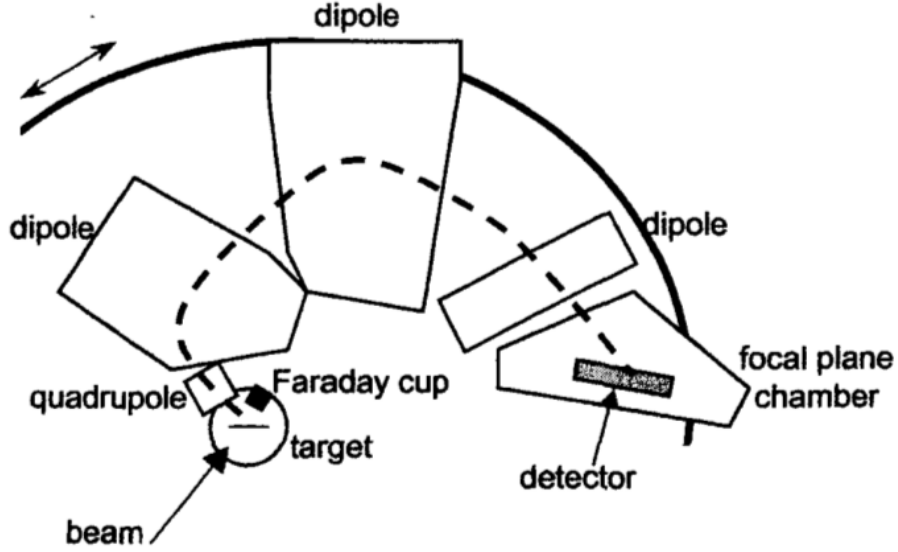


Figure 1.6. Schematic of the Q3D magnetic spectrograph at Munich used for precision $(p,t)/(t,p)$ spectroscopy [54].

In the case of a $\Delta L=0$ transition, the angular distribution of detected particles will be extremely forward-peaked; this is an easily observed experimental signature, and is completely unique to $\Delta L=0$, as the measured intensity (differential cross section) can drop by an order of magnitude from $\sim 5^\circ$ to $\sim 17^\circ$ [55]. Confirmation of the $J^\pi=0^+$ assignments can be made by comparing the relative cross sections from the experimental data to a Distorted Wave Born Approximation (DWBA) calculation, where an example of this can be seen in Figure 1.7 for the 0^+ states in ^{158}Gd .

This renaissance of $(p,t)/(t,p)$ reaction studies has emerged in the past decade, as well as a coordinated flurry of theoretical and experimental efforts and campaigns to begin to answer the still open and important query of the nature of 0^+ excitations in the rare-earth region of nuclei [1, 13, 15, 23, 28, 38, 63, 72, 79, 82]. Figure 1.8 shows the number of 0^+ states for rare earth nuclei, due in large part to the two nucleon

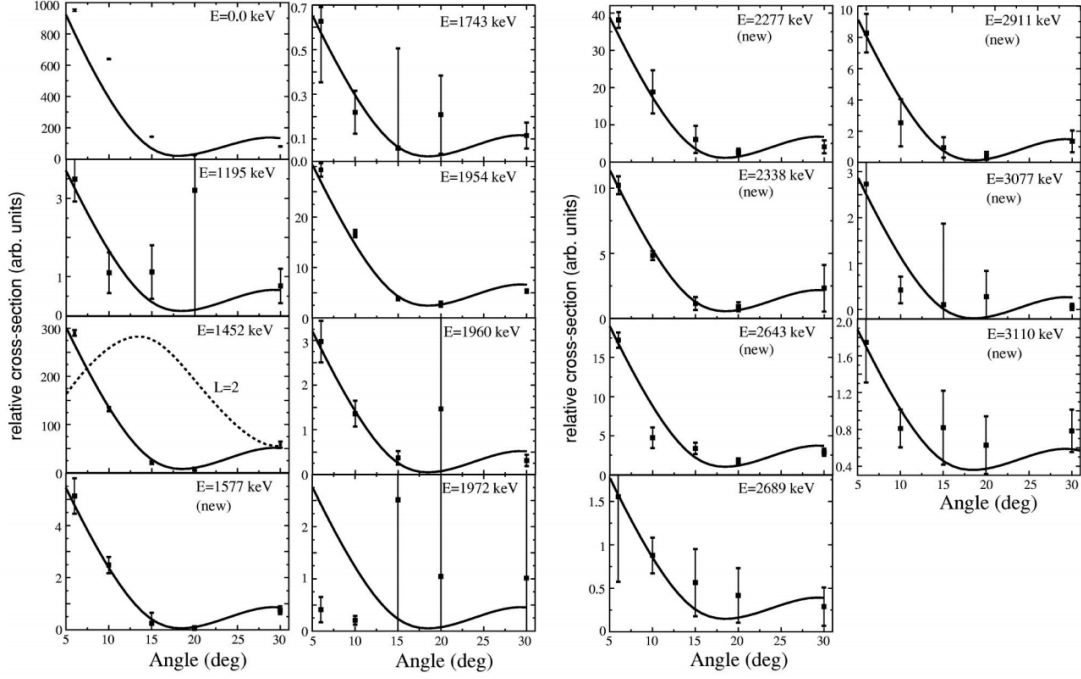


Figure 1.7. Angular distribution data for all 0^+ states in ^{158}Gd observed in the (p,t) reaction in [55]. A DWBA calculation for an $L=2$ transition is shown as a dotted line in the $E=1452$ keV plot to show the unique nature of the $L=0$ transitions (in solid black).

transfer reaction studies by Meyer and Leshner [47, 55].

In their recent review [38], Heyde & Wood outline several criteria (key experimental fingerprints) to successfully elucidate the true nature of these 0^+ excitations.

- I. Two nucleon transfer reaction strengths, (p,t) or (t,p)
- II. Monopole $E0$ strengths, $\rho^2(E0)$
- III. Absolute reduced transition probability measurements, $B(E2;0_i^+ \rightarrow 2_{g.s.}^+)$

Individually, the experimental quantities listed above cannot fully probe any collective nature of excitations within the nucleus, but in tandem, can uncover much of the mystery of the makeup of nuclear states.

In many cases (due in part to [47, 55]) throughout the rare-earth region of nuclei,

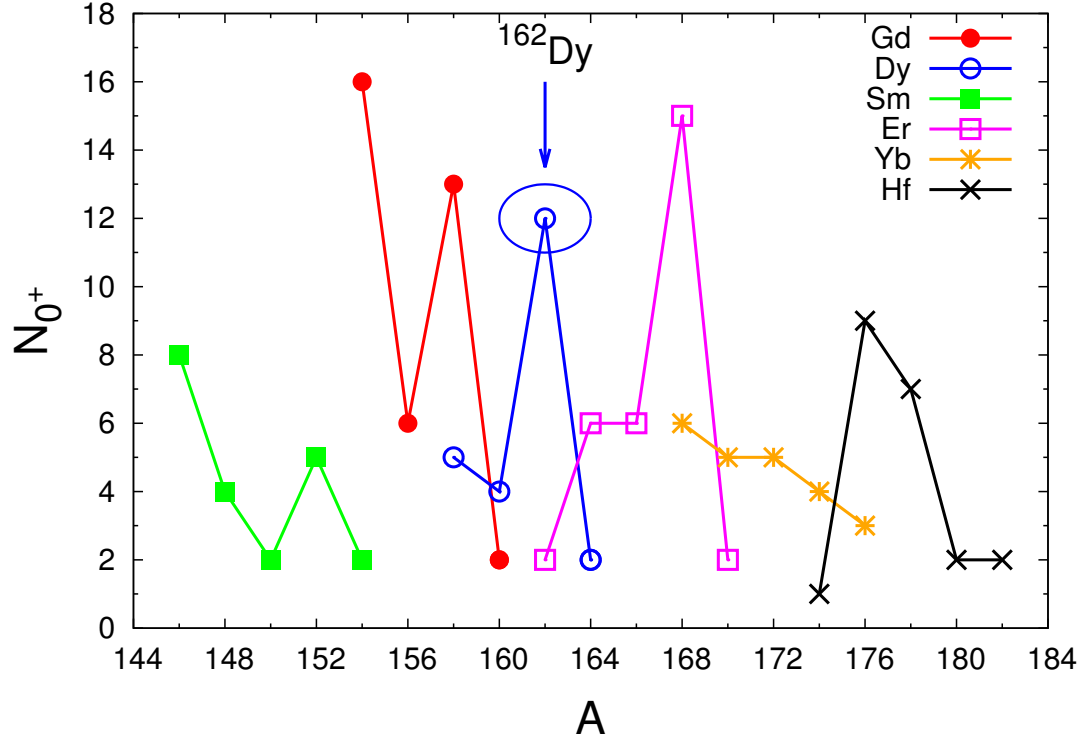


Figure 1.8. Number of 0^+ states in rare earth isotopes of Sm, Gd, Dy, Er, Yb, and Hf. ^{162}Dy is highlighted with a blue circle.

two nucleon transfer reaction strengths are available; the relative cross sections can provide a clue to pairing configurations in nucleons [38]. This implies that a large relative cross section between two-nucleon transfers will signify a large single- or two-quasiparticle nature of a particular excited state. Historically, inflated two-nucleon transfer reaction cross sections between 0^+ states were observed as evidence of rapid shape change of the nucleus [23]. Multinucleon transfer reactions also offer a double-pronged attack, in that the spectroscopy can also find/confirm the existence of 0^+ excitations, recalling the (p,t) reactions outlined in §1.4.

Monopole E0 transitions, the γ -ray forbidden decay of a $0^+ \rightarrow 0^+$ transition, provide insight into a unique facet of the nuclear structure, as the transition is directly related to the mean-square nuclear radius, and thus, the extent of deformation. The

measurement of E0 transitions offers clues to the nature of 0^+ states, but these experimental signatures are far from easy to obtain [37]. Since a γ -ray carries *at least* one unit of angular momentum away from the nucleus, and no angular momentum transfer takes place in a $0^+ \rightarrow 0^+$ transition, the nucleus must decay via internal conversion electrons. The transition probability of an E0 transition differs in form from the traditional γ -ray reduced transition probability (see §1.5.2), but is expressed by the monopole strength, the internal conversion electron analogue, $\rho^2(\text{E0})$, instead. Recent studies using the IBA have examined the behavior of E0 transitions in nuclei [27] at both the limits of the SU(3) symmetry and in the middle of the symmetry triangle, with connections to the collectivity of states discussed.

Finally, the absolute B(E2) transition probabilities (inversely proportional to the lifetime of excited states) are the largest clue to the collectivity of states, as they hold a vital part in testing both the IBA and the geometric collective model. The measurement of excited state lifetimes (as seen in the upcoming §1.5.1) are the main focus on this work.

Strong octupole shape correlations have been experimentally observed in spherical/transitional nuclei (and recently in neutron-rich ^{144}Ba) by the observation of strong E3 multipolarity radiation that decays to the ground state [16, 31]. Similarly, strong quadrupole-octupole coupling has been observed in the form of $2^+ \otimes 3^-$ coupling in several cases by the observation of $K^\pi=2^- \rightarrow 2_\gamma^+$ transitions [58, 71, 74]. In all of these cases, we see and stress the importance of reduced transition probabilities connecting nuclear states. One experimental observable that points toward any octupole correlation (as a means to measure reflection asymmetry, a signature of octupole deformation) is the measurement of E1-multipolarity radiation, which we employ in this work.

1.5 Assessing Nuclear Structure from Decay Radiation

The detection of electromagnetic γ radiation is of great value when studying the structure of the nucleus. Since γ -decay of the nucleus is one of the dominant methods of de-excitation for states below the energy threshold for particle emission, a link (some quantum mechanical operator) between two quantum states can be made via the electromagnetic Coulomb process. Usually expressed as a matrix element, Equation 1.8 is the manifestation of observables from some corresponding operator (in this case, the electromagnetic operator acting on the nuclear eigenfunctions). In the case of electromagnetic decays, the matrix elements of the E2 multipole transition operators remain a key facet of nuclear structure, as the quadrupole electromagnetic operator drives collective quadrupole transitions in nuclei, lending its importance almost immediately. Similarly, the other multipole expansions of the electromagnetic operator (isovector dipole, isoscalar dipole, octupole, etc.) directly link the charge distributions of two nuclear states, such as the E3 operator for octupole shape change.

$$\mathcal{M}_{fi} = \langle \psi_f | \mathcal{H} | \psi_i \rangle \quad (1.8)$$

When studying excited states in nuclei, measurement of the transition probability (related to the matrix element) becomes the basis for understanding nuclear structure phenomena.

1.5.1 Why Measure Lifetimes?

The transition probability (\mathcal{W}) for a γ -decay that de-excites the nucleus from an initial state to a final state can be expressed in terms of the mean lifetime (τ), the average time the nucleus stays in an excited state, or by the half-life ($t_{1/2}$). The exact relationship can be seen in Equation 1.9.

$$\mathcal{W} = \frac{1}{\tau} = \frac{t_{1/2}}{\ln 2} \quad (1.9)$$

For an excited state with multiple γ -decay channels, we can expand the total \mathcal{W} as a sum of all transition probabilities weighted by the branching ratio (BR_i) and internal conversion coefficient (α_i) of each transition (Equation 1.10).

$$\mathcal{W} = \sum_i \frac{BR_i}{\tau(1 + \alpha_i)} \quad (1.10)$$

The number of full mathematical derivations of Fermi's Golden Rule from time-dependent perturbation theory rivals that of Talmi's estimation of 2^+ configurations in Samarium-154 ($\sim 3 \times 10^{14}$) [19]. The exhaustive treatment can be seen in much greater detail in various sources ([77],[37],[10]), where (in this work) we will start with Fermi's Golden Rule [77] in Equation 1.11.

$$\mathcal{W} = \frac{2\pi}{\hbar} |\langle \psi_f | \mathcal{H}_{EM,int} | \psi_i \rangle|^2 \rho(E_\gamma) \quad (1.11)$$

Here, we can see the direct relationship between the nuclear matrix element and γ -ray energy-dependent density of states ($\rho(E_\gamma)$) to the transition probability, \mathcal{W} . This square of the matrix element describes the coupling of the nuclear-based interaction Hamiltonian to an external electromagnetic field, which brings the nucleus from some initial state $|\psi_i\rangle$ to a final state $|\psi_f\rangle$. This transition, for γ -decay in the nucleus, is represented by the electric or magnetic multipole operator(s) of order λ , \mathcal{O}_λ . From Wigner-Eckhart theory, we can remove any angular momentum dependence from the full matrix element ($|\mathcal{M}_{fi}| = \langle \psi_f | \mathcal{H}_{int} | \psi_i \rangle$) to give us the reduced transition probability in Equation 1.12.

$$B(\pi\lambda; J_i \rightarrow J_f) = |\mathcal{M}_{fi}|^2 = \frac{1}{2J_i + 1} |\langle J_f | \mathcal{O}_\lambda | J_i \rangle|^2 \quad (1.12)$$

Performing a multipole (and subsequent series) expansion of \mathcal{O}_λ into the spherical Bessel functions, spherical harmonics, and the nuclear current density $\mathcal{J}(\vec{r})$ (Equations 1.13 and 1.14) [77], we arrive at Equation 1.15.

$$\mathcal{O}_{\lambda\mu}(E\lambda) = -\frac{(2\lambda+1)!!}{c(\lambda+1)k^{\lambda+1}} \mathcal{J}(\vec{r}) \cdot \vec{\nabla} \times (\vec{r} \times \vec{\nabla})(j_\lambda(kr)Y_{\lambda\mu}(\theta, \phi)) \quad (1.13)$$

$$\mathcal{O}_{\lambda\mu}(M\lambda) = -\frac{(2\lambda+1)!!}{c(\lambda+1)k^\lambda} \mathcal{J}(\vec{r}) \cdot (\vec{r} \times \vec{\nabla})(j_\lambda(kr)Y_{\lambda\mu}(\theta, \phi)) \quad (1.14)$$

$$\mathcal{W} = \frac{8\pi}{\hbar} \frac{(\lambda+1)}{\lambda[(2\lambda+1)!!]^2} \left(\frac{E_\gamma}{\hbar c} \right)^{2\lambda+1} B(\pi\lambda; J_i \rightarrow J_f) \quad (1.15)$$

Now, simply recall Equation 1.10 to make Equation 1.16, an extremely important quantity for nuclear structure studies, as every non-constant quantity can be determined in laboratory experiments.

$$B(\pi\lambda; J_i \rightarrow J_f) = \frac{\hbar}{8\pi} \mathcal{F}(\pi\lambda) \frac{BR}{\tau(1+\alpha)} \frac{\lambda[(2\lambda+1)!!]^2}{(\lambda+1)} \left(\frac{\hbar c}{E_\gamma} \right)^{2\lambda+1} \quad (1.16)$$

In Equation 1.16, $\mathcal{F}(\pi\lambda)$ is a measure of the mixing from differing multipolarity γ radiation; For pure E1, E2, or M1 transitions, this factor collapses to unity, where $\mathcal{F}(\pi\lambda)$ for mixed E2 & M1 radiation follows the relations in 1.17 & 1.18:

$$\mathcal{F}(E2) = \frac{\delta^2}{1+\delta^2} \quad (1.17)$$

$$\mathcal{F}(M1) = \frac{1}{1+\delta^2} \quad (1.18)$$

The multipole mixing fraction δ is an experimentally measured quantity (to be discussed later) as a ratio of the E2/M1 transition strengths.

1.5.2 Importance of Transition Probabilities

To provide a comparison of the relative collectivity of a transition on a meaningful scale, it is generally prudent to express $B(\pi\lambda)$ in terms of a Weisskopf estimate. This formulation assumes that only one nucleon is involved in a particular transition [77], and is given in Equations 1.19 and 1.20 for electric-type transitions and magnetic-type transitions, respectively.

$$B(E\lambda) = \frac{0.12^{2\lambda}}{4\pi} \left(\frac{3}{\lambda+3} \right)^2 A^{\frac{2\lambda}{3}} \quad (1.19)$$

$$B(M\lambda) = 0.12^{2\lambda-2} \frac{10}{\pi} \left(\frac{3}{\lambda+3} \right)^2 A^{\frac{2\lambda-2}{3}} \quad (1.20)$$

These colloquial ‘Weisskopf Units’ (W.u.) act as the standard candle for collective strength in nuclei, as $B(\pi\lambda) \gg 1$ imply strong collective motion in the nucleus. Weisskopf units are not universally adopted however, with some (especially older) works relying on the natural units of $e^2 b^\lambda$. Transition probabilities in this work are reported in W.u., but for the purposes of unit conversion, Table 1.2 shows this conversion for E1, M1, E2, and E3 transition probabilities for both ^{160}Gd and ^{162}Dy .

To give these transition probabilities context in a vibrational sense, the electric and magnetic multipole operator is proportional to the phonon annihilation operator, \mathbf{b} [77]. This is again, analogous to the classic harmonic oscillator problem in quantum mechanics, where the basis states that make up the eigenfunctions of the phonon creation/destruction operators. Since the matrix element of this annihilation operator and two harmonic oscillator states is $\sqrt{N_{phonon}}$, the reduced transition probability for a γ -decay that destroys an N_{phonon} state will be proportional to the number of phonons in the state, N_{phonon} , outlined in Equation 1.21.

$$\mathcal{O}_\lambda \propto \mathbf{b}_\lambda \rightarrow \langle \psi_f | \mathbf{b}_\lambda | \psi_i \rangle = \sqrt{N_{phonon}} \rightarrow B(\pi\lambda) \propto N_{phonon} \quad (1.21)$$

$\pi\lambda$			^{160}Gd	^{162}Dy	
1 mW.u.	E1	=	1.90	1.91	e^2b
1 W.u.	E2	=	5.16E-7	5.25E-7	e^2b^2
1 W.u.	E3	=	1.52E-9	1.56E-9	e^2b^3
1 W.u.	M1	=	1.79	1.79	μ_N^2

TABLE 1.2

Unit conversion for transition probabilities from Weisskopf units to $\text{e}^2\text{b}^\lambda$

(μ_N^2 for M1s) for ^{160}Gd and ^{162}Dy .

This fact implies the transition probability for a double phonon vibrational state will be enhanced in relation to the already inflated $B(E2)$ of a single phonon vibration (in W.u.). These high $B(E2)$ values should be a ‘signature’ of collective motion, however, recall that $B(E2) \propto E_\gamma^{-5}$, meaning higher energy transitions will be suppressed in relation to the lower energy transition probabilities. The delicate balance between interband and full de-exciting transitions must be stressed to fully understand the structure of these states.

Transition probabilities can also be compared to the colloquial ‘Alaga’ rules to provide a model-independent benchmark of relative transition strength. The Alaga rules imply that the intrinsic matrix elements for two transitions leaving the same level will be identical, so the ratio of their reduced transition probabilities are only dependent on the square of the Clebsch-Gordan coefficients (Equation 1.22). As a first-order approximation, these rules agree remarkably well with experimentally measured $B(E2)$ values, especially for the lowest spin members of a rotational band (again, the bulk of this work).

$$\frac{B(E2; J_i \rightarrow J_f)}{B(E2; J_i \rightarrow J'_f)} = \frac{\langle J_i K_i 2(\Delta K) | J_f K_f \rangle^2}{\langle J_i K_i 2(\Delta K) | J'_f K_f \rangle^2} \quad (1.22)$$

Of course, a limitation behind the Alaga rules is that it only gives relative transition probabilities, where the absolute $B(E2)$ is needed, and also can only be used to compare transition probabilities for multiple decays out of the same parent state.

1.6 Decay and Structure Systematics in the $150 < A < 180$ Region

As seen in [38], the jury is still out on the nature of low-lying excitations in rare-earth nuclei and the evolution of collectivity with nuclear deformation. Globally, the lifetimes presented in this work aim to elucidate some of the mystery behind the systematic behavior (or lack thereof) of quadrupole and octupole vibrations in deformed nuclei. Many of the lifetime measurements made in this work are new, in an region of nuclei where literature lifetimes (especially lifetimes of 0^+ states) are scarce. Figures ??, and 1.14 show the even isotopes of rare-earth nuclei throughout varying degrees of deformation (marked by the $R_{\frac{4}{2}}$ value). Each set of level schemes displays the ground state band, excitation energies of the first excited 2^+ bandhead, the energies of all excited 0^+ states, literature $B(E2)$ values (in W.u.) for any 2^+ or 0^+ de-excitations, as well as the proton & neutron pairing gap ($2\Delta_\pi$ in green and $2\Delta_\nu$ in blue) for each isotope (calculated from Equations 1.4 and 1.5 in [6] & [50]).

In these figures, we can immediately observe some key motivations for performing lifetime measurements in the rare earth region. First, there are currently pockets where we lack literature lifetime information for 0^+ excitations in the $150 < A < 180$ region, especially below the proton and neutron pairing gaps, where we would expect to find macroscopic collective motion. Second, in the Gadolinium nuclei, a particular suppression of the collectivity of the lowest-lying 0^+ state appears as the static deformation increases. This decrease in collective strength compliments the long-standing

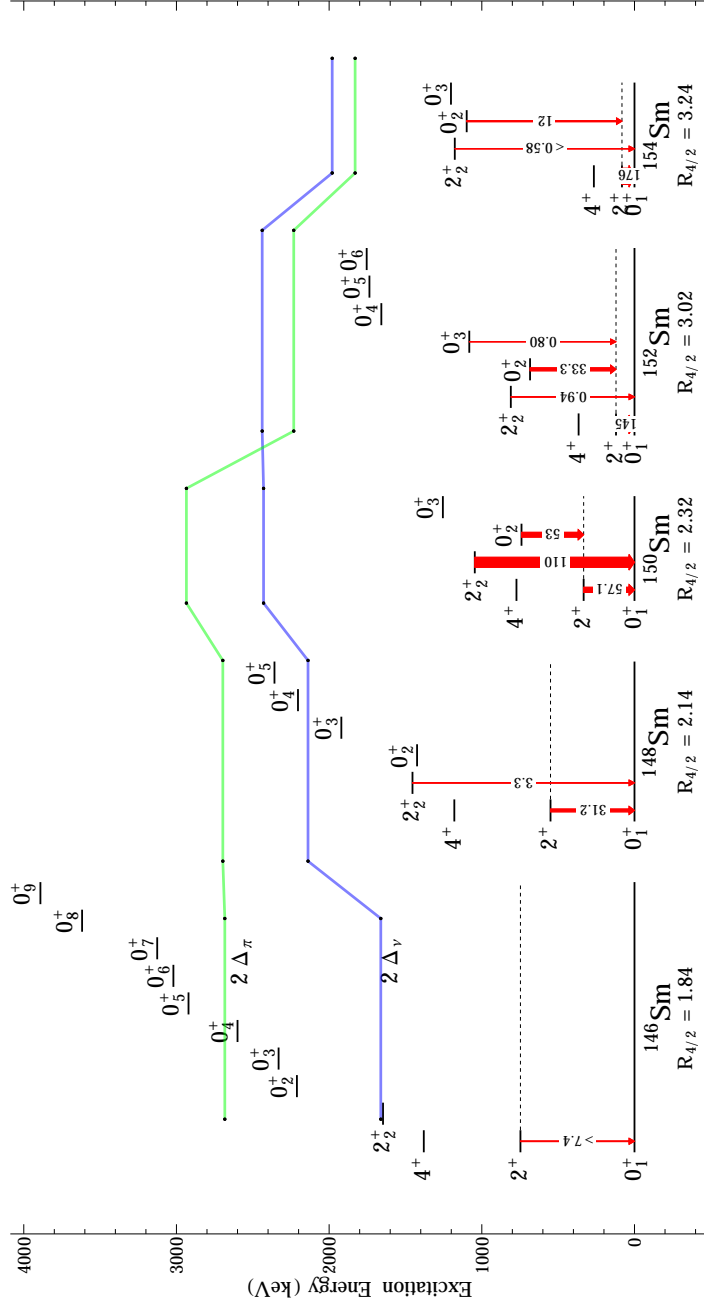
irregularities in collective strength of 0^+ excitations, highlighted by the otherwise ‘well-behaved’ collectivity of the lowest lying $K^\pi=2^+$ bands [13, 20]. Lastly, this general inconsistency in collective strength of the 0^+ states must be further investigated (previous studies include [29, 67, 68]) to match the assertions provided in [38]. It is entirely reasonable to make the case for strongly collective β -vibrations in spherical or transitionally deformed nuclei with strong $B(E2)$ s to the ground state 2^+ , (see $^{150,152}\text{Sm}$ in Figure 1.9 and ^{154}Gd in 1.10) where $R_{\frac{4}{2}} < 3$, but as we move to the well-deformed, rotational limit of nuclei, the story definitively changes, and the behavior of the lowest-lying 0^+ state changes drastically!

We can also see the lack of lifetime information for low-lying negative parity states in rare-earth nuclei, of which, we will study the same cases (^{160}Gd and ^{162}Dy) for the isotopic chains of even-even rare-earth nuclei. Figures 1.15 and 1.16 show the energy systematics for the lowest-lying negative parity bands across isotopes. Immediately again, we see the energies of the negative parity states mentioned in §1.3 in regards to the shifting and re-ordering of the split negative parity bands. Again, just like the $K^\pi=0^+$ bands, crucial lifetime information for these states is scarce (only 6 lifetimes of negative parity states are known in Dysprosium nuclei); given the number of excitations below the pairing gap (where we expect to see collective excitations), measurement of the $B(E1)$ transition probabilities can allude to any octupole correlations as a phonon excitation in the nuclei discussed in this work, yet the most important piece of experimental evidence (which still remains out of the scope of this work) is the absolute $B(E3)$ transition probabilities.

We end discussion of the systematics of rare-earth nuclei with any known multiphonon configurations ($K^\pi=0^+, 4^+$ $\gamma\gamma$ type, $K^\pi=0^+$ $\beta\beta$). Figure 1.19 contains a series of level schemes of rare-earth nuclei with measured and confirmed two-phonon states; these states are evident by the observation of collective decays to known collective states. For example, the 4^+ $\gamma\gamma$ -vibration in ^{166}Er decays via a 7.4 Weisskopf

unit $B(E2)$ to the bandhead of the 2^+ γ -vibration (it then subsequently decays via a collective $B(E2)$ to the ground state). As with previous assertions about the ‘reliability’ of the γ -vibration as a paradigm of nuclear collective vibrations, Figure 1.18 shows the absolute $B(E2; 2^+_{\gamma} \rightarrow 0^+_{gs})$ measurements in the literature from the $K^{\pi}=2^+$ bandheads, simply to highlight its uniformity over the entire deformed rare-earth region. The trend for Samarium nuclei is drastic, but these isotopes lie in a region of extremely fast shape-change, from nearly spherical to fully deformed within a few nucleons! In a perplexing change of rhetoric in the rare-earths, we observe (and continue to investigate) that many well-deformed nuclei do not exhibit the traditional Bohr-Mottelson behavior of a collective β -vibration existing as the lowest-lying 0^+ state. Instead, many of these lowest-lying 0^+ states exist as the $\gamma\gamma$ -vibration, with distinctly collective transitions to the 2^+ γ -band. Truly, whether or not the notion of a traditional β -type vibration is valid seems to be lacking in the deformed case, from the current experimental data. Compare the number of known 0^+ $\gamma\gamma$ configurations to the preceding Figures (??) that highlight the status of lifetime measurements of the states and we observe the distinct lack of structure information that still plagues the rare-earth region. No known $\beta\gamma$ -vibrations have been observed in the rare-earth nuclei at any excitation energy via a collective transition to a collective β or γ -vibration. However, the 0^+_5 state in ^{178}Hf *could* be the first experimental evidence of a $\beta\beta$ vibration, pending the confirmation of the 0^+ state as a collective β -vibration; as it stands now, the collectivity of the band is tentative, ranging from non-collective to a distinct level of collectivity. Furthermore, we stress that this problem in nuclear structure is very open, with varied systematic behavior of all $K=0$ bands in deformed nuclei. In some cases, a collective β vibration can be found as the lowest-lying 0^+ state, or at a higher excitation energy, in others, the lowest-lying 0^+ acts like a collective two-phonon vibration built on top of the γ -vibration, and in others, one of the higher excitations acts as a $\gamma\gamma$ -vibration.

Gadolinium-160 and Dysprosium-162 nuclei both offer a very well-deformed shape ($R_{\frac{4}{2}}=3.31$) as well as a modest number of confirmed and tentative 0^+ excitations to study the feasibility of vibrational degrees of freedom superimposed on top of a rotational ground state. Literature lifetimes for most states (especially 0^+ states and the negative parity states of interest for any octupole correlations) in these nuclei are also scarce, further motivating the lifetime measurements. A great deal of effort and importance is placed on the evolution of nuclear structure across isotopic changes, or at least in a regional scale on the chart of nuclides; the emergence of nuclear data aids in the simultaneous evolution of theoretical effort to explain the various nuclear structure phenomena at the forefront of nuclear physics. In order to fully ascertain the nature of low-lying excitations (whether they are macroscopic, collective vibrations superimposed on top of a deformed ground state, multiconfigurative particle-quasiparticle states, or something completely different), consistent, precise, and accurate lifetime measurements of excited states must be performed.



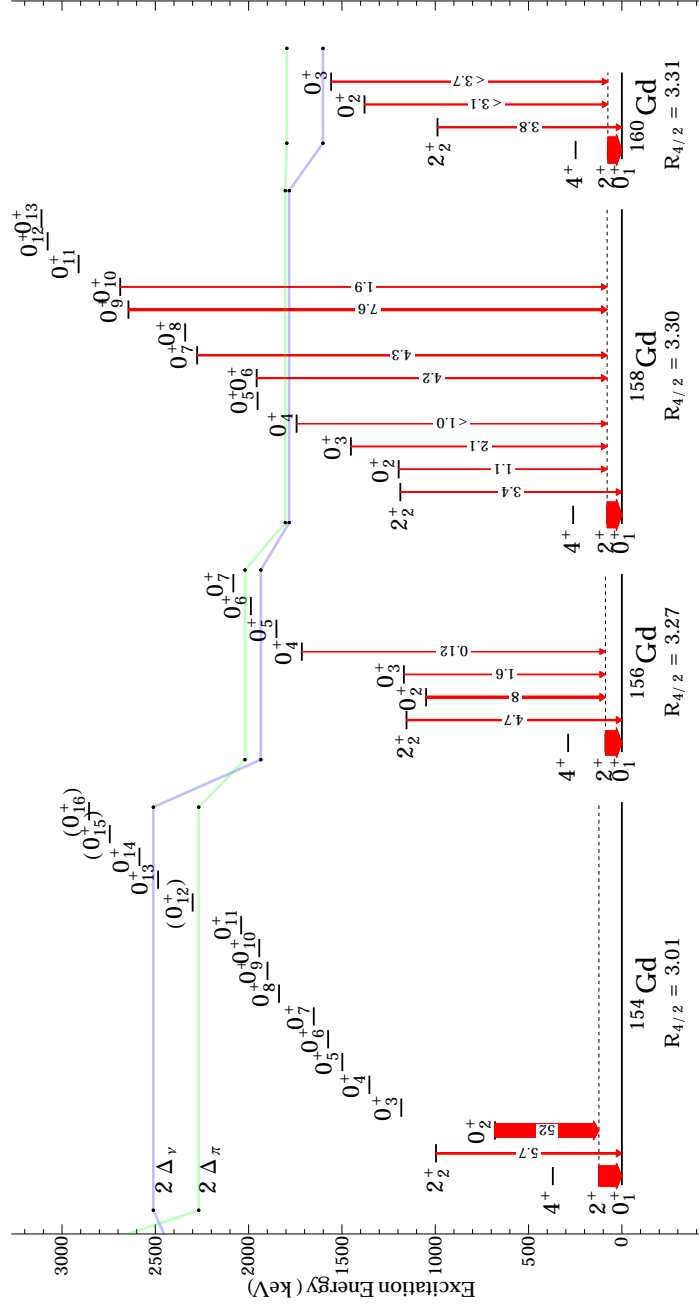


Figure 1.10. Systematics for the energies of excited 0^+ states, the first excited 2^+ bandhead, and low-lying ground state band members for even-even Gadolinium nuclei. Proton and neutron pairing gaps ($2\Delta_\pi$ and $2\Delta_\nu$, respectively) are drawn in green and blue and are calculated from Equations 1.4 and 1.5. Transition arrows represent known experimental B(E2) measurements for 0^+ bandheads and 2^+ bandheads (in W.u. where known).

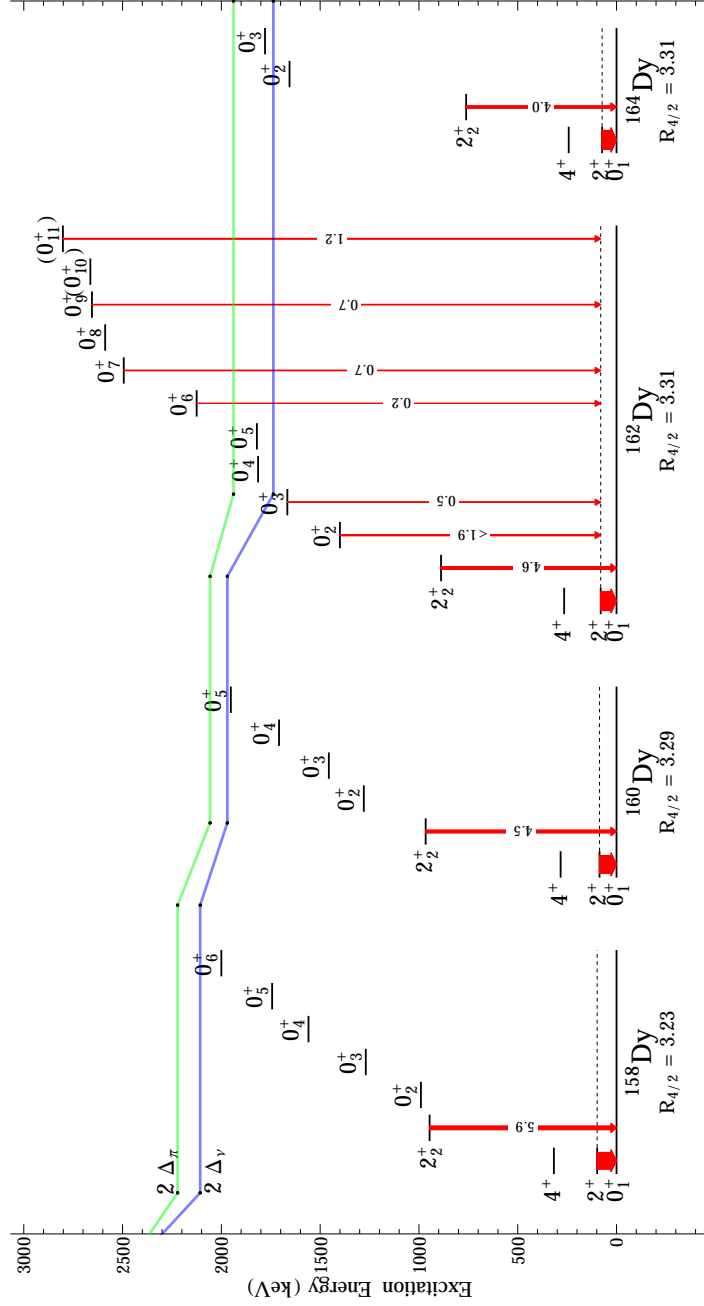


Figure 1.11. Systematics for the energies of excited 0^+ states, the first excited 2^+ bandhead, and low-lying ground state band members for even-even Dysprosium nuclei. New transition probabilities are presented in ^{162}Dy , with the widths proportional to $B(E2)$ values (in W.u.); also shown are the proton and neutron pairing gap ($2\Delta_\pi$ and $2\Delta_\nu$, respectively) for each isotope.

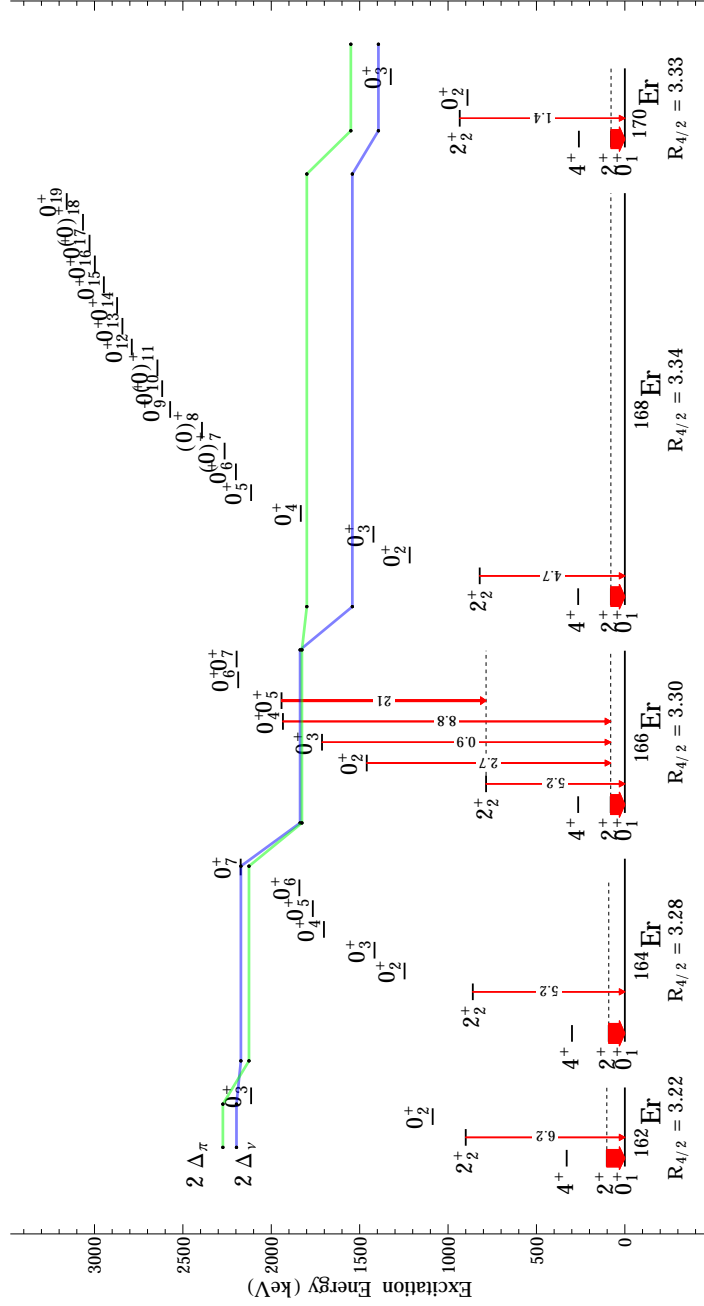


Figure 1.12. Systematics for the energies of excited 0^+ states, the first excited 2^+ bandhead, and low-lying ground state band members for even-even Erbium nuclei. Proton and neutron pairing gaps ($2\Delta_\pi$ and $2\Delta_\nu$, respectively) are drawn in green and blue and are calculated from Equations 1.4 and 1.5. Transition arrows represent known experimental B(E2) measurements for 0^+ bandheads and 2^+ bandheads (in W.u. where known).

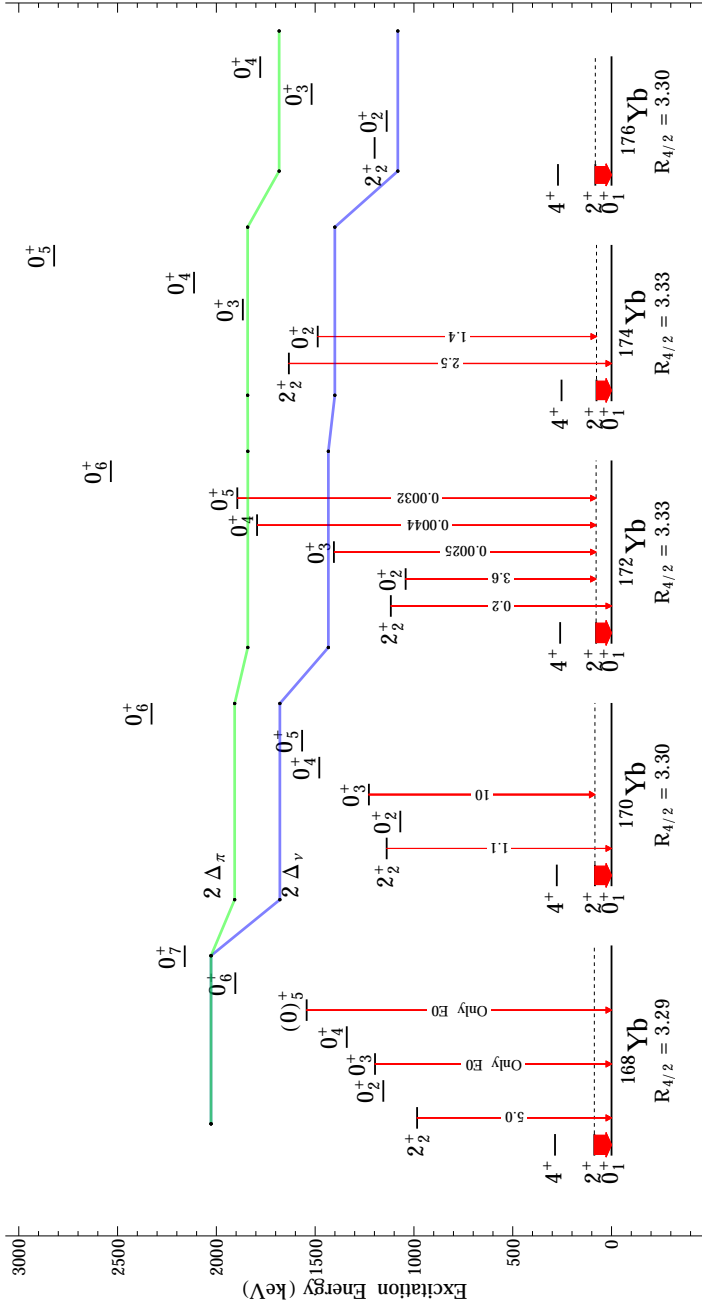


Figure 1.13. Systematics for the energies of excited 0^+ states, the first excited 2^+ bandhead, and low-lying ground state band members for even-even Ytterbium nuclei. Proton and neutron pairing gaps ($2\Delta_\pi$ and $2\Delta_\nu$, respectively) are drawn in green and blue and are calculated from Equations 1.4 and 1.5. Transition arrows represent known experimental B(E2) measurements for 0^+ bandheads and 2^+ bandheads (in W.u. where known).

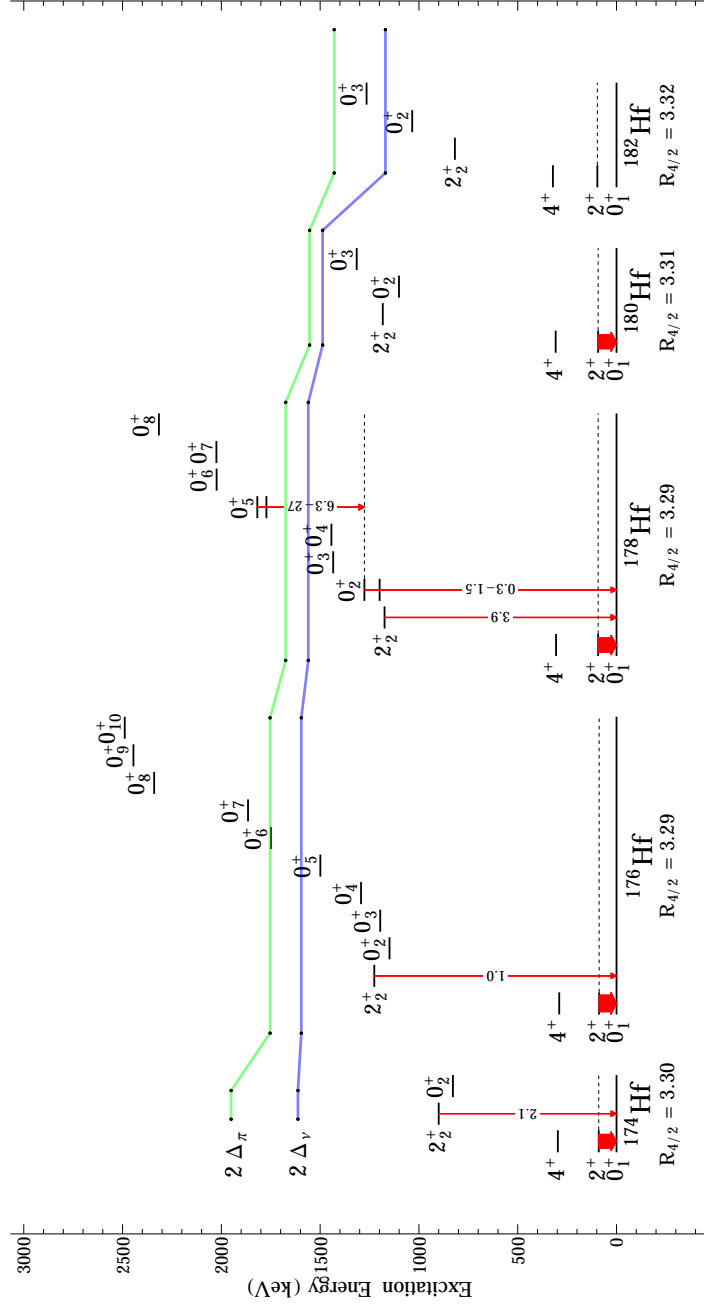


Figure 1.14. Systematics for the energies of excited 0^+ states, the first excited 2^+ bandhead, and low-lying ground state band members for even-even Hafnium nuclei. Proton and neutron pairing gaps ($2\Delta_\pi$ and $2\Delta_\nu$, respectively) are drawn in green and blue and are calculated from Equations 1.4 and 1.5. Transition arrows represent known experimental $B(E2)$ measurements for 0^+ bandheads and 2^+ bandheads (in W.u. where known).

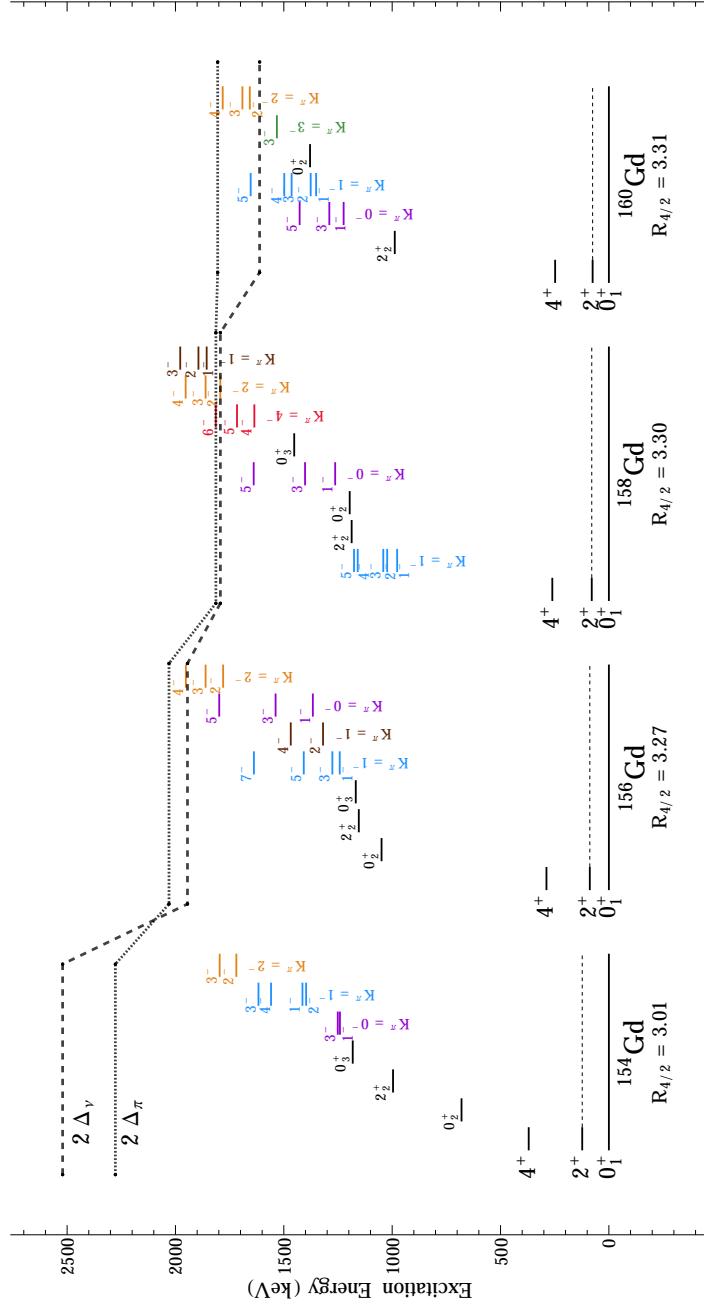


Figure 1.15. Systematics for the energies of excited negative parity states, the first excited 2^+ bandhead, and low-lying excited 0^+ states below the pairing gap ($2\Delta_\pi$ and $2\Delta_\nu$) for even-even Gadolinium nuclei.

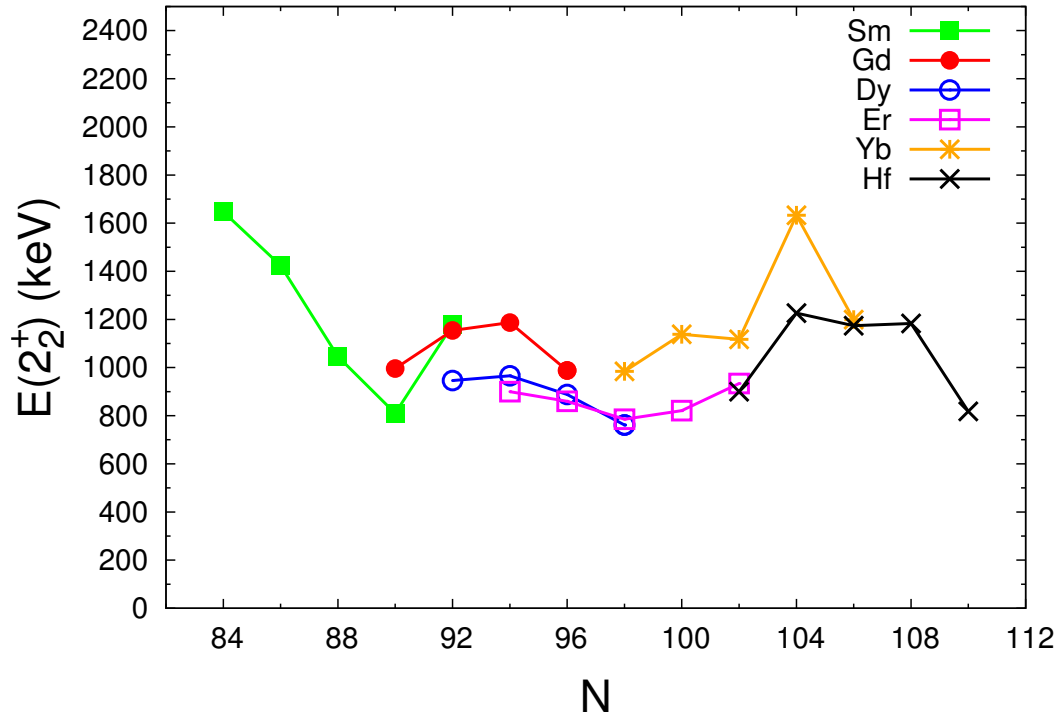
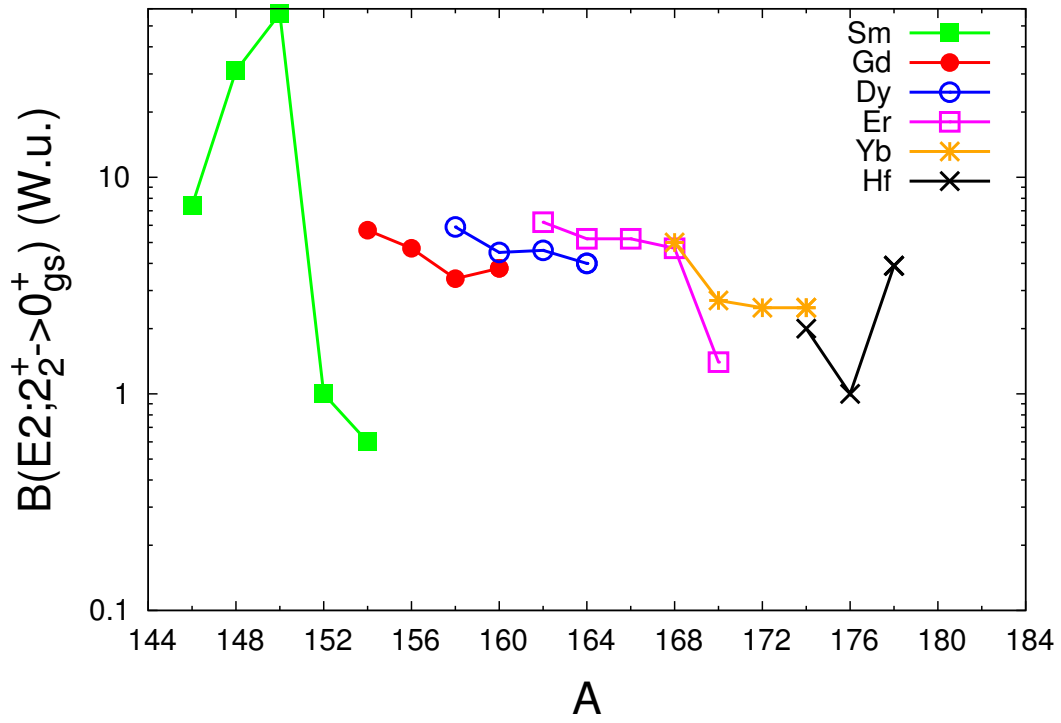


Figure 1.17. Absolute $B(E2; 2_2^+ \rightarrow 0_{gs}^+)$ (in Weisskopf units) measurements for rare-earth nuclei, showing the uniformity of the γ -vibration in a deformed nucleus. The bottom plot shows the energy of the 2_2^+ bandheads as a function of N , highlighting the smoothly varying energies.

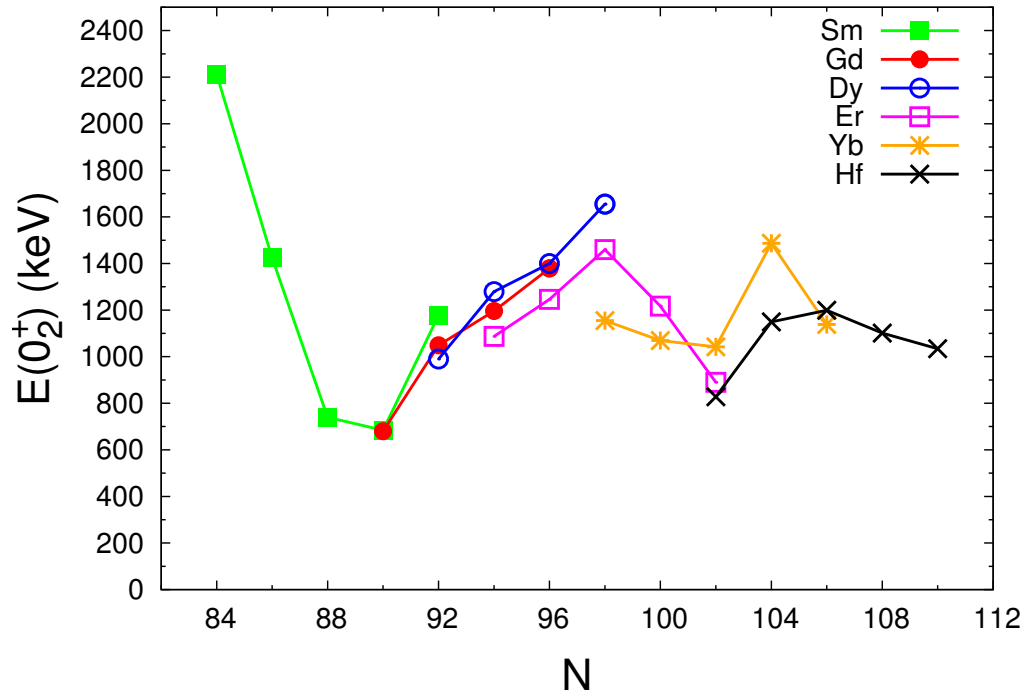
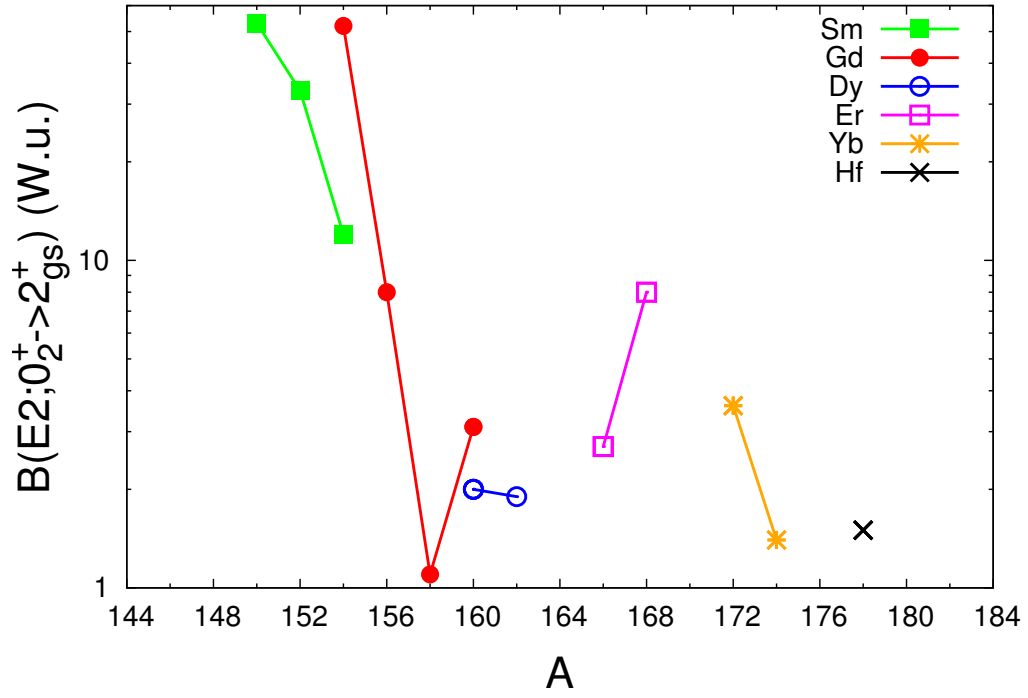


Figure 1.18. Absolute $B(E2; 0_2^+ \rightarrow 2_{gs}^+)$ (in Weisskopf units) measurements for rare-earth nuclei, showing the scattered experimental data that spans an order of magnitude variance. The bottom plot shows the energy of the 0_2^+ bandheads as a function of N , which shows a slightly more variant energy systematic than the 2^+ bandheads.

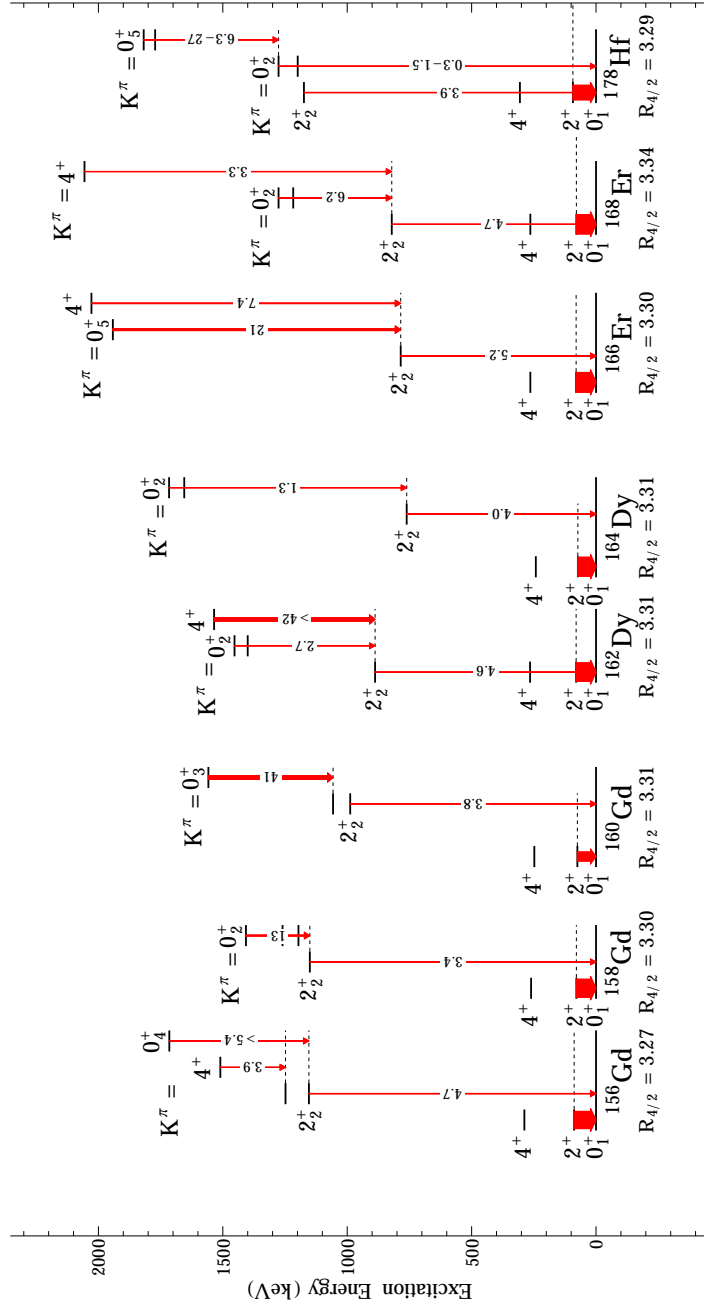


Figure 1.19. Summary of all known multiphonon ($\gamma\gamma$, $\beta\gamma$, or $\beta\beta$) configurations in rare-earth nuclei, absolute $B(E2)$ from literature are shown in Weisskopf units to signify collective decays to γ -vibrational and/or potential β -vibrational states.

CHAPTER 2

EXPERIMENTS AND DATA ACQUISITION

2.1 Lifetime Measurements of Excited States

In the laboratory, the measurement of excited state lifetimes remains an integral part in discerning information about the structure of the nucleus. An abundance of techniques, applicable/sensitive lifetime ranges, and facilities can be implemented to measure these lifetimes in the massive landscape of existing isotopes in nuclei. A schematic of experimental measures available for use with several lifetime measurement techniques can be found in Figure 2.1:

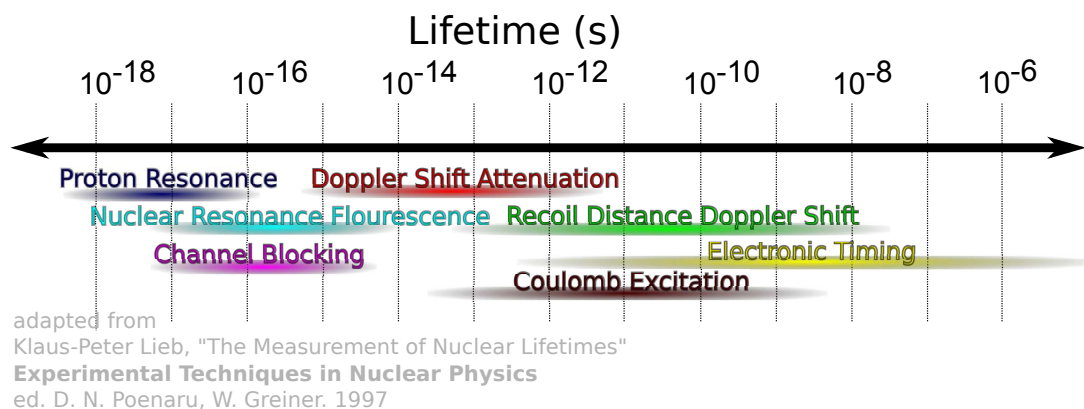


Figure 2.1. Techniques available to nuclear physicists to measure lifetimes as short as a few attoseconds (10^{-18} s) to the more long-lived lifetimes on the order of microseconds (10^{-6} s). (Adapted from [64], courtesy of M. K. Smith)

The various lifetime measurement techniques span a tremendous and continuous range of possible lifetimes for nuclear excitations, from $\sim 10^{-18}$ to $\sim 10^{-6}$ s, and can be applied to the vast majority of the ~ 3339 known nuclei in existence (stable and unstable). Several lifetime measurement techniques directly measure the lifetime (or a lifetime-dependent factor in the case of the Doppler Shift Attenuation Method) via various means; techniques like the Recoil Distance Doppler Shift, Coulomb Excitation, and Electronic Timing rely on fast-timing techniques for multiple γ -ray and/or particle coincidences to measure the lifetimes of metastable states. These direct lifetime measurements apply to the longer-lived excitations (picosecond and above lifetimes), and are contrasted with the more exotic, indirect methods (Proton Resonance, Nuclear Resonance Fluorescence, and Channel Blocking) that measure the partial or total Lorentzian energy ($\Gamma \approx \hbar/\tau$) width(s) to extract the lifetime of a state.

Specifically, level lifetimes in the tens to hundreds of femtosecond ($\sim 10^{-15}$) range can be measured with the Doppler Shift Attenuation Method (DSAM), a technique that exploits a recoiling nucleus to produce Doppler shifted γ -rays when observed at various laboratory angles. The magnitude of the Doppler shift is reliant on a lifetime-dependent factor, which we can easily extract from experiments in the laboratory. DSAM holds a unique place in the overall landscape of lifetime measurement techniques in that it is almost exclusively sensitive in this near-femtosecond timescale. The level lifetimes can then be quickly extracted from the angular energy shift(s) of any γ -rays that de-excite the nucleus. All of the presented lifetimes in this work are measured with this DSAM technique.

2.2 DSAM-INS Formalism

A γ -ray observed from a recoiling nucleus will be energy-shifted linearly as a function of the laboratory angle, θ_{lab} , shown in Equation 2.1.

$$E_\gamma(\theta_{lab}) = E_{\gamma,o}[1 + \beta F(\tau) \cos(\theta_{lab})] \quad (2.1)$$

Here, $E_{\gamma,o}$ is the unshifted γ -ray energy, $F(\tau)$ is an attenuation factor, dependent on the lifetime of the excited state (to be discussed in detail in §3.2.2.2, as this is one of the key experimental quantities we measure), and β is the ratio of the recoil velocity of the target nucleus to the speed of light, c ; this recoil velocity is derived in Pelte and Schwalm [60] from the kinematics involving conservation of momentum and energy in the laboratory frame, and is given by Equation 2.2.

$$\beta = 0.04635 \frac{A_n}{A_n + A_A} \sqrt{\frac{E_n}{A_n}} \quad (2.2)$$

The mass numbers of the bombarding particle and solid target are A_n and A_A , respectively, with the bombarding particle energy given by E_n in MeV. In $(n,n'\gamma)$ experiments, A_n is unity, while A_n must take into account the full molecular weight of the target, *e.g.* for Dysprosium-Oxide powder ($^{162}\text{Dy}_2^{16}\text{O}_3$), $A_n=162\times 2+16\times 3=372$. For rare-earth nuclei and $E_n<5$ MeV, the nuclear recoil velocities are generally less than 1 % of the speed of light, meaning relativistic effects do not need to be taken into account as they normally would with other lifetime measurement techniques (*e.g.* Recoil Distance Doppler Shift measurements). For example, the recoil velocity β for a $^{162}\text{Dy}_2^{16}\text{O}_3$ molecule recoiling from a bombarding neutron of 3.1 MeV is 2.1878e-4. To highlight this centroid energy shift, Figure 2.2 shows a 1902.055 keV γ -ray Doppler shifting as the detector changes laboratory angle, with the centroids drawn to guide the eye.

From Equation 2.1, the only undetermined parameter is $F(\tau)$, an attenuation factor directly dependent on the specific lifetime of the decaying state. $F(\tau)$ can be calculated via multiple formulations, where all formulations rely on an understanding of the nuclear and electronic stopping power of a medium to produce this lifetime

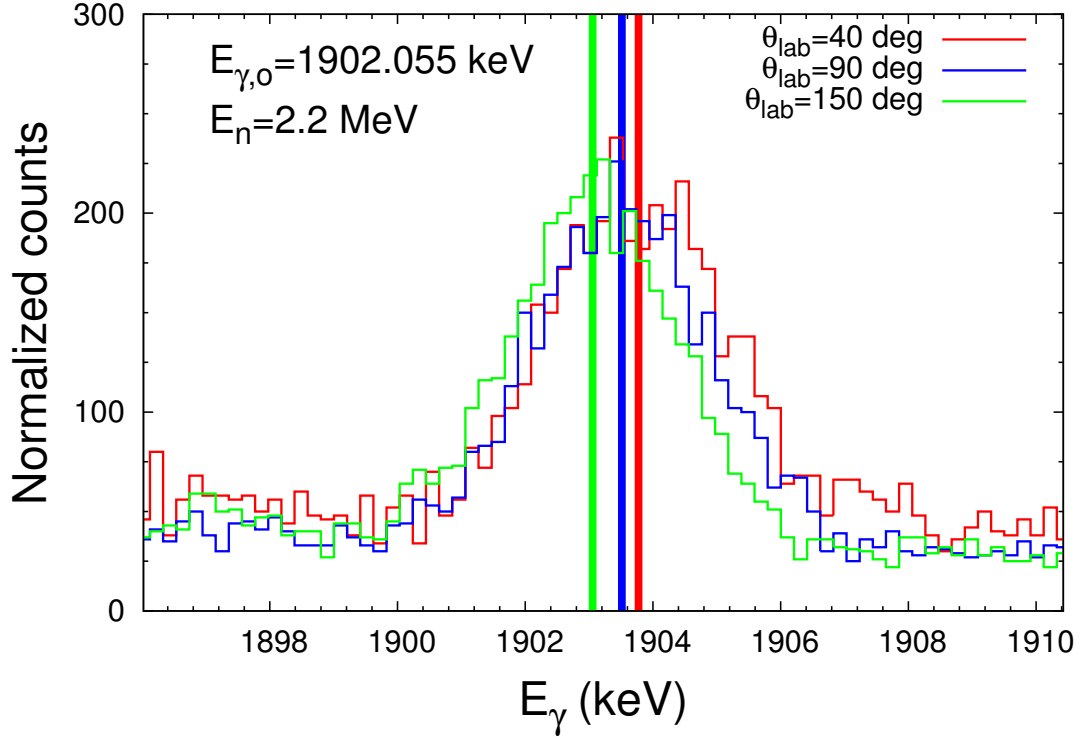


Figure 2.2. Doppler shift of an $E_\gamma=1902.055$ keV de-excitation from the $\theta_{lab}=40, 90$, and 150 degrees in red, blue, and green, respectively. The vertical lines mark the centroid of each peak of corresponding color.

dependent attenuation. In this work, the Winterbon formalism will be used, where the underlying framework is outlined in [76] and [5]. Key improvements were made to this attenuation factor calculation in the early 1970s by taking the possibility of nuclear deflection during the recoil as well as slowing inside the material lattice into account. This refinement is a necessary addition with the use of large, molar amounts and physical weights of target material, where the electronic stopping power of the medium plays a finite aspect in the calculation of the Winterbon curve; previous (Lindhard and Blaugrand) formulations of the theoretical $F(\tau)$ factors were unable to successfully represent both the nuclear and electronic stopping powers correctly, vastly and systematically underestimating the attenuation. Further advancement of

the Winterbon formalism was investigated in [61], with attention being placed on the chemical makeup of the target to better characterize the lattice relaxation needed to quantify the nuclear recoil inside the sample. This placed an important focus on the dependence on the oxide powder’s consistency and packing density of the molar quantity of the target material inside a container (in our case, a polyethelene vial) when calculating the Winterbon curve.

2.3 (n,n’ γ) Experiments at the University of Kentucky

DSAM requires the nucleus to be recoiling from a nuclear reaction as it decays from an excited state for it to be effective, and the preferred probe to excite the nucleus used at the University of Kentucky Accelerator Laboratory (UKAL) is the inelastic scattering of neutrons. In years past, thermal neutrons from various fission sources have been utilized to perform the inelastic scattering reactions, but the accessibility of monoenergetic neutrons has made UKAL a popular and unique setting in the realm of experimental structure physics. Energetic neutrons cannot be accelerated with a standard electrostatic accelerator due to their neutral charge-state, so non-thermalized neutrons must be produced via a primary reaction. This mechanism is outlined in Equation 2.3.

$${}^3\text{H}(\text{p},\text{n}){}^3\text{He}, Q = -0.763 \text{ MeV} \quad (2.3)$$

This ${}^3\text{H}(\text{p},\text{n})$ reaction produces quasi-monoenergetic neutrons in the 0.5 - 5.5 MeV range, ideal for studying the low-lying states in nuclei. UKAL uses their on-site 7 MV single-ended Van DeGraff accelerator to accelerate a bunched, pulsed beam of protons to impinge on a pressurized (slightly above atmospheric at ~ 110 kPa) tritium gas cell, prompting the reaction to produce a forward cone of neutrons. Slight energy spread is present in the outgoing neutrons due to a thin molybdenum foil to prevent the gas

cell from out-gassing upstream, which would catastrophically contaminate the entire beamline with radioactive ^3H . This energy straggling is minute, however, providing a $\sim 2.5\%$ energy spread on average at 50-100 keV standard deviation on neutron energy [5].

The choice of neutrons as a probe can be justified for multiple reasons, and brings its set of distinct advantages; the inelastic scattering and low-spin transfer leaves the nucleus in excited, aligned states with relatively low angular momentum. Specifically, spin 5^\pm states are the practical limit of angular momentum that can be imparted in an inelastic scattering reaction. This low-spin population of states is because the spin- $1/2$ neutron would naturally not be able to produce a higher spin state without the addition of a very large amount of angular momentum during the inelastic scattering reaction. The neutral charge of the neutron also implies that the scattering reaction is not impeded by the Coulomb barrier; this means that levels are populated very close to the bombarding neutron energy. Lastly, the excited states populated by inelastic neutron scattering are generally nonselective, in that either single-particle excitations or collective states, allowing the study of both types of excitation. The Doppler Shift method also offers the unique ability to tune bombarding neutron energies to populate states at or very near their threshold energies. This effect is two-fold: first, the experimentally determined $F(\tau)$ factor from Equation 2.1 is directly dependent on the incoming neutron energy, so minimization of the neutron energy is key to extraction of the lifetime, as $F(\tau)$ will be inflated for higher neutron energies. Secondly, this ‘dialing-in’ of neutron energy can completely remove any lifetime inflation due to feeding from higher-lying states; DSAM is unique in this aspect because the other methods of measuring a nuclear lifetime will be unable to remove this feeding, or in some cases (such as the Gamma Ray Induced Doppler Broadening technique), the feeding will manifest as a large uncertainty in measurement.

DSAM following inelastic neutron scattering is not without its downsides or ex-

perimental challenges to overcome. Since the target has significant thickness and involves molar quantities of target powder, γ rays from deep inside the sample will be attenuated in their trajectory out of the sample. This has a two-fold effect, in that the absolute intensity must be corrected for (explained in detail in §3.1.4) low-energy γ rays that could easily become fully attenuated and absorbed by the target material, and that any lifetimes extracted from the linear shift of energy *may* not be trustworthy, as the energy attenuation is strongly angular dependent, effectively ‘flattening’ the Doppler energy shift.

The ensemble of $(n,n'\gamma)$ experiments performed at UKAL can be achieved with the relatively simple experimental setup, shown in Figure 2.3.

The single 50% relative efficiency Ortec HPGe planar detector (named after the 1904 Kentucky Derby winner Elwood) sits ~ 125 cm away from the end of the beamline on a goniometer equipped circular track ~ 2 m in radius to observe γ -rays at various laboratory angles. In Figure 2.3, the target (a cylindrical polyethelene vial of enriched target powder) is suspended a few (~ 4) inches away from the end of the tritium gas cell, where monoenergetic neutrons will inelastically scatter off the target, prompting γ decay from the sample to be observed by the HPGe detector. The proximity of the target in relation to the end of the tritium gas cell ensures that the highest possible neutron flux from the forward cone of neutrons will strike the majority of the target material. The castle of passive shielding materials are two-fold in use: to lower background radiation in spectra and to diminish fast neutron damage to the HPGe detector itself. The viewing channel of the detector is lined with copper plating to absorb fast neutrons from the tritium gas cell at the end of the beamline. In addition, borated polyethelene surrounds the detector to reduce secondary & tertiary scattering of neutrons and γ -rays from reaching the detector; the typical ensemble of lead rings also aid in regular γ background reduction. Lastly, a wedge of tungsten is placed in direct view of tritium gas cell to act as a shadow bar

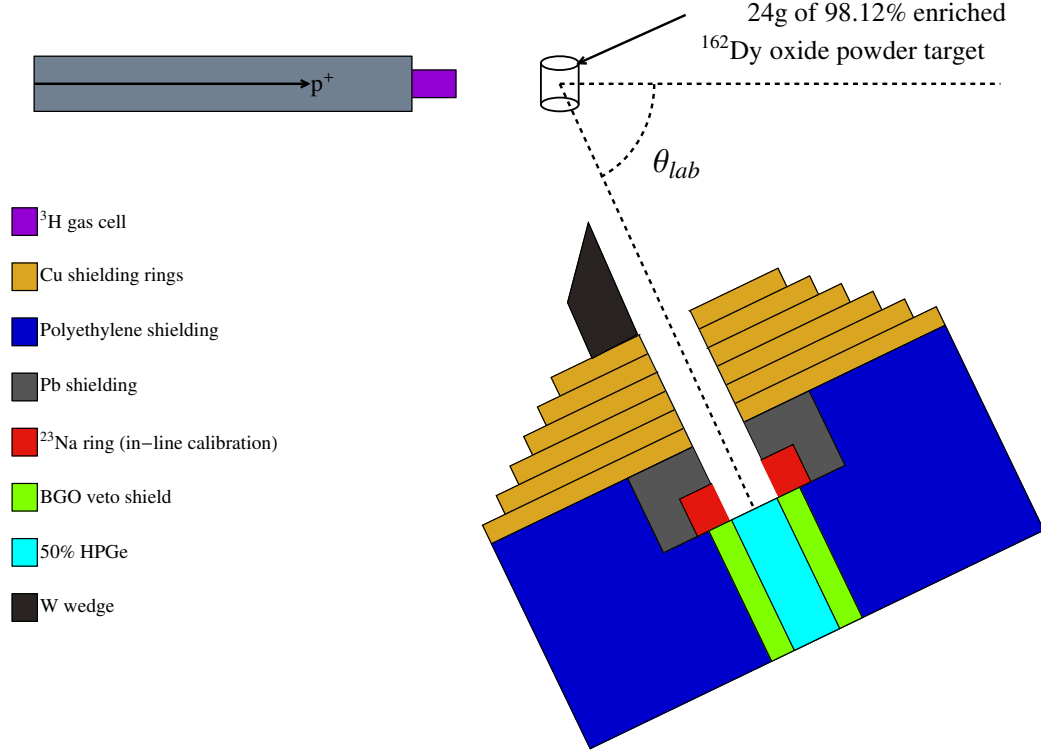


Figure 2.3. Sample Experimental Setup at UKAL for γ -singles measurements (Made in M. Caprio's SciDraw software for Mathematica [18])

to prevent neutrons from directly entering the detector from the gas cell. An ensemble of BGO (Bismuth Germanate Oxide) scintillators are placed annularly around the HPGe detector to further aid in Compton scattering background suppression; these scintillation detectors provide an anti-coincidence to veto background events that occur, actively cleaning spectra.

Spectra are generated from the Time of Flight (TOF) technique to discriminate background events from prompt γ events; a time-to-amplitude converter (TAC) measures the relative time between events in the HPGe detector and a beam pick-off

signal near the end of the beamline. The familiar concept of the TOF technique is that particles and γ -rays require different amounts of time to reach a detector, dependent on their velocity (neutrons of a velocity $\ll c$ take longer to reach a detector than a γ -ray traveling at the speed of light). This time difference between measured events is recorded by the TAC, and TOF spectra are generated through a built-in single channel analyzer (SCA). The resultant spectrum is used to properly gate the experimental datasets in the analog-to-digital converter (ADC) by only selecting corresponding prompt γ -ray events from the histogram. An example of a typical TOF spectrum is shown in Figure 2.4.

The single-detector setup and γ -singles based experiments provide more distinct downsides to lifetime measurements via DSAM at the University of Kentucky in particular. The limitations of not using γ - γ coincidences can have profound implications on the visibility and overall statistics of spectra gathered from the experiment(s); being able to apply timing gates on individual γ -decays is an extremely powerful tool in determining decay patterns, cascades, and lower-intensity peaks for interband decays. One detector setups provide a considerable length to the experimental campaign, and is a severe limitation to the facilities, where the experimenters must enter the target room periodically throughout the run to physically move the detector across the entire range of angles used in the measurements, and must systematically scan through the entire range one angle at a time. Given an unlimited amount of beamtime with little to no deadlines, this is not a problem, however, a modest amount of statistics for γ -decays observed in a typical measurement require almost (in some cases in excess) of a week of continuous beamtime for a single neutron energy angular distribution.

2.3.1 Excitation Function Measurements

Typically, the first measurements to be made are excitation function measurements; these supplement the γ -singles nature of the angular distribution measure-

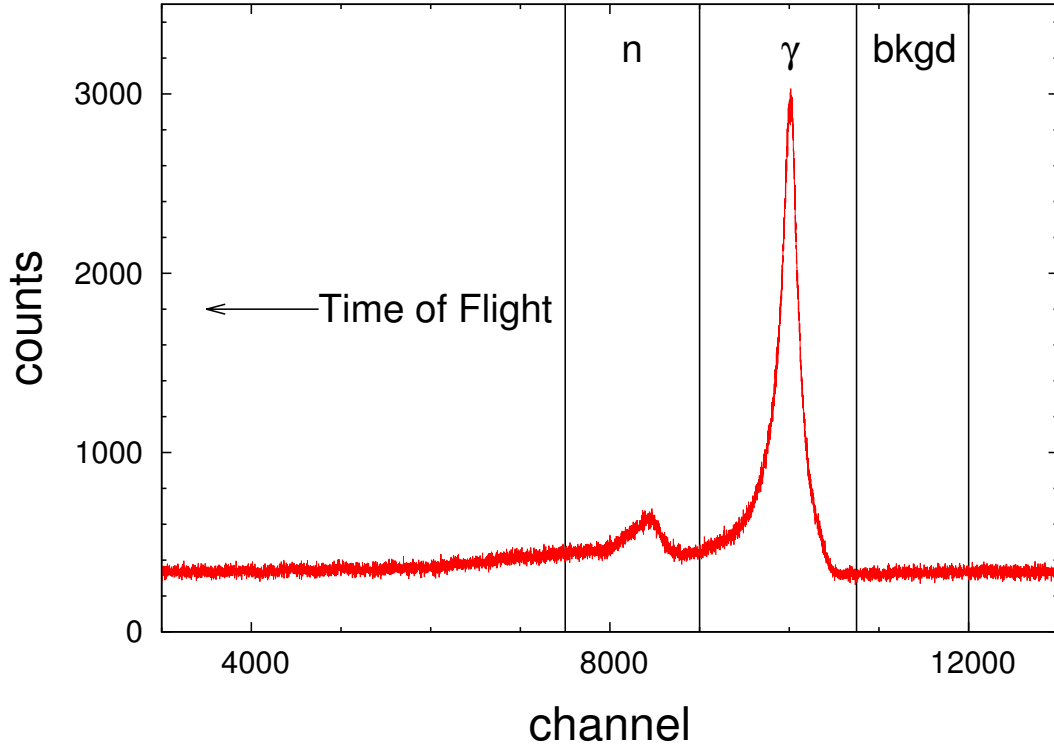


Figure 2.4. Typical TOF spectrum with labeled regions for corresponding γ , neutron, and background events. Note the passage of time to the left, starting at the prompt γ -ray peak, followed by a neutron bump, and wrapping back around the x-axis.

ments, to help infer the ideal bombarding neutron energy for peak γ -ray population rates. In stark contrast to the angular distributions where the neutron energy is kept constant, the excitation functions modulate the bombarding neutron energy to provide the γ -ray population strengths as a function of neutron energy. Similarly in contrast, the HPGe detector is kept at a constant laboratory angle of 90 degrees with respect to the beamline. An extremely powerful tool, these excitation functions provide important insight into the nature of any observed γ -rays; for a particular excited state that de-excites via multiple channels, the corresponding γ -rays will have both the same a) quantitative threshold, and b) qualitative shape. The absolute

threshold allows previously unidentified or unplaced γ -ray transitions to be placed into a known level scheme, as the threshold for the de-excitation must match the level energy. If the populated level's spin are high (5^\pm), the threshold will be higher than the level energy, as the bombarding neutron must have higher linear momentum (energy) to successfully provide enough angular momentum transfer during the reaction. The qualitative shape of the excitation functions is heavily dependent on the initial spin and parity of the de-exciting level, making γ -ray discrimination and identification from different levels a trivial task. This identical shape also allows the relative intensities of γ -rays to be inferred (independent of the absolute intensities we can gather from the angular distribution measurements), since we can take the ratio of matched-shape excitation functions. An example of two matching γ -ray transitions from the same level ($J^\pi=5^-$), contrasted with a γ -ray from another level ($J^\pi=1^-$) is shown in Figure 2.5.

The excitation function measurements serve as a quasi-replacement for γ - γ coincidences in a particular experiment, as it allows retention of good statistics that one would get from γ -singles spectroscopy. With γ - γ coincidences, a level scheme can be built extremely easily, because coincident γ -decay chains into and out of levels are unquestionably vivid in multiple HPGe detectors; this is not the case in a γ -singles experiment, since a) particular γ -rays appear only in the single HPGe detector, and b) discrimination of decay chains is impossible with γ -singles. The excitation function allows a level scheme to be built in a similar fashion to γ - γ coincidences, while only requiring a single detector, because threshold energies are obvious, and that the qualitative shape of the excitation functions will be identical. Without either implemented technique (excitation function measurements or γ - γ coincidences), proper γ -spectroscopy would be rendered impossible, as we would no longer be able to confidently place γ decays to levels or assign level lifetimes from the Doppler Shift Attenuation measurements.

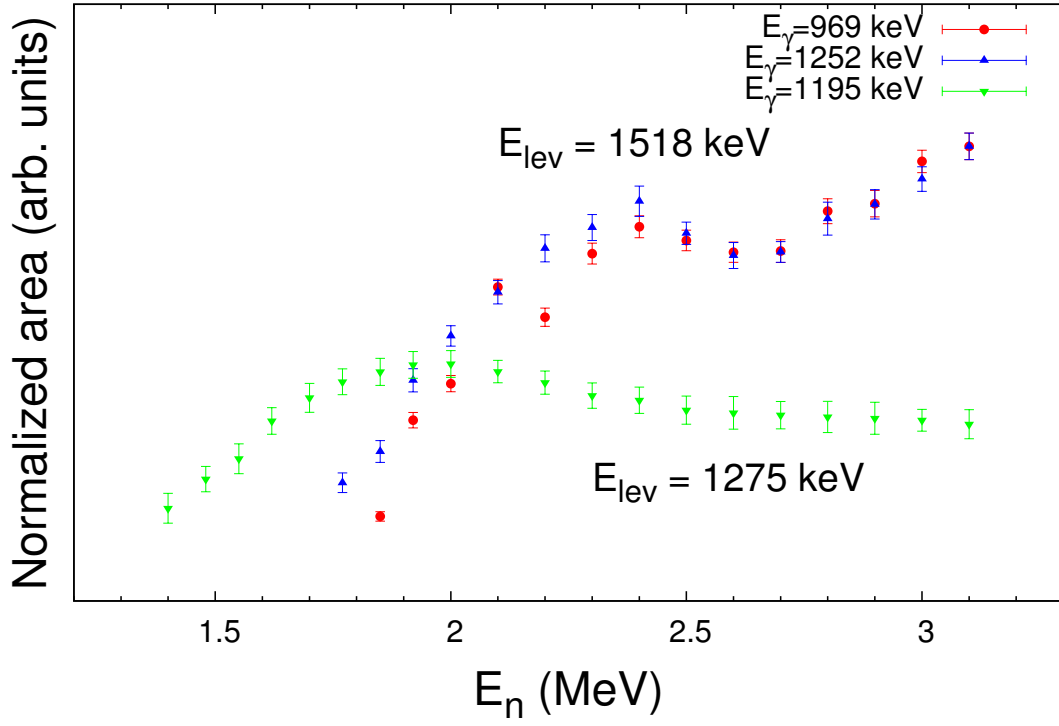


Figure 2.5. Superimposed excitation functions for two gamma rays ($E_\gamma=969$ & 1252 keV) leaving the same level ($E_{lev}=1518$ keV), and a single 1195 keV γ -ray leaving a separate $E_{lev}=1275$ keV level in ^{162}Dy . The different thresholds and shape of the 1195 keV and 969 keV de-excitations imply that these decays are from two different levels, clearly showing their placement in the level scheme.

2.3.2 Angular Distribution Measurements

To extract the lifetimes of excited states, the angular distribution of gamma rays must be measured; this is achieved at UKAL with the same single High-Purity Germanium detector used in the excitation function measurements. By physically moving the HPGe detector to different laboratory angles on the circular track, we can extract multiple observable quantities from the angular distribution measurements. First, $F(\tau)$ is found by plotting E_γ as a function of $\cos(\theta)$; the relation in Equation 2.1 states that the centroid energy shift of a γ -ray will be linear with cosine, with

$F(\tau)$ being the slope. Comparison of this experimental $F(\tau)$ factor with the theoretical calculation for $F(\tau)$ allows extraction of a lifetime τ for the decay radiation and excited state. Special care must be taken when measuring the lifetimes, because higher-lying levels can introduce feeding transitions into lower-lying states, inflating the measured lifetimes. Since the theoretical $F(\tau)$ factor is directly dependent on the recoil velocity (the bombarding neutron energy), additional inflation will also be introduced when extracting lifetimes for levels far below the bombarding neutron energy. Performing the excitation function measurements first allows for the minimization of lifetime inflation while maximizing population rate for a particular excited state, as we know the approximate population as a function of bombarding neutron energy.

When the nucleus decays from an aligned state, the classical radiation pattern of the γ -ray can be expressed by the sum of even Legendre polynomials as a function of $\cos(\theta)$ (Equation 2.4), where the coefficients for each order polynomial are directly related to the multipolarity of the transition. Realistically, only the coefficients a_2 and a_4 are considered, since the higher order terms correspond to the contributions from the insignificantly intense multipolarities for $\Delta J > 2$.

$$W(\theta) = \sum_{\text{even } k} \alpha_k P_k \cos(\theta) \Rightarrow W(\theta) \approx A_0 [1 + a_2 P_2 \cos(\theta) + a_4 P_4 \cos(\theta)] \quad (2.4)$$

The anisotropic nature of the γ radiation produced arises from the fact that parity conserving nuclear reactions, *e.g.* (n,n' γ), and a defined beam direction, create a plane of interaction. Otherwise, the random orientation of nuclei in space would mean all multipolarities of γ radiation have isotropic angular distributions. By comparing the relative magnitude and sign of the a_2 and a_4 coefficients, limits can be placed on both the spin and parity of the de-exciting level, because dipole and quadrupole

radiation patterns have distinct shapes (shown in Figure 2.6). These same Legendre Polynomial coefficients can also be compared to theoretical calculations to extract multipole mixing fractions (δ) for mixed-multipolarity transitions. This multipole mixing fraction is simply the ratio of E2 transition strength to M1 transition strength:

$$\delta = \frac{\langle \eta | E2 | \nu \rangle}{\langle \eta | M1 | \nu \rangle} \quad (2.5)$$

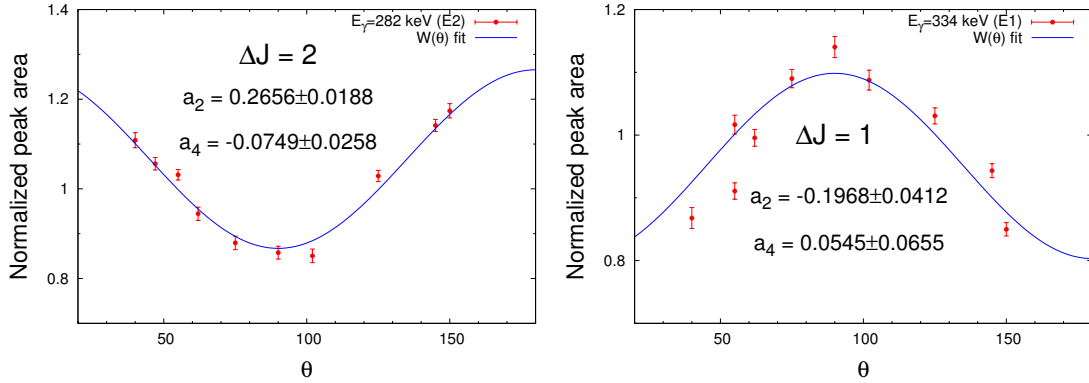


Figure 2.6. Angular distributions for two different multipolarity γ -rays in ^{162}Dy , an E2 transition of $E_\gamma = 282$ keV (the $6_{gs}^+ \rightarrow 4_{gs}^+$ transition) & an E1 transition of $E_\gamma = 334$ keV (a $3^- \rightarrow 2_\gamma^+$ transition), showing distinct, inverted shapes.

Lastly, the angular distributions allow us to measure the absolute intensity of emitted γ -rays from the A_0 coefficient. In experiments with static, symmetric detectors (*e.g.* two detectors at 90°), only the relative intensity of γ rays can be extracted. Though seemingly simple in form and function, the γ -singles measurements made at UKAL are an incredibly powerful tool that yield a wealth of knowledge about the

structure of the nucleus.

2.4 Experimental Campaigns

Two sets of experimental campaigns were performed at the University of Kentucky to measure the level lifetimes for deformed rare-earth nuclei, ^{160}Gd and ^{162}Dy . Both targets were acquired from Oak Ridge National Laboratory in the form of an isotopically enriched oxide powder (specifically, $^{160}\text{Gd}_2^{16}\text{O}_3$ & $^{162}\text{Dy}_2^{16}\text{O}_3$); the sample powder was then placed into a $1.5'' \times 3''$ cylindrical polyethelene vial for the experiments.

2.4.1 The ^{160}Gd Campaign

In July/August of 2012 and 2013, inelastic neutron scattering experiments were performed to study the low-lying excitations of ^{160}Gd . The 29.4564 g of 98.12 % enriched powder vial was placed 4.82 cm from the end of the ^3H gas cell and 119.3 cm from the face of the detector for all experiments. First, an excitation function measurement was performed at the neutron energies shown in Table 2.1:

E_n (MeV)							
1.40	1.50	1.60	1.70	1.80	1.90	2.00	2.075
2.15	2.225	2.3	2.375	2.45	2.525	2.6	2.625

TABLE 2.1

Bombarding energy of neutrons used to populate the excitation functions
for the ^{160}Gd experiment.

Once proper γ -ray identification and placement in the level scheme was completed from examining the excitation functions, angular distributions were measured at three (3) bombarding neutron energies, 1.5, 2.0, and 2.8 MeV at the angles shown in Table 2.2.

θ_{lab}										
E _n =1.5, 2.0, & 2.8 MeV	40°	55°	62°	75°	90°	102°	125°	137°	145°	150°

TABLE 2.2

Angles used for lifetime measurements for the suite of ^{160}Gd experiments at 1.5, 2.0, and 2.8 MeV bombarding neutron energies.

2.4.2 The ^{162}Dy Campaign

Throughout August of 2013 and March of 2014, we performed an excitation function measurement and three (3) angular distributions to measure lifetimes of levels for levels $\leq 1.6, 2.2$, and 3.1 MeV in excitation energy. Similarly to the ^{160}Gd experiments, the 24 g of 98.12 % enriched powder vial was placed 4.80 cm from the end of the ^3H gas cell and 120.2 cm from the face of the detector for all experiments. The excitation function measurement was taken first to discern the population rate for levels and γ -rays similar to the ^{160}Gd ; this allowed us to estimate the beam-on time required to give good statistics for desired and important γ -rays.

Following suit of the ^{160}Gd experiments, the angular distributions were measured

E_n (MeV)									
1.40	1.48	1.55	1.62	1.70	1.775	1.85	1.925	2.0	2.1
2.2	2.3	2.4	2.4	2.5	2.6	2.7	2.8	2.9	3.0

TABLE 2.3

Bombarding energies of neutrons used to populate the excitation functions for the ^{162}Dy experiment. ~ 75 keV steps were used at the lower energies (≤ 2 MeV) to enhance the resolution of the threshold and population shape for low-lying excitations.

to extract level lifetimes from ^{162}Dy . The specific angles used for each angular distribution are given in Table 2.4, and are drawn in Figure 2.7, where angles in black are used in all angular distributions, angles in red are used in the $E_n=1.6$ MeV measurements and blue angles correspond to the angles used in $E_n=2.2$ & 3.1 MeV runs.

Once data is collected for both experimental campaigns, we carry out the analysis process to extract the various experimental quantities needed for nuclear structure studies (lifetimes of excited states, branching ratios/absolute intensities of γ -rays, etc) outlined in §3.

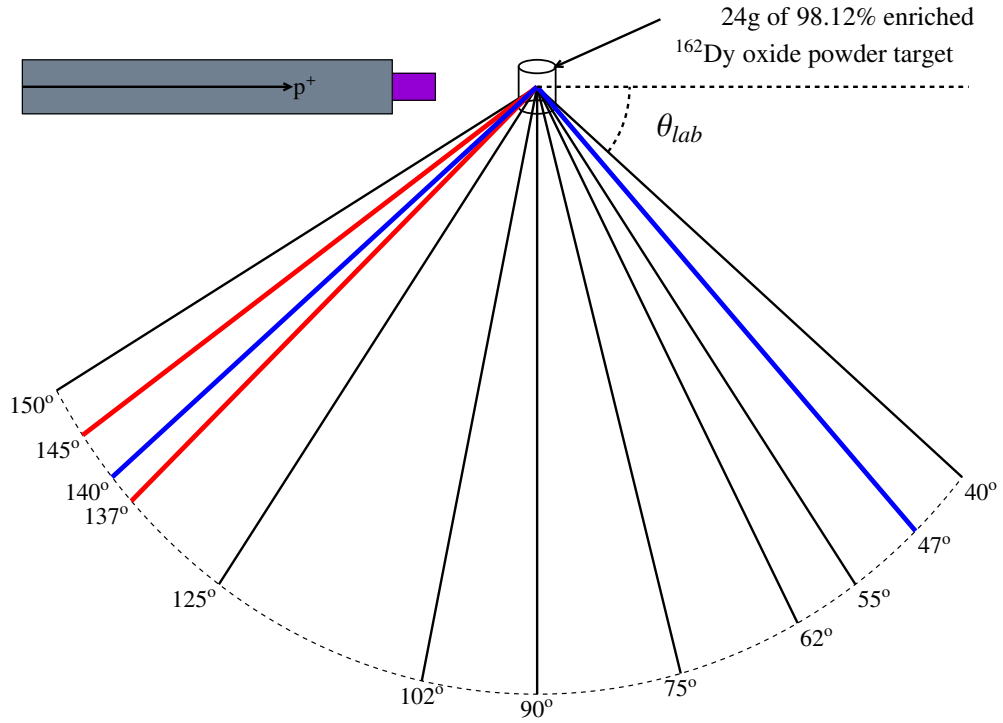


Figure 2.7. Angles used in $^{162}\text{Dy}(n,n'\gamma)$ angular distributions. Angles in black are used in all measurements, while angles in red (137° and 145°) are used for the $E_n=1.6$ MeV measurements and angles in blue are used for both $E_n=2.2$ and 3.1 MeV datasets.

θ_{lab}										
$E_n=1.6$ MeV	40°	55°	62°	75°	90°	102°	125°	137°	145°	150°
$E_n=2.2$ MeV	40°	47°	55°	62°	75°	90°	102°	125°	140°	150°
$E_n=3.1$ MeV	40°	47°	55°	62°	75°	90°	102°	125°	140°	150°

TABLE 2.4

Angles used for lifetime measurements for the suite of ^{162}Dy experiments at 1.6, 2.2, and 3.1 MeV bombarding neutron energy. Angles in bold are to emphasize differences in measurements.

CHAPTER 3

DATA ANALYSIS

3.1 Calibrations and Corrections

In order to account for systematic errors inherent to the laboratory, several corrections and calibrations must be made to ensure proper γ -ray spectroscopy. A suite of in-beam (^{24}Na & ^{60}Co) and offline calibration (^{226}Ra & ^{152}Eu) sources were implemented during the experimental campaigns to provide the numerous corrections that must be made; successful calibration hinges on the implementation of a wide energy range of strong calibration lines that do not shift. An ADC nonlinearity, a detector efficiency, and a target sample self-absorption correction are all applied to energy calibrated spectra before the analysis of data can begin.

3.1.1 Energy Calibrations

Proper energy calibration is extremely vital to the success of DSAM lifetime measurements; the precision in peak centroid location determines the sensitivity of the lifetime measurement, as centroid energy shifts for longer-lived levels (~ 1 ps) can be as small as 20 eV. With its large range of energetic decays (from 185 keV to 2.4 MeV shown in Table 3.1), ^{226}Ra is an ideal candidate to energy calibrate our spectra; the ^{226}Ra spectrum from the $^{162}\text{Dy}(n,n'\gamma)$ experiments can be seen in Figure 3.1. Angular distribution measurements saw the presence of an in-line calibration source in the form of a ring of ^{23}Na that had been irradiated with an on-site neutron source to produce radioactive ^{24}Na . The β -decay to $^{24}\text{Mg}^*$ leads to a cascade of two intense

γ -rays, 1368.626 and 2754.007 keV, providing a calibration point at a higher energy than a typical ^{60}Co source can provide (1173.228 & 1332.492 keV). This sodium ring is placed around the detector crystal to ensure the two calibration γ -rays are not attenuated by the passive shielding from the experimental setup shown in Figure 2.3. While far from an ideal candidate for an energy calibration point, radioactive ^{28}Al from a $^{27}\text{Al}(n,\gamma)$ channel will emit a high intensity γ -ray at 1778.785 keV; this peak originates from the aluminum housing for the HPGe detector and is often not well-defined in width, especially compared to the traditional Radium and Cobalt sources normally used, and as such, the ^{28}Al should not be a main energy calibration point. A table of all online and offline calibrations used in the ^{160}Gd and ^{162}Dy experiments can be found in Table 3.2:

The linear energy calibrations from the $^{162}\text{Dy}(n,n'\gamma)$ experiments can be seen in figure 3.2:

The difference in linear energy calibrations is the result of a change in exact gain settings between the two ^{162}Dy experiments; the excitation function measurements and $E_n=1.6$ & 2.2 MeV angular distributions occurred in August of 2013, while the single $E_n=3.1$ MeV angular distribution took place months later, in March of 2014. The specific difference in energy calibration can be seen in Figure 3.2, where the electronics gain settings were changed (a natural, necessary, and sometimes unintentional occurrence in the laboratory).

3.1.2 Nonlinearity Calibrations

The first of these corrections is an ADC nonlinearity calibration, where a binning nonlinearity is introduced in the data acquisition's ADC. In the ideal case, an ADC correlates an analog voltage to a specific bin (in this case, the energy of a γ -ray on the absissca), with the bins being equally spaced and sized. We, of course, do not live

^{226}Ra decays							
E_γ (keV)	I_γ (rel)	E_γ (keV)	I_γ (rel)	E_γ (keV)	I_γ (rel)	E_γ (keV)	I_γ (rel)
186.053	3.502	487.090	0.431	1120.287	14.66	1661.280	1.063
241.997	7.130	580.130	0.369	1155.190	1.611	1729.595	2.791
258.870	0.525	609.312	44.83	1238.110	5.750	1764.494	15.03
274.800	0.472	665.453	1.506	1280.960	1.411	1847.420	1.994
295.224	18.09	768.356	4.780	1377.669	3.895	2118.550	1.137
351.932	35.04	785.960	1.097	1385.310	0.782	2204.210	4.820
455.000	0.287	806.174	1.250	1401.500	1.311	2293.400	0.298
480.430	0.336	934.061	3.041	1509.228	2.065	2447.860	1.525

TABLE 3.1

Energies (in keV) and relative intensities (in arbitrary units) for γ -ray emissions from the ^{226}Ra decay chain used in data calibrations for this work.

in a perfect world, and some bins cover a larger energy range than others, generating an easily correctable error in the measurement of peak centroids. To perform this offline correction, a radioactive ^{226}Ra source is placed at the same location the target is suspended, and is allowed to decay. Since the multitude of decays from ^{226}Ra have very well defined and precise centroids, we can compare the measured position of these peaks to literature values for the peak centroids. By plotting a relationship between the change in channel as a function of energy, we can generate the specific nonlinearity curve to make the correction. Generally, the nonlinearity correction introduces a ± 2 channel difference (at most a 0.5 keV correction), and this nonlinearity can be fit to an order 5 polynomial, shown in Figure 3.3:

Special care must be taken to ensure a realistic polynomial fit for the ADC non-

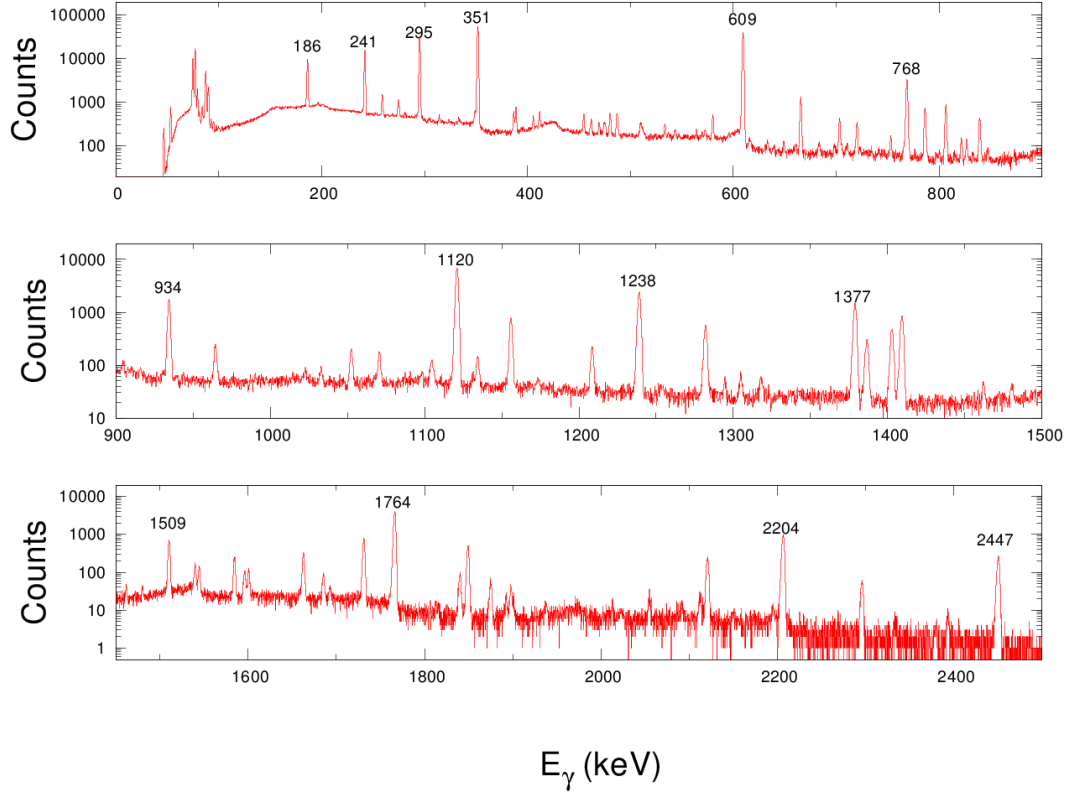


Figure 3.1. Spectrum from a ^{226}Ra calibration run during the ^{162}Dy experiments. Sampled, higher intensity peaks are labeled by their energy in keV (refer to Table 3.1).

linearity; polynomials of order >5 can gravely mis-characterize the ADC behavior outside of the range of calibration points used (in our case, ^{226}Ra decays). In Figure 3.3, the downward turn in the fifth-order extrapolation above 2.5 MeV γ -rays would be magnified for higher order odd polynomials, and would turn upward (at a similarly unrealistic rate) for the even polynomials. To justify the use of an order-5 polynomial, the highest energy γ -ray observed in the ^{162}Dy experiments is a 2779 keV de-excitation, keeping in line with a $\sim \pm 1$ keV nonlinearity correction.

$^{160}\text{Gd}(\text{n},\text{n}'\gamma)$ calibration E_γ (keV)						
$E_n=1.5$ MeV	1173.228	1332.492	2223.245			
$E_n=2.0$ MeV	1173.228	1332.492	2223.245			
$E_n=2.8$ MeV	1173.228	1332.492	1778.885	2223.245		
Excitation Function	185.002	351.932	609.312	1120.287	1764.494	2223.245

$^{162}\text{Dy}(\text{n},\text{n}'\gamma)$ calibration E_γ (keV)								
$E_n=1.6$ MeV	185.002	1173.228	1332.492	2223.245				
$E_n=2.2$ MeV	185.002	1173.228	1332.492	2223.245				
$E_n=3.1$ MeV	351.932	609.312	1120.287	1173.228	1332.492	1764.494	2223.245	2754.007
Excitation Function	185.002	351.932	609.312	1120.287	1764.494	2223.245		

TABLE 3.2

Calibration points used for all ^{160}Gd and ^{162}Dy spectra energy calibrations.

3.1.3 Efficiency Calibrations

High Purity Germanium detectors have an intrinsic detection efficiency, dependent on the energy of a particular γ -ray that enters the Ge crystal; higher energy γ -rays have a lower probability of depositing their entire energy into the detector, so this must be accounted for in angular distribution data to get correct γ -ray intensities. The same spectrum from the nonlinearity calibrations is used, as we can simply compare the measured intensities of γ -rays from the ^{226}Ra source to the literature values of γ -ray intensity. This efficiency correction is shown in Figure 3.4 as a function of E_γ :

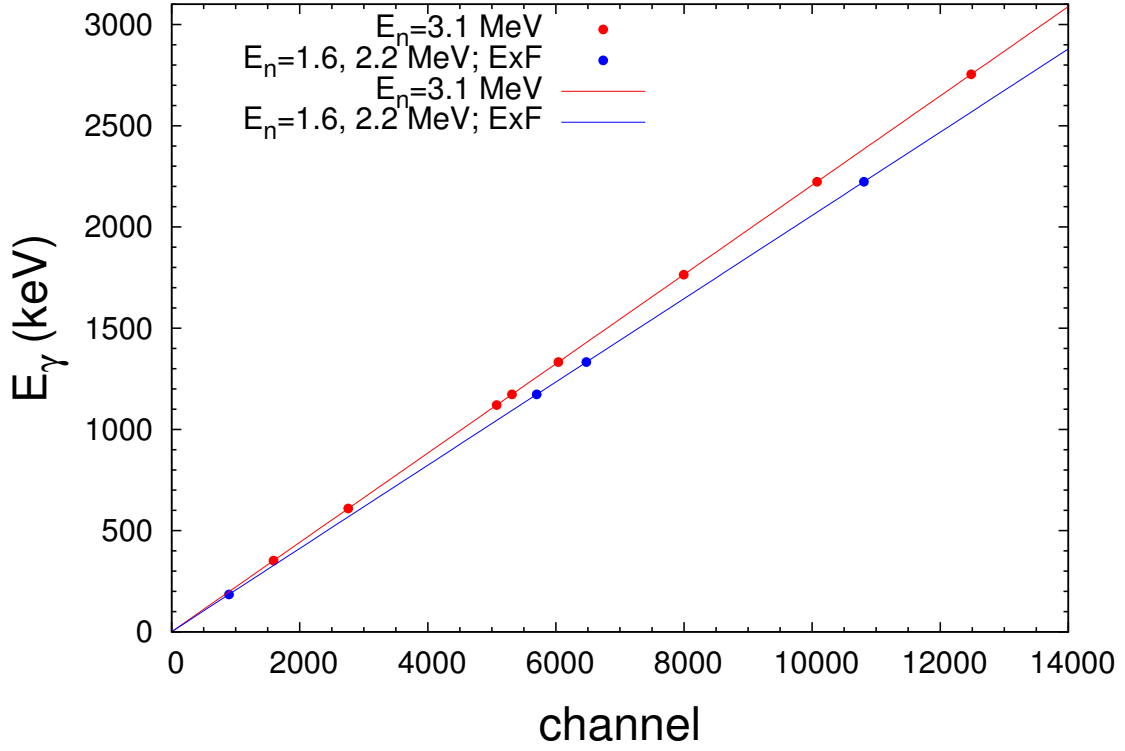


Figure 3.2. Linear energy calibration, taken from the three $^{162}\text{Dy}(n,n'\gamma)$ angular distributions and single excitation function (ExF in the legend).

3.1.4 Self-Absorption Corrections

One of the key characteristics of the Winterbon formalism for determining $F(\tau)$ as a function of τ is the use of large quantities of target material to provide sufficient nuclear and electronic stopping power [76]. Of course, a downside to using these molar quantities of powder targets is that incoming neutrons and outgoing γ -rays will be attenuated by the physical thickness of material. Much like the efficiency calibration, the self-absorption correction must be made to get proper γ -ray intensities, since low-energy gamma rays may be drastically attenuated by the thickness of the sample. Both the physical geometry of the experimental setup and size of the sample affect this highly-angular dependent correction, used solely in the angular distribution data

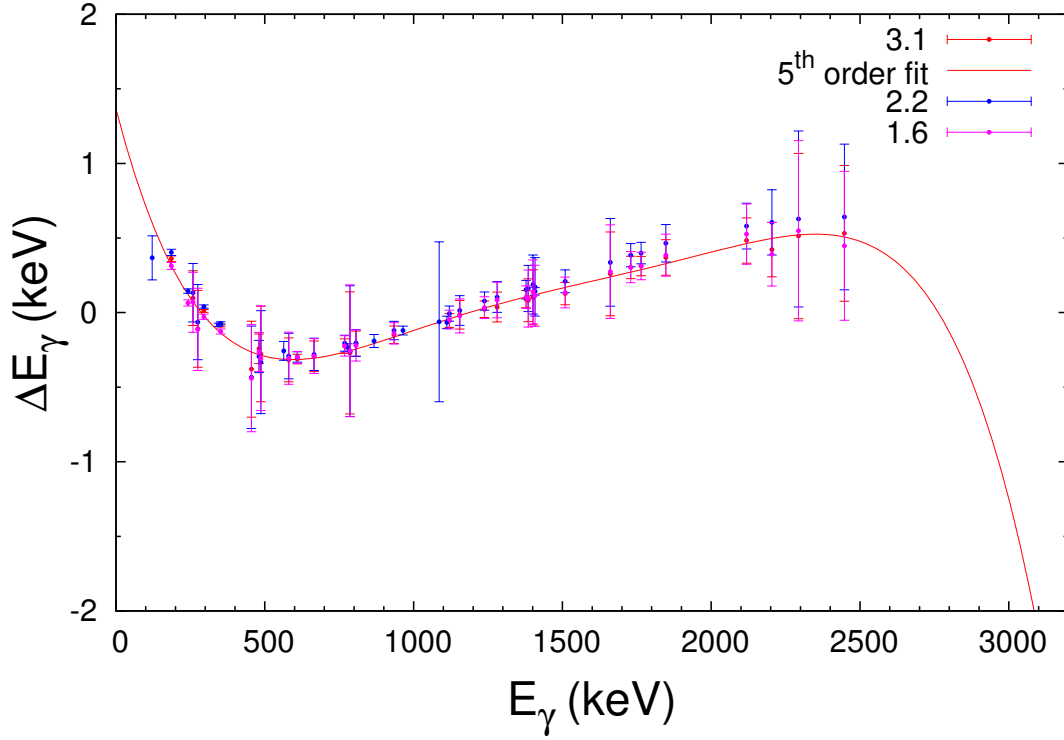


Figure 3.3. Order-5 polynomial nonlinearity correction, taken from the $^{162}\text{Dy}(n,n'\gamma)$ angular distribution with $E_n=3.1$ MeV

in the presented analysis. The **GAMBIT** ([25], [65], [14]) codes and subroutines are well-equipped to perform this correction for any experiment performed at UKAL involving a cylindrical target cell; **GAMBIT** takes into account differential elastic neutron cross sections ($\frac{d\sigma_n}{d\Omega}$ at 0° and 180°), total neutron cross sections ($\sigma_{n,tot}$), elastic neutron scattering cross sections ($\sigma_{n,el.}$), and the photon absorption cross sections (σ_γ for each composite material found in the sample ($^{162}\text{Dy}_2^{16}\text{O}_3$)). Figure 3.5 shows the multiplicative factor needed to give the correct peak areas from this self-absorption of γ -rays as a function of θ_{lab} . Factors near unity indicate little to no correction is needed (at higher energies, a γ -ray can easily escape the physical target), while a significant correction must be made to low-energy (<200 keV) γ -rays that are

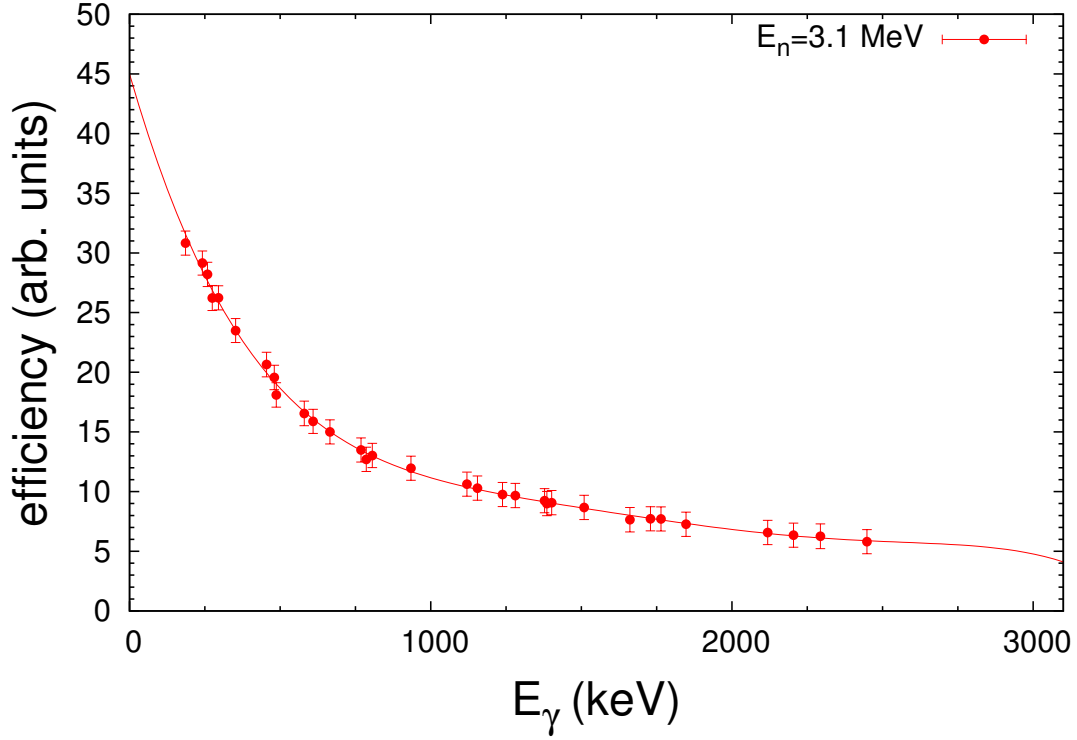


Figure 3.4. Fifth-order relative efficiency curve taken from the $^{162}\text{Dy}(n,n'\gamma)$ angular distribution with $E_n=3.1$ MeV

partially or heavily attenuated by the sample.

This self-absorption correction given by **GAMBIT** is sufficient and appropriate for use in the $(n,n'\gamma)$ experiments at UKAL, even though much more modern approaches to characterize the self-absorption exist. Molecular dynamics calculations can be made to generate this angularly and energetically dependent attenuation, but require a much higher amount of computational power to complete. Since the newer, refined methods do not offer a more efficient or accurate self-absorption calculation, we can confidently use the more simplistic approach given by the **GAMBIT** code.

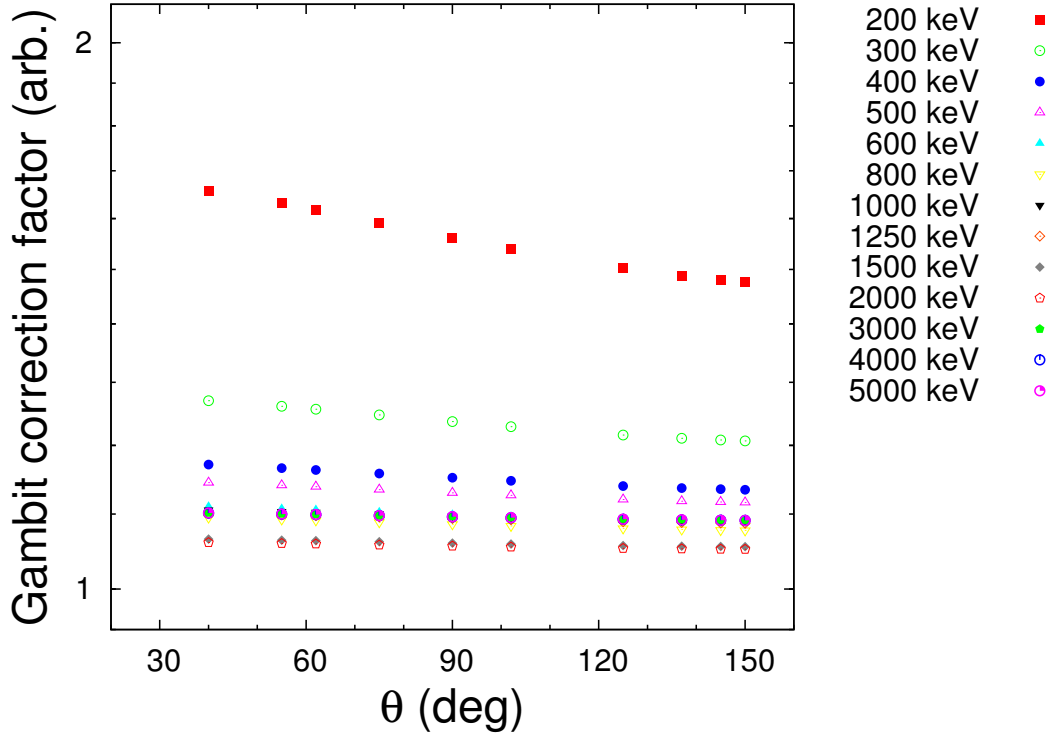


Figure 3.5. Multiplicative factor calculated by **GAMBIT** to correct for the angular dependent γ -ray self-absorption by a finite-size target.

3.2 Statistical Analysis

The wealth of information that can be extracted from γ -ray spectroscopy hinges on consistent, precise statistical analysis of spectra. An example of a properly TOF gated, energy calibrated, and background subtracted spectrum can be seen in Figure 3.6:

3.2.1 Fitting Procedures

A γ -ray event recorded in the HPGe detector will manifest itself as a skewed, defined-width gaussian distribution on the histogram of the form shown in Equation 3.1, and is fit according to:

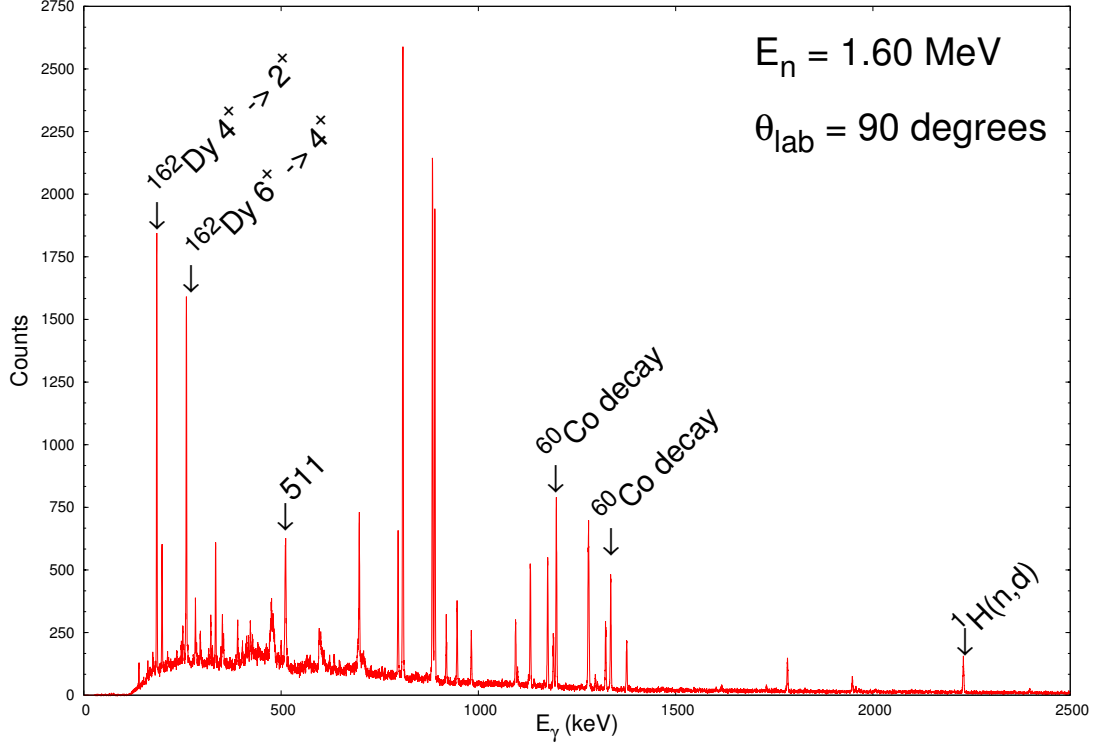


Figure 3.6. Example of an energy-calibrated spectrum from the ^{162}Dy angular distribution at $E_n=1.6$ MeV and $\theta_{lab}=90^\circ$, outlining typical background levels and miscellaneous γ -ray transitions.

$$y = \sum_k \frac{A_k}{(2\pi)^{\frac{1}{2}}\sigma} e^{-\frac{1}{2}\left(\frac{Z-Z_k}{\sigma}\right)^2} \left[1 + P_{left,1} \left(\frac{Z-Z_k}{\sigma} \right)^4 + P_{left,2} \left(\frac{Z-Z_k}{\sigma} \right)^{12} \right] \quad (3.1)$$

The multiple parameter fitting procedure in Equation 3.1 can be qualitatively described as measures of σ , the width of the peak, Z_k , the centroid location of a peak, A_k , the peak height, and two parameters relating to the low-energy tail (a measure of the skewedness of the gaussian), $P_{left,1}$ & $P_{left,2}$. This trailing edge is the result of Bremsstrahlung escape from the detector itself [44], but is necessary to accurately fit low-intensity peaks that exist as a doublet with higher-intensity peaks. For a given peak, three parameters are interpolated separately into a χ^2 fit,

the width, σ , and the two left-polynomial terms, $P_{left,1}$ & $P_{left,2}$. Typically, the polynomial terms are a small, but significant contribution ($P_{left,1} < 0.010$), and σ is bounded between ~ 2 and ~ 7 channels (~ 0.5 to ~ 1.5 keV energy resolution). These open parameters are iteratively fit one at a time to best recreate the shape of the gaussian distribution in the histogram; once all peaks have been properly fitted, the fit parameters are exported to a peak list with peak areas, centroids (subsequently the energy of the γ -ray), and the associated statistical errors from each parameter. *FitPac* [73] was used to interpolate fit parameters for all experimental data in both ^{160}Gd and ^{162}Dy . Peaks are assigned to groups with up to five other peaks to ensure a locally linear background for each gaussian.

3.2.2 Observable Extraction

From the peak list, we can extract a wealth of knowledge about the decay radiation observed, even with the seemingly basic information gained from fitting the peaks in a given histogram.

3.2.2.1 Excitation Functions

Although no direct measurable quantities (γ -ray energies, branching ratios, etc) can be extracted from the excitation function data, previously unplaced γ rays can be assigned to de-exciting levels simply by looking at the raw threshold of γ -ray population. Two plots per γ -ray are generated, the relationship between E_γ and E_n , and peak area as a function of E_n ; the first plot allows confirmation that each peak is fit uniformly, where the relationship between peak area and neutron energy will allow us to determine an approximate threshold energy. Any modulation of the γ -ray energy as a function of bombarding neutron energy is a signature of non-uniform peak fitting or that another γ -ray of similar energy has been populated in the level scheme at a different threshold. When this latter case occurs, the peak area as a function

of neutron energy will also show a corresponding bump at the same threshold. An example of this ensemble of plots is shown in Figure 3.7:

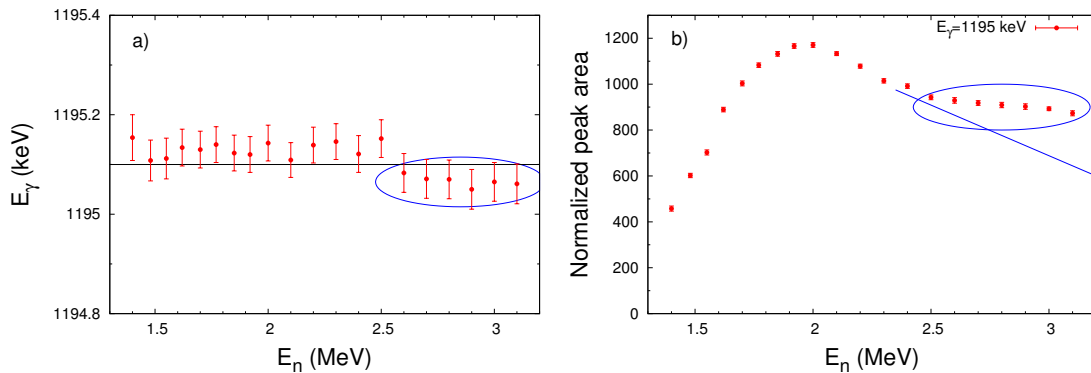


Figure 3.7. A set of plots from a typical excitation function for a single γ -ray transition, in ‘a)’, E_γ vs. E_n , and in ‘b)’, the peak area vs E_n . Note the dip in γ -ray energy at 2.6 MeV, and corresponding bump in peak area (shown as a blue ellipse to guide the eye), indicating a second transition of a similar (slightly lower) energy being populated.

The absolute threshold energies for γ -rays are used to determine where a γ -ray comes in, and to determine which level is providing the de-excitation, a problem that would otherwise require γ - γ coincidence measurements. Since the excitation functions give γ -ray placements in the nucleus, we are no longer reliant on the more complex coincidence measurements.

Figure 3.8 shows an example of the population rate of a γ -decay in ^{162}Dy by superimposing multiple neutron energy spectra on top of each other. Take note that the $E_n=1.4$ and 1.7 MeV datasets are below the energy threshold of the level that the 1647 keV decay leaves, with a sharp increase of counted statistics just above the level energy threshold, growing until a well-defined gaussian peak is seen at $E_n=2.3$ MeV.

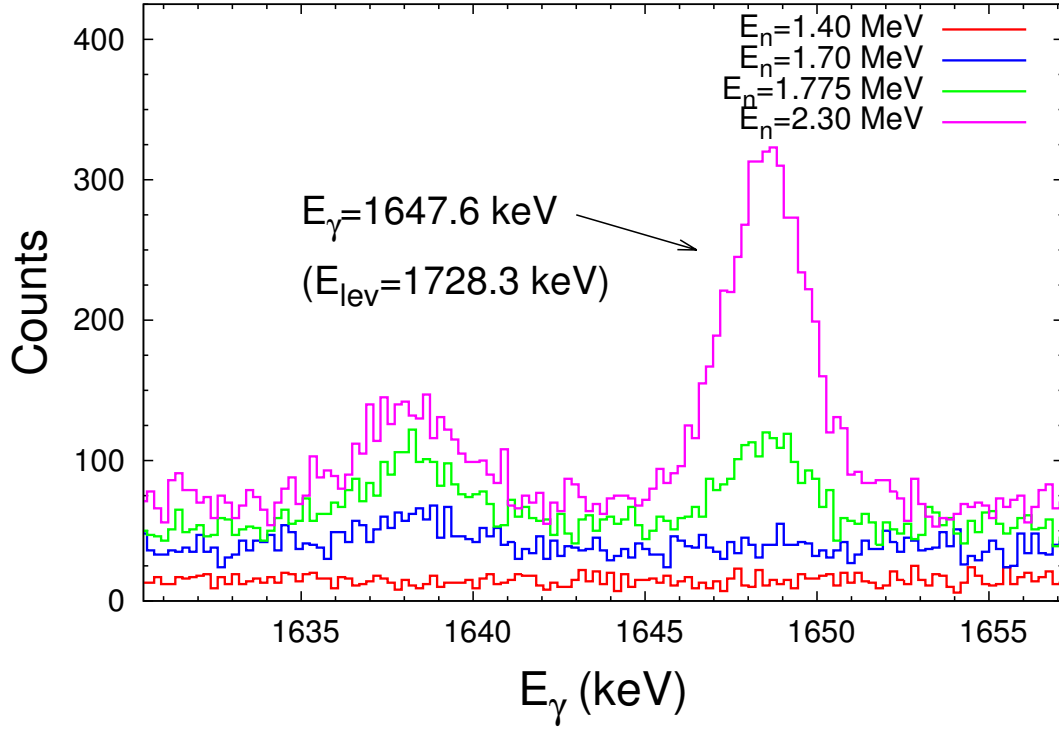


Figure 3.8. Spectra from four bombarding neutron energies ($E_n=1.4$, 1.7, 1.775, and 2.3 MeV datasets) to show the typical increase of statistics for a single peak, a 1647 keV decay from the 1728 keV state in ^{162}Dy . Note the peak area emerge just above the level energy threshold (1.775 MeV neutron dataset), with optimal statistics in the $E_n=2.3$ MeV set.

Proper placement of γ -rays in the level scheme is vital to confident, precise measurement of level lifetimes, absolute intensities, and multipole mixing fractions. Although the experiments at UKAL are not designed to find new $J=0$ states (*e.g.* something the Q3D spectrometer can better achieve with two nucleon transfer reactions), tentative spin assignments and/or confirmation of spin can be placed with information from both the excitation functions and angular distributions. $J=0$ excitations should have a threshold very close to the energy of the state, as there is very little angular momentum needed to populate the state, and since inelastic neutron scattering can only realistically populate up to spin 5^\pm states (a consequence of the

limited angular momentum transfer from the spin- $\frac{1}{2}$ neutron to the nucleus during inelastic scattering), stringent upper limits on the spin and parity of a parent level can be placed by examining the spin and parity of the daughter state. For example, if a transition between two levels is energetically feasible, we know that the spin and parity of the parent state will be within ± 2 units of angular momentum of the daughter level because only $\Delta J < 2$ multipolarities are observed in the laboratory with any appreciable or measurable intensity, as the relative intensity of E3, E4 and higher multipolarities are orders of magnitude less intense than the strong E2 quadrupole radiation observed in the lab. For example, in cases where the daughter level is spin-5, we know that the parent state will be spin-3 or spin-4, due to the low spin-population of inelastic neutron scattering.

3.2.2.2 Angular Distributions

Spectra from the angular distributions have all corrections applied (nonlinearity, detector efficiency, and self-absorption), where the peak list is separated and sorted into groups based on the γ -ray energy as a function of angle. Careful bounding of groups must be made to ensure good γ -ray separation in the event of a close-lying doublets, while maintaining sufficient overhead to account for large-order Doppler energy shifts (very short lifetimes on the order of ~ 10 fs).

In order to extract the lifetime of a particular state, precise calculation of the theoretical values for $F(\tau)$ (Winterbon curve) must be made to compare the extracted $F(\tau)$ from the Doppler shifted γ -rays. This calculation is achieved via `v1pgm`, which takes into account the calculated recoil velocity from Equation 2.2, the target density and atomic weight of each element in the target, and a range of lifetimes to iterate over (from 1 fs to 10 ps). Since the target does not change composition or density, the only input parameter that changes is the nuclear recoil velocity, dependent solely on the bombarding neutron energy. The calculated Winterbon curves for the ^{162}Dy

experiments can be seen in Figure 3.9, with an emphasis to highlight the ideal range (~ 10 - ~ 600 fs) to measure lifetimes with DSAM:

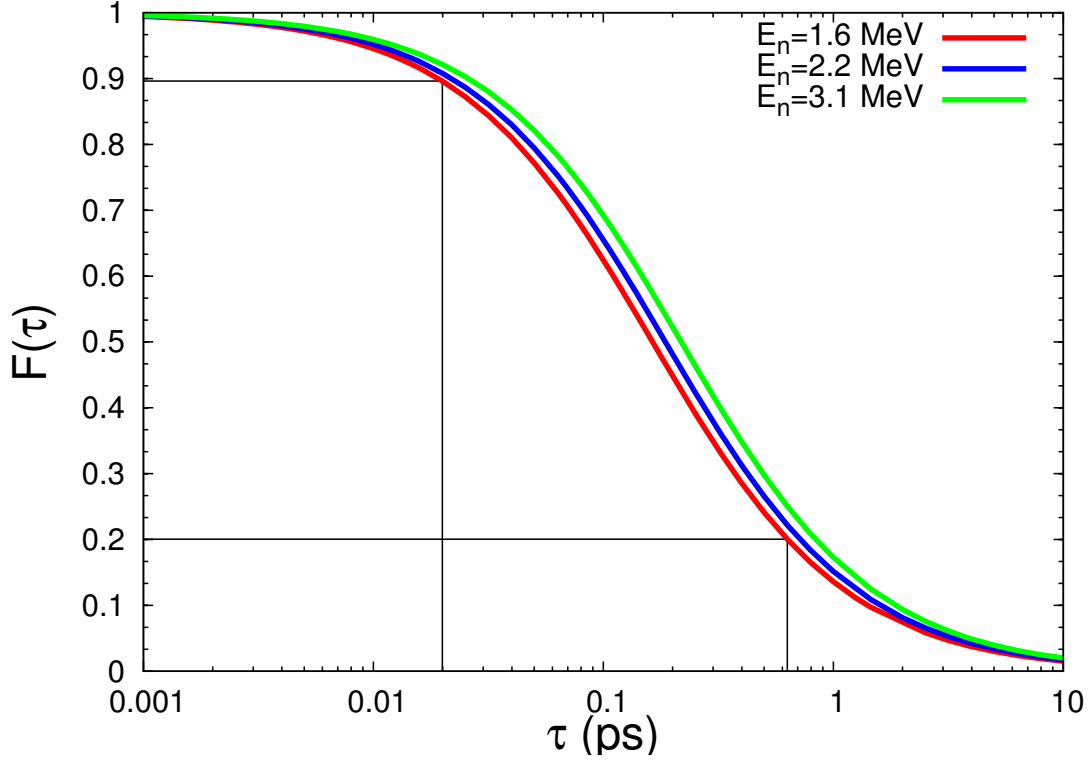


Figure 3.9. Calculated Winterbon curves ($F(\tau)$) as a function of τ for $E_n=1.6$, 2.2, and 3.1 MeV ^{162}Dy angular distributions. Sensitive lifetime ranges from DSAM are shown as vertical black lines, with the corresponding $F(\tau)$ values as horizontal lines.

Direct comparison of the experimental $F(\tau)$ value to the calculated Winterbon curve for a particular γ -ray is straightforward; in Figure 3.10, the measured slope of the Doppler shift of 0.665 correlates to a τ of 21 fs. For excited states with only one de-exciting transition, the extracted γ -ray lifetime is equivalent to the level lifetime,

where level lifetimes with multi-channel γ -ray de-excitations are extracted from the weighted average of all de-exciting $F(\tau)$ values, weighted by the uncertainty in each measured $F(\tau)$. This standard statistical average can be explicitly seen in Equation 3.2 taken from [9]. Special care must be taken, however, to ensure accurate and precise Doppler shifts are obtained from the various de-excitation channels from a level. In several cases for low energy and/or intensity γ rays, the shift (magnitude of $F(\tau)$) will be negative or consistent with zero; in this case, any lifetime deduced from the Doppler shift is not accounted in the weighted average of the level lifetime. The same rules apply when a particular γ ray has the potential to be coincident with a background line, where the $F(\tau)$ value may be unreliable. As a rule of thumb, $F(\tau)$ should be about 1σ variance from zero to be considered a good candidate for DSAM, however, this is sometimes impossible if the physical lifetime is on the precipice of the sensitive range of lifetimes DSAM can measure. Large upper uncertainties are not uncommon for the near-picosecond lifetimes with ‘shallow’ values for $F(\tau)$ measured with DSAM (e.g. 3000^{+4800}_{-1300} fs for the 1666 keV state in ^{162}Dy), yet another experimental challenge we must overcome when measuring the lifetimes of states.

$$\widehat{F(\tau)} = \frac{\sum_i F_i(\tau) \sigma_i^{-2}}{\sum_i \sigma_i^{-2}}, \sigma^2(\widehat{F(\tau)}) = \frac{1}{\sum_i \sigma_i^{-2}} \quad (3.2)$$

Further refinement of any spin assignments made in the literature can be deduced by examining the a_2 and a_4 coefficients from Equation 2.4; isotropic or near-isotropic angular distributions could suggest significant multipole mixing of γ radiation, as pure E2, E1, or M1 radiation will mimic the classical radiation patterns displayed in Figure 2.6. The decay radiation pattern leaving a 0^+ excitation will also be isotropic in the angular distribution, as this is the equivalent of an unaligned decaying state. The angular distributions can be used to confirm or deny tentative spin-0 states by examining the angular distribution, but this technique should not be used to find new 0^+ excitations (two nucleon transfer reactions are still a much higher resolution

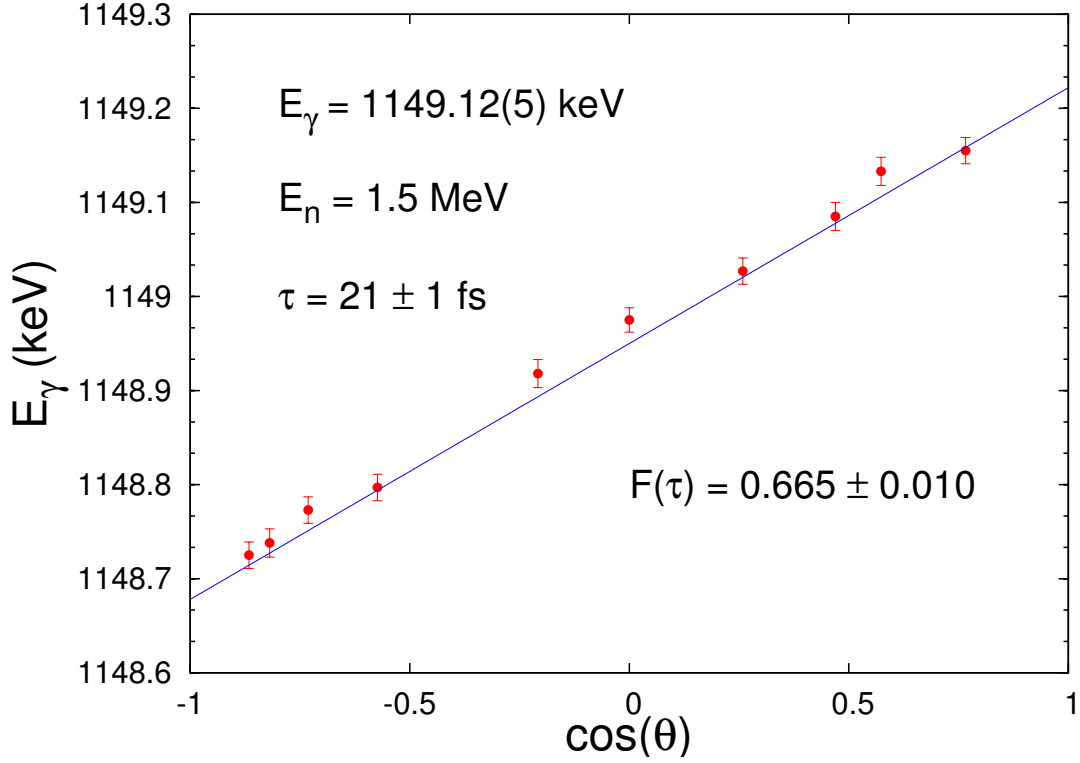


Figure 3.10. Example Doppler Shift for a 1149 keV γ -ray populated in the $1.5 \text{ MeV } ^{160}\text{Gd}(n,n'\gamma)$ experiment. Here, the $F(\tau)$ value of 0.665 ± 0.010 corresponds to a lifetime of $21 \pm 1 \text{ fs}$.

method). For all angular distributions presented, the peak areas are normalized in a way to force the decay from the first excited 0^+ state isotropically. This is justified in [49], where we examined multiple angular distribution normalizations: once with the above normalization, and once where we normalized the peak area to another tentative (now repudiated) 0^+ state with disastrous results. Under this secondary normalization, strong E2 transitions that show no mixing ceased to have the same qualitative shape of a pure quadrupole in Figure 2.6, implying this was not a suitable candidate for normalization (or as an isotropic $0^+ \rightarrow 2^+$ transition). Special care must also be taken with the evaluation of the angular distributions, as there are multiple ways to create an isotropic distribution, via proper mixing of multipole radiation

(admixture of E2 and M1 radiation).

If the angular distribution is not isotropic or indicative of a pure quadrupole or dipole radiation (Figure 2.6), then the γ -ray may be of a mixed multipolarity. This commonly occurs in transitions where $J_i^\pi \approx J_f^\pi$, but is not to be confused with an E0 monopole transition, which is strictly forbidden by γ decay and must occur via internal conversion electrons. In order to characterize this mixing, we compare the a_2 and a_4 coefficients to theoretical calculations of the same a_2 and a_4 coefficients for a particular J^π value for a level, assuming there is no mixing. The statistical model for a compound nucleus is used to calculate cross sections for a $(n,n'\gamma)$ reaction with the target nucleus being treated as an optical model potential (the combination of a real Woods-Saxon potential with a diffuse, imaginary Gaussian surface potential). The FORTRAN code used to achieve this calculation is CINDY (a Hauser-Feshbach formalism taken from [69]). The multipole mixing fraction (effectively a_2 and a_4) is then varied in the statistical model to reproduce the angular distribution for a possible J^π ; the direct comparison of experimental Legendre Polynomial coefficients to those calculated in this statistical model lead directly to χ^2 as a function of δ , the multipole mixing fraction. Any γ -ray observed in our experiments that has a known placement in the level scheme can be added to the optical model to perform this χ^2 minimization, where the smallest value of χ^2 corresponds to the optimal value of δ for a particular de-excitation. These experimental mixing fractions aid in the calculation of the reduced transition probabilities for mixed multipolarity γ decays given in Equation 1.16, also using Equations 1.17 or 1.18. An example extraction of δ from the angular distribution of γ -rays can be seen in Figure 3.11; χ^2 is minimized locally for this γ ray at a δ value ~ 1 , which indicates $\sim 50\%$ E2/M1 mixing. In Figure 3.11, the top left plot shows the measured angular distribution of the 1308 keV γ ray, with CINDY calculations for a range of starting spins decaying to a spin-4 state. The intersection of the black ellipse and the colored ellipses (calculations) correspond to

the projections in the bottom plot, where we verify the lowest χ^2 value on the y-axis for a particular delta on the x-axis for the $4^+ \rightarrow 4^+$ transition.

To round out the cadre of important experimental information, we can extract the absolute intensity of γ -rays that de-excite the nucleus from the angular distribution data. The A_o coefficient from Equation 2.4 is proportional to the absolute intensity, and simply needs to have the efficiency & self-absorption corrections applied to the measured A_o (gross peak area). The branching ratios immediately follow from the absolute intensities, since we know all γ -decay channels open to a particular level, and these are used to calculate absolute transition probabilities (Equation 1.16).

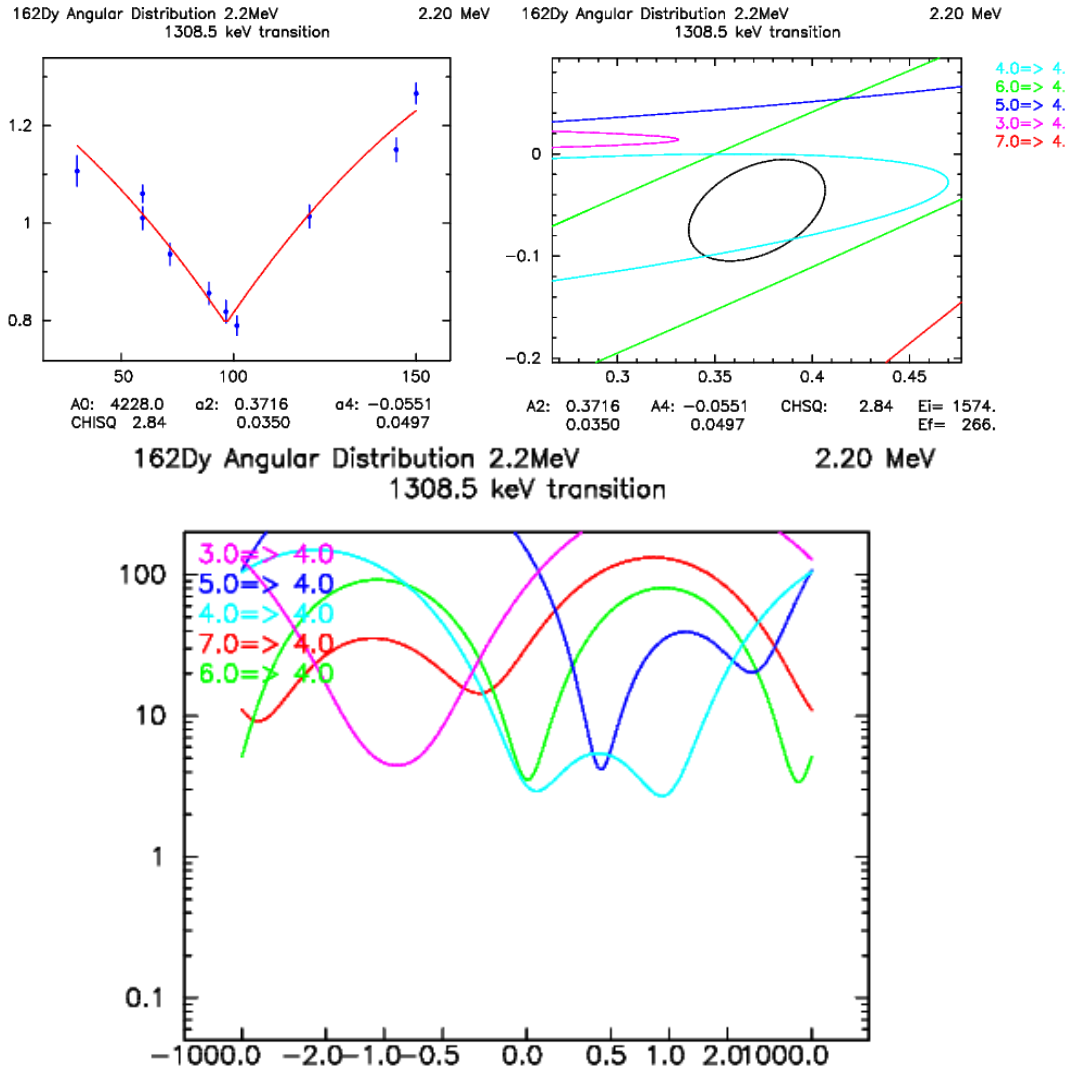


Figure 3.11. Example extraction of multipole mixing fraction (δ) for a $4^+ \rightarrow 4^+$ transition in ^{162}Dy . Top-left plot: angular distribution of the 1308 keV γ ray. Top-right plot: CINDY comparison for a range of initial spins (color online) decaying to the final spin of 4; intersections with the black ellipse mark local/global minima of χ^2 vs δ . Bottom plot: projection of CINDY comparison as χ^2 as a function of δ minimization (note the lowest χ value corresponds to the $\delta \approx 1$ for the cyan-colored $4^+ \rightarrow 4^+$ transition). (color online)

CHAPTER 4

RESULTS

When reporting the lifetimes in this work, it is prudent to distinguish which angular distribution is used, as the lifetimes are sensitive to inflation from multiple sources. First, recall Figure 3.9, where we observe inflation of the lifetimes due to the calculation of $F(\tau)$ from a higher neutron energy, and thus, a modified value for the nuclear and electronic stopping powers that allows us to extract the lifetime. Second, the extracted lifetime can be inflated due to level-feeding effects from higher-lying excitations in the nucleus; for these reasons, we want to report lifetimes from the *lowest* energy threshold possible to reduce the effect of this lifetime inflation. An example of the proportional lifetime inflation for two excited states caused by level-feeding and bombarding neutron energy differences can be seen in Figure 4.1.

For the interest of discussion in §5, lifetimes are separated into smaller, more digestible tables based on their corresponding discussion sections (*e.g.* a table containing lifetimes of 0^+ states, one for the 2_γ^+ band, etc). Unless otherwise noted, tables in this chapter will contain experimentally determined level energies, γ -ray energies, branching ratios measured from our angular distributions, multipole mixing fractions where applicable, and the lifetime of the state with applicable uncertainties for all of the above quantities.

4.1 ^{160}Gd Results

Results from the ^{160}Gd campaign were published in [49] and [REF TBA], where this work also outlines and reiterates the major results taken from the suite of experi-

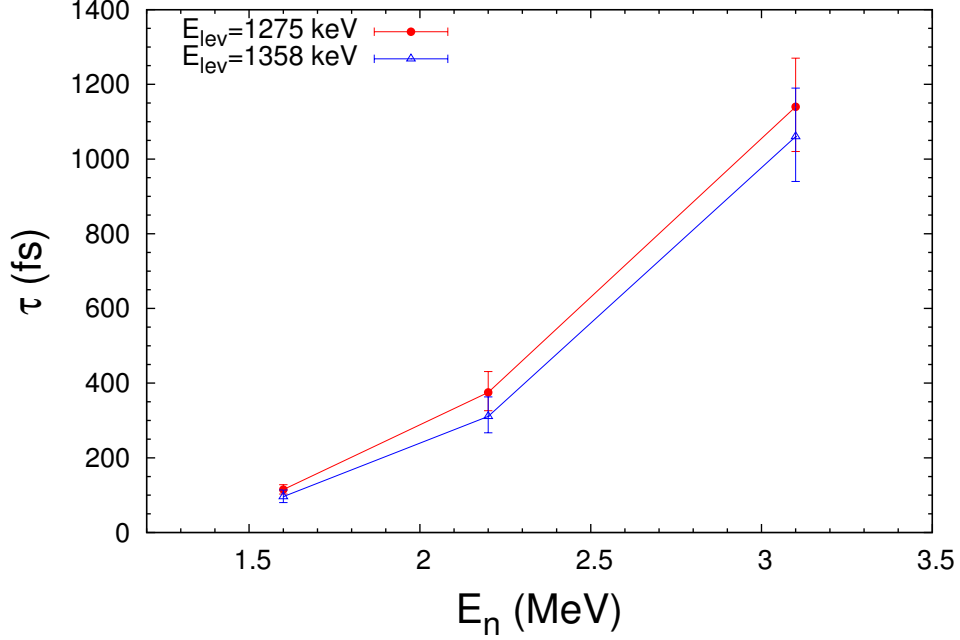


Figure 4.1. Lifetime inflation of the measured lifetimes for two levels ($E_{lev}=1275$ keV and $E_{lev}=1358$ keV) in ^{162}Dy caused by effects due to a higher bombarding neutron energy and unknown level-feeding from higher-lying states.

ments in §2.4.1. A level scheme outlining all measured lifetimes in the ^{160}Gd campaign is shown in Figure 4.2, with previously existing literature lifetimes in blue and new lifetime measurements in red. Gadolinium-160 suffers from a complete paucity of lifetime information as a whole (most notably for 0^+ bands and negative parity bands), and as such, we add 29 new lifetimes, a factor of 7 increase, to the pool of placed literature values.

High resolution angular distribution measurements were performed by Govor in [33] and provide us with an overall benchmark for our measurements, and as a whole, our reported γ -ray intensities, angular distribution coefficients, and multipole mixing ratios are found to be in good agreement with the work. One key contrasted element

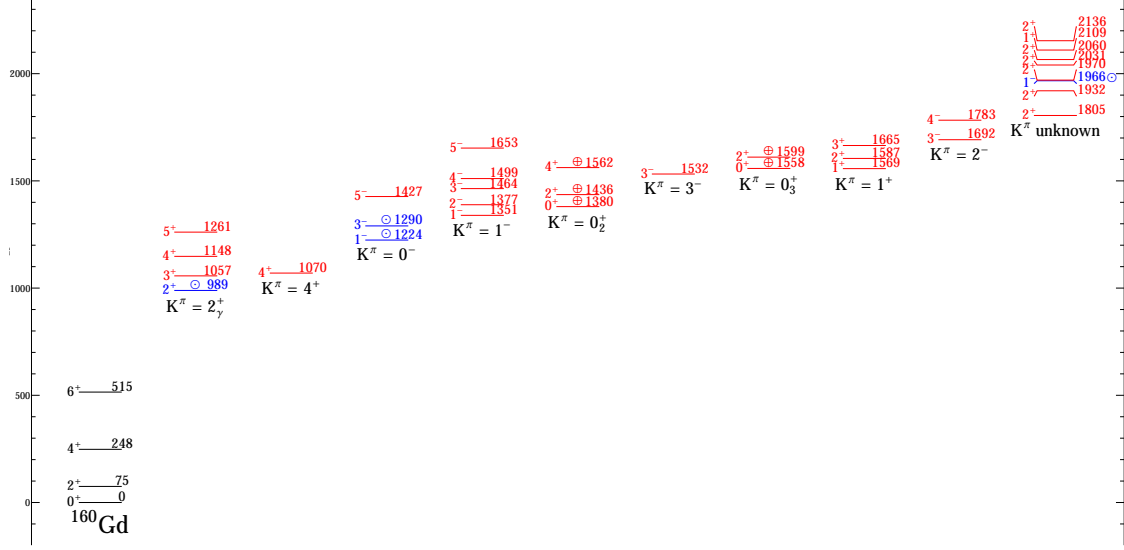


Figure 4.2. Level scheme for all level lifetimes measured in the ^{160}Gd experiments, with confirmed band and spin assignments shown. Previously measured lifetimes are in blue, with newly presented lifetimes in red. Individual levels and bands will be discussed in following sections.

in our work with the Govor paper is the use of monoenergetic neutrons for DSAM-INS rather than the continuum energies of reactor neutrons to extract the lifetimes in addition to any decay information (γ -ray energies, multipole mixing fractions, etc). A visual representation of the all the measured lifetimes in ^{160}Gd is shown in Figure 4.3, with literature values in black and new lifetimes in red (corresponding to lifetime extracted from the $E_n=1.5$ MeV dataset), green for 2.0 MeV neutrons, and blue for the final dataset using 2.8 MeV neutrons bombardement.

An example of the $E_n=2.0$ MeV angular distribution singles-spectrum for $^{160}\text{Gd}(n,n'\gamma)$ can be seen in Figure 4.4 with select peaks labeled for reference.

4.1.1 Lifetimes of 0^+ States

The tabulation of lifetimes for the 0^+ bands in ^{160}Gd is given in Table 4.1. In many cases, $F(\tau)$ values for γ rays were small, and as such, we are only able to

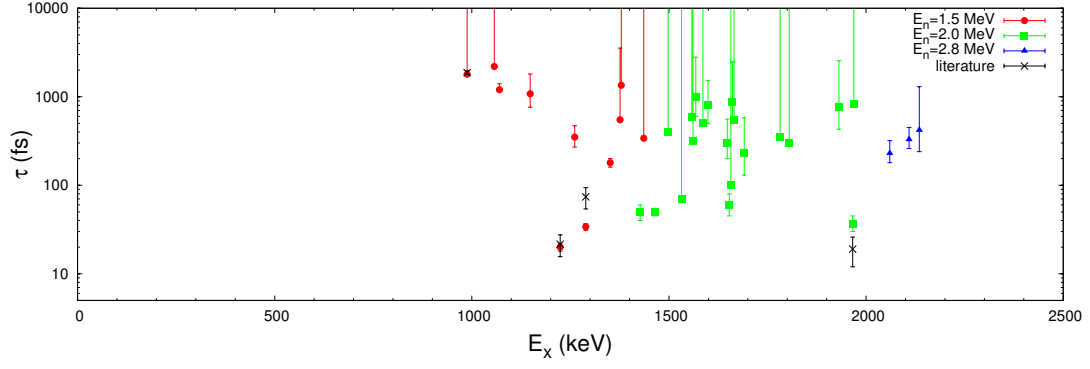


Figure 4.3. Visual representation of all measured lifetimes with respect to literature values (in blue). Each separate color outlines the specific regimes (<1.5 MeV, $1.5 - 2.0$ MeV, and >2.0 MeV excitation energy) of energies studied in the ^{160}Gd angular distributions.

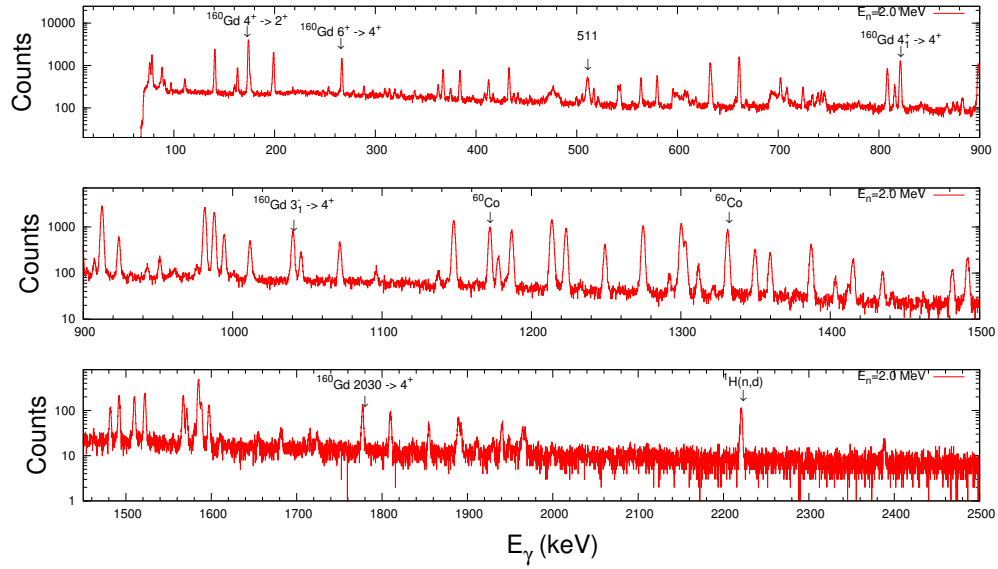


Figure 4.4. Singles spectra from the $\theta_{lab}=90^\circ$ and $E_n=2.0$ MeV angular distributions of ^{160}Gd .

extract lower limits for the level lifetimes. Further refinement of the level lifetime for the $E_x=1599$ keV state was provided in [TBA REF], where any negative (and consequently impossible) $F(\tau)$ attenuation factors were removed from the weighted average for the level lifetime.

E_{level} (keV)	E_γ (keV)	$J_{K_i^\pi}$	$J_{K_f^\pi}$	τ (fs)	BR	Mult.	B(E2) (W.u.)	B(E1) (mW.u.)
1379.70 (7)	1304.46 (5)	$0_{0_2}^+$	$2_{0_1}^+$	>1350	1.000	E2	<3.10	
1436.47 (4)	1187.81 (5)	$2_{0_2}^+$	$4_{0_1}^+$	>340	0.667	E2	<13.1	
	1361.05 (6)	$2_{0_2}^+$	$2_{0_1}^+$		0.243	E2/M1 ^[a]	<2.42	
	1436.34 (6)	$2_{0_2}^+$	$0_{0_1}^+$		0.090	E2	<0.68	
1561.59 (6)	1046.67 (6)	$4_{0_2}^+$	$6_{0_1}^+$	>320	0.572	E2	<22	
	1313.03 (6)	$4_{0_2}^+$	$4_{0_1}^+$		0.428	E2/M1 ^[b]	<0.4	
1558.30 (7)	1483.06 (6)	$0_{0_3}^+$	$2_{0_1}^+$	>590	1.000	E2	<3.74	
1599.00 (4)	309.32 (6)	$2_{0_3}^+$	$3_{0_1}^-$	800_{-300}^{+730}	0.037	E1		$0.34_{-0.31}^{+0.13}$
	374.78 (6)	$2_{0_3}^+$	$1_{0_1}^-$		0.062	E1		$0.32_{-0.29}^{+0.12}$
	541.53 (6)	$2_{0_3}^+$	$3_{2_7}^+$		0.154	E2/M1 ^[c]	41_{-37}^{+16}	
	1523.59 (6)	$2_{0_3}^+$	$2_{0_1}^+$		0.418	E2/M1 ^[d]	$0.34_{-0.32}^{+0.68}$	
	1598.85 (6)	$2_{0_3}^+$	$0_{0_1}^+$		0.329	E2	$0.41_{-0.37}^{+0.15}$	

$$^{[a]}\delta=0.00_{-0.08}^{+0.08}, ^{[b]}\delta=0.28_{-0.12}^{+0.34}, ^{[c]}\delta=-5.57_{-5.00}^{+1.91}, ^{[d]}\delta=-1.04_{-2.10}^{+0.72}$$

$$1 \text{ W.u. (E2)}=5.16\text{E-7 e}^2\text{b}^2, 1 \text{ mW.u. (E1)}=1.90 \text{ e}^2\text{b}$$

TABLE 4.1

Lifetimes of excited 0^+ bands in ^{160}Gd , with experimentally determined B(E2) in W.u and B(E1) in mW.u. (1 mW.u. = 1.90 e²b).

4.1.2 Lifetimes of 2^+ Band

We have measured lifetimes for the 4 lowest-lying members of the $K\pi=2^+$ band in ^{160}Gd in our campaign of experiments. Throughout the rare-earth region of nuclei, the 2^+ band lifetimes are generally well known and fall in the near-picosecond lifetime range [17, 36, 41, 53]. Due to the sensitive range of DSAM, these near-picosecond lifetimes manifest as lower-limits due to the shallow $F(\tau)$ values observed in our experiments; however, we obtain well-defined values for the 4^+ and 5^+ members of the 2^+ band via some well-defined energy shifts, all shown in Table 4.2.

4.1.3 Lifetimes of Negative Parity Bands

Population of the $K\pi=0^-$ bands in rare-earth nuclei is abundant [83], showing up as some of the strongest peaks in our γ -singles spectra, with a very low angular momentum transfer needed to populate the states ($\Delta K=0$). Typically, since the lowest-lying negative parity states are collective octupole vibrations on top of the deformed ground state, the mean lifetimes of these states are comparatively short, acting as a practical benchmark for lifetimes measurable by DSAM-INS. All three level lifetimes from the $K\pi=0^-$ band in ^{160}Gd were measured from the inelastic scatter of 1.5 MeV neutrons, using the five γ -rays listed in Table 4.3.

Similar to the $K\pi=0^-$ band, the $K\pi=1^-$ band in ^{160}Gd is richly populated in our $(n,n'\gamma)$ experiments, with four band members ($1^-, 2^-, 3^-, 4^-$) all proposed by Govor in another $(n,n'\gamma)$ study [33] using continuum energy reactor neutrons in contrast to our monoenergetic probe. Of the specific lifetimes measured from the Doppler shifting γ -rays, we observe a weak decay from the 2^- state to the γ -vibrational band; this branching ratio is so weak that it *could* be misplaced, however, the threshold of the de-excitation in our excitation function does not place it leaving any other level. The resulting lifetime from the 1301 keV γ ray is only a lower-limit due to the shallow

E_{level} (keV)	E_γ (keV)	$J_{K_i^\pi}$	$J_{K_f^\pi}$	τ (fs)	BR	Mult.	B(E2) (W.u.)
988.72 (6)	913.43 (5)	$2_{2\gamma}^+$	$2_{0_{gs}}^+$	>1800	0.530	E2/M1 ^[a]	<1.2
	988.68 (5)	$2_{2\gamma}^+$	$0_{0_{gs}}^+$		0.470	E2	<4.1
1057.42 (6)	809.06 (5)	$3_{2\gamma}^+$	$4_{0_{gs}}^+$	>2200	0.171	E2/M1 ^[b]	<0.04
	982.28 (5)	$3_{2\gamma}^+$	$2_{0_{gs}}^+$		0.829	E2/M1 ^[c]	<6.5
1148.15 (7)	899.59 (5)	$4_{2\gamma}^+$	$4_{0_{gs}}^+$	1080_{-320}^{+730}	0.631	E2/M1 ^[d]	16_{-10}^{+5}
	1072.85 (5)	$4_{2\gamma}^+$	$2_{0_{gs}}^+$		0.369	E2	$3.8_{-1.1}^{+2.6}$
1261.24 (9)	746.34 (5)	$5_{2\gamma}^+$	$6_{0_{gs}}^+$	350_{-80}^{+120}	0.164	E2/M1 ^[e]	31_{-11}^{+7}
	1012.65 (5)	$5_{2\gamma}^+$	$4_{0_{gs}}^+$		0.836	E2/M1 ^[f]	35_{-12}^{+8}
$^{[a]}\delta=-0.45_{-0.05}^{+0.04}$, $^{[b]}\delta=0.11_{-0.03}^{+0.03}$, $^{[c]}\delta=47_{-10}^{+18}$, $^{[d]}\delta=21_{-7}^{+21}$, $^{[e]}\delta=8_{-4}^{+13}$, $^{[f]}\delta=15_{-6}^{+17}$ 1 W.u.(E2)=5.16E-7 e ² b ²							

TABLE 4.2

Lifetimes of $K^\pi=2_\gamma^+$ band in ^{160}Gd , with experimentally determined B(E2) in W.u. and multipole mixing fractions δ taken from the $E_n=1.5$ MeV angular distributions.

$F(\tau)$ value.

Grigoriev [34] places a $K^\pi=2^-$ assignment on the band with the $E_x=1691$ & 1782 keV members that was tentatively either a 2^- or 3^- . We adopt this 2^- assignment from our observed γ -decay channels, even without the measurement or observation of the 2^- bandhead in our data.

4.1.4 Lifetimes of Positive Parity Bands

In addition to the measurement of lifetimes of $K=0,2$ and negative parity bands, we are also able to populate the vast majority of states below $J=5$. Lifetimes of

E_{level} (keV)	E_γ (keV)	$J_{K_i^\pi}^\pi$	$J_{K_f^\pi}^\pi$	τ (fs)	BR	Mult.	B(E1) (mW.u.)
1224.33 (6)	1149.12 (5)	$1_{0_1}^-$	$2_{0_1}^+$	20_{-2}^{+2}	0.597	E1	$6.5_{-0.6}^{+0.6}$
	1224.38 (5)	$1_{0_1}^-$	$0_{0_1}^+$		0.403	E1	$3.6_{-0.4}^{+0.4}$
1289.90 (7)	1041.37 (5)	$3_{0_1}^-$	$4_{0_1}^+$	34_{-3}^{+3}	0.353	E1	$3.0_{-0.3}^{+0.3}$
	1214.79 (5)	$3_{0_1}^-$	$2_{0_1}^+$		0.647	E1	$3.5_{-0.3}^{+0.3}$
1427.40 (12)	1214.79 (5)	$5_{0_1}^-$	$4_{0_1}^+$	50_{-10}^{+10}	1.000	E1	$4.0_{-0.8}^{+0.8}$
1351.30 (6)	1276.06 (5)	$1_{1_1}^-$	$2_{0_1}^+$	180_{-20}^{+20}	0.833	E1	$0.74_{-0.08}^{+0.08}$
	1351.30 (5)	$1_{1_1}^-$	$0_{0_1}^+$		0.167	E1	$0.12_{-0.01}^{+0.01}$
1376.70 (8)	319.38 (6)	$2_{1_1}^-$	$3_{2_\gamma}^+$	>550	0.017	E1	<0.18
	1301.46 (5)	$2_{1_1}^-$	$2_{0_1}^+$		0.982	E1	<0.27
1464.00 (10)	1388.75 (5)	$3_{1_1}^-$	$2_{0_1}^+$	50_{-5}^{+5}	1.000	E1	$2.5_{-0.2}^{+0.2}$
1498.94 (10)	1250.39 (5)	$4_{1_1}^-$	$4_{0_1}^+$	>400	1.000	E1	<0.41
1691.68 (7)	543.45 (6)	$3_{2_1}^-$	$4_{2_\gamma}^+$	230_{-100}^{+350}	0.226	E1	2_{-3}^{+1}
	634.56 (6)	$3_{2_1}^-$	$3_{2_\gamma}^+$		0.370	E1	$2.1_{-3.2}^{+0.9}$
	702.84 (6)	$3_{2_1}^-$	$2_{2_\gamma}^+$		0.372	E1	$1.5_{-2.3}^{+0.7}$
	1442.93 (8)	$3_{2_1}^-$	$4_{0_1}^+$		0.032	E1	$0.01_{-0.02}^{+0.01}$
1782.67 (10)	521.53 (8)	$4_{2_1}^-$	$5_{2_\gamma}^+$	>350	0.208	E1	<2.0
	725.19 (6)	$4_{2_1}^-$	$3_{2_\gamma}^+$		0.792	E1	<1.4

TABLE 4.3

Lifetimes of excited negative parity bands in ^{160}Gd , with experimentally determined B(E1) in mW.u. (1 mW.u. = 1.90 e²b).

positive parity bands were measured in ^{160}Gd , namely of the $K^\pi=4^+$ and 1^+ bands.

The full tabulation of measured lifetimes can be found in Table 4.4.

E_{level} (keV)	E_γ (keV)	$J_{K_i^\pi}$	$J_{K_f^\pi}$	τ (fs)	BR	Mult.	$B(\pi\ell)$
1070.57 (7)	555.45 (8)	$4_{4_1}^+$	$6_{0_1}^+$	>1200	0.010	E2	<2.4
	822.06 (5)	$4_{4_1}^+$	$4_{0_1}^+$		0.603	E2/M1 ^[a]	<7.2
	995.30 (5)	$4_{4_1}^+$	$2_{0_1}^+$		0.387	E2	<5.2
1568.77 (6)	217.51 (6)	$1_{1_1}^+$	$1_{1_1}^-$	1000_{-400}^{+1800}	0.030	E1	$0.97_{-1.8}^{+0.7}$
	580.20 (6)	$1_{1_1}^+$	$2_{2_\gamma}^+$		0.305	E2/M1 ^[b]	$5.3_{-13}^{+6.7}$
	1493.40 (6)	$1_{1_1}^+$	$2_{0_1}^+$		0.323	E2/M1 ^[c]	$0.44_{-0.88}^{+0.23}$
	1568.70 (6)	$1_{1_1}^+$	$0_{0_1}^+$		0.342	E2/M1 ^[*]	$0.56_{-1.01}^{+0.22}$
1586.61 (12)	1511.36 (6)	$2_{1_1}^+$	$2_{0_1}^+$	>500	1.000	E2	<4.01
1665.16 (8)	288.57 (6)	$3_{1_1}^+$	$2_{1_1}^-$	>540	0.115	E1	<2.9
	1416.59 (6)	$3_{1_1}^+$	$4_{0_1}^+$		0.462	E2/M1 ^[d]	<0.73
	1589.81 (6)	$3_{1_1}^+$	$2_{0_1}^+$		0.423	E2/M1 ^[e]	<0.95

^[a] $\delta=-0.72_{-0.05}^{+0.06}$, ^[b] $\delta=0.28_{-0.18}^{+0.25}$, ^[c] $\delta=1.34_{-0.6}^{+1.6}$, ^[d] $\delta=0.67_{-0.08}^{+0.11}$, ^[e] $\delta=-1.87_{-0.18}^{+0.18}$

^[*] Full E2 strength is reported (no δ was calculated)

1 W.u.(E2)=5.16E-7 e²b², 1 mW.u.(E1)=1.90 e²b

TABLE 4.4

Lifetimes of excited positive parity bands in ¹⁶⁰Gd, with experimentally determined B(E2) in W.u and B(E1) in mW.u. (1 mW.u. = 1.90 e²b).

4.1.5 Lifetimes of States with No K ^{π} Assignment

The remaining lifetimes of states with no rotational band assignment are tabulated in Table 4.5 and presented with deduced transition probabilities in Figure 5.6. We place stringent limits on the spin and parity of these states by confirming all de-excitations exhibit the same qualitative shape in the excitation functions, and by examining the Legendre polynomial coefficients to ascertain changes in angular

momentum. In many cases, this is easily done if the radiation pattern is strongly E2 or E1; for mixed-multipolarity γ rays, comparison to the **CINDY** code is possible to restrict possible spin assignments. Generally, **CINDY** is used as a baseline, rough assignment, as the statistical model behaves much better at lower mass nuclei, such as ^{76}Ge or ^{106}Pd [24, 62], where the density of states above the pairing gap is smaller, and as such are tentative assignments placed by our $(n,n'\gamma)$ study.

E_{level} (keV)	E_γ (keV)	$J_{K_i^\pi}^\pi$	$J_{K_f^\pi}^\pi$	τ (fs)	BR	Mult.	$B(\pi\ell)$
1805.13 (9)	734.50 (6)	$2_{[\Upsilon]}^+$	$4_{4_1}^+$	>300	0.307	E2	<76
	816.46 (6)	$2_{[\Upsilon]}^+$	$2_{2_1}^+$		0.693	E2/M1 ^[a]	<37
1931.96 (7)	874.51 (6)	$2_{[\Upsilon]}^+$	$3_{2_1}^+$	760_{-330}^{+1800}	0.197	E2/M1 ^[b]	$8_{-19}^{+3.5}$
	1683.45 (7)	$2_{[\Upsilon]}^+$	$4_{0_1}^+$		0.206	E2	$0.32_{-0.75}^{+0.14}$
	1856.65 (6)	$2_{[\Upsilon]}^+$	$2_{0_1}^+$		0.454	E2/M1 ^[c]	$0.20_{-0.47}^{+0.17}$
	1932.00 (7)	$2_{[\Upsilon]}^+$	$0_{0_1}^+$		0.143	E2	$0.11_{-0.26}^{+0.05}$
1966.66 (10)	1891.33 (6)	$1_{[\Upsilon]}^+$	$2_{0_1}^+$	37_{-7}^{+8}	0.637	E1	$0.84_{-0.21}^{+0.28}$
	1966.97 (13)	$1_{[\Upsilon]}^+$	$0_{0_1}^+$		0.363	E1	$0.43_{-0.11}^{+0.16}$
1969.84 (9)	1894.50 (6)	$2_{[\Upsilon]}^+$	$2_{0_1}^+$	>830	0.582	E2/M1 ^[*]	<0.45
	1969.93 (7)	$2_{[\Upsilon]}^+$	$0_{0_1}^+$		0.418	E2	<0.27
2030.90 (9)	1782.14 (6)	$2_{[\Upsilon]}^+$	$4_{0_1}^+$	>255	0.139	E2/M1 ^[*]	<0.47
	1955.93 (7)	$2_{[\Upsilon]}^+$	$2_{0_1}^+$		0.861	E2	<1.84
2060.43 (11)	2060.42 (6)	$2_{[\Upsilon]}^+$	$6_{0_1}^+$	230_{-50}^{+90}	1.000	E2	$1.82_{-0.71}^{+0.40}$
2109.32 (7)	1051.87 (6)	$1_{[\Upsilon]}^+$	$3_{2_1}^+$	330_{-70}^{+120}	0.170	E2	$6.23_{-2.28}^{+1.34}$
	1119.71 (13)	$1_{[\Upsilon]}^+$	$2_{2_1}^+$		0.208	E2/M1 ^[*]	$5.57_{-2.04}^{+1.21}$
	2034.26 (6)	$1_{[\Upsilon]}^+$	$2_{0_1}^+$		0.359	E2/M1 ^[*]	$0.49_{-0.18}^{+0.10}$
	2109.31 (6)	$1_{[\Upsilon]}^+$	$0_{0_1}^+$		0.263	E2/M1 ^[*]	$0.30_{-0.11}^{+0.06}$
2135.76 (13)	2135.74 (7)	$2_{[\Upsilon]}^+$	$0_{0_1}^+$	420_{-180}^{+880}	1.000	E2	$0.83_{-1.75}^{+0.36}$

^[a] $\delta=-0.76_{-0.13}^{+0.10}$, ^[b] $\delta=-3.3_{-2.4}^{+1.1}$, ^[c] $\delta=0.92_{-0.64}^{+0.41}$
^[*] Full E2 strength is reported (no δ was calculated)

1 W.u.(E2)=5.16E-7 e²b², 1 mW.u.(E1)=1.90 e²b

[Υ]: No rotational K^π band assignment given in literature.

TABLE 4.5

Lifetimes of excited states in ¹⁶⁰Gd that have no band assignment, with experimentally determined B(E2) in W.u and B(E1) in mW.u. (1 mW.u. = 1.90 e²b).

4.2 ^{162}Dy Results

^{162}Dy , one of the most studied nuclei on the chart of nuclides, with over 24 different reactions and probes (from electron capture, stripping/pickup (t,p)/(p,t) reactions, neutron capture, $(\alpha,2n)$ reactions, and $(^3\text{He},\alpha)$ reactions, to name a few) which have been implemented to extract information on the structure of ^{162}Dy [3]. Several previous $(n,n'\gamma)$ campaigns were carried out to measure level lifetimes of the isovector M1 scissors mode in ^{162}Dy ([43]), as well as a series of precision angular distribution measurements by Govor *et. al* ([32]) to extract multipole mixing fractions and γ -ray intensities. Analogous to the ^{160}Gd case study, the angular distributions carried out by Govor act as a complimentary guide and benchmark for our measurements. While the initial and chief goal is to measure the lifetimes of 0^+ excitations and low-lying negative parity states, we are also able to populate and measure the lifetimes of the vast majority of low spin ($J < 5$) states under the bombarding neutron energy threshold. The full result of all measured lifetimes in the ^{162}Dy experimental campaign (§2.4.2) is displayed in the level scheme in Figure 4.5.

In Figure 4.5, levels colored blue are pre-existing lifetimes in literature, where the levels in red are newly presented lifetime measurements in this work. Due to the limitations of DSAM outlined in §3.2.2.2, cases where $F(\tau)$ is strictly less than zero or consistent with 0 within 1σ , unreliable lifetimes are colored green. Again, it must be reiterated that while these lifetimes do not have previously measured literature values, our $(n,n'\gamma)$ lifetimes should not be trusted as a good measurement. Other techniques must be implemented to fully measure the lifetime of these states (Coulomb Excitation, RDDM plunger method, etc). Excitations are placed into bands where available, along with the well-measured and studied isovector M1 scissors mode lifetimes at ~ 2.4 MeV that results in $J^\pi = 1^\pm$ excitations [43, 51, 75]. In total, we observed 108 discrete γ -rays to measure sixty eight (68) lifetimes, fifty seven (57)

of which were measured for the first time. Of the newly measured lifetimes, however, only forty seven (47) are considered reliable from our measurement of Doppler energy shifted γ rays. These measured lifetimes were extracted from the three angular distribution measurements ($E_n=1.6, 2.2, \& 3.1$ MeV), with three effective ranges of lifetime sensitivity, in the hopes of limiting any lifetime feeding from higher levels and bombarding neutron energy. Visually, the ranges of lifetimes reported can be seen in Figure 4.6, where we have a comparison of the presented lifetimes (and corresponding errors) in to literature lifetimes in the three separate ranges of lifetime sensitivity (excitation energies of <1.6 MeV in red, $1.6 - 2.2$ MeV in green, and 2.2 MeV - 3.1 MeV in blue).

The discrepancies from the literature lifetimes are clearly visible in Figure 4.6, where we can attribute slight inflation of the lifetimes as a result of either feeding from higher-lying states, or from the bombarding neutron energy effects mentioned at the beginning of §4. We can make the justification that our lifetimes agree reasonably with literature because the accuracy of measurement is roughly on the same order of magnitude for every sensitive range of lifetimes measured, with scattered cases of good agreement. In other words, the lifetimes measured at intermediate energies (~ 900 keV, ~ 1850 keV, and ~ 2400 keV) are inflated by the same proportional amount for each bombarding neutron energy. Further discrepancies in our measured lifetimes to those in literature stem from the differences in measurement techniques (DSAM-INS versus deduction of lifetimes via direct $B(E1/M1)\uparrow$). For example, the weighted average of the $F(\tau)$ values for multi-channel decays out of a state can result in a lower average $F(\tau)$ if only one γ -ray decay is used in the determination of the lifetime, resulting in a longer lifetime.

An example of the $E_n=2.2$ MeV angular distribution singles-spectrum for $^{162}\text{Dy}(n,n'\gamma)$ can be seen in Figure 4.7 with select peaks labeled for reference.

E_{lev} (keV)	$\tau_{(n,n'\gamma)}$ (fs)	τ_{lit} (fs)
265	$>1500[\ddagger]$	0.190E6 (7) $[\oplus]$
548	$>960[\ddagger]$	26.5E3 (14) $[\oplus]$
888	>3700	2840 (3) $[\oplus]$
1148	2100^{+7200}_{-1200}	0.30E6 (6) $[\ominus]$
1275	120^{+10}_{-10}	28.8 (6) $[\ddagger][\oplus]$
1485	400^{+210}_{-140}	2.76E6 (16) $[\ddagger][\otimes]$
2394	14^{+13}_{-11}	16^{+10}_{-10} $[\Omega]$
2520	110^{+30}_{-20}	11^{+9}_{-9} $[\Omega]$
2537	460^{+160}_{-120}	141^{+30}_{-30} $[\Omega]$
2569	90^{+30}_{-20}	56^{+6}_{-6} $[\Omega]$
2815	200^{+130}_{-60}	56^{+19}_{-19} $[\Omega]$

$[\ddagger]$: Measured lifetime not reliable ($F(\tau)$ within 1σ of 0) - resulting lifetimes fall well outside the range of DSAM. $[\ddagger]$: Lifetime called into question in this work. $[\ominus]$: from ^{162}Tb β^- decay [66]. $[\otimes]$: from ^{162}Ho ε -decay [39]. $[\oplus]$: from B(E2) \uparrow via Coul. Ex [35]. $[\Omega]$: from (γ, γ') [51] and $(n, n'\gamma)$ [43]

TABLE 4.6

Comparison of lifetimes measured in the campaign of $(n, n'\gamma)$ experiments
with literature lifetimes

4.2.1 Lifetimes of 0^+ States

In stark contrast to the results of the ^{160}Gd experiments (namely the lower limit lifetimes and existence of anisotropies in angular distributions), we are able to determine definite level lifetimes for the majority of 0^+ bands and confirm isotropic angular distributions from the ^{162}Dy data. DSAM plots and angular distributions for the full $0_i^+ \rightarrow 2_{g.s.}^+$ de-excitations are seen in Figures 4.9 and 4.8, respectively. We

also do not exclude any of the proposed 0^+ states from our observation of isotropic or anisotropies in the angular distributions similar to our ^{160}Gd results.

Lifetimes for six (6) of the eleven (11) confirmed and tentative excited 0^+ states [55] were measured in the campaign of experiments (shown in Table 5.2). We have also measured lifetimes (including a few lower limits) of the five lowest-lying rotational members of the $K^\pi=2^+$ band, the bandheads of both $K^\pi=4^+$ bands, and a total of 52 other states in ^{162}Dy . The absolute intensities of decays discussed in this work were extracted from the angular distributions and are shown in Table 5.3, with unobserved transition intensities taken from literature [3, 78, 81] to provide pertinent discussion later in this manuscript.

The full tabulation of γ decays observed for the de-excitation of $K^\pi=0^+$ bands is shown in Table 4.7, which includes experimentally measured lifetimes in femtoseconds, branching ratios, and γ -ray energies in keV. Mixed multipolarity de-excitations are assigned a multipole mixing fraction (δ_{mixing}) from comparison of our gathered angular distributions to a statistical model calculation, performed with CINDY [69]. A level scheme outlining all observed decays from 0^+ bands to the ground state band is also shown in Figure 5.8.

Lifetimes for the three lowest-lying rotational members of the 0_2^+ band were measured; the single, most intense γ ray at 1319 keV was used to measure (a shallow) $F(\tau)$ to extract the lifetime from the $E_n=1.6$ MeV dataset. The weighted average of $F(\tau)$ from both the 1187 & 1372 keV γ ray is used to measure the lifetime of the 2^+ state. Only the 1308 keV de-excitation contributes to the lifetime of the 4^+ state at $E_x=1574$ keV, as the 1025 keV transition exhibits a negative $F(\tau)$ value.

We have measured the lifetime of the bandhead and 2^+ member of the 0_3^+ band at $E_x=1666$ keV, with good lifetime resolution extracted from the $E_n=2.2$ MeV dataset. The single 1585 keV transition from the bandhead to the ground state yields a 3000^{+4800}_{-1300} fs lifetime, while only the 1647 and 1728 keV γ rays offer contri-

butions to the 2^+ lifetime of 1800^{+880}_{-430} fs, as the decay at 1462 keV is coincident with a background line, making that particular $F(\tau)$ unreliable.

We adopt the placement [8] of the (2^+) state at 2189 keV as the 2^+ rotational band member of the 0_6^+ band at $E_x=2128$ keV, and have measured lifetimes for these two states from the single-channel decays of 2109 & 2047 keV, respectively. The lifetime of the bandhead was found to be 2300^{+1500}_{-860} fs, and 530^{+220}_{-160} fs for the 2^+ member.

The seventh and ninth 0^+ states decay via full energy de-excitations to the ground state at $E_\gamma=2417$ & 2575 keV, respectively. These corresponding lifetimes extracted from the $E_n=3.1$ MeV dataset are 270^{+110}_{-60} fs for the 0^+ state at 2497 keV, and 210^{+300}_{-100} fs at 2655 keV.

Due to the isotropic radiation observed for the 2721 keV γ -ray that depopulates the (0_{11}^+) state at 2802 keV, we support the assignment of this state as a 0^+ excitation, where further mentions of this state are considered as a confirmed 0^+ state. The Doppler shift from this 2721 keV decay gives us our shortest 0^+ lifetime of 90^{+110}_{-60} fs.

4.2.2 Lifetimes of $K^\pi=2_\gamma^+$ and 4^+ Bands

In the eight decays from the 2^+ band, two of the γ rays (the 697 keV and 634 keV de-excitations) are not used in the calculation of the level lifetime, as they have Doppler shifts that correspond to an $F(\tau)<0$. Lower limits for the lifetime are measured in several cases due to the inherent limitations of sensitive lifetimes DSAM can measure (up to a few picoseconds).

The lifetime of the bandhead 4^+ state at 1535 keV is extracted from the Doppler shift of the 572 keV γ ray, as the 475 keV decay lies on top of a background, and as such, the Doppler shift is unreliable; the 647 keV line exhibits a negative $F(\tau)$ value, and is not used in the lifetime calculation. Evidence for the existence of a background contaminant can be seen in the branching ratios for the decays, as they

are not consistent with literature intensities. In Table 4.8, deduced $B(E2)$ values from our experiments are reported alongside calculations using the literature intensities from [3] in parentheses.

We have measured the lifetime of the second 4^+ state at 2181 keV, via a 1217 keV γ ray to the 3^+ member of the γ band, but we have not observed the 1294 keV decay to the bandhead (this line would also be coincident with an inherent $^{115}\text{In}(n,n'\gamma)$ background). The $\tau=240^{+190}_{-80}$ fs lifetime and mostly M1 radiation observed from the 1217 keV decay

4.2.3 Lifetimes of Negative Parity Bands ($K^\pi=2^-, 0^-$, and 2^-_2)

A total of 10 well-convergent level lifetimes were measured (8 of which are new) for three negative parity bands in ^{162}Dy . All observed transitions from negative parity bands can be seen in Figure 5.12, with corresponding transition strengths from Table 4.9. Absolute intensities of γ -decays reported in this work can be seen in Table 5.6. The traditional picture of octupole collectivity in well-deformed nuclei exists with the initial, lowest-lying and quartet of states of $K^\pi=0^-, 1^-, 2^-$, & 3^- . However, the current ordering of negative parity bands in ^{162}Dy is difficult (read: impossible) to predict with modern models [3]. We have measured lifetimes for two bands of this lowest-lying set of states in ^{162}Dy , where we provide individual discussion on our measurements.

We are immediately presented with some of the limitations of DSAM with our measurement of the lifetime of the bandhead of the $K^\pi=2^-$ band. Firstly, γ -ray energies can be heavily attenuated in the physical size of the near-molar-weight target; while we correct for this γ absorption in the peak area/intensity, lifetimes from the Doppler shift of γ -rays sub-500 keV are difficult to extract, as $F(\tau)$ can be within 1 or 2σ of 0. Normally, DSAM measurements are taken at the lowest possible bombarding

neutron energy, but due to this attenuation of low-energy γ rays, a more precise measurement of the lifetimes in this band are taken from the 2.2 MeV bombarding neutron dataset. While we expect a natural inflation of the lifetimes because of this choice of neutron energy, the vast majority of observed transitions displayed negative (or consistent with zero within 1σ uncertainty) $F(\tau)$ values. This justification is supported by Figure 4.11, which shows all excitation functions for γ rays that both de-excite this band and contribute to the lifetime; take note that the gain in statistics by a factor of ~ 2 by increasing the neutron energy, where we are exempt from higher-lying decays acting as a contaminant (see the trajectories as the neutron energy increases to 3.1 MeV). Extraction of the lifetime for the bandhead at 2100^{+7200}_{-950} fs involves the measurement of a 260 keV γ ray, shown in Figure 4.11, and does not agree with the literature value of 303 ps [66], as the shallow $F(\tau)$ is just over 1σ away from 0, making this lifetime partially unreliable. We do not observe the other decay channel to the 3^+ member of the γ -band, as that decay energy is 185 keV, directly on top of our strongest line in our spectra, the ground state $4^+ \rightarrow 2^+$ transition. With no higher energy decays observed to the ground state, we report this measurement of the bandhead's lifetime, but it should be taken as a tentative, cautious measurement, given the very large discrepancy from literature. However, we regain good lifetime resolution on the measurement of the 3^- and 4^- bandmembers; the former state's lifetime of 3100^{+3700}_{-1200} fs comes from the 944 keV γ ray, where the other exit channels have either a negative $F(\tau)$ value.

We have measured lifetimes for the 3 lowest-lying members of the 0^- band, currently assigned as the single octupole vibration in ^{162}Dy from the clearly collective literature $B(E3; 3^- \rightarrow 0_{gs}^+)$ measurements ranging from 1.4-4.7 W.u. [45, 56]. The deduced lifetime from the direct $B(E1)\uparrow$ measurement in [83] of the bandhead of the $K^\pi=0^-$ band has been called into question by the NDS evaluator, with the distinct comment that the γ -branches of E1 radiation depopulating the state differs drasti-

cally from the adopted values. We are confident in our lifetime measurement from the extremely well-defined Doppler energy-shifts of the two de-excitations from this $E_x=1275$ keV level (shown in Figure 5.11). The 5^- state at 1518 keV is below the threshold to be populated by $E_n=1.6$ MeV neutrons, the de-excitations are not observed until the $E_n=2.2$ MeV dataset; this implies that the resulting lifetime will be inflated, as $F(\tau)$ is directly related to the bombarding neutron energy.

The final set of lifetime measurements of negative parity states is the second $K^\pi=2^-$ band. Two γ -ray placements from [3] are made into the bandhead of this 2^- band, the 900 and 975 keV transitions, both showing a well-behaved Doppler shift to yield a level lifetime of 420^{+120}_{-80} fs. We have also placed two γ -ray transitions from the $E_x=1974$ keV 4^- state [8], a 912 keV and a 1010 keV decay to the γ -vibrational band. Confirmation of the placement of these de-excitations is made with the measurement of the excitation functions, shown in Figure 4.12; these γ -rays were also observed in [3], but were unplaced in their level scheme. Our absolute intensities are in reasonable agreement with the literature values in [3, 8], further justifying their correct placement in the level scheme.

4.2.4 Lifetimes of Other Negative Parity Bands ($K^\pi=5^-$, 3^- , 1^- and 3_2^-)

Our discrepancy in lifetime measurement with respect to the literature value for the $K^\pi=5^-$ bandhead is striking, much like the case for the $E_x=1148$ keV level, yet we repeat the same assertions made in the previous section. The two de-exciting γ -rays exhibit a rather unambiguous placement in the level scheme from our measurement of the excitation function (both $E_\gamma=937$ & 1220 keV γ rays match qualitative shape and have the same threshold, consistent with a 5^- state at 1485 keV), and show well-defined Doppler energy-shifts that correspond to a lifetime of 450 fs, compared to the literature value of 1.92 ns [39]. We contest this lifetime measurement via delayed-coincidence from the β -decay of ^{162m}Ho , from our unambiguous placement

of de-exciting γ rays in the level scheme, accurate branching ratios in comparison to literature intensities, and well-behaved DSAM shifts. In scrutinization of the literature, it is found that the 1.92 ns lifetime measurement by [39] is explicitly placed for the nearby 1490 keV state, and very little discussion is made on the delayed-coincidence measurements made in [22]. It is not entirely unreasonable that the measured lifetime in [22, 39] are instead seeing this nearby state at 1490 keV. This 7^+ state de-excites via a very similar energy (940 keV versus 937 keV) γ ray, and is populated via first-forbidden Fermi-type β -decay, in contrast to the preferred Gamov-Teller decay to the 5^- at 1485 keV.

Absolute intensities from γ rays depopulating the $K^\pi=3^-$ band at 1570 keV show an obvious preference to the previously established 0^- octupole band [3] in the literature, where we do not observe the full $3^- \rightarrow g.s.$ transitions due to the low branching ratios listed. Shallow shifts in the DSAM fitting only gives a lower limit to the lifetime of the 3^- bandhead of >3050 fs, where, in contrast, we get good lifetime resolution on the 4^- member. That being said, we yet again encounter some of the limitations behind the Doppler Shift Attenuation Method, in that lower energy γ rays (<500 keV) are easily attenuated by the sample size and may not exhibit reliable energy shifts. Further investigation of this level lifetime with another measurement technique (Coulomb excitation, ‘plunger’ method with RDDM, etc) is desired to more confidently understand the transition probabilities here, as the lifetimes measured in our campaign of experiments seem to be fairly unreliable.

The $K^\pi=1^-$ band at 1637 keV provides some of the least consistent and reliable results from our experimental campaign to measure lifetimes in ^{162}Dy . Starting with the bandhead, the only γ ray to attribute to the lifetime measurement is the de-excitation of $E_\gamma=1637$ keV. The questionability of this γ -ray placement is an issue, in that (n,γ) reactions by [3] do not observe it, yet other $(n,n'\gamma)$ experiments do. Nevertheless, the other two observed decays cannot be used because the 427 keV

line is coincident with a background line, and as such, the extracted $F(\tau)$ is not reliable; the 489 keV γ provides an alternate discussion on its exclusion from the level lifetime. First, the relative intensity of the radiation does not fall in line with the other de-excitations according to the literature, and second, the extracted $F(\tau)$ from the 427 keV line varies wildly (by more than 2σ) from the 1637 keV line, and lastly, the excitation function(s) (Figure 4.14) for de-excitations out of the bandhead show an inconclusively similar pattern, qualitatively. These reasons are indicative of a bad placement of this decay in the level scheme, and is indicated by parentheses in Table 4.10. Further proof of the 489 keV γ ray being a contaminant can be seen in the nonconvergence of a multipole mixing fraction (ranging from 33-91% E2, with a large χ^2 value on the angular distribution).

The 2^- member of the band also yields some less than stellar resolution on the nuclear lifetime. With two decays observed at intermediate energies (but still below 1 MeV), we are only able to rely on the 728 keV γ ray to measure the lifetime, as the 416 keV decay lies on top of a background. The resulting lifetime limit of >1000 fs extracted from the Doppler Shift is not reliable, with $F(\tau)$ being consistent with zero within 1σ uncertainty. Since the 416 keV γ ray is coincident with a background, a reliable multipole mixing fraction cannot be extracted from the angular distributions, as we do not know the distribution of the background as a function of angle.

The 3^- member offers a slight tangent from the echoed rhetoric of lifetime measurements in the 1^- band, but still does not provide well-defined DSAM lifetimes. The extracted average level $F(\tau)$ value is just over 1σ deviant from 0, giving both a) a borderline unreliable lifetime extraction, and b) an extremely low magnitude lower limit of >740 fs. In this sea of delinquent behavior, the branching ratios for the 3^- state of the 1^- band agree well with literature [3], but the multipole mixing fraction for the 529 keV γ is deviant from literature ($\sim 50\%$ mixed, vs $>99\%$ M1 in literature).

$F(\tau)$ values for the bandhead of the second $K^\pi=3^-$ band at 1766 keV fail to display

any definite shift in energy, in fact, having a negative (completely unphysical) value with a very large error. The unreliable lifetime reported in this work is simply the lower limit where $F(\tau)$ is the most positive, at a value of 0.044, but this extracted lifetime of 3400 fs should not be taken with any amount of confidence. The same can be said about the 4^- member at 1826 keV: the extracted $F(\tau)$ is *very* consistent with zero, as the only available transition to γ -band at 863 keV transition energy gives an appreciably nonzero shift (though not by much). Again, the lower limit of the lifetime is taken at the very edge of what $F(\tau)$ can be (at a value of 2400 fs). The statistical model employed (CINDY [69]) to calculate multipole mixing fractions was able to converge on a value for the mixing ratio from the 556 keV γ ray's angular distribution, however.

4.2.5 Lifetimes of $K^\pi=1^+$ Band and Members of M1 Scissors

Our measurement of lifetimes in the 1^+ band can be seen in Table 4.11, where we have two good $F(\tau)$ shifts, and two unreliable measurements of the lifetime of states. The bandhead is the first of the unreliable lifetimes measured. Here, the only γ decay that contributes to the calculation of a level lifetime is the 857 keV γ ray, but the energy shift is consistent with zero within 1σ uncertainty. While this is not a low-energy decay that would be more susceptible to attenuation in the sample, it *may* be a contaminant, as the angular distribution does not yield a reliable mixing ratio for the decay.

The 2^+ member of this band echoes a similar story; one de-excitation is not used in the determination of the nuclear lifetime, as the $F(\tau)$ measured is negative. However, unlike the bandhead, this γ -ray angular distribution that is excluded (1701 keV) converges on a good, reliable value for E2/M1 mixing, at just under 50% mixing. That being said, the extracted lifetime is still not reliable, since $F(\tau)$ for this level is

negative.

The decays to both the ground state 4^+ and the γ -band 4^+ are used to extract the lifetime of 1400^{+4500}_{-1000} fs for this 3^+ state at 1840 keV. To round out the $K^\pi=1^+$ band, the 4^+ state at 1951 keV offers good lifetime resolution, similar to the 3^+ state.

4.2.6 Lifetimes of States with No K^π Assignment

We direct the reader to the fact that lifetimes above the pairing gap in ^{162}Dy exhibit very well-behaved and precise lifetime measurements; this is an artifact of the DSAM measurements at UKAL, where, generally, the higher energy γ rays that completely de-excite the nucleus fare better in escaping the sample size and displaying a noticeable energy shift than those at lower energy thresholds. Tables 4.12 and 4.13 list these ‘miscellaneous’ lifetimes for which there is no rotational band assignment for the state. In many of these states, we place liberal limits on the spin/parity, based solely on our measurement of the angular distributions. Because of the tentative spin assignments, multipole mixing fractions extracted from the angular distributions are often unavailable, as the statistical model employed requires known spins and parities to be known.

4.2.7 All Decays Observed (Intensities)

As a capstone for the experimental campaign to measure lifetimes in ^{162}Dy , Table 4.14 lists every γ -ray observed in our experiments with all possible origins (prompt Dy decay, background, or unknown), its intensity from the 3.1 MeV neutron energy dataset, its placement in the level scheme if applicable, and any notes for the reader as justification for any assignments.

E_γ (keV)	Thresh. (MeV)	I_γ abs.	Origin	E_{level} (keV)	Notes
185.002 (3)	<1.4	11831.273 (291.130)	^{162}Dy	265	F(τ) 'calibrant' ($\tau=190$ ps)
212.856 (9)	1.62	257.926 (8.709)	^{162}Dy	1570	
236.061 (11)	<1.6	48.538 (5.613)	^{162}Dy	1297	
247.173 (14)	<1.6	265.174 (5.347)	^{162}Dy	1210	
250.903 (13)	[†]	205.447 (4.354)	bkg	???	
253.098 (18)	[†]	124.111 (3.481)	bkg	$^{74}\text{Ge}(\text{n},\gamma)$	
258.157 (11)	[†]	92.943 (8.501)	bkg	$^{72}\text{Ge}(\text{n},\gamma)$	
260.136 (3)	<1.4	280.854 (7.729)	^{162}Dy	1148	[★] [A^2] Isotropic probable background
262.929 (19)	<1.4	3027.698 (52.841)	[‡]		
278.131 (26)	~ 2.0	106.087 (2.859)	[‡]		
282.937 (5)	<1.4	2679.570 (45.708)	^{162}Dy	548	
295.233 (6)	1.62	482.315 (0.539)	^{162}Dy	1571	Doublet with $^{70}\text{Ge}(\text{n},\gamma)$ and $^{72}\text{Ge}(\text{n},\gamma)$
311.252 (7)	1.70	297.539 (5.342)	^{162}Dy	1669	
322.012 (7)	<1.4	321.899 (6.243)	^{162}Dy	1210	
326.260 (18)	[†]	268.417 (4.960)	bkg		
328.363 (129)	[†]	73.814 (3.512)	bkg	$^{72}\text{Ge}(\text{n},\gamma)$	[A^2]
334.120 (4)	<1.4	1470.283 (33.471)	^{162}Dy	1297	
347.482 (11)	<1.4	273.997 (5.784)	[‡]		
351.276 (11)	[†]	90.213 (2.284)	bkg	???	
354.259 (15)	[†]	65.674 (2.019)	bkg	???	Unidentified UKY bkg
411.787 (38)	~ 1.6	46.863 (3.657)	[‡]		
416.221 (17)	[†]	89.239 (3.162)	bkg	$^{115}\text{In}(\text{n},\gamma)$	
422.011 (19)	[†]	89.692 (3.627)	[‡]		
427.504 (14)	1.7	138.412 (3.312)	^{162}Dy	1637	coinc. with a background, F(τ) not reliable
441.529 (41)	1.775	40.169 (2.790)	^{162}Dy	1738	low statistics

E_γ (keV)	Thresh. (MeV)	I_γ abs.	Origin	E_{level} (keV)	Notes
475.215 (18)	~1.62	186.404 (12.199)	^{162}Dy	1535	a little low threshold for 4^+ population
489.120 (24)	1.7	51.876 (3.312)	$[\#]$???	$[A^2]$
493.991 (38)	$[\dagger]$	55.272 (3.010)	bkg		$^{73}\text{Ge}(\text{n},\gamma)$ & $^{74}\text{Ge}(\text{n},\text{n}'\gamma)$
529.034 (13)	1.85	227.886 (5.240)	^{162}Dy	1738	
543.660 (10)	1.85	318.589 (7.364)	$[\#]$???	ExF does not support 1691 placement
556.023 (23)	1.85	136.124 (4.082)	^{162}Dy	1766	
572.944 (9)	~1.62	624.137 (13.351)	^{162}Dy	1535	
584.247 (28)	2.2	163.025 (5.805)	^{162}Dy	2102	
590.633 (36)	1.85	79.883 (3.454)	^{162}Dy	1739	
622.528 (23)	$[\dagger]$	95.089 (4.721)	^{162}Dy		low intensity, should be part of 888
630.455 (54)	1.85	45.621 (3.320)	^{162}Dy	1840?	
634.131 (11)	<1.4	394.139 (11.353)	^{162}Dy	1182	
643.548 (46)	1.925	66.334 (2.786)	^{162}Dy	1826	
647.537 (8)	1.7	993.135 (16.799)	^{162}Dy	1535	
669.640 (22)	1.775	115.485 (22.367)	bkg	$^{63}\text{Cu}(\text{n},\gamma)$	
671.516 (44)	1.775	214.988 (4.646)	$^{162}\text{Dy}?$	1634?	too low threshold for a 5^+ population
678.113 (18)	1.85	125.946 (3.396)	^{162}Dy	1739	
697.283 (7)	<1.4	1277.950 (31.781)	^{162}Dy	963	
728.490 (17)	1.775	170.713 (4.611)	^{162}Dy	1691	
748.235 (20)	1.925	126.131 (4.586)	^{162}Dy	1895	
768.763 (58)	~2.3	112.711 (5.692)	$[\#]$		$[A^2]$
770.711 (51)	2.2	75.373 (10.643)	^{162}Dy	2129	$[A^2]$ ($^{65}\text{Cu}(\text{n},\text{n}'\gamma)$)
776.014 (19)	1.925	299.865 (6.510)	^{162}Dy	1324?	could be a doublet
779.515 (27)	1.925	76.857 (2.643)	^{162}Dy	1840	$F(\tau)$ likely not reliable (doublet)
795.370 (6)	<1.4	2534.118 (51.240)	^{162}Dy	1060	

E_γ (keV)	Thresh. (MeV)	I_γ abs.	Origin	E_{level} (keV)	Notes
803.596 (27)	1.85	191.698 (4.408)	^{162}Dy	1766	$^{73}\text{Ge}/^{27}\text{Al}(\text{n},\text{n}'\gamma)$ F(τ)=0.137 \pm 0.179
807.544 (6)	<1.4	5603.611 (108.346)	^{162}Dy	888	
819.633 (18)	1.85	117.917 (4.035)	^{162}Dy	1782	
842.393 (20)	\sim 1.62	353.148 (9.502)	[$\#$]		
846.561 (43)	[\dagger]	70.108 (6.611)	bkg	^{56}Fe	
849.768 (42)	2.0	111.364 (4.651)	[$\#$]		
857.590 (12)	1.775	210.646 (4.502)	^{162}Dy	1745	
863.833 (21)	1.925	184.136 (4.102)	^{162}Dy	1826	
878.039 (24)	1.85	305.545 (9.103)	^{162}Dy	1766	
882.316 (6)	<1.4	6774.521 (135.466)	^{162}Dy	963	
888.195 (6)	<1.4	5140.372 (102.292)	^{162}Dy	888	Doublet with Pb background $^{207}\text{Pb}(\text{n},\text{n}'\gamma)$
894.849 (37)	2.0	234.163 (7.245)	[$\#$]		
896.295 (74)	[\dagger]	120.660 (14.171)	bkg		
901.014 (26)	1.925	150.159 (8.600)	^{162}Dy	1863	
912.030 (27)	2.1	82.148 (3.125)	^{162}Dy	1974	
917.116 (8)	<1.4	1809.219 (33.885)	^{162}Dy	1183	
932.237 (35)	1.925	68.438 (4.803)	[\otimes]		
937.110 (23)	1.775	240.267 (7.937)	^{162}Dy	1485	
944.438 (8)	<1.4	1160.957 (24.752)	^{162}Dy	1210	
947.415 (28)	2.0	173.498 (4.547)	^{162}Dy	1910	
953.210 (103)	2.6	86.864 (3.249)	^{162}Dy	2524	[A^2]-placed
955.939 (32)	2.3	175.548 (4.160)	^{162}Dy	2230	[A^2]-placed
962.080 (16)	[\dagger]	189.023 (48.170)	bkg	$^{63}\text{Cu}(\text{n},\text{n}'\gamma)$	
969.756 (20)	1.775	227.299 (4.847)	^{162}Dy	1518	
975.597 (12)	1.925	490.458 (7.426)	^{162}Dy	1863	

E_γ (keV)	Thresh. (MeV)	L_γ abs.	Origin	E_{level} (keV)	Notes
980.359 (8)	<1.4	1554.147 (25.227)	^{162}Dy	1060	
1007.010 (34)	2.2	126.177 (7.111)	$[\otimes]$		$[\star] [A^2] F(\tau)=0.221\pm0.074$
1010.050 (21)	2.1	251.922 (15.219)	^{162}Dy	1974	$[A^2]$ -placed
1014.672 (19)	2.0	174.587 (9.489)	bkg	$^{27}\text{Al}(\text{n},\text{n}'\gamma)$	
1017.626 (35)	2.2	149.667 (3.812)	$[\otimes]$		$[\star] F(\tau)=0.205\pm0.063$
1022.172 (19)	1.925	216.003 (6.133)	^{162}Dy	1910	
1025.861 (32)	~ 1.7	98.003 (5.045)	^{162}Dy	1574	
1092.277 (9)	1.4	1066.432 (20.498)	^{162}Dy	1357	
1096.904 (14)	$[\dagger]$	172.976 (4.071)	bkg	$^{115}\text{In}(\text{n},\gamma)$	
1114.721 (57)	2.4	109.426 (32.990)	$[\otimes]$		$[\star] [A^2] (F(\tau) \text{ also looks like a background})$
1124.974 (12)	1.7	925.209 (24.488)	^{162}Dy	1390	
1129.427 (8)	<1.4	1970.898 (45.151)	^{162}Dy	1210	
1133.244 (42)	2.4	181.084 (5.630)	$[\#]$		$[\star] [A^2] F(\tau)=0.133\pm0.077$
1141.793 (36)	2.4	263.234 (6.981)	^{162}Dy	2324	$[A^2]$ -placed
1160.958 (102)	2.7	55.458 (3.187)	$[\#]$		$[\star]$
1164.954 (23)	$[\dagger]$	87.576 (3.279)	bkg		Unidentified UKY bkg
1169.142 (83)	2.8	80.855 (3.944)	$[\#]$		$[\star] [A^2]$
1187.759 (10)	1.5	477.002 (10.302)	^{162}Dy	1453	
1195.113 (8)	<1.4	1817.697 (38.720)	^{162}Dy	1276	
1204.352 (50)	$[\dagger]$	81.093 (3.574)	bkg		$^{73}\text{Ge}(\text{n},\gamma) \text{ \& } ^{74}\text{Ge}(\text{n},\text{n}'\gamma)$
1207.069 (45)	2.2	205.221 (6.721)	$[\#]$	1754?	$[A^2] F(\tau)>0$, assigned (7^-), could only be 5
1217.733 (32)	2.2	300.230 (5.134)	^{162}Dy	2181	$[A^2]$ -placed
1219.971 (20)	1.775	687.409 (10.737)	^{162}Dy	1485	
1222.787 (49)	2.3	182.663 (4.252)	^{162}Dy	2283	$[A^2]$ -placed
1231.897 (75)		71.342 (4.794)			$[A^2]$

E_γ (keV)	Thresh. (MeV)	L_γ abs.	Origin	E_{level} (keV)	Notes
1252.721 (15)	1.775	407.559 (11.873)	^{162}Dy	1518	
1275.847 (16)	<1.4	1268.297 (29.632)	^{162}Dy	1275	
1277.317 (19)	<1.4	1601.847 (35.621)	^{162}Dy	1357	
1293.539 (14)	<1.4	319.833 (9.558)	bkg	$^{115}\text{In}(\text{n},\text{n}'\gamma)$	
1298.577 (29)	[†]	374.596 (69.27)	bkg	$^{70}\text{Ge}(\text{n},\gamma)$	
1308.563 (14)	1.7	534.359 (11.016)	^{162}Dy	1574	
1311.851 (42)	2.5	216.796 (6.529)	^{162}Dy	2494	$[A^2]$ -placed
1317.544 (92)	2.4	114.659 (4.166)	$[\otimes]$		$[\star] [A^2]$
1319.617 (12)	1.4	390.315 (5.095)	^{162}Dy	1400	
1342.508 (27)	2.3	239.620 (6.282)	^{162}Dy	2230	
1350.928 (36)	2.3	164.208 (5.629)	$[\#]$		$[\star]$
1355.959 (42)	2.3	106.563 (4.235)	$[\otimes]$		$[\star]$
1363.757 (60)	2.4		$[\otimes]$		$[\star]$
1372.781 (12)	1.48	617.669 (7.637)	^{162}Dy	1453	
1390.598 (298)	2.4	107.377 (11.778)	$[\otimes]$		$[\star]$
1404.315 (39)	2.5	167.399 (7.776)	$[\otimes]$		$[A^2]$
1408.437 (75)		82.543 (2.747)			potentially $^{54}\text{Fe}(\text{n},\text{n}'\gamma)$
1412.530 (91)	2.5	109.346 (26.646)	$[\otimes]$		$[\star] [A^2] (F(\tau)<0)$
1415.814 (131)	2.5	45.376 (2.745)	$[\#]$		$[\star]$
1421.871 (44)	2.4	124.074 (3.683)	$[\otimes]$		$[\star]$
1427.853 (56)	2.4	90.089 (3.362)	$[\otimes]$		$[\star] [A^2]$
1438.444 (33)	2.4	201.808 (4.037)	$[\otimes]$		$[\star] [A^2]$
1462.818 (17)	1.775	175.495 (4.773)	^{162}Dy	1728	
1473.398 (26)	1.85	122.538 (4.393)	^{162}Dy	1738	
1556.569 (14)	1.7	357.876 (8.297)	^{162}Dy	1637	

E_γ (keV)	Thresh. (MeV)	I_γ abs.	Origin	E_{level} (keV)	Notes
1574.796 (27)	1.925	109.935 (3.331)	^{162}Dy	1840	
1585.360 (16)	1.7	263.215 (5.591)	^{162}Dy	1666	
1610.972 (26)		266.080 (15.360)			
1637.372 (25)	1.7	140.831 (3.488)	^{162}Dy	1637	
1647.687 (16)	1.775	361.040 (8.131)	^{162}Dy	1728	
1665.078 (18)	1.775	223.042 (5.032)	^{162}Dy	1745	
1685.695 (33)	2.0	129.259 (3.760)	^{162}Dy	1951	
1701.886 (26)	1.85	52.493 (2.679)	^{162}Dy	1782	
1725.354 (39)	[†]	136.405 (4.725)	bkg	$^{208}\text{Pb}(\text{n}, \text{n}'\gamma)$	
1728.321 (29)	1.85	129.035 (4.985)	^{162}Dy	1728	
1757.250 (102)	2.0	132.588 (4.867)	[⊗]		[★] [A^2]
1759.795 (63)	1.925	105.035 (2.993)	^{162}Dy	1840	
1773.654 (30)	2.2	246.807 (5.247)	[⊗]		[★] [A^2]
1778.848 (14)	[†]	503.480 (8.628)	bkg	$^{27}\text{Al}(\text{n}, \gamma)$	
1782.541 (29)	1.85	214.099 (4.790)	^{162}Dy	1782	[A^2]-placed
1787.095 (31)	2.0	177.804 (6.700)	[⊗]		[★] [A^2]
1805.890 (20)	1.925	476.203 (9.733)	^{162}Dy	1886	
1814.670 (20)	2.0	511.834 (11.294)	^{162}Dy	1895	
1902.017 (23)	2.0	366.455 (9.911)	^{162}Dy	1982	
1918.538 (23)	2.1	401.636 (7.254)	^{162}Dy	1999	
1939.217 (81)	2.3	78.670 (3.337)	[‡]		potentially $^{73}\text{Ge}(\text{n}, \text{n}\gamma)$
1942.544 (19)	[†]	204.334 (7.313)	bkg		
1950.812 (26)	~2.3	194.064 (4.664)	[‡]		doublet with background (unidentified)
1982.342 (24)	2.0	429.197 (12.363)	^{162}Dy	1982	
1999.951 (28)	2.2	516.006 (12.427)	[⊗]		[★]

E_γ (keV)	Thresh. (MeV)	I_γ abs.	Origin	E_{level} (keV)	Notes
2047.329 (30)	2.2	286.080 (6.065)	^{162}Dy	2125	
2067.759 (30)	2.2	294.084 (6.351)	[$\#$]		[\star]
2109.243 (95)	2.4	140.677 (3.860)	^{162}Dy	2189	
2111.981 (57)	<2.3	132.805 (4.279)	[$\#$]		close to $^{115}\text{In}(n,\gamma)$
2124.122 (41)	2.3	159.010 (5.192)	[\otimes]		
2128.643 (92)	2.2		[\otimes]		[\star] very low statistics
2223.245 (21)	[\dagger]	705.920 (22.408)	bkg	$^1\text{H}(n,d)$	used as a long-lived $F(\tau)$ 'calibrant'
2232.738 (95)	2.5	119.372 (3.553)	^{162}Dy	2314	
2239.929 (108)	2.6	141.186 (3.724)	^{162}Dy	2506	
2290.397 (104)	2.5	150.971 (4.446)	^{162}Dy	2371	
2305.762 (96)	2.5	171.415 (6.605)	^{162}Dy	2386	
2310.392 (89)	2.5	294.379 (9.312)	[$\#$]		
2315.363 (103)	2.4	91.237 (4.904)	[$\#$]	???	ExF does not match 2395
2323.726 (156)		66.339 (3.358)			
2331.301 (184)	2.7	121.744 (3.916)	^{162}Dy	2413	
2339.223 (134)	2.7	131.612 (5.132)	^{162}Dy	2338	
2346.871 (99)	2.5		^{162}Dy	2427	
2350.287 (175)		225.186 (13.310)			
2360.440 (113)	2.5	105.996 (6.241)	[$\#$]		[\star]
2382.239 (120)	2.6		[$\#$]		[\star]
2390.254 (58)	[\dagger]	74.443 (4.035)	bkg		
2395.010 (112)	2.4	114.428 (4.232)	^{162}Dy	2394	
2399.305 (134)	[\dagger]	122.468 (6.482)	bkg		
2407.410 (127)	2.6	124.465 (5.250)	^{162}Dy	2488	
2417.161 (118)	2.6	116.520 (4.933)	^{162}Dy	2497	

E_γ (keV)	Thresh. (MeV)	I_γ abs.	Origin	E_{level} (keV)	Notes
2424.728 (166)	2.5	160.604 (4.627)	$[\otimes]$		
2428.689 (107)	2.6	188.999 (6.585)	^{162}Dy	2510	
2438.349 (99)	2.6	184.794 (18.924)	^{162}Dy	2520	
2455.969 (295)	2.7	98.061 (3.800)	^{162}Dy	2537	
2470.100 (421)		140.857 (6.639)			
2473.841 (112)	2.6	147.281 (11.689)	^{162}Dy	2554	
2479.469 (118)		117.953 (5.147)			
2489.552 (128)	2.6	187.124 (6.513)	$[\#]$???	ExF does not match 2569
2492.495 (279)	2.7	96.375 (8.575)	$[\otimes]$		$[\star]$
2505.770 (143)	2.6	125.320 (7.327)	^{162}Dy	2506	
2511.291 (161)		106.273 (4.584)			
2516.713 (1392)		48.648 (5.320)			
2519.586 (115)	2.6	142.992 (4.806)	^{162}Dy	2520	
2527.923 (128)	$[\dagger]$		bkg		UKY background
2532.614 (159)	2.7	117.331 (4.261)	^{162}Dy	2614	
2536.782 (147)	2.6	136.463 (4.552)	^{162}Dy	2537	
2552.567 (137)	2.9	123.938 (4.342)	^{162}Dy	2818	
2554.600 (150)	2.7	106.138 (4.030)	^{162}Dy	2614	
2563.244 (341)		89.539 (4.989)			
2568.615 (141)	2.6	103.737 (4.847)	^{162}Dy	2569	
2576.711 (207)		59.373 (5.424)			
2586.345 (164)		147.886 (6.975)			
2590.526 (247)	2.6	87.177 (6.186)	^{162}Dy	2656	
2630.032 (230)	2.8	62.653 (3.161)	^{162}Dy	2630	low statistics

E_γ (keV)	Thresh. (MeV)	I_γ abs.	Origin	E_{level} (keV)	Notes
2655.583 (172)	2.8	106.138 (4.030)	[\otimes]		
2720.684 (176)	2.9	50.490 (15.032)	^{162}Dy	2802	
2734.232 (286)	2.9	56.949 (2.991)	^{162}Dy	2815	
2777.299 (271)	2.9	48.416 (4.752)	[\otimes]		
2783.474 (331)	2.9	54.723 (3.180)	[\otimes]		
2959.198 (204)	2.9				not realistic
3101.594 (306)	3.0				not realistic

TABLE 4.14

All γ rays observed in ^{162}Dy experimental campaign, with approximate energy threshold where first observed, the absolute intensity of the observed decay (taken from the $E_n=3.1$ MeV dataset), the origin and/or placement of the de-excitation in the level scheme (whether it is a prompt ^{162}Dy decay or a background), and any notes for the reader.

[\dagger]: γ -ray excitation function is flat (definitive background)

[\otimes]: γ -ray does not belong to ^{162}Dy (not populated by inelastic neutron scattering or energetically between any level in ^{162}Dy)

[\star]: γ -ray does not fit energetically inbetween levels in ^{162}Dy , or with favored spin for $(n,n'\gamma)$ reactions.

[A^2]: γ -ray observed, but not placed in [3].

[$\#$]: Origin of γ ray unknown (presumed to *not* be ^{162}Dy from energetics considerations)

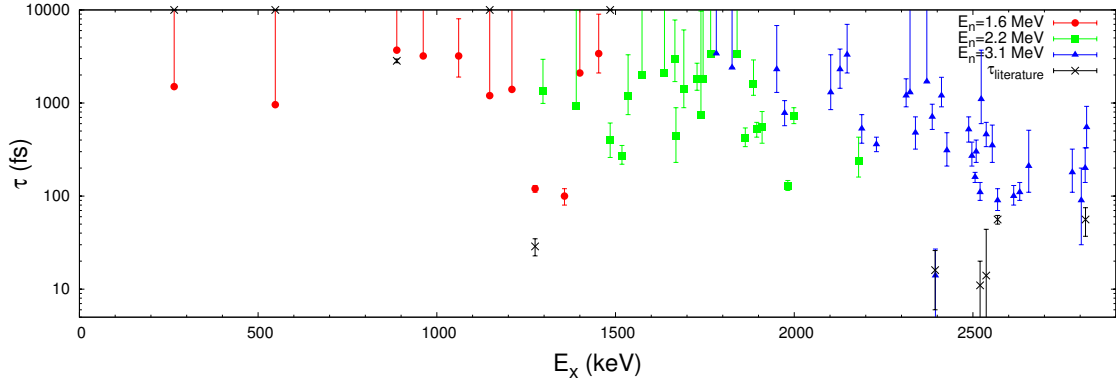


Figure 4.6. All measured lifetimes in ^{162}Dy (in femtoseconds) plotted as a function of excitation energy in keV. Data points in red are extracted from the $E_n=1.6$ MeV angular distributions, points in green correspond to lifetimes extracted from the 2.2 MeV angular distributions, and blue points are lifetimes from the 3.1 MeV dataset. (color online)

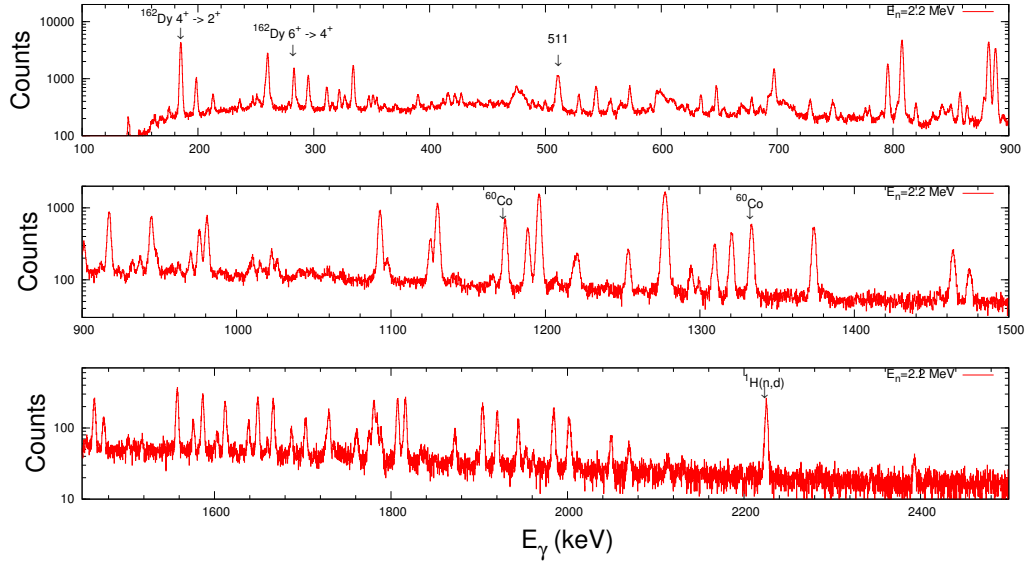


Figure 4.7. Singles spectra from the $\theta_{lab}=90^\circ$ and $E_n=2.2$ MeV angular distributions of ^{162}Dy .

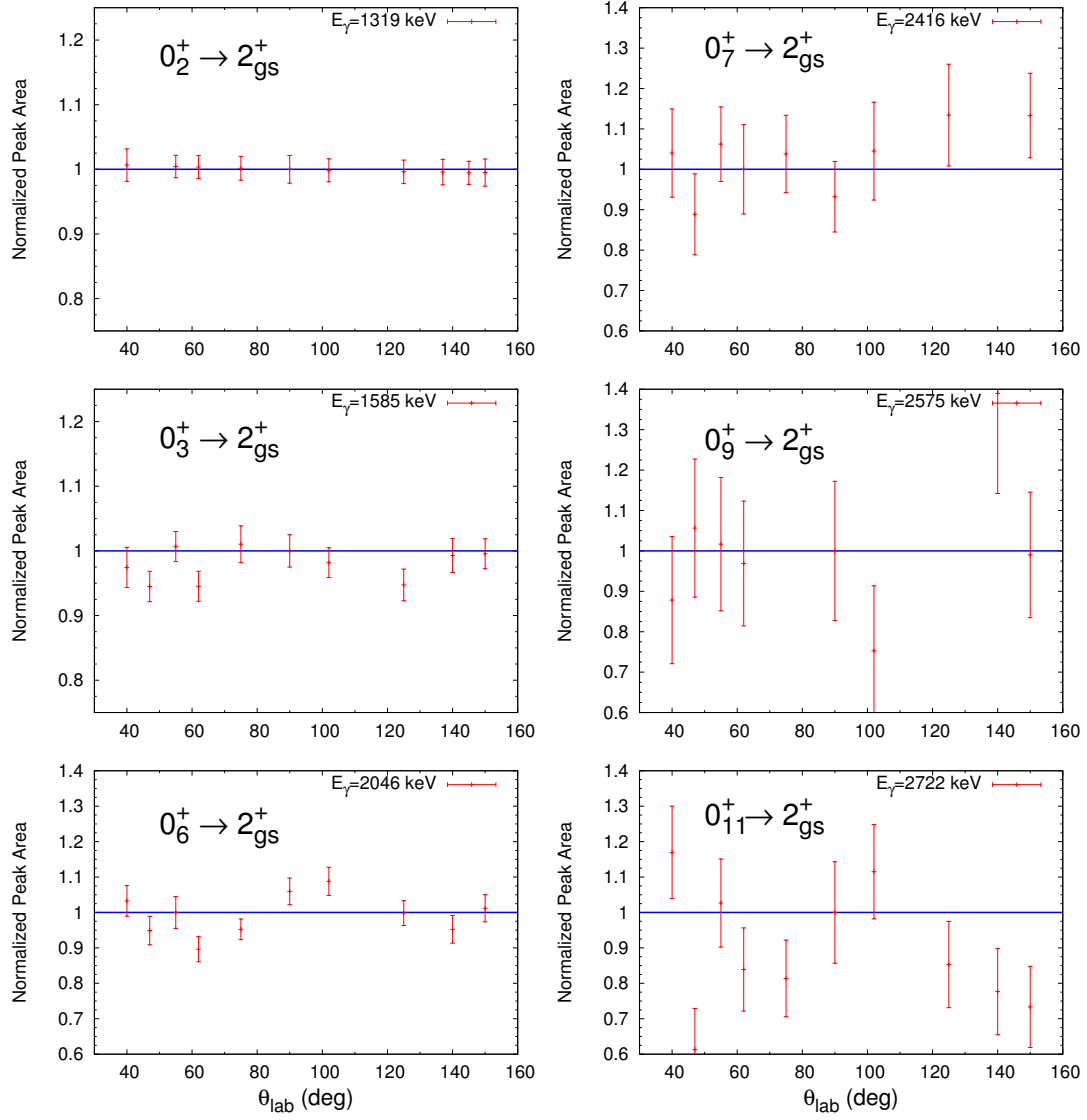


Figure 4.8. Angular distributions of $0_i^+ \rightarrow 2_{g.s.}^+$ γ -rays, highlighting their isotropic nature (color online).

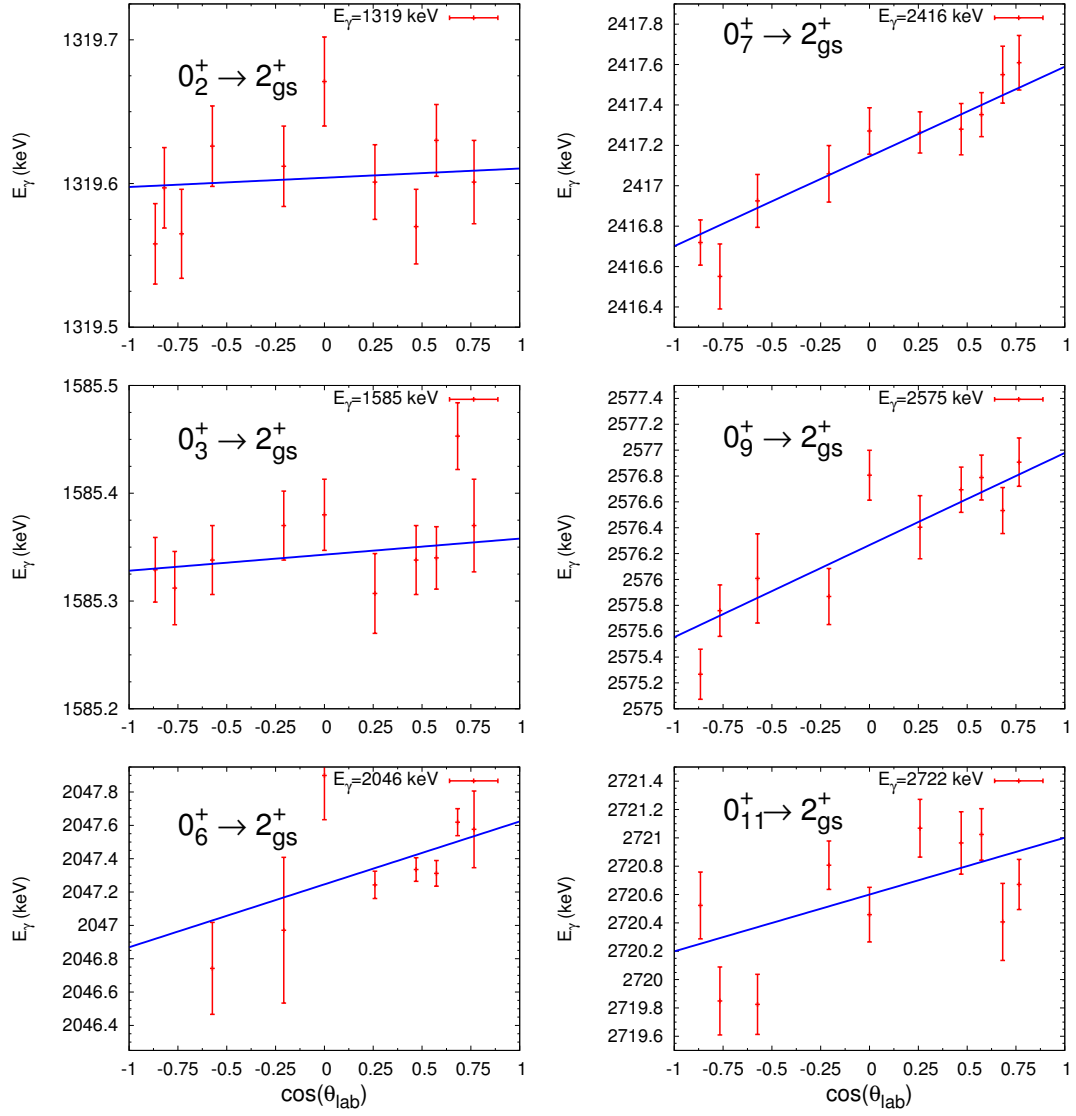


Figure 4.9. Doppler energy shifts of $0_i^+ \rightarrow 2_{g.s.}^+$ γ -rays (color online).

K^π	E_{level} (keV)	E_γ (keV)	$J_{K_i^\pi}^\pi$	$J_{K_f^\pi}^\pi$	$F(\tau)_{av}$	τ (fs)	BR	$\pi\ell$	$B(\pi\ell)$ (W.u.)
$K^\pi=0_2^+$	1400.29(36)	512.0(2)	$0_{0_2}^+$	$2_{2_1}^+$	0.031 ± 0.038	$>2100^{[g]}$	[†]	E2	(<16)
		1319.60(51)	$0_{0_2}^+$	$2_{0_1}^+$			1.000	E2	<1.9
	1453.50(30)	395.49 (10)	$2_{0_2}^+$	$4_{2_1}^+$	0.042 ± 0.026	$3400_{-1300}^{+5600} [g]$	[†]	E2	$(2.7_{-1.7}^{+1.7})$
		565.32 (12)	$2_{0_2}^+$	$2_{2_1}^+$			[†]	E2[‡]	$(0.9_{-0.6}^{+0.6})$
		1187.81(51)	$2_{0_2}^+$	$4_{0_1}^+$			0.425(4)	E2	$0.8_{-0.5}^{+0.5}$
	1574.34(29)	1372.80(51)	$2_{0_2}^+$	$2_{0_1}^+$			0.575(4)	E2/M1 ^[a,c]	$0.3_{-0.2}^{+0.2}$
		513.31 (2)	$4_{0_2}^+$	$4_{2_1}^+$	0.043 ± 0.031	$>2000^{[s]}$	[†]	E2[‡]	(<3.7)
		611.23 (5)	$4_{0_2}^+$	$3_{2_1}^+$			[†]	E2[‡]	(<0.4)
		686.15 (6)	$4_{0_2}^+$	$2_{2_1}^+$			[†]	E2	(<0.5)
		1025.84(58) ^[o]	$4_{0_2}^+$	$6_{0_1}^+$			0.157(5)	E2	<1.1
$K^\pi=0_3^+$	1666.01(33)	1585.35(51)	$0_{0_3}^+$	$2_{0_1}^+$	0.051 ± 0.033	$3000_{-1300}^{+4800} [s]$	1.000	E2	$0.5_{-0.3}^{+0.4}$
	1728.31(20)	1462.70(51) ^[o]	$2_{0_3}^+$	$4_{0_1}^+$	0.081 ± 0.023	$1800_{-430}^{+880} [s]$	0.334(5) ^[*]	E2	$0.4_{-0.1}^{+0.1}$
		1647.64(51)	$2_{0_3}^+$	$2_{0_1}^+$			0.407(5)	E2/M1 ^[c,s]	$0.01_{-0.01}^{+0.01}$
		1728.29(53)	$2_{0_3}^+$	$0_{0_1}^+$			0.259(4)	E2	$0.2_{-0.1}^{+0.1}$
$K^\pi=0_6^+$	2128.02(33)	2047.34(61)	$0_{0_6}^+$	$2_{0_1}^+$	0.071 ± 0.031	$2300_{-860}^{+1500} [\varpi]$	1.000	E2	$0.2_{-0.1}^{+0.1}$
	2189.65(52)	2109.10(50)	$(2)_{0_6}^+$	$2_{0_1}^+$	0.267 ± 0.058	$530_{-160}^{+220} [\varpi]$	1.000	(E2/M1) ^[d,\varpi]	$0.7_{-0.2}^{+0.3}$
$K^\pi=0_7^+$	2497.77(52)	2417.22(50)	$0_{0_7}^+$	$2_{0_1}^+$	0.376 ± 0.055	$270_{-60}^{+110} [\varpi]$	1.000	E2	$0.7_{-0.2}^{+0.2}$
$K^\pi=0_9^+$	2655.83(33)	2575.28(53)	$0_{0_9}^+$	$2_{0_1}^+$	0.436 ± 0.164	$210_{-100}^{+300} [\varpi]$	1.000	E2	$0.7_{-0.4}^{+0.6}$
$K^\pi=0_{11}^+$	2802.04(61)	2721.48(55)	$0_{0_{11}}^+$	$2_{0_1}^+$	0.653 ± 0.200	$90_{-60}^{+110} [\varpi]$	1.000	E2	$1.2_{-0.6}^{+2.3}$

[a]: $\delta=1.3_{-0.2}^{+0.2}$, [b]: $\delta=0.93_{-0.15}^{+0.14}$, [c]: $\delta=-0.22_{-0.08}^{+0.08}$, [d]: $\delta=2.7_{-0.9}^{+1.8}$

[†]: Intensity information taken from [3, 81] (γ -ray not seen in this work), [‡]: Mixing information not available, full E2 strength reported, [o]: γ ray not used in $F(\tau)$ calculation ($F(\tau)<0$).

[g]: $F(\tau)$ or δ_{mixing} extracted from $E_n=1.6$ MeV angular distributions, [s]: $F(\tau)$ or δ_{mixing} extracted from $E_n=2.2$ MeV angular distributions, [ϖ]: $F(\tau)$ or δ_{mixing} extracted from $E_n=3.1$ MeV angular distributions, [o]: γ ray coincident with background, not used in calculation of lifetime.

1 W.u.=5.25E-7 e²b²

TABLE 4.7

Lifetimes of excited 0^+ bands in ^{162}Dy , with calculated $B(E2)$ in W.u., from our measured multipole mixing fractions, branching ratios, γ -ray energies, and lifetimes, all extracted from the angular distributions. $B(E2)$ strengths in parentheses are calculated using literature intensities.

K^π	E_{level} (keV)	E_γ (keV)	$J_{K_i^\pi}^\pi$	$J_{K_f^\pi}^\pi$	$F(\tau)_{av}$	τ (fs)	BR	$\pi\ell$	$B(\pi\ell)$ (W.u.)
$K^\pi=2^+_\gamma$	888.18(22)	807.54(50)	$2^+_{2^+}$	$2^+_{0^+}$	0.022 ± 0.018	>3700 ^[g]	0.524(3)	E2/M1 ^[a,g]	<1.1
		888.18(50)	$2^+_{2^+}$	$0^+_{0^+}$			0.476(3)	E2	<3.6
	962.96(27)	697.30(50) ^[c]	$3^+_{2^+}$	$4^+_{0^+}$	0.021 ± 0.025	>3200 ^[g]	0.159(3)	E2/M1 ^[b,g]	<0.2
		882.31(50)	$3^+_{2^+}$	$2^+_{0^+}$			0.841(3)	E2/M1 ^[c,g]	<7.6
	1061.05(29)	795.35(50)	$4^+_{2^+}$	$4^+_{0^+}$	0.047 ± 0.030	3200^{+4800}_{-1300} ^[g]	0.637(3)	E2/M1 ^[d,g]	$4.5^{+2.7}_{-3.1}$
		980.36(51)	$4^+_{2^+}$	$2^+_{0^+}$			0.363(3)	E2	$2.0^{+1.3}_{-1.2}$
	1182.88(26)	634.24(61)	$5^+_{2^+}$	$6^+_{0^+}$	0.034 ± 0.030	>2500 ^[s]	0.239(5)	E2/M1 ^[e,g]	<14
		917.18(51)	$5^+_{2^+}$	$4^+_{0^+}$			0.761(5)	E2/M1 ^[f,g]	<7.3
$K^\pi=4^+_1$	1535.97(23)	475.27(54) ^[c]	$4^+_{4^+}$	$4^+_{2^+}$	0.124 ± 0.077	1200^{+2100}_{-450} ^[s]	0.186(10) ^[*]	E2/M1 ^[g,s]	44^{+34}_{-40} (23^{+18}_{-21})
		572.96(50)	$4^+_{4^+}$	$3^+_{2^+}$			0.317(6)	E2/M1 ^[h,s]	66^{+42}_{-40} (98^{+63}_{-59})
		647.61(50) ^[c]	$4^+_{4^+}$	$2^+_{2^+}$			0.497(7)	E2	57^{+34}_{-36} (120^{+74}_{-78})
$K^\pi=4^+_2$	2180.69(53)	1217.73(58)	$4^+_{4^+}$	$3^+_{2^+}$	0.383 ± 0.095	240^{+190}_{-80} ^[s]	1.000 (113(24) ^[t])	E2/M1 ^[i,s]	$1.3^{+1.0}_{-0.9}$ ($0.7^{+0.6}_{-0.5}$)
		1292.51(58) ^[t]	$4^+_{4^+}$	$3^+_{2^+}$			(100 ^[t])	E2	$(8.3^{+4.2}_{-3.7})$
$K^\pi=(2^+)$	2231.06(38)	1342.57(50)	$(2,3,4)^+_{[\Upsilon]}$	$2^+_{2^+}$	0.333 ± 0.031	360^{+70}_{-60} ^[w]	0.577(9)	E2/M1 ^[j,w]	$5.2^{+0.9}_{-1.2}$

^[a]: $\delta=-0.45^{+0.05}_{-0.06}$, ^[b]: $\delta=0.20^{+0.06}_{-0.06}$, ^[c]: $\delta < -21$, ^[d]: $\delta=-0.92^{+0.04}_{-0.05}$
^[e]: $\delta < -7$, ^[f]: $\delta < -21$, ^[g]: $\delta=-0.89^{+0.32}_{-0.80}$, ^[h]: $\delta < -21$, ^[i]: $\delta=0.24^{+0.07}_{-0.06}$, ^[j]: $\delta=3.1^{+2.1}_{-1.0}$
^[c]: γ ray not used in $F(\tau)$ calculation ($F(\tau)<0$), ^[c]: γ ray not used in $F(\tau)$ calculation
(doublet with background line), ^[*]: Measured branching ratio unreliable (γ -ray on top of background)
^[g]: $F(\tau)$ or δ_{mixing} extracted from $E_n=1.6$ MeV angular distributions, ^[s]: $F(\tau)$ or δ_{mixing} extracted from $E_n=2.2$ MeV angular distributions, ^[w]: $F(\tau)$ or δ_{mixing} extracted from $E_n=3.1$ MeV angular distributions
^[Y]: No K^π band assignment for this level, ^[t]: Intensity information taken from Ref. [78]
(γ -ray not seen in this work)
1 W.u.=5.25E-7 e²b²

TABLE 4.8

Lifetimes of excited 2^+ band, both 4^+ bands, and tentative 2^+ state at 2230 keV in ^{162}Dy , with calculated $B(E2)$ in W.u., from our measured multipole mixing fractions, branching ratios, γ -ray energies, and lifetimes, all extracted from the angular distributions. $B(E2)$ strengths in parentheses are calculated using literature intensities.

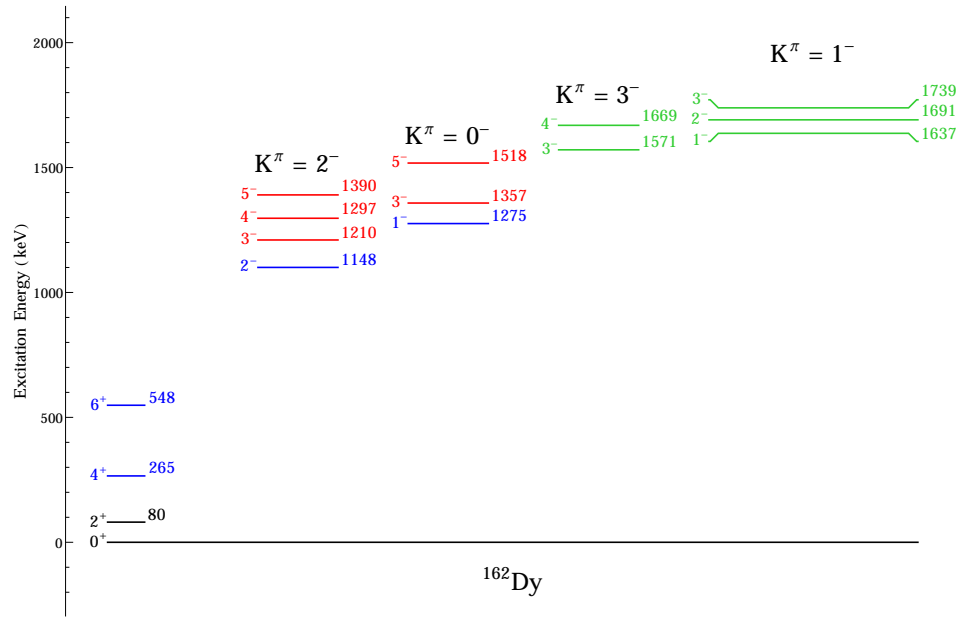


Figure 4.10. Lowest-lying negative parity bands in ^{162}Dy with reliable lifetimes measured in our experiments in red, existing literature values in blue, and unreliable lifetimes measured in green (color online).

E_{level} (keV)	E_γ (keV)	$J_{K_i^\pi}^\pi$	$J_{K_f^\pi}^\pi$	$F(\tau)_{av}$	τ (fs)	BR	B(E1) (mW.u.)
1148.20(20)	260.16(50)	$2_{2_1}^-$	$2_{2_1}^+$	0.074 ± 0.058	2100_{-950}^{+7200} [s]	1.000	$8.9_{-6.9}^{+7.3}$
1210.05(18)	247.27(55) ^[⊗]	$3_{2_1}^-$	$3_{2_1}^+$	0.052 ± 0.030	3100_{-1200}^{+3700} [s]	0.056(2)	$0.2_{-0.1}^{+0.2}$
	322.05(51) ^[⊗]	$3_{2_1}^-$	$2_{2_1}^+$			0.083(2)	$0.2_{-0.1}^{+0.1}$
	944.48(50)	$3_{2_1}^-$	$4_{0_1}^+$			0.310(4)	$0.04_{-0.02}^{+0.03}$
	1129.46(50) ^[⊗]	$3_{2_1}^-$	$2_{0_1}^+$			0.552(4)	$0.04_{-0.02}^{+0.03}$
1297.06(27)	236.09(60) ^[⊗]	$4_{2_1}^-$	$4_{2_1}^+$	0.103 ± 0.049	1400_{-350}^{+1500} [s]	0.150(5)	$2.7_{-1.4}^{+0.9}$
	334.15(50)	$4_{2_1}^-$	$3_{2_1}^+$			0.850(5)	$5.3_{-2.8}^{+1.8}$
1390.52(35)	1124.88(88)	$5_{2_1}^-$	$4_{0_1}^+$	0.090 ± 0.082	>920 [s]	1.000	<0.3
1275.81(24)	1195.10(50)	$1_{0_1}^-$	$2_{0_1}^+$	0.568 ± 0.028	120_{-10}^{+10} [⊖]	0.605(6)	$1.0_{-0.1}^{+0.1}$
	1275.82(53)	$1_{0_1}^-$	$0_{0_1}^+$			0.395(6)	$0.5_{-0.1}^{+0.1}$
1358.00(30)	1092.27(71)	$3_{0_1}^-$	$4_{0_1}^+$	0.612 ± 0.043	100_{-20}^{+20} [⊖]	0.429(9)	$1.1_{-0.2}^{+0.3}$
	1277.33(58)	$3_{0_1}^-$	$2_{0_1}^+$			0.571(9)	$0.9_{-0.2}^{+0.2}$
1518.47(29)	970.01(55)	$5_{0_1}^-$	$6_{0_1}^+$	0.372 ± 0.041	270_{-50}^{+80} [s]	0.294(7)	$0.4_{-0.1}^{+0.1}$
	1252.74(51)	$5_{0_1}^-$	$4_{0_1}^+$			0.706(7)	$0.4_{-0.1}^{+0.1}$
1863.85(26)	900.90(55)	$2_{2_2}^-$	$3_{2_1}^+$	0.297 ± 0.035	420_{-80}^{+120} [s]	0.251(5)	$0.3_{-0.1}^{+0.1}$
	975.65(50)	$2_{2_2}^-$	$2_{2_1}^+$			0.749(5)	$0.6_{-0.1}^{+0.1}$
1910.50(26)	947.51(56)	$3_{2_2}^-$	$3_{2_1}^+$	0.250 ± 0.063	550_{-180}^{+260} [s]	0.552(8)	$0.4_{-0.1}^{+0.2}$
	1022.33(53)	$3_{2_2}^-$	$2_{2_1}^+$			0.448(8)	$0.3_{-0.1}^{+0.1}$
1972.99(66)	912.09(50)	$4_{2_2}^-$	$4_{2_1}^+$	0.205 ± 0.053	780_{-210}^{+280} [⊖]	0.246(13)	$0.1_{-0.1}^{+0.1}$
	1010.19(50)	$4_{2_2}^-$	$3_{2_1}^+$			0.754(13)	$0.3_{-0.1}^{+0.1}$

[⊗]: γ ray not used in $F(\tau)$ calculation ($F(\tau) < 0$).

[⊖]: $F(\tau)$ extracted from $E_n=1.6$ MeV angular distributions, [s]: $F(\tau)$ extracted from $E_n=2.2$ MeV angular distributions, [⊖]: $F(\tau)$ extracted from $E_n=3.1$ MeV angular distributions

[†]: Lifetime not reliable ($F(\tau)$ consistent with zero within 1σ)

1 mW.u.=1.91 e²b

TABLE 4.9

Lifetimes of negative parity bands (2^- , 0^- , 2_2^-) in ^{162}Dy , with
¹¹⁶
experimentally deduced B(E1) in mW.u.

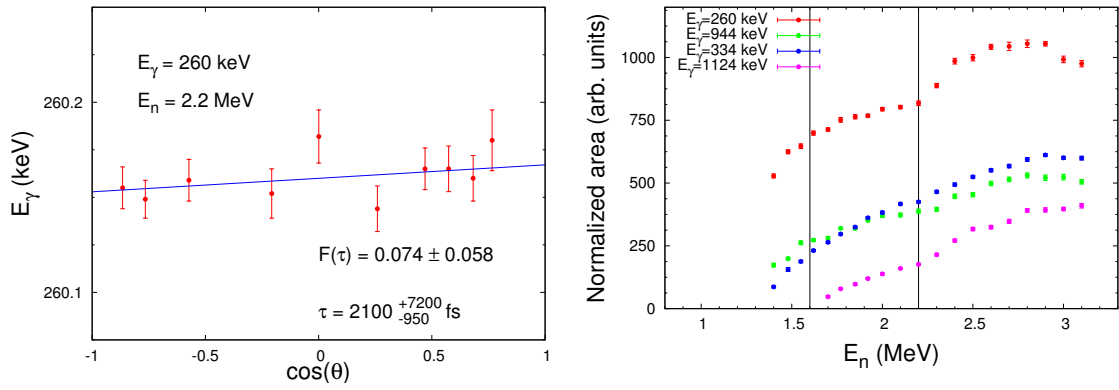


Figure 4.11. $E_\gamma=260$ keV γ ray (from the $E_x=1148$ keV level) Doppler shift and excitation functions for decays from the first 2^- band (color online). The vertical black lines highlight our justification for using a slightly higher bombarding neutron energy, for the sake of better statistics, without the potential for contaminant decay channels from other states.

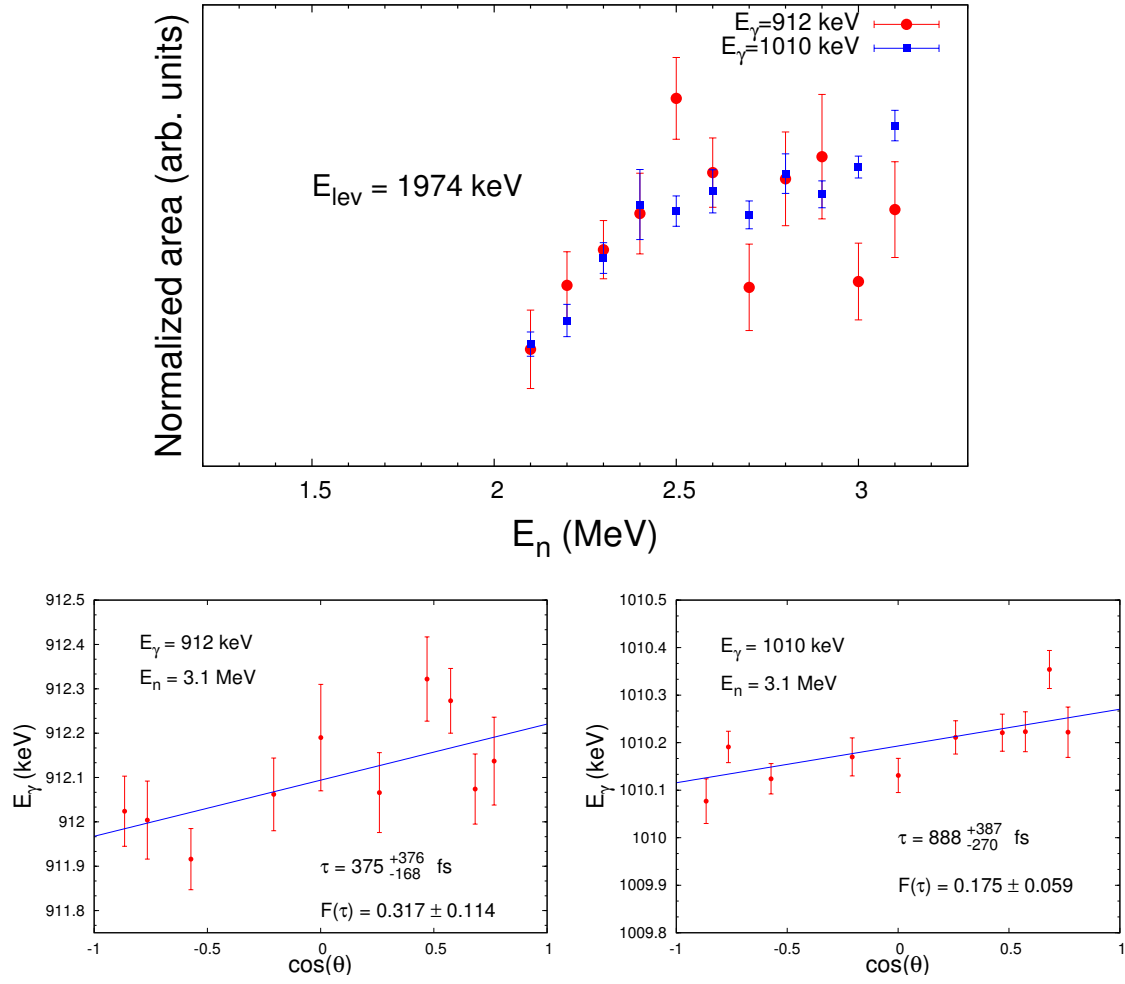


Figure 4.12. $E_\gamma=912$ & 1010 keV (de-excitations from the $E_x=1974$ keV level) Doppler shifts and excitation functions (color online). The excitation function (in blue) for the 1010 keV γ ray is scaled by a factor of 0.33 to normalize to the branching ratio of the level.

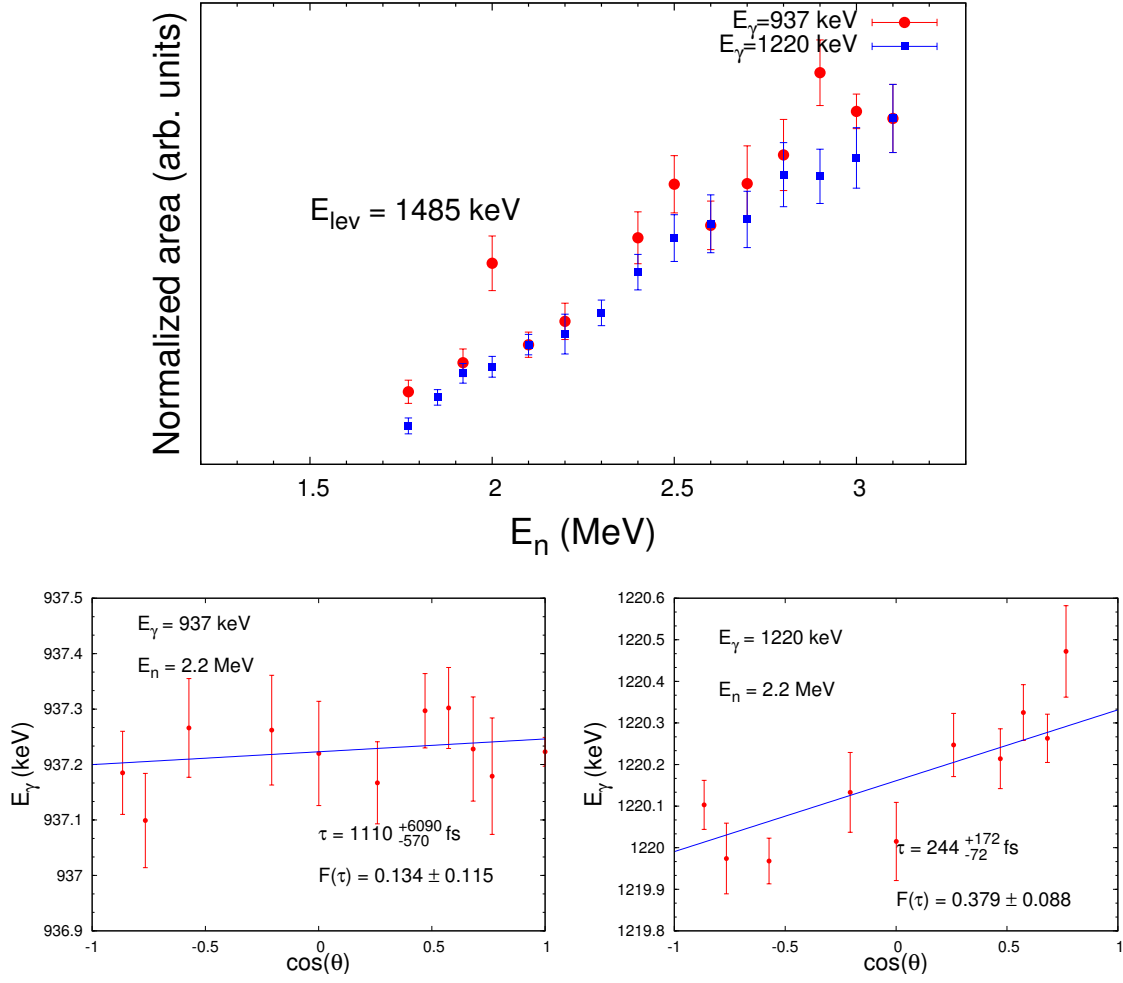


Figure 4.13. $E_\gamma=937$ & 1220 keV (de-excitations from the $E_x=1485$ keV level) Doppler shifts and overlaid excitation functions (color online). The excitation function (in blue) for the 1220 keV γ ray is scaled by a factor of 0.291.

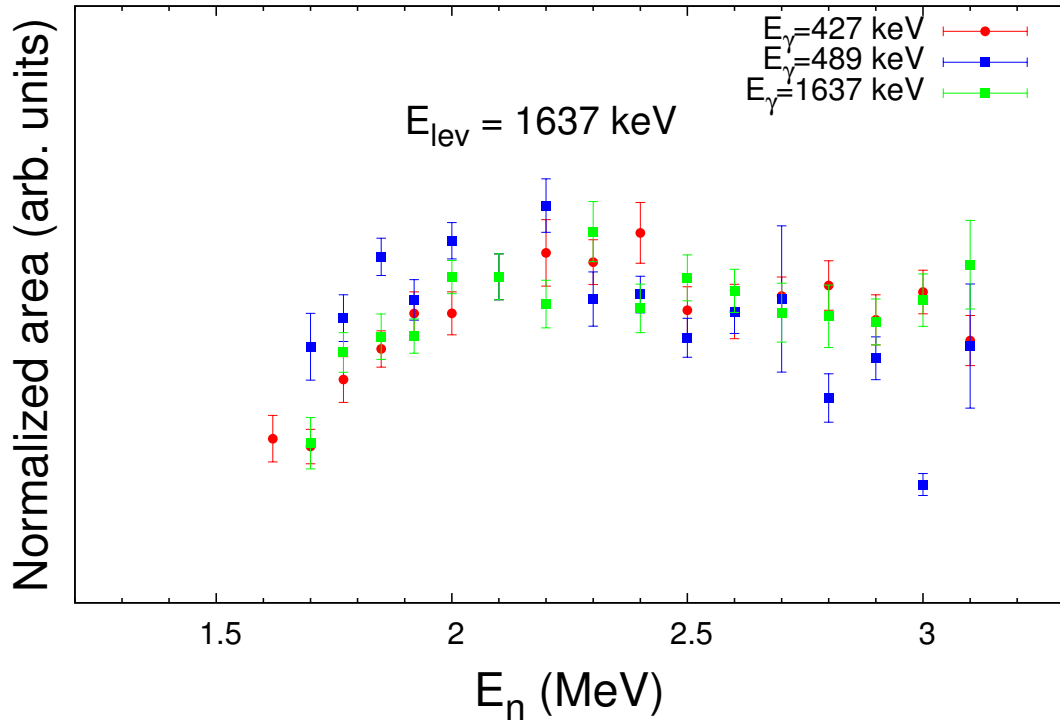


Figure 4.14. Excitation functions for the decays leaving the $E_x = 1637$ keV state. Note the differing population threshold energies for each γ -ray.
(color online)

E_{lev} (keV)	E_γ (keV)	J_i	J_f	$F(\tau)_{av}$	τ (fs)	BR	$\pi\ell$	δ_{mix}	$B(\pi\ell)$
1485.79(29)	937.23(56)	$5_{5_1}^-$	$6_{0_1}^+$	0.310 ± 0.070	400_{-140}^{+210} [s]	0.257(10)	E1		$0.3_{-0.1}^{+0.1}$
	1220.16(56)	$5_{5_1}^-$	$4_{0_1}^+$			0.743(10)	E1		$0.3_{-0.1}^{+0.2}$
1570.82(27)	212.89(51) ^[⊗]	$3_{3_1}^-$	$3_{0_1}^-$	0.015 ± 0.036	>3200 [⊗, †]	0.348(9)	E2/M1	$-0.48_{-0.16}^{+0.13}$ [s]	<720
	295.23(50)	$3_{3_1}^-$	$1_{0_1}^-$			0.652(9)	E2		<1400
1669.26(38)	311.27(50)	$4_{3_1}^-$	$3_{0_1}^-$	0.289 ± 0.116	440_{-210}^{+450} [s]	1.000	E2/M1	$-6.9_{-2.2}^{+1.6}$ [s]	12000_{-11000}^{+6000} [†]
1637.52(20)	427.62(52) ^[⊗]	$1_{1_1}^-$	$3_{2_1}^-$	0.081 ± 0.052	2000_{-800}^{+3500} [⊗]	0.418(8) [*]	E2		230_{-140}^{+150}
	(489.05(56) ^[⊗])	$1_{1_1}^-$	$2_{2_1}^-$			0.157(9)	E2/M1	$0.7 < \delta < 3.2$ [s]	40_{-27}^{+25}
	1637.68(55)	$1_{1_1}^-$	$0_{0_1}^+$			0.425(9)	E1		$0.02_{-0.01}^{+0.01}$
1691.72(23)	416.00(51) ^[⊗]	$2_{1_1}^-$	$1_{0_1}^-$	0.060 ± 0.087	>1000 [s, †]	0.483(8) ^[*]	E2/M1	— [†]	<630
	728.50(51)	$2_{1_1}^-$	$3_{2_1}^+$			0.517(8)	E1		<0.4
1739.02(21)	529.06(51) ^[⊗]	$3_{1_1}^-$	$3_{2_1}^-$	0.107 ± 0.098	>740 [s]	0.375(6)	E2/M1	$1.4_{-0.2}^{+0.2}$ [s]	<130
	590.74(54)	$3_{1_1}^-$	$2_{2_1}^-$			0.139(5)	E2/M1	$1.2_{-0.3}^{+0.5}$ [s]	<24
	678.12(53)	$3_{1_1}^-$	$4_{2_1}^+$			0.238(5)	E1		<0.3
	1473.36(53) ^[⊗]	$3_{1_1}^-$	$4_{0_1}^+$			0.248(5)	E1		<0.03
1766.56(26)	556.67(59) ^[⊗]	$3_{3_2}^-$	$3_{2_1}^-$	-0.061 ± 0.105	>3400 [s, †]	0.310(12)	E2/M1	$-0.54_{-0.21}^{+0.16}$ [s]	<6 [†]
	878.21(55) ^[⊗]	$3_{3_2}^-$	$2_{2_1}^+$			0.690(12)	E1		<0.1 [†]
1826.64(28)	643.99(54) ^[⊗]	$4_{3_2}^-$	$5_{2_1}^+$	0.002 ± 0.066	>2400 [⊗, †]	0.265(9) [*]	E1		<0.1
	863.84(54)	$4_{3_2}^-$	$3_{2_1}^+$			0.735(9)	E1		<0.2

[⊗]: γ ray not used in $F(\tau)$ calculation ($F(\tau) < 0$).

[ϑ]: $F(\tau)$ extracted from $E_n=1.6$ MeV angular distributions, [s]: $F(\tau)$ extracted from $E_n=2.2$ MeV angular distributions, [⊗]: $F(\tau)$ extracted from $E_n=3.1$ MeV angular distributions

[†]: Lifetime not reliable ($F(\tau)$ consistent with zero within 1σ)

[⊗]: γ ray not used in $F(\tau)$ calculation (coincident with background), [*]: branching ratio not reliable due to background contamination.

1 W.u.(E2)= $5.25 \times 10^{-7} e^2 b^2$, 1 mW.u.(E1)= $1.91 e^2 b$

TABLE 4.10

Lifetimes of 5^- , 3^- , 1^- , and second 3^- bands in ^{162}Dy , with experimentally deduced $B(E1)$ in mW.u. and $B(E2)$ in W.u.

E_{lev} (keV)	E_γ (keV)	J_i	J_f	$F(\tau)_{av}$	τ (fs)	BR	$\pi\ell$	δ_{mix}	$B(\pi\ell)$
1745.80(25)	857.65(50)	1^+_{1+}	2^+_{2+}	0.039 ± 0.044	>1800 ^[s,†]	0.538(5)	E2/M1	— ^[†]	<0.02 ^[†]
	1665.09(51) ^[⊙]	1^+_{1+}	2^+_{0+}			0.462(5)	E2/M1	$0.41^{+0.27}_{-0.19}$ ^[s]	<0.04 ^[†]
1782.54(22)	1701.90(53) ^[⊙]	2^+_{1+}	2^+_{0+}	0.013 ± 0.033	>3400 ^[⊙,†]	0.389(10)	E2/M1	$0.33^{+0.24}_{-0.13}$ ^[s]	<0.01
	1782.63(53)	2^+_{1+}	0^+_{0+}			0.611(10)	E2		<0.2
1840.44(21)	630.51(68) ^[⊙]	3^+_{1+}	3^-_{2-}	0.104 ± 0.074	1400^{+3500}_{-500} ^[s]	0.180(10)	E1		$0.2^{+0.1}_{-0.1}$
	779.58(60)	3^+_{1+}	4^+_{2+}			0.283(11)	E2/M1	<-4.8 ^[s]	10^{+8}_{-6}
	1574.82(57)	3^+_{1+}	4^+_{0+}			0.262(12)	E2/M1	$4.4^{+18}_{-2.1}$ ^[s]	$0.3^{+0.2}_{-0.2}$
	1759.60(75) ^[⊙]	3^+_{1+}	2^+_{0+}			0.276(16)	E2/M1	$0.21^{+0.15}_{-0.13}$ ^[s]	$0.01^{+0.01}_{-0.01}$
1951.17(34)	1685.80(56)	4^+_{1+}	4^+_{0+}	0.071 ± 0.048	2300^{+4500}_{-1000} ^[⊙]	1.000	E2/M1	$-0.38^{+0.14}_{-0.17}$ ^[⊙]	$0.1^{+0.1}_{-0.1}$
2395.60(39)	2395.00(50)	1^+_{Ω}	0^+_{0+}	0.926 ± 0.061	14^{+13}_{-11} ^[⊙]	1.000	M1		$0.14^{+0.61}_{-0.08}$
2519.43(36)	2438.00(51)	1^-_{Ω}	2^+_{0+}	0.595 ± 0.054	110^{+30}_{-20} ^[⊙]	0.564(27)	E1		$0.1^{+0.1}_{-0.1}$
	2520.27(51)	1^-_{Ω}	0^+_{0+}			0.436(27)	E1		$0.1^{+0.1}_{-0.1}$
2537.26(30)	2537.24(51)	1^+_{Ω}	0^+_{0+}	0.290 ± 0.049	460^{+160}_{-120} ^[⊙]	1.000	M1		$0.004^{+0.001}_{-0.001}$
2569.35(22)	2568.83(51)	1^+_{Ω}	0^+_{0+}	0.653 ± 0.066	90^{+30}_{-20} ^[⊙]	1.000	M1		$0.021^{+0.006}_{-0.005}$
2814.80(33)	2734.24(55)	1^+_{Ω}	2^+_{0+}	0.442 ± 0.099	200^{+130}_{-60} ^[⊙]	1.000	M1		$0.008^{+0.003}_{-0.003}$

^[⊙]: γ ray not used in $F(\tau)$ calculation ($F(\tau)<0$).

^[⊙]: $F(\tau)$ extracted from $E_n=1.6$ MeV angular distributions, ^[s]: $F(\tau)$ extracted from $E_n=2.2$ MeV angular distributions, ^[⊙]: $F(\tau)$ extracted from $E_n=3.1$ MeV angular distributions

^[†]: Lifetime not reliable ($F(\tau)$ consistent with zero within 1σ)

1 W.u.(E2)= $5.25E-7$ e²b², 1 mW.u.(E1)= 1.91 e²b

TABLE 4.11

Lifetimes of 1^+ band and 1^\pm members of the isovector M1 scissors mode

($[\Omega]$ marker) in ^{162}Dy , with experimentally deduced $B(E1)$ in mW.u.,

$B(M1)$ in μ_N^2 and $B(E2)$ in W.u.

E_{lev} (keV)	E_γ (keV)	J_i	J_f	$F(\tau)_{av}$	τ (fs)	BR	$\pi\ell$	δ_{mix}	$B(\pi\ell)$
1886.53(33)	1805.86(52)	$4^+_{[r]}$	$2^+_{0^+}$	0.086 ± 0.034	1600^{+1300}_{-390} [s]	1.000	E2		$0.5^{+0.2}_{-0.2}$
1895.44(26)	747.34(57) ^[⊗]	$2^+_{[r]}$	$2^-_{2^-}$	0.258 ± 0.029	530^{+100}_{-90} [s]	$0.249(6)^{[*]}$	E1		$0.4^{+0.1}_{-0.1}$
	1814.69(52)	$2^+_{[r]}$	$2^+_{0^+}$			0.751(6)	E2/M1	$-0.58^{+0.07}_{-0.08}$ [s]	$0.3^{+0.1}_{-0.1}$
1982.61(22)	1902.06(53)	$2^+_{[r]}$	$2^+_{0^+}$	0.547 ± 0.031	130^{+17}_{-15} [s]	0.522(5)	E2/M1	— ^[‡]	$2.5^{+0.3}_{-0.3}$
	1982.50(56)	$2^+_{[r]}$	$0^+_{0^+}$			0.478(5)	E2		$1.9^{+0.2}_{-0.2}$
1999.23(33)	1918.57(52)	$2^+_{[r]}$	$2^+_{0^+}$	0.203 ± 0.031	730^{+160}_{-130} [s]	1.000	E2/M1	$-0.12^{+0.03}_{-0.04}$ [s]	$0.01^{+0.01}_{-0.01}$
2102.42(57)	584.22(50)	$(3)^-_{[r]}$	$5^-_{0^-}$	0.122 ± 0.073	1300^{+2000}_{-450} [⊗]	1.000	(E2)		180^{+93}_{-110}
2148.47(33)	2067.92(50)	$(2)^{\pm}_{[r]}$	$2^+_{0^+}$	0.048 ± 0.026	3300^{+3700}_{-1200} [⊗]	1.000	(E2/M1)	— ^[‡]	$0.1^{+0.1}_{-0.1}$
2180.69(53)	1217.73(58)	$4^+_{[r]}$	$3^+_{2^+}$	0.383 ± 0.095	240^{+190}_{-80} [s]	1.000	E2/M1	$0.24^{+0.07}_{-0.06}$ [s]	$1.3^{+1.0}_{-0.9}$
2231.06(38)	955.75(50)	$(2,3,4)^+_{[r]}$	$1^-_{0^-}$	0.333 ± 0.031	360^{+70}_{-60} [⊗]	0.423(9)	E1		$0.4^{+0.1}_{-0.1}$
	1342.57(50)	$(2,3,4)^+_{[r]}$	$2^+_{2^+}$			0.577(9)	E2/M1	$3.1^{+2.1}_{-1.0}$ [⊗]	$5.2^{+0.9}_{-1.2}$
2313.75(52)	2233.20(50)	$(2)^+_{[r]}$	$2^+_{0^+}$	0.133 ± 0.048	1200^{+620}_{-290} [⊗]	1.000	(E2/M1)	— ^[‡]	$0.2^{+0.1}_{-0.1}$
2324.59(39)	1141.96(50)	$(4,5)^+_{[r]}$	$5^+_{2^+}$	0.051 ± 0.063	>1300 [⊗, †]	1.000	(E2/M1)	— ^[‡]	<6.16
2339.31(50)	2339.29(50)	$(2)^+_{[r]}$	$0^+_{0^+}$	0.285 ± 0.067	480^{+230}_{-160} [⊗]	1.000	(E2)		$0.5^{+0.2}_{-0.2}$
2371.55(52)	2291.00(50)	$(1,2,3)^-_{[r]}$	$2^+_{0^+}$	0.011 ± 0.079	>1700 [⊗, †]	1.000	E1		<0.02

[⊗]: γ ray not used in $F(\tau)$ calculation ($F(\tau) < 0$).

[‡]: $F(\tau)$ extracted from $E_n=1.6$ MeV angular distributions, [s]: $F(\tau)$ extracted from $E_n=2.2$ MeV angular distributions, [⊗]: $F(\tau)$ extracted from $E_n=3.1$ MeV angular distributions

[†]: Lifetime not reliable ($F(\tau)$ consistent with zero within 1σ)

[⊗]: γ ray not used in $F(\tau)$ calculation (coincident with background), [*]: branching ratio not reliable due to background contamination.

1 W.u.(E2)= $5.25E-7$ e²b², 1 mW.u.(E1)= 1.91 e²b

TABLE 4.12

Lifetimes of states with no rotational K^π band assignment in ^{162}Dy , with experimentally deduced $B(E1)$ in mW.u., $B(M1)$ in μ_N^2 and $B(E2)$ in W.u.

E_{lev} (keV)	E_γ (keV)	J_i	J_f	$F(\tau)_{av}$	τ (fs)	BR	$\pi\ell$	δ_{mix}	$B(\pi\ell)$
2386.48(52)	2305.92(50)	$(2)_{[\Upsilon]}^+$	2_{0+}^+	0.217 ± 0.053	$710_{-190}^{+260} [\varpi]$	1.000	(E2/M1)	— ^[‡]	$0.3_{-0.1}^{+0.1}$
2411.96(36)	2331.40(50)	$(4_{[\Upsilon]}^+)$	2_{0+}^+	0.126 ± 0.046	$1200_{-290}^{+690} [\varpi]$	1.000	(E2)		$0.2_{-0.1}^{+0.1}$
2427.02(52)	2346.46(50)	$(2,3)_{[\Upsilon]}^+$	2_{0+}^+	0.355 ± 0.074	$310_{-100}^{+170} [\varpi]$	1.000	(E2/M1)	— ^[‡]	$0.7_{-0.3}^{+0.3}$
2487.99(33)	2407.43(50)	$(3,4)_{[\Upsilon]}^+$	2_{0+}^+	0.270 ± 0.052	$520_{-140}^{+190} [\varpi]$	1.000	(E2/M1)	— ^[‡]	$0.4_{-0.1}^{+0.1}$
2505.75(26)	2240.40(50)	$(2)_{[\Upsilon]}^+$	4_{0+}^+	0.500 ± 0.032	$160_{-20}^{+20} [\varpi]$	0.530(16)	(E2)		$0.9_{-0.1}^{+0.1}$
	2505.66(51)	$(2)_{[\Upsilon]}^+$	0_{0+}^+			0.470(16)	(E2)		$0.5_{-0.1}^{+0.1}$
2509.43(33)	2428.88(50)	$(2,3)_{[\Upsilon]}^+$	2_{0+}^+	0.361 ± 0.050	$300_{-70}^{+100} [\varpi]$	1.000	(E2/M1)	— ^[‡]	$0.6_{-0.2}^{+0.2}$
2523.76(85)	952.94(50)	$(1,2,3,4)_{[\Upsilon]}^\pm$	3_{3-}^-	0.151 ± 0.109	$1100_{-500}^{+2600} [\varpi]$	1.000	(E2/M1)		18_{-13}^{+15}
2555.66(33)	2475.11(51)	$(2,3)_{[\Upsilon]}^+$	2_{0+}^+	0.330 ± 0.082	$350_{-130}^{+230} [\varpi]$	1.000	(E2/M1)	— ^[‡]	$0.3_{-0.1}^{+0.2}$
2613.30(33)	2532.75(51)	$(3)_{[\Upsilon]}^+$	2_{0+}^+	0.613 ± 0.059	$100_{-20}^{+30} [\varpi]$	1.000	(E2/M1)	— ^[‡]	$0.02_{-0.01}^{+0.01}$
2630.66(30)	2630.63(52)	$(2,3)_{[\Upsilon]}^+$	2_{0+}^+	0.602 ± 0.056	$110_{-20}^{+30} [\varpi]$	1.000	(E2/M1)	— ^[‡]	$1.1_{-0.2}^{+0.3}$
2777.62(60)	2777.59(56)	$(2)_{[\Upsilon]}^+$	0_{0+}^+	0.465 ± 0.117	$180_{-70}^{+140} [\varpi]$	1.000	(E2/M1)	— ^[‡]	$0.5_{-0.2}^{+0.3}$
2816.53(43)	2551.00(55)	$(4,5)_{[\Upsilon]}^+$	4_{0+}^+	0.256 ± 0.085	$550_{-220}^{+370} [\varpi]$	1.000	(E2/M1)	— ^[‡]	$0.3_{-0.1}^{+0.2}$

^[⊙]: γ ray not used in $F(\tau)$ calculation ($F(\tau)<0$).

^[⊘]: $F(\tau)$ extracted from $E_n=1.6$ MeV angular distributions, ^[‡]: $F(\tau)$ extracted from $E_n=2.2$ MeV angular distributions, ^[⊖]: $F(\tau)$ extracted from $E_n=3.1$ MeV angular distributions

^[†]: Lifetime not reliable ($F(\tau)$ consistent with zero within 1σ)

^[⊗]: γ ray not used in $F(\tau)$ calculation (coincident with background)

1 W.u.(E2)= $5.25E-7$ e²b², 1 mW.u.(E1)= 1.91 e²b

TABLE 4.13

Lifetimes of states with no rotational K^π band assignment (cont'd) in

¹⁶²Dy, with experimentally deduced B(E1) in mW.u., B(M1) in μ_N^2 and

B(E2) in W.u.

CHAPTER 5

DISCUSSION AND INTERPRETATION

5.1 ^{160}Gd Discussion

5.1.1 Excited 0^+ States and the $K^\pi=2_\gamma^+$ Band

The 0^+ excitations in ^{160}Gd serve to highlight some of the distinct advantages of $(n,n'\gamma)$ studies performed at UKAL. Previous literature assertions list four 0^+ excitations in ^{160}Gd , from various experiments, two of which are tentative assignments [7, 26]. In [49], we exploit two facets from the angular distribution and excitation function measurements to rule out the two tentative assignments. First, angular distributions for γ radiation leaving a 0^+ state must be isotropic, and secondly, that energy thresholds of a γ -ray leaving a 0^+ state will come in at precisely the level energy (recall that there is no extra energy needed to make non-zero angular momentum transfers).

The previous assignment of a 0^+ excitation at $E_{lev}=1325.73$ keV was made by [7] in a $(n,n'\gamma)$ reaction using continuous energy reactor neutrons, with refutation of this assignment made in this work and by angular distribution measurements performed in [33]. The justification for this refutation of a $J=0$ assignment is shown in Figure 5.1, a clearly anisotropic angular distribution of the $E_\gamma=1250.4$ keV de-excitation, explicitly stating that this radiation cannot stem from a 0^+ excitation. A similar check was made via the normalization of angular distributions; absolute intensities of γ rays were normalized so that radiation from the lowest-lying 0^+ state is isotropic. In the case where we used a normalization to this $E_\gamma=1250.4$ keV γ

ray, angular distributions of well-behaved dipole and quadrupole radiation (*e.g.* E2 radiation from strong ground-state band transitions) ceased to exhibit the expected behavior of a classically oscillating charge distribution from Figure 2.6. Contrast this catastrophic result from this normalization attempt to the one in use by normalizing to the $E_\gamma=1304.46$ keV from the 1379 keV state, and we see the return of ‘concave-up’ angular distributions for quadrupole radiation, leaving us with a clear choice for normalization and furthermore pointing away from the assignment of the 1325 keV state as a 0^+ excitation.

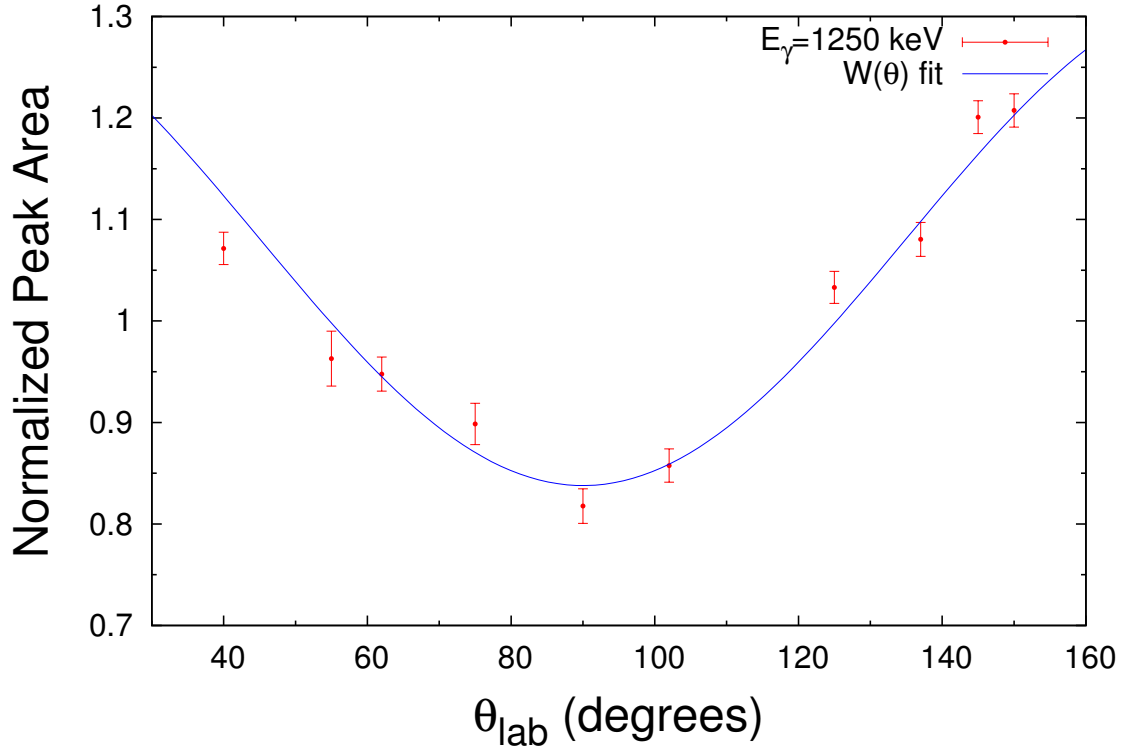


Figure 5.1. Non-isotropic decay from the tentative 0^+ state in ^{160}Gd at $E_x=1325$ keV.

The second tentative 0^+ excitation at $E_{lev}=2236$ keV was placed in [26] via a (t,p) transfer reaction study; we also reject this assignment based on, again, the non-isotropic nature of γ -radiation from the single observed $E_\gamma=2162.74$ keV de-excitation, as well as a threshold energy below that of the excitation energy of the state. This creates a completely illogical and unphysical system, where a γ -ray is populated below the energy of the state, and as such, cannot be attributed to this excitation. The excitation function measurement for this decay can be seen in Figure 5.2, with a threshold clearly below 2100 keV.

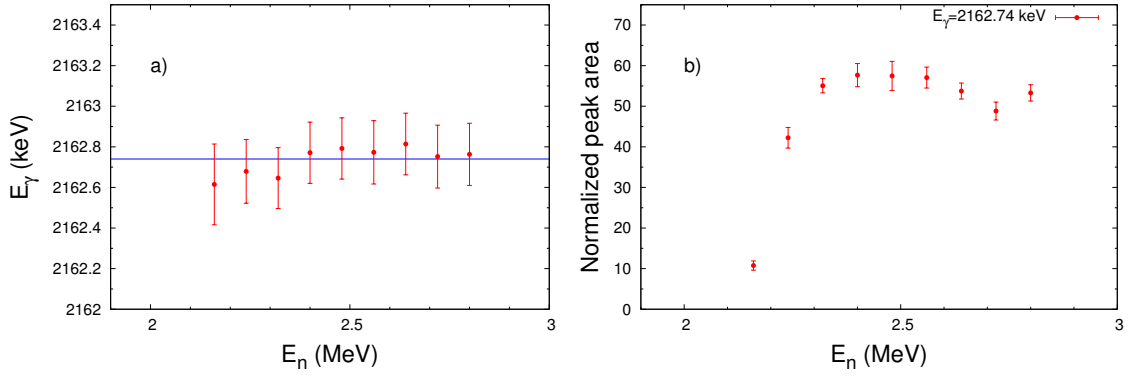


Figure 5.2. Excitation function measurement from the tentative 0^+ state in ^{160}Gd at $E_x=2236$ keV.

This leaves only two 0^+ excitations remaining in ^{160}Gd as candidates for either a single-phonon β vibration or a double-phonon ($\gamma\gamma$, double octupole, etc) type, now labeled as the 0_2^+ and 0_3^+ bands. A corresponding level scheme with the decays out of $K^\pi=0^+$ bandmembers is shown in Figure 5.3.

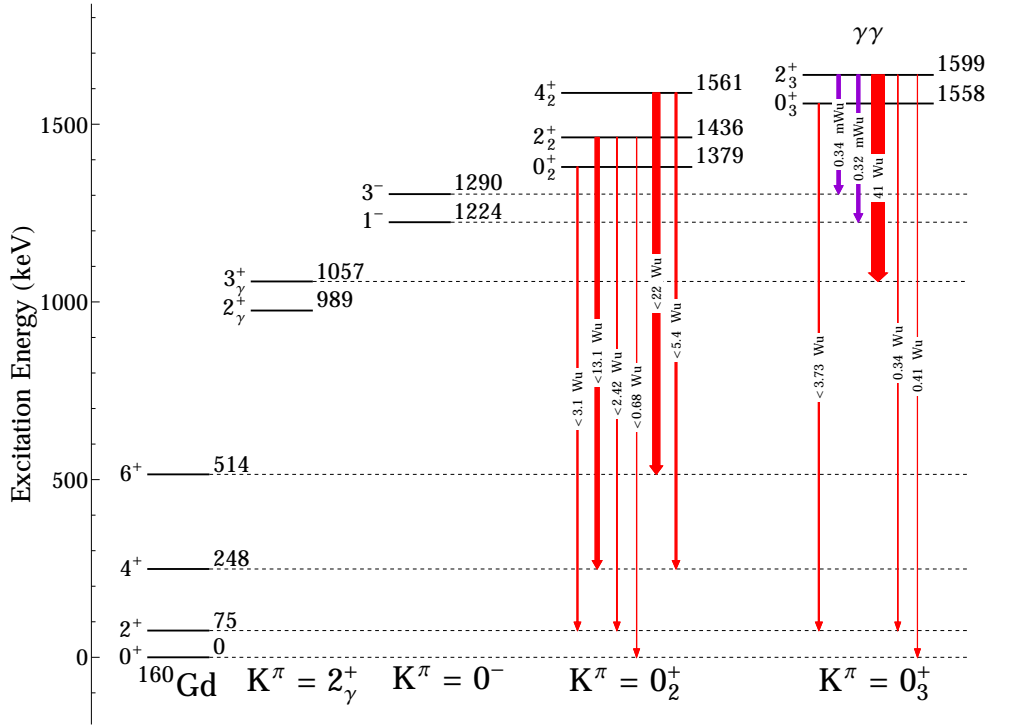


Figure 5.3. Level scheme showing the calculated $B(E2)$ in W.u. and $B(E1)$ in mW.u. for the confirmed 0^+ excitations in ^{160}Gd .

Six (6) γ rays were detected to determine the lifetimes of three levels in the $K^\pi=0_2^+$ band in our $^{160}\text{Gd}(n,n'\gamma)$ experiments. Decays leaving the 0_2^+ band display varying levels of collectivity based off our lower-limit lifetime measurements in the band (at least >320 fs for each state). In terms of offering a concrete case for assessing this band as a β -vibration, we can tentatively point to this band as a single-phonon quadrupole vibration from its potentially strong transition probabilities to the ground state (or from our measurement of upper limits on the collectivity). Given the limitations of what lifetimes DSAM can measure, we are left with an obviously murky picture for any possible β -vibration in ^{160}Gd due to our measurement of lifetime

limits, although the potentially collective decays to the ground state tend to suggest some (albeit weak) β -vibrational interpretation of this band at $E_x=1379$ keV. Due to the lack of intraband transitions observed in our experiment, we cannot place any two-phonon characteristics to this set of excitations, as we should expect strong $B(E2)$ values connecting the 0_2^+ band to the 2_γ^+ band at $E_x=988$ keV. An ideal situation for further study includes the refinement of the lifetime measurements of this band via another measurement technique to concretely assign a β -vibration to this band, as the collective upper limit is *indicative* of a β -vibration, but is not conclusive enough to say for certain.

A similar, yet also contrasted story emerges with the discussion of any single-phonon characteristics in the 0_3^+ band at $E_x=1558$ keV; six (6) γ rays were detected to measure the lifetime of two states in the $K^\pi=0_3^+$ band. The decays to the ground state exhibit characteristically weak collectivity (<4 W.u. for the bandhead and <0.5 W.u. for the 2^+ member), pointing away from the interpretation as a β -vibration. However, the refinement of the 1599 keV state's lifetime opens up key discussion for the 0_3^+ band. We have measured a γ ray that corresponds to an intraband transition, namely to the $K^\pi=2^+$ γ -vibrational band, with an inflated $B(E2)$ value of 41_{-37}^{+16} Weisskopf units. While the uncertainty of this transition probability is large due to the measured lifetime's uncertainty, this strong, preferential decay is indicative of signatures for the antialigned ($K=0$) double-phonon $\gamma\gamma$ -vibration. Our measurement of the angular distribution for this γ ray led to our overwhelmingly E2-type mixing ratio ($\delta=-5.57_{-5.00}^{+1.91} \rightarrow 96.8\%$ E2). Of further note, the 0_3^+ band displays some slightly inflated transition probabilities to the lowest lying $K^\pi=0^-$ band at ~ 0.3 mW.u. strength. These somewhat inflated $B(E1)$ probabilities would otherwise be indicative of some double-octupole phenomena in the nucleus, but with the presence of the extraordinarily large $B(E2)$ to the γ -vibrational band, more interest and a higher feasibility is placed on the interpretation of this band as a double

quadrupole vibration ($K^\pi=0^+$, $\gamma\gamma$ -type).

Staying within the same vein of quadrupole excitations, we turn our attention to any γ -vibrational characteristics of ^{160}Gd . While the nature of $K^\pi=2^+$ bands is not as heavily debated as the 0^+ bands [17, 36, 41, 53], our lifetime measurements of the states in this γ -vibrational band warrant discussion, as any collective excitations built on-top of this band should be a multiphonon configuration. The decays observed from the lowest $K^\pi=2_\gamma^+$ band are shown in Table 4.2 and Figure 5.4. Overall, we see systematically expected behavior (inflated levels of collectivity averaging about 5-10 W.u.) in terms of the strength of the other 2_γ^+ excitations in the rare-earth region of nuclei [35, 45, 52, 53], and as such, we can assign and confirm this band as a quadrupole γ -vibration in ^{160}Gd . Generally, it is prudent to obtain this base-level of collectivity in the nucleus to compare the feasibility of other phonon excitations, or to make claims on any two-phonon characteristics in ^{160}Gd . We are yet again presented with the well-behaved γ -vibration that has stood the test of time for and has been a figurehead in nuclear structure in deformed rare-earth nuclei.

5.1.2 Negative Parity States

The determination of any reflection-asymmetry and thus, potential octupole shape correlations in ^{160}Gd will lie in the measurement of $B(E1)$ transition probabilities of de-excitations from the low-lying negative parity states. The decays from all observed negative parity bands in ^{160}Gd are shown in Figure 5.4 alongside the $K^\pi=2_\gamma^+$ decays from the previous section. The tabulated results from all E1 decays observed in the experiments can be seen in Table 4.3.

The deduced $B(E1)$ s from the $K^\pi=0^-$ band show large inflation of collectivity from these states, strongly indicating a well-behaved octupole vibration in ^{160}Gd . This octupole collectivity in the $B(E1)$ s are corroborated by the experimentally measured and distinctly collective $B(E3;0^+ \rightarrow 3^-)$ transition probability ($0.118(7) \text{ e}^2\text{b}^3$) by [53].

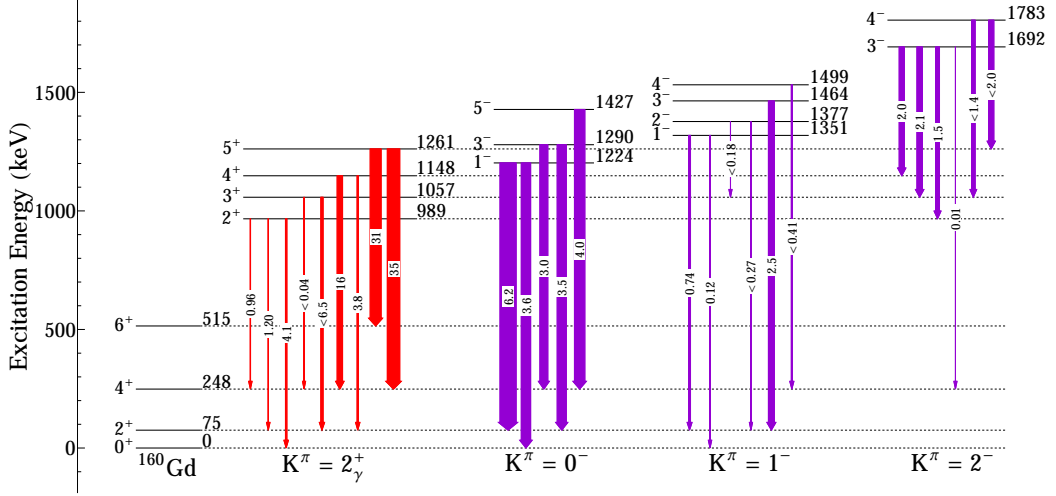


Figure 5.4. Level scheme showing the decays with calculated reduced transition probabilities for the $K^\pi=2_\gamma^+$ band and low-lying negative parity states in ^{160}Gd .

We also measure comparably short lifetimes for two of the four members that result in distinctly collective (yet not as collective as the $K^\pi=0^-$ band), indicating that this band could indeed be a part of the fragmented octupole vibration in ^{160}Gd . The shallow values for $F(\tau)$ in this state cannot offer a concrete idea of the collectivity of the state. A similar argument applies for the 4^- state at 1498 keV, where we only observe a shallow shift from the Doppler plots; luckily, these other members of the 1^- band can offer some insight from the well-defined lifetime measurements. Overall, the observation of moderately inflated levels of collectivity in the band seems to indicate that these rotational members of the $K^\pi=1^-$ band are indeed a part of the octupole vibration.

We measure distinct collectivity from the 3^- member of the $K^\pi=2^-$ band connecting to the γ -vibrational band, following a recent trend of observation by [58, 71] of strong E1 radiation in $2^- \rightarrow 2^+$ transitions. The same trend of (potentially) collective

E1s to the γ -vibrational band occur in the 4^- member of the band, where we only have a lower limit to the lifetime. This is obviously a curious behavior and needs more work to assign any conclusive detail to the rotational band. B(E3) transition probabilities to the γ -band are critical in achieving this goal; barring those measurements, only the ideas presented in current, developing works can be applied, but this is still a significant contribution to the total E1 strength in deformed nuclei, whether or not it is a part of the octupole vibration. Furthermore, we can safely adopt this $K^\pi=2^-$ assignment from the well-behavedness and agreement of the deduced B(E1)s in comparison to the Alaga rules (Table 5.1).

Our measurement of lifetimes in the lowest-lying negative parity bands begs the question: where is the 3^- member of the traditional octupole multiplet? Or at least, if this band is *not* the $K^\pi=2^-$ band and instead the $K^\pi=3^-$ band, where is the missing part of the octupole quartet of states? Population of $\Delta K=3$ states is difficult (but not impossible) to accomplish with $(n,n'\gamma)$ reactions, but the states would be very weak, and we may simply lack the statistics needed to observe such states with any reliability. In a soon to be echoed tone throughout this work, more sensitive experiments (or much higher statistics in terms of beam time, reaction rates, etc) are needed to have fully spectroscopy and measurement of lifetimes in ^{160}Gd . Especially from our observation of negative parity states that do not decay strongly to the ground state (the $K^\pi=2^-$ band), the traditional picture of fragmented octupole collectivity seems tentative as we impede on the rotational limit ($R_{\frac{4}{2}} \sim 3.3$).

5.1.3 Other Lifetime Measurements in ^{160}Gd

5.1.3.1 $K^\pi=4^+$ band as a Hexadecapole Vibration?

The study of even, positive parity states continues into the interpretation of $K^\pi=4^+$ bands in deformed nuclei. We know from earlier assertions, that a $\gamma\gamma$ two-

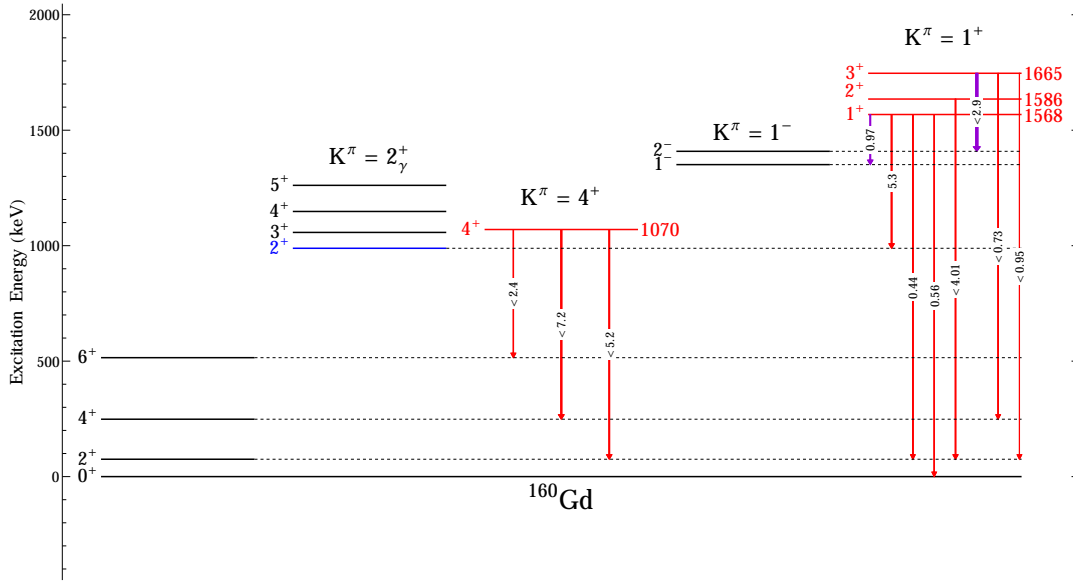


Figure 5.5. Level scheme showing the decays with calculated reduced transition probabilities for the $K^\pi=4^+$ and 1^+ bands in ^{160}Gd .

phonon vibration can have this $K=4$ angular momentum projection, but must also exhibit strongly collective decays to the γ -band, as each phonon must be ‘broken’ individually, and in single steps. Any existence of this $\gamma\gamma$ -type behavior in ^{160}Gd is already dubious from energy considerations, as the expected energy for a harmonic two-phonon state should be roughly double the energy of the single-phonon counterpart. The $E_x=1070$ keV state lies 100 keV above the γ -vibrational band, and in our measurement of the lifetime of this single 4^+ bandhead of the $K^\pi=4^+$ band, we find somewhat enhanced $B(E2)$ transition probabilities to the ground state, with no de-excitations or preference of decay to the γ -vibrational band. This implies a lack of two-phonon characteristic in this excitation, and instead points towards a single phonon vibration of order $\lambda=4$; this hexadecapole nature is yet another expansion of the dynamic deformation in the geometric model set out by Bohr and Mottelson, and has been investigated in several works [17, 59, 74] for spherical and nearly-spherical

nuclei. Again, much like the need for strong B(E3) radiation in determining octupole characteristics, the direct observation of E4 radiation depopulating K=4 bands would fully elucidate any hexadecapole nature in these states. We can, however, not say anything about hexadecapole vibrational characteristics in ^{160}Gd with B(E2) measurements alone. Any assertions made would be tentative, as we are only able to extract a lower limit to the lifetime of this state at 1070 keV; further spectroscopy is needed to concretely say anything about the makeup of this state. That being said, Solviev has produced quasiparticle-phonon calculations that surmise this 4^+ state to be mostly hexadecapole in nature [74]. Tangible experimental evidence for hexadecapole phonon behavior is nearly unprecedented in well-deformed nuclei, which our data could be one of the first signatures of this structure. This curious behavior in ^{160}Gd begs further research, and, if this band is confirmed as a hexadecapole vibration built on top of the deformed ground state, it would be one of the lowest excitation energies of its kind, especially in a well-deformed nucleus.

5.1.3.2 $K^\pi=1^+$ band

Our measurement of lifetimes for the $K^\pi=1^+$ band yields some interesting discussion in a potential quasiparticle-phonon coupling to either the established 1^- band mentioned in §5.1.2, as well as the γ -vibrational band. We measured lifetimes for the 1^+ , 2^+ , and 3^+ members of this band, with several intraband transitions. Overall, we observe generally weak collectivity from members of this band to the ground state, with enhanced E1 transitions to the weakly collective $K^\pi=1^-$ band; normally and at first glance, this would imply some double-phonon collectivity, but this picture is obscured with a discretely preferential decay to the γ -vibrational band. This ~ 5 W.u. B(E2) is hard to ignore, given its large branching ratio (30%), especially in the context of strong intra-band transitions to known vibrational states in deformed nuclei. The most realistic outcome of interpretation of this band is of purely quasiparticle na-

ture, where there is a strong implication that a majority of the corresponding nuclear wavefunction overlaps with the predominant configuration of the γ -vibrational band. Following in line with the major contributions to γ -vibrational bands in deformed nuclei from [19], we should expect and there is implication that significant overlap with the Nillson neutron wavefunctions of $\nu(\frac{3}{2}[521]+\frac{1}{2}[521])$ exist for these states.

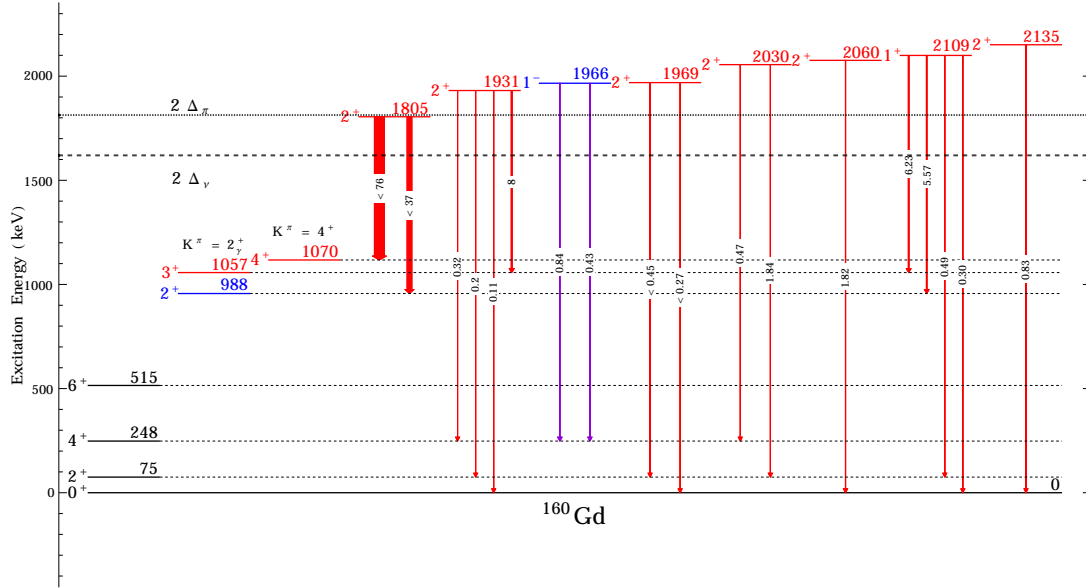


Figure 5.6. Level scheme showing the decays with calculated reduced transition probabilities for the levels that are not assigned to rotational bands in ^{160}Gd . Note the neutron and proton pairing gaps drawn as dotted lines ($2\Delta_\nu \sim 1625$ keV and $2\Delta_\pi \sim 1810$ keV).

The inflated level density, uncertain spin-assignment, and higher probability for state-mixing to occur [19] make band-assignments for these states well above the pairing gap increasingly difficult. That does not imply that the lifetimes measured are of

diminished value; several instances of subtle nuclear structure exist at the higher energies studied in our experiments, such as the upcoming isovector dipole resonance in ^{162}Dy . We have also not exhausted every possible two-phonon candidates in deformed nuclei, as the excessively rare ‘ $\beta\gamma$ ’-type that would have a K-projection of 2^+ . The signatures for this excitation follow the case for any two-phonon vibration, enhanced E2 transitions to a well-established vibrational band (in this case either a ‘ γ ’ or ‘ β ’ vibration). The best such candidate for a $\beta\gamma$ vibration is the 2^+ state at 1931 keV. We measure four decays from this state, and have a very well-defined lifetime from the Doppler Shifted γ rays. The B(E2) probabilities here are very indicative of collective behavior built on top of the γ -band, with a collective 8 Weisskopf unit transition to the γ -band via a mostly ($\sim 92\%$) E2 decay to the 3^+ member. To say that this is indeed a two-phonon collective vibration would be cavalier, of course, since we do not have complete and unambiguous assignment of the β vibration. Since there are no other decays to the γ -vibrational band, we cannot make an Alaga comparison of transition strengths, and unfortunately, the large error (upper bound) shows the limiting power of DSAM near picosecond lifetimes. That all being said, given any rotational band assignment of this state, it could be a key asset in the search for a $\beta\gamma$ -type vibration, and as we will see, the viability for anharmonic multiphonon configurations below an energy ratio of 2.

In the remaining states, we see some more of the mirrored assertions on any $K^\pi=1^+$ bands, with a strong coupling to the γ -vibrational band coming from another 1^+ state at 2109 keV. Of course, the macroscopic treatment of quadrupole vibrations by Bohr and Mottelson do not attribute any $K^\pi=1^+$ bands [11], so these states *must* be of single- or multi-quasiparticle configurations. Yet again, the significantly preferred branching ratio and B(E2) strengths to the 2^+ band implies a dominant quasiparticle configuration involving the $\nu(\frac{3}{2}[521]+\frac{1}{2}[521])$ shell using Nillson model considerations.

5.1.4 Implications & Further Discussion

In terms of a vibrational phonon model, we have measured new lifetimes for key states in ^{160}Gd , the first being a potential (read: tentative) β -vibration existing as the lowest 0^+ state at 1379 keV. However, our assignment here is not conclusive enough to say for certain, as we only have upper limits to the collectivity, yet the potential for large $B(E2)$ probabilities exists (>7 W.u. in strength for some transitions). We do see a fairly definitive excitation of the $\gamma\gamma$ -vibration as the third 0^+ state at 1558 keV via a highly collective transition from the 2^+ member of the band to the γ -vibrational band. Speaking of the γ -vibration, we measured lifetimes for the four lowest-lying members of the $K^\pi=2^+$ band that leads to the trademark $\sim 6\text{--}7$ W.u. collectivity for the γ -vibrational band.

The measurement of lifetimes in the negative parity bands yields some expected results from the systematic study of states in the region, with two well-defined octupole members (0^- and 1^-), and a curious emerging decay pattern of $K^\pi=2^-$ bands to the γ -vibrational state. In all of these states, we measured distinctly inflated $B(E1)$ transition probabilities, indicating some amount of dipole strength or asymmetry in the nuclear shape. In the case of the 0^- and 1^- bands, literature $B(E3)$ values aid in the assessment of an octupole vibration built on top of the deformed ground state, and we have opened the question to find the remaining members of the vibration expected from the base Bohr-Mottelson formulation of the geometric model.

Comparisons of the deduced $B(E2)$ and $B(E1)$ transition probabilities to the Alaga rules round out our discussion of the lifetimes measured in ^{160}Gd . The ratios of our experimental transition probabilities and the Clebsch-Gordan coefficients squared are shown in Table 5.1, where we observe somewhat mixed agreement for the various bands in ^{160}Gd . The comparison of our deduced $B(E2)$ limits for the 0_2^+ band seems to be in stark disagreement, however, our measurement of upper limits of $B(E2)$ s does not exclude agreement for *any* combination of $B(E2)$ value. For the 0_3^+ band, we note

reasonable agreement (within the full range of uncertainty) for the Alaga comparisons; this includes both the decay channels to the $K^\pi=0^-$ octupole band and to the ground state band. The 2_γ^+ band is in reasonable agreement within error where we have convergent lifetimes (the 4^+ and 5^+ members), but we mirror the same assertions as the 0_2^+ band, where the disagreement for the upper limits of B(E2) do not offer much insight. Lastly, all of the negative parity band comparisons to the Alaga rules offer good agreement! Furthermore, the agreement of the $K^\pi=2^-$ band's measured B(E1)s imply that the $K^\pi=2^-$ assignment is valid, since a $K^\pi=3^-$ assignment would produce wildly variant Alaga expectations (*e.g.* the ratio of Clebsch-Gordan coefficients in the $K=3$ case are 0.14, 0.05, 0.35 and 0.11 going down the table in the same order).

K^π	$\frac{J_i \rightarrow J'_f}{J_i \rightarrow J''_f}$	CG ²	Exp
$K^\pi=0_2^+$	$\frac{2^+ \rightarrow 4^+}{2^+ \rightarrow 2^+}$	1.8	5.4
	$\frac{2^+ \rightarrow 4^+}{2^+ \rightarrow 0^+}$	2.6	19
	$\frac{2^+ \rightarrow 2^+}{2^+ \rightarrow 0^+}$	1.4	3.6
	$\frac{4^+ \rightarrow 6^+}{4^+ \rightarrow 4^+}$	1.8	4.1
$K^\pi=0_3^+$	$\frac{2^+ \rightarrow 3^-}{2^+ \rightarrow 1^-}$	1.5	1.1
	$\frac{2^+ \rightarrow 2^+}{2^+ \rightarrow 0^+}$	1.4	0.8
$K^\pi=2_\gamma^+$	$\frac{2^+ \rightarrow 2^+}{2^+ \rightarrow 0^+}$	1.4	0.3
	$\frac{3^+ \rightarrow 4^+}{3^+ \rightarrow 2^+}$	0.4	0.01
	$\frac{4^+ \rightarrow 4^+}{4^+ \rightarrow 2^+}$	2.9	4.2
	$\frac{5^+ \rightarrow 6^+}{5^+ \rightarrow 4^+}$	0.6	0.9
$K^\pi=0^-$	$\frac{1^- \rightarrow 2^+}{1^- \rightarrow 0^+}$	2.0	1.8
	$\frac{3^- \rightarrow 4^+}{3^- \rightarrow 2^+}$	1.3	0.9
$K^\pi=1^-$	$\frac{1^- \rightarrow 2^+}{1^- \rightarrow 0^+}$	0.5	0.7
$K^\pi=2^-$	$\frac{3^- \rightarrow 4_\gamma^+}{3^- \rightarrow 3_\gamma^+}$	1.3	1.0
	$\frac{3^- \rightarrow 4_\gamma^+}{3^- \rightarrow 2_\gamma^+}$	1.8	1.4
	$\frac{3^- \rightarrow 3_\gamma^+}{3^- \rightarrow 2_\gamma^+}$	1.4	1.3
	$\frac{4^- \rightarrow 5_\gamma^+}{4^- \rightarrow 3_\gamma^+}$	1.4	1.4

TABLE 5.1

Alaga comparisons of reduced transition probabilities in ^{160}Gd .

5.2 ^{162}Dy Lifetimes

In the remaining level schemes in Chapter 5, the widths of transitions are proportional to the calculated reduced transition probabilities for a particular γ -ray and are scaled and normalized to guide the eye; for example, a 1 mW.u. B(E1) is approximately equal in width to a 5 W.u. B(E2) transition strength and ~ 0.1 W.u. for a B(M1), unless otherwise noted in a particular section of discussion. This scaling is in line with the understanding that enhanced E1 transitions are ~ 1 mW.u., large E2 transition strengths are > 5 W.u., and inflated M1 transitions are ~ 0.1 W.u. in strength. To further aid the eye, E1, E2, and M1 multipolarities are colored discretely, with E1 transitions being violet, E2 transitions colored red, and M1 transitions in green.

5.2.1 0^+ Excitations Not Observed in $(n, n'\gamma)$

We did not observe γ rays for every excited 0^+ state seen in (p,t) experiments by [55] in ^{162}Dy , namely the excitations at 1814.6, 1820.3, 2588, and 2663 keV (Table 5.2). Figure 5.7 shows cuts of our γ -singles spectra above the level energy thresholds where we would expect to see the full energy ($0_i^+ \rightarrow 2_{gs}^+$ transitions at the drawn vertical lines) de-excitations of the aforementioned states. Locally, there are no obvious peaks above our background, with the exception of the expected γ -ray leaving the 2588 keV state; if this peak exists, it would be a doublet with a γ at 2506 keV, belonging to a state of the same energy, making its energy shift unreliable and thus difficult to extract a lifetime with DSAM.

The tentative 0^+ assigned in [55] as a probable contaminant at $E_x=774.2$ keV was not observed in our experiment. The only decay channel available to such a state was not observed at $E_\gamma \approx 693.5$ keV ($(0_{774.2}^+ \rightarrow 2_{g.s.}^+)$), due to the prominent Ge(n, γ) detector background at the expected peak location. We can place a generous upper

0_i^+	E_x	Observed?
[†]	774.2 (3)	[†]
0_2^+	1398.3 (3)	✓
0_3^+	1666.3 (4)	✓
0_4^+	1814.6 (5)	
0_5^+	1820.3 (5)	
0_6^+	2126.5 (6)	✓
0_7^+	2496.7 (7)	✓
0_8^+	2588.8 (7)	
0_9^+	2655.3 (7)	✓
(0_{10}^+)	2663.0 (7)	
(0_{11}^+)	2802.9 (7)	✓

TABLE 5.2

Observed 0^+ states in our $(n,n'\gamma)$ experiments compared with (p,t) experiments from [55], with [†] as the labeled ‘contaminant’ at $E_x=774.2$ keV.

limit to the intensity of any peak on top of this background of 3% of the intensity of the strong 807 keV γ ray that de-excites the γ -band bandhead. This upper limit is well below half of the intensity of the lowest intensity γ rays observed in this $(n,n'\gamma)$ study, and as such, we are unable to measure a lifetime for this state using the Doppler Shift Attenuation Method. Govor in [32] observes an unplaced γ ray at 694.19 keV (well within the detector resolution to consider this γ ray as a candidate) at a lower intensity than our upper limit discussed above; it is entirely possible that this state exists, but the experiments so far have lacked the sensitivity to detect the

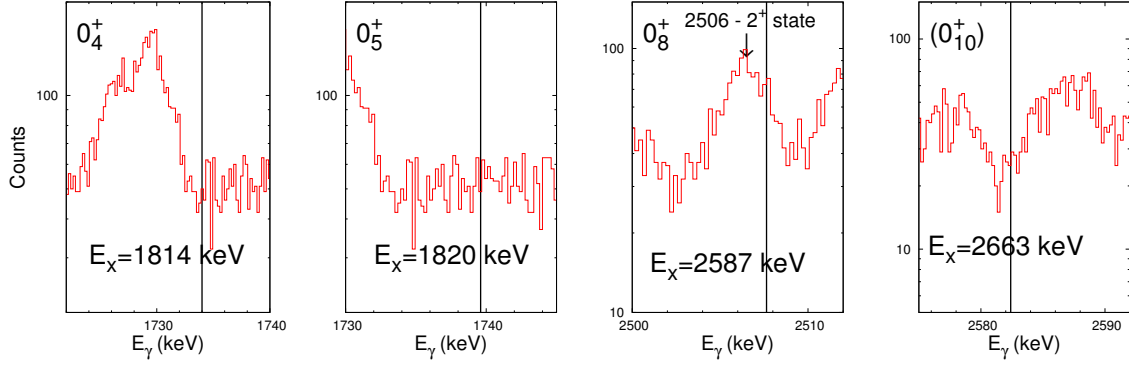


Figure 5.7. Singles spectra cuts where remaining 0^+ excitations should be observed. Spectra for $0_{4,5}^+$ placements are from the $E_n=1.925$ MeV excitation function measurements, with $0_{8,10}^+$ from the $E_n=2.9$ MeV dataset.

de-excitation at ~ 693.5 keV. The ‘contaminant’ state at 774.2 keV is not observed in any other ^{162}Dy studies ($(\alpha, 2n)$, (n, γ) , $(n, n'\gamma)$, etc [3]), further justifying its lack of detection in this campaign of experiments. We emphasize the use of other reactions such as $(\alpha, \alpha'\gamma)$ to remove the (n, γ) background in hopes of finding this state at 774.2 keV.

5.2.2 A Lack of Strong β Vibrations in ^{162}Dy

As it stands from our measurement of the lifetimes, the generally weakly-collective ($B(E2) < 2$ W.u.) transitions to the ground state band point away from a single-phonon β -vibration assignment for *any* observed 0^+ state in ^{162}Dy , shown in Table 4.7. Common allegations on the collectivity of a β -vibration are that the $B(E2; 0_i^+ \rightarrow 2_{g.s.}^+) \sim 12\text{--}33$ W.u. [28], with decays from higher-lying members of the band falling around 6-10 W.u. in strength, when in reality, this behavior is far from common across the nuclear landscape. While the E0 strengths are not available for the states in the 0^+ bands of ^{162}Dy , and the two nucleon transfer reaction cross sections to all but one 0^+ excitation are small ($< 10.6\%$ of the ground state cross section [55]), order

of magnitude differences in the above assertions on B(E2) strength, and the low absolute value of our B(E2) measurements do not lend credence to this β -vibration picture. In addition, our evaluation of upper limits to the B(E2) strength in a few cases is not conclusive enough to confirm any band as a β -vibration, even in the face of a potentially collective transition to the ground state at 1.9 Weisskopf units. Traditionally, the lowest lying K=0,2 bands were tenaciously defended as quadrupole vibrations, but this paradigm has evolved as the experimental data trickles in, and as we notice the unclear nature of 0^+ excitations in deformed nuclei [29, 68]. The search for higher-lying collective 0^+ excitations in ^{162}Dy has merit, as both ^{166}Er and ^{158}Gd show signs of strong (>2 W.u.) collectivity in states above the first excited 0^+ band [30, 48], but again, our findings fail to reveal any concrete signature of a strongly collective β -vibration at *any* excitation energy in ^{162}Dy . Our most likely candidate and correspondingly most collective B(E2) ($1.2^{+2.3}_{-0.6}$ W.u.) to the ground state lies in the 0^+_{11} state at 2802 keV excitation energy. *If* this state is the true β vibration in ^{162}Dy and the state at 774.2 keV is *not* the lowest 0^+ , it follows the empirical behavior of well-deformed rare-earth nuclei, where the β mode of quadrupole vibration does not exist as the lowest-lying $K^\pi=0^+$ band. The curious lack of an observed collective β vibration in our data is alarming, but we must not forget the unobserved excitations below the pairing gap(s) at 774, 1814, & 1820 keV, as any one of these states *could* be the collective β -vibration in ^{162}Dy .

5.2.3 On the Two-Phonon Characteristics

With the experimental evidence of two-phonon quadrupole vibrations in nearby rare-earth nuclei (^{178}Hf), we are given impetus to further examine any multiphonon configurations in the 0^+ states in ^{162}Dy .

5.2.3.1 2^+_γ band

The axial symmetry-breaking γ vibration has stood up as one of the benchmarks and cornerstones of quadrupole surface vibrations in the geometric model. While not as enigmatic in behavior as their $K^\pi=0^+$ counterparts (the proposed β vibration), the lowest $K^\pi=2^+$ band provides the basis of understanding nuclear collective motion in deformed nuclei. Lifetimes of the $K^\pi=2^+$ band up to $J=5$ were measured and are shown in Table 4.8 and Figure 5.10. Systematics for the γ -vibrational band decays to the ground state across the even Dysprosium nuclei show inflated levels of collectivity on the order of ~ 5 W.u. in strength [35, 53], where we observe similarly collective (~ 4 W.u.) transitions in our $(n,n'\gamma)$ experiments; this gives a reasonable, unambiguous assignment as the $K^\pi=2^+$ γ -vibration in ^{162}Dy , and provides the foundation for the multiphonon configurations in the nucleus. Since our deduced $B(E2)$ does not offer refinement beyond the previously measured transition probabilities from Coulomb Excitation, we report our measured value, but adopt the literature values in discussion.

5.2.3.2 0^+_2 band $\gamma\gamma$ -vibration

Considerable theoretical and experimental focus [8, 36, 55, 81] has been placed into the assessment of the 0^+_2 band as a $\gamma\gamma$ -vibration, and its confirmation is contingent on the measurement of level lifetimes and the $0^+ \rightarrow \gamma$ -vibration interband transitions: a weak $E_\gamma=565$ keV line decaying from the 2^+ member of the band, a $E_\gamma=686$ keV line leaving the 4^+ member, and the elusive $E_\gamma=512$ keV line from the 0^+ bandhead, to name a few. The broad annihilation peak in our spectra prevents detection of this latter γ ray in our γ -singles-based experiments, and the low literature intensities of the other two make detection less than straightforward. We can, however, calculate the transition probabilities using our measured lifetimes, the literature values for the intensities [3, 81], and with assumption that no multipolarity mixing is

present. The existence of this double-phonon characterization in the 0_2^+ seems fairly evident as a $\gamma\gamma$ -vibration from our lifetime measurements (with lower limits of lifetimes in a few cases), with calculated $B(E2; 2^+ \rightarrow 4_\gamma^+) = 2.7$, $B(E2; 4^+ \rightarrow 4_\gamma^+) < 3.7$, and $B(E2; 0^+ \rightarrow 2_\gamma^+) < 16$ W.u. Clearly, the $B(E2)$ probabilities greater than 1 are plausible in the interband cases for decays of the 2^+ member, and the upper limit of a 16 Weisskopf unit $B(E2)$ for the 512 keV γ ray is difficult to ignore, which points toward some collective behavior built on top of the γ -vibrational band. However, the overall $B(E2)$ strength observed is not blatantly conclusive, so we emphasize a *tentative* two-phonon ($\gamma\gamma$) vibration characterization of the $K^\pi = 0_2^+$ band. That being said, the relative inflation and enhancement of transition probabilities to the γ -vibrational band is evident in Table 5.5, where we see more than a factor of 2 increase in $B(E2)$ for like-spin changing transitions ($2^+ \rightarrow 2_\gamma^+$ versus $2^+ \rightarrow 2_{gs}^+$, for example), strengthening our argument for this $\gamma\gamma$ assignment in ^{162}Dy . Comparison of our deduced transition probabilities out of the 0_2^+ band to the Alaga rules (Table 5.4) yield some mixed results; for decays to the ground state, we observe good agreement, but the decays to the γ -vibrational band are in stark disagreement. The disagreement cannot be explained due to multipole mixing in any case (recall that our reported $B(E2)$ s to the γ -band assume no mixing and are practically upper limits). An inset level scheme for the 0_2^+ band is shown in Figure 5.10, showing our measured decays and the interband decays (with literature intensities). These interband transition strengths are also seen in Table 4.7, marked by a $[\dagger]$ symbol in the column for the branching ratio, corresponding to literature branching ratios taken from [3]. The measurement and confirmation of $\gamma\gamma$ collectivity in this 0_2^+ band also implies certain degrees of anharmonicity at work in the two-phonon vibration, as the 0_2^+ band lies 375 keV below the expected excitation energy for a harmonic $\gamma\gamma$ -vibration (at 1.6 times the energy of the single γ -vibrational phonon case). Anharmonic double-phonon vibrations are not completely unprecedented in the literature (^{178}Hf [2] & ^{232}Th [45]), but this is one of

the lowest-lying $\gamma\gamma$ vibrations in well-deformed rare-earth nuclei at $E_x=1400$ keV. On top of this, the nuclei in the actinides (Th and Os) that exhibit two-phonon vibrations have energy ratios very close to the expected value of 2, with ^{232}Th less than 2, yet ^{162}Dy is contrasted with the intriguing evidence of other rare-earth two-phonon vibrations that have a $\frac{E_{\text{gamma}\gamma}}{E_\gamma}$ ratio >2 [80].

5.2.3.3 $K^\pi=4_{1,2}^+$ bands at 1535,2181 keV as $\gamma\gamma$ -vibrations

In the case of an aligned $K^\pi=4^+$ $\gamma\gamma$ -vibration, strong $B(E2)$ transition probabilities are expected between the 4^+ band and the existing γ -vibration. In our experiments, we do not observe full-energy de-excitations of the $K^\pi=4^+$ band to the ground state due to K-forbidedness, but instead with transitions to the previously mentioned γ -vibrational band (shown in Figure 5.10). The level of collectivity in these interband transitions (in either our deduced $B(E2)$ strengths or the ones calculated with literature intensities) is striking and extremely hard to ignore! Due to the preferential decays observed and the collective transitions to the $2^+\gamma$ -band, it seems definitive that this lowest-lying $K^\pi=4^+$ band is the second $\gamma\gamma$ -vibration in ^{162}Dy , at a slightly anharmonic energy ($R_{\frac{E_{\gamma\gamma}}{2E_\gamma}} \approx 0.86$).

Wu characterizes the $\gamma\gamma$ vibration in ^{162}Dy as a highly fragmented excitation, with significant collective strength lying in the two 4^+ states at 1535 & 2181 keV [78]. The M1 mixing present in the $4^+ \rightarrow 3^+$ decay translates to a deduced $B(E2)$ of 1.3 W.u.; this deduced value from our experiments does not account for the $\sim 50\%$ branch of the 1294 keV decay, where in reality, this $B(E2)$ is cut in half by using literature intensities [8, 78]. Using the literature intensities from [78], we do observe a distinctly collective E2 transition from this higher-lying 4^+ state to the bandhead of 8.5 W.u., however, this degree of collectivity is contrasted with the lower-lying 4^+ state that we assign as a $\gamma\gamma$ -vibration, where the authors in [78] imply that there is a significant component of a two-phonon vibration in this state at 2181 keV. Instead, we

observe an overwhelming portion of collectivity in the lower-lying 4^+ state, with the calculated transition strengths leaving this higher-lying state in Table 4.8. This is not to imply complete disagreement with [78], as we still observe a highly fragmented and collective $\gamma\gamma$ -vibration in these two states at 1535 and 2181 keV. Falling in line with other 4^+ $\gamma\gamma$ -vibrations in rare-earth nuclei, this two-phonon vibration is anharmonic, with a $R_{\frac{E_{\gamma\gamma}}{E_\gamma}}=2.5$ [30].

5.2.3.4 $(2,3,4)^+$ state at 2230 keV

Our comprehensive lifetime measurements of $J \leq 5$ states below 3.1 MeV has yielded an interestingly strong transition from a state at 2230 keV excitation energy to the γ -vibrational band. From our measurement of a mixed E2/M1 multipolarity γ -ray ($\sim 89\%$ E2 if the state is a 2^+) at $E_\gamma=1342$ keV that decays to the bandhead of the γ -band, we can place a tentative $(2,3,4)^+$ spin assignment on this level. Aprahamian observed a similar energy γ -ray, but places an E1 multipolarity assignment, where our angular distribution is consistent with a $\Delta L=2$ transition (Figure 5.9) [3]. Given any of the tentative positive parity, low-spin assignments, our measured $B(E2)$ is distinctly collective, at 5.2 W.u. in strength; this behavior of distinct collectivity is completely expected for a two-phonon $\beta\gamma$ -vibration in structure, and would be one of the first experimental evidences of this mode of multiphonon configuration. These are, of course, large assumptions to make about the rotational band assignment of this state, but provide an interesting avenue to continue research into the structure of this nucleus.

This begs the question, once again: where is the single-phonon β vibration in ^{162}Dy ? If we take this state at 2230 keV as part of the $\beta\gamma$ -vibration and with close to harmonic vibrations, the β vibration *should* be around $E_x \approx 1350$ keV; this is clearly not the case based on our lifetime measurements of the 0_2^+ band and its characterization as the $K=0$ $\gamma\gamma$ -vibration. That being said, it is entirely possible

that a strong β -vibration exists at either of the 0^+ excitations at 1814 or 1820 keV (or at the unobserved and elusive state at 774 keV). In the case of a β vibration at ~ 1800 keV, it would imply that the $\beta\gamma$ is fairly anharmonic, clocking in at $\sim 80\%$ of the expected two-phonon energy, which is reasonable, considering that the $K^\pi=0^+$ $\gamma\gamma$ -vibration in ^{162}Dy is $\sim 79\%$ harmonic ($R_{\frac{E_{\gamma\gamma}}{2E_\gamma}} \approx 0.79$), and the $K^\pi=4^+$ $\gamma\gamma$ -vibration is similarly anharmonic at $R_{\frac{E_{\gamma\gamma}}{2E_\gamma}} \approx 0.86$. We strongly emphasize further study on the 0^+ states in ^{162}Dy to find the collective β -vibration at 774, 1814, or 1820 keV (if the β -vibration even exists in this nucleus).

E_{lev} (keV)	E_γ (keV)	$I_{\gamma,abs}$ (n,n' γ)	I_γ (lit.)
888.18(22)	807.54(50)	976.596(9.252)	
	888.18(50)	887.460(7.953)	
962.96(27)	697.30(50) ^[⊙]	166.366(2.981)	
	882.31(50)	877.632(9.095)	
1061.05(29)	795.35(50)	213.256(1.374)	
	980.36(51)	121.782(1.166)	
1182.88(26)	634.24(61)	67.548(1.514)	
	917.18(51)	214.971(2.635)	
1400.29(36)	512.0(2)	[†]	11(5)* [81]
	1319.60(51)	163.971(1.238)	133(3)* [81]
1453.50(30)	395.49 (10)	[†]	0.18(2) [3]
	565.32 (12)	[†]	0.37(6) [3]
	1187.81(51)	125.506(1.610)	12.7(3) [3]
	1372.80(51)	169.820(1.989)	18.1(8) [3]
1535.97(23)	475.27(54) ^[⊗]	53.276(3.388)	4.5(3) [3]
	572.96(50)	90.678(1.588)	21.8(9) [3]
	647.61(50) ^[⊙]	141.966(2.084)	50.1(8) [3]

E_{lev} (keV)	E_γ (keV)	$I_{\gamma,abs}$ (n,n' γ)	I_γ (lit.)
1574.34(29)	513.31 (2)	[†]	0.51(3) [3]
	611.23 (5)	[†]	0.12(2) [3]
	686.15 (6)	[†]	0.29(8) [3]
	1025.84(58) ^[⊗]	25.251(0.916)	5.0(2) [3]
	1308.65(51)	135.879(1.997)	24(2) [3]
1666.01(33)	1585.35(51)	131.018(1.476)	
1728.31(20)	1462.70(51) ^[⊗]	110.002(1.779)	0.81(6) [32]
	1647.64(51)	133.790(2.206)	1.21(7) [32]
	1728.29(53)	85.273(1.611)	0.66(6) [32]
2128.02(33)	2047.34(61)	286.080(6.065)	
2180.69(53)	1217.73(58)	300.230(5.134)	1.13(24) [78]
	1292.51(58) ^[⊗]	319.833(9.558)	1.00 [78]
2189.65(52)	2109.10(50)	140.677(3.860)	
2231.06(38)	1342.57(50)	239.620(6.282)	
2497.77(52)	2417.22(50)	116.520(4.933)	
2655.83(33)	2575.28(53)	59.373(5.424)	
2802.04(61)	2721.48(55)	50.490(15.032)	

TABLE 5.3

Absolute intensities for γ -decays observed in (n,n' γ) experiments. [†]: γ ray not observed, reporting literature intensity ([3, 32] gives absolute intensities, while [78, 81] report relative intensities).

K^π	$\frac{J_{K_i \rightarrow J'_{K_f}}}{J_{K_i \rightarrow J''_{K_f}}}$	Exp	CG ²
<u>$K_i^\pi=2_\gamma^+$</u>	$\frac{4^+ \rightarrow 4^+}{4^+ \rightarrow 2^+}$	2.3	2.9
<u>$K_i^\pi=0_2^+$</u>	$\frac{2^+ \rightarrow 4^+}{2^+ \rightarrow 2^+}$	1.5	1.8
	$\frac{4^+ \rightarrow 6^+}{4^+ \rightarrow 4^+}$	1.4	1.7
	$\frac{2^+ \rightarrow 4_\gamma^+}{2^+ \rightarrow 2_\gamma^+}$	3.1	0.8
	$\frac{4^+ \rightarrow 4_\gamma^+}{4^+ \rightarrow 2_\gamma^+}$	10	44
	$\frac{4^+ \rightarrow 4_\gamma^+}{4^+ \rightarrow 3_\gamma^+}$	9.3	3.2
	$\frac{4^+ \rightarrow 3_\gamma^+}{4^+ \rightarrow 2_\gamma^+}$	0.8	14
<u>$K_i^\pi=4_1^+$</u>	$\frac{4^+ \rightarrow 4^+}{4^+ \rightarrow 3^+}$	0.5 ^[*] (0.2)	0.4
	$\frac{4^+ \rightarrow 4^+}{4^+ \rightarrow 2^+}$	0.8 ^[*] (0.2)	0.2
<u>$K_i^\pi=4_2^+$</u>	$\frac{4^+ \rightarrow 3^+}{4^+ \rightarrow 2^+}$	0.1	0.6

TABLE 5.4

Alaga rule comparisons of measured B(E2) strengths for the $K^\pi=2_\gamma^+$, 0_2^+ , and 4_1^+ band in ^{162}Dy . [*]: Alaga comparison shown in parentheses uses literature intensities to calculate B(E2) strengths.

K	$\frac{J_i \rightarrow J_f}{J_i \rightarrow J_f}$	$\frac{B(E2 \rightarrow \gamma)}{B(E2 \rightarrow g.s.)}$
<u>$K^\pi=0_2^+$</u> :	$\frac{0^+ \rightarrow 2_\gamma^+}{0^+ \rightarrow 2_{g.s.}^+}$	8.4
	$\frac{2^+ \rightarrow 2_\gamma^+}{2^+ \rightarrow 2_{g.s.}^+}$	3.0
	$\frac{2^+ \rightarrow 4_\gamma^+}{2^+ \rightarrow 4_{g.s.}^+}$	3.4
	$\frac{4^+ \rightarrow 4_\gamma^+}{4^+ \rightarrow 4_{g.s.}^+}$	4.6

TABLE 5.5

Ratios of B(E2) probabilities of the transitions to the γ -band over the ground state band transitions, highlighting an enhancement or preference of decay to the $K^\pi=2^+\gamma$ -band.

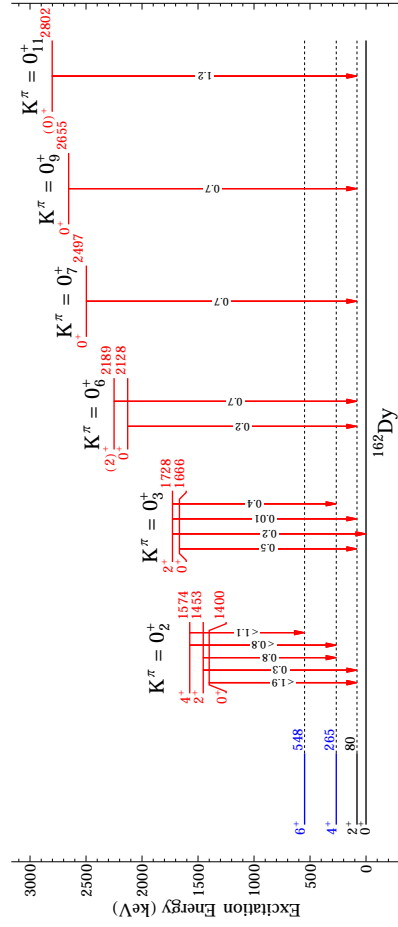


Figure 5.8. Level scheme outlining all measured lifetimes for $K^\pi=0^+$ bands in ^{162}Dy . New lifetime measurements are shown in red (color online), and new $B(E2;0_i^+ \rightarrow \text{g.s.})$ calculations are expressed in Weisskopf units (W.u.).

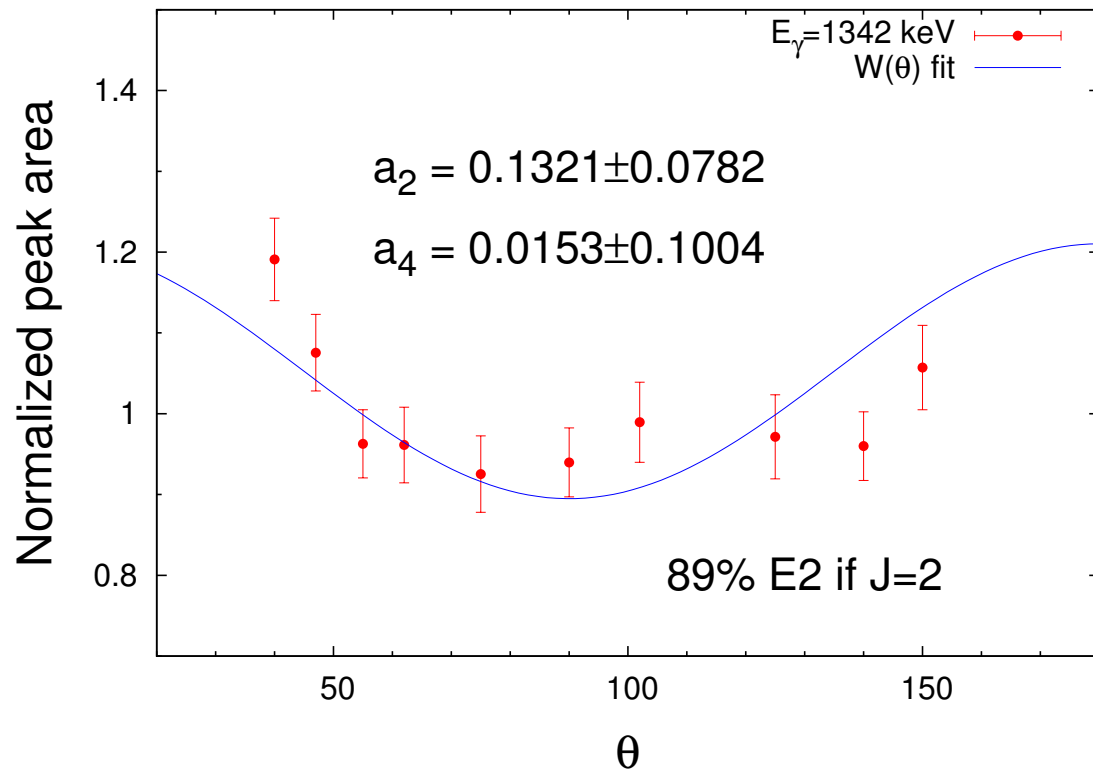


Figure 5.9. Measured angular distribution of 1342 keV γ ray leaving the 2230 keV level, $W(\theta)$ fit is shown with a_2 and a_4 coefficients from the $E_n=3.1$ MeV angular distribution.

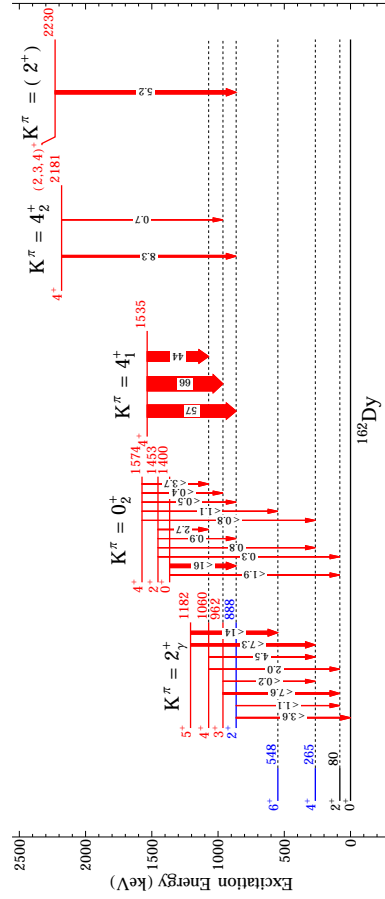


Figure 5.10. Level scheme showing all observed transitions from the lowest-lying 2^+_{γ} , 0^+_2 , and 4^+_1 band with all interband ($K^{\pi}=J^+_i \rightarrow K^{\pi}=2^+_{\gamma}$) decays. Intensities for transitions to the γ -band are taken from [3]. Also shown is a tentative (2^+) state at 2230 keV with a strong decay to the 2^+_{γ} band.

5.2.4 Negative Parity States

5.2.4.1 $K^\pi=2^-$ Band at 1148 keV

Modestly collective transitions to the known γ -vibrational states are observed leaving the 2^- band at 1148 keV. This highly-favored trend of γ -rays to the $K^\pi=2^+$ band is difficult to ignore in the face of notably strong ($\sim 2\text{--}5$ mWu), absolute $B(E1)$ measurements between these two modes of excitations. Pascu [58] stresses the importance of this preferential $K^\pi=2^- \rightarrow K^\pi=2^+$ decay in nearby nuclei via the measurement of direct E3 radiation as a potential octupole-quadrupole coupling, however, this decay pattern could be a product of K-forbidedness, as any decays to the ground state involve $\Delta K=2$ versus the $\Delta K=0$ transitions to the γ -band. We also mirror these same concerns on the continued study of interband decay radiation in the rare-earth region to fully understand this band; $B(E3; 5^- \leftrightarrow 2_\gamma^+)$ strengths would be remarkably useful in this aspect. ^{162}Dy offers some distinct challenges in terms of the detection of radiation for low-lying excitations; for example, measurement of the interband $2^- \rightarrow 3_\gamma^+$ transition lies at 185 keV, placing it directly on top of our most strongly populated $4_{g.s.}^+ \rightarrow 2_{g.s.}^+$ transition. This experimental challenge is out of the scope of the γ -singles-based experiments performed in this work at UKAL, and would require much more discriminating coincidence measurements to observe the γ -decays.

5.2.4.2 $K^\pi=0^-$ Band at 1275 keV

Overall in the $K^\pi=0^-$ band, we observe inflated, clearly collective $B(E1)$ transition probabilities to the ground state (Table 4.9), with excellent agreement to Alaga predictions (Table ??). Although these $B(E1)$ s are weaker overall than other confirmed single-phonon octupole vibrations in the region (^{168}Er [52]), the transition probabilities are well above the threshold for what is considered generally non-collective in the mass region ($\sim 10^{-5}$ mWu strengths). Furthermore, our measured

$B(E1; 1_{K^\pi=0^-}^- \rightarrow 0_{g.s.}^+)$ of $0.002 \text{ e}^2\text{fm}^2$ compares very nicely with the systematic behavior of E1 strengths leaving the bandhead of $K^\pi=0^-$ bands in deformed rare-earth nuclei ($B(E1) \sim 0.002\text{--}0.004 \text{ e}^2\text{fm}^2$) [15]. From these measured collective E1 strengths, this suggests some significant reflection asymmetry in this $K^\pi=0^-$ band, which is especially and notably consistent with the picture of well-behaved octupole collectivity.

5.2.4.3 $K^\pi=2_2^-$ Band at 1863 keV

Much like the lower 2^- band, our measurement of mildly inflated $B(E1)$ transition probabilities to the γ -band is striking, and supports the arguments in numerous works of new, emerging decay patterns [21, 58, 71] of enhanced E1 transitions to the 2^+ band as a differing form of collective dipole excitation built on top of the γ -vibration. Along the same lines, assertions from IBM considerations with the inclusion of p and f bosons imply that the structure of the lowest-lying negative parity bands *may not* be of purely collective nature [3, 40], which supports our experimental findings. Deduced $B(E1)$ s behave well when compared to Alaga considerations (Table ??), giving us confidence of correct lifetime measurements. Of particular note, however, is the lower relative $B(E1)$ strength than its lower-energy cousins in the first 2^- band, however, the decays from this band are still above the threshold for what would be considered non-collective. Once again, the interband $B(E3)$ strengths to/from these negative parity bands would be invaluable in the further discussion and feasibility of this pattern.

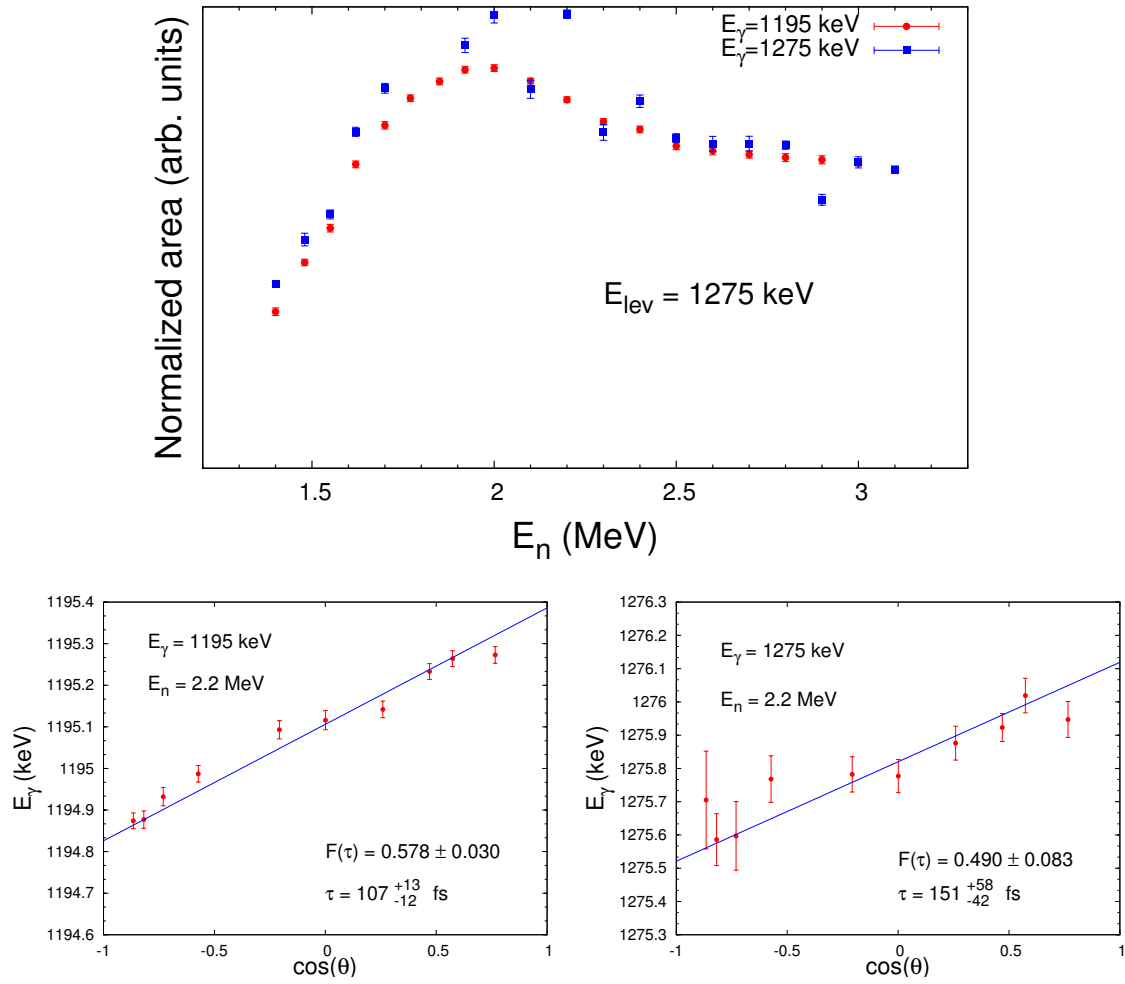


Figure 5.11. $E_\gamma=1195$ & 1275 keV (de-excitations from the $E_x=1275$ keV level) Doppler shifts and excitation functions (color online). The excitation function (in blue) for the 1275 keV γ ray is scaled by a factor of 1.53 to normalize to the branching ratio of the level.

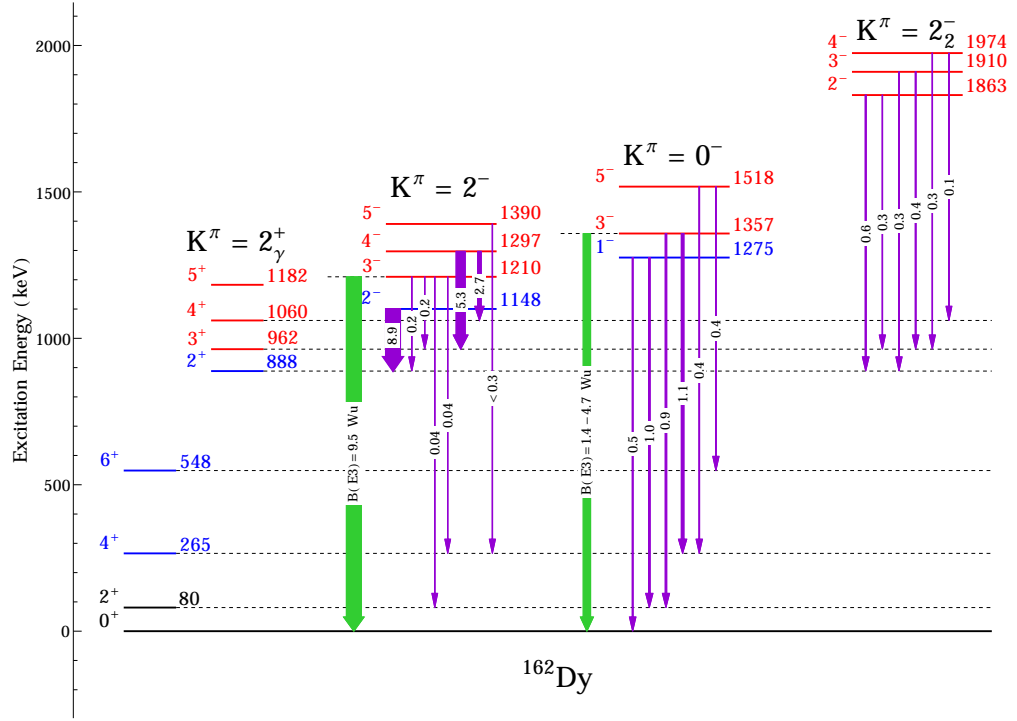


Figure 5.12. Observed γ -decays from negative parity, $K^\pi=2^-$, 0^- , 2_2^- bands in ^{162}Dy . Transition strengths are drawn proportional in width to their deduced $B(E1)$, with E1 transitions ($B(E1)$ in milli-Weksskopf units) in violet (color online). Literature $B(E3)$ values are drawn in green, expressed in W.u., and are from Refs. [53, 56]

E_{lev} (keV)	E_γ (keV)	$I_{\gamma,abs}$ (n,n' γ)
1148.20(20)	260.16(50)	658.762(7.577)
1210.05(18)	247.27(55)	38.973(1.420)
	322.05(51)	57.699(1.240)
	944.48(50)	216.160(3.227)
	1129.46(50)	384.769(5.182)
1297.06(27)	236.09(60)	43.374(1.380)
	334.15(50)	245.585(4.666)
1390.52(35)	1124.88(88)	94.848(2.193)
1275.81(24)	1195.10(50)	429.944(4.249)
	1275.82(53)	280.443(6.356)
1358.00(30)	1092.27(71)	134.371(1.271)
	1277.33(58)	178.995(6.684)
1518.47(29)	970.01(55)	32.453(0.775)
	1252.74(51)	78.039(1.893)
1863.85(26)	900.90(55)	47.527(1.219)
	975.65(50)	141.639(1.587)
1910.50(26)	947.51(56)	48.580(0.955)
	1022.33(53)	39.474(0.978)
1972.99(66)	912.09(50)	82.148(3.125)
	1010.19(50)	251.922(15.219)

TABLE 5.6

Absolute intensities for γ -decays from the $K^\pi=2^-$, 0^- , and 2_2^- bands observed in (n,n' γ) experiments, taken from the $E_n=3.1$ MeV angular distributions.

5.2.5 Other Negative Parity Bands

5.2.5.1 $K^\pi=5^-$ band

The current status/insight of this $K^\pi=5^-$ band is of a two-quasiparticle origin [3], where we can verify this interpretation with our (albeit slightly inflated at ~ 0.3 mWu) weak E1 transition strengths to the ground state. Furthermore, $K^\pi=5^-$ bands are not surmised to be a part of the octupole vibration splitting in a deformed nucleus, yet the refinement of this lifetime from older literature values is important nonetheless.

Assertions from IBM considerations with the inclusion of p and f bosons imply that the structure of the lowest-lying negative parity bands may not be of purely collective nature [3, 40], where the traditional picture of octupole collectivity in well-deformed nuclei exists with the initial, lowest-lying and fragmented quartet of states of $K^\pi=0^-, 1^-, 2^-, \& 3^-$. However, the current ordering of negative parity bands in ^{162}Dy is difficult (read: impossible) to predict with modern models [3]. We have measured lifetimes for a few other of the lowest-lying set of states in ^{162}Dy , where we provide individual discussion on our measurements.

5.2.5.2 $K^\pi=3^-$ band

This creates a somewhat murky picture for any interpretation of the $K^\pi=3^-$ band. The $E_\gamma=311$ keV de-excitation from the 4^- member is overwhelmingly E2 radiation, based on our measurement of a mixing ratio of $-6.9^{+1.6}_{-2.2}$ ($\sim 98\%$ E2), but the very large (potentially) E2 transition probabilities that de-excite the bandhead are impressive, even in the face of heavy M1 mixing for the 212 keV γ ray that leaves the bandhead at 1570 keV. Whether this band is some higher collective behavior on top of the existing octupole vibration or if it is even part of the $0^-, 1^-, 2^-, 3^-$ quartet is still an open question, however, the preference of decay to the lower-lying octupole band ($K^\pi=0^-$ band) should not be understated.

5.2.5.3 $K^\pi=1^-$ band

As such, the deduced transition probabilities should not be taken without careful attention and heavy skepticism. Interband $B(E2)$ strengths of 630 W.u. are unprecedented in *any* nuclear transition, flagging a clear departure from a consistent measurement of the lifetime. The generally low limits for lifetimes measured do not offer vast insight into the collectivity of the band.

5.2.5.4 $K^\pi=3_2^-$ band

Decays from the second $K^\pi=3^-$ band have the potential for some interesting structure effects, with the extremely preferential branching ratios to the γ -band and the $K^\pi=2^-$ band. However, our measurements of the second $K^\pi=3^-$ band's lifetimes cannot reveal any insight to the octupole collectivity in these levels. In the case of mostly E2 radiation and the lowest possible lifetime, the alarmingly large $B(E2)\sim 6$ Wu to the 2^- band could indicate some collectivity on top of the $K^\pi=2^-$ octupole band, based solely on the decay pattern, but nothing concrete can be said, barring a reliable measurement of the actual lifetime of the states in the band.

5.2.6 $K^\pi=1^+$ band

In terms of rotational bands in ^{162}Dy , our discussion on results ends with the $K^\pi=1^+$ band and the isovector M1 scissors mode. The latter excitations have been extensively studied with photon scattering experiments by [43, 51], and as mentioned before, offer a good calibration point or benchmark for our lifetime measurements, as the literature values fall within the sensitive range of what DSAM can measure.

As we go higher in energy in this band, more channels are open to decay, which can be seen in Figure 5.14. While we do measure a fairly collective transition to the γ -vibrational band, this should be taken as the exception to the rule, rather than implying that it is any collective behavior built on top of the existing quadrupole

vibration. Oftentimes, a state can pick up a large two-quasiparticle amplitude from the ‘daughter’ state that would give rise to a nonzero $B(E2)$, however, this does not mean the state is collective in nature.

Overall, these transitions observed out of the 1^+ band are noncollective to any other excitation in ^{162}Dy , an assertion made very early by Soloviev [70], suggesting that the $K^\pi=1^+$ band cannot stem from one or two-phonon coupling from the detailed quasiparticle-phonon nuclear model (QPNM) formalism outlined there.

5.2.7 States above 2.2 MeV excitation energy

With the increasing level density and uncertainty in spin-parity assignments above 2.0 MeV, differentiation of negative parity bands (or *any* band structure) becomes difficult. Incidentally, levels above this energy threshold lie well above the pairing gap; recall that we are most likely to find the most collective excitations below this energy, however, above the pairing gap, we can expect to see mixing between multi-quasiparticle states and collective excitations. Since the nature and goal of $(n, n'\gamma)$ experiments at UKAL is *not* to identify new levels in the level scheme, but to confidently place existing γ -rays from the excitation functions, higher-lying states often cannot be confidently discussed in the scope of a vibrational phonon picture in this work. Of course, this does not imply that there is a lack of structure above this threshold, as we can observe multiphonon excitations at energies above the pairing gap [79, 82]. Reduced transition probabilities for transitions out of these states should not be given much weight, as a) the full E2 strength is reported for any potentially mixed multipolarity decays, and b) the $E_\gamma^{2\ell+1}$ factor for the calculation of reduced transition probabilities tends to dominate at this higher energy regime. Nevertheless, we still present our measured lifetimes and any observed branching ratios from multi-channel decays in the tables.

5.2.8 Implications & Discussion

Lifetime measurements for ^{162}Dy offer a remarkable survey of nuclear structure in this deformed nucleus. The definitive existence of single- and double-phonon quadrupole vibrations at the excitation energies $E_{K^\pi=2_\gamma^+}=888$ keV, $E_{K^\pi=0_{\gamma\gamma}^+}=1400$ keV, $E_{K^\pi=4_{1,\gamma\gamma}^+}=1535$ keV, $E_{K^\pi=4_{2,\gamma\gamma}^+}=2181$ keV has set a new precedent for anharmonic quadrupole vibrations, as the majority of two-phonon cases in deformed rare-earth nuclei are at higher energies than a purely harmonic case. A new opening for a potential collective state built on-top of the γ -vibrational band has been proposed as a candidate for a $\beta\gamma$ -vibration, an excitation that has eluded experimentalists for years.

In a trend that continues throughout the rare-earth nuclei, we have only measured lifetimes for a few negative parity states that are surmised to be a part of the octupole vibrational states. The new decay patterns for the negative parity states in $2^- \rightarrow 2_\gamma^+$ transitions has been observed in our campaign of lifetime measurements, via strong E1 transitions to the γ -band. These measured $K^\pi=2^-$ bands seem to not be a part of the octupole vibration, but we cannot say for certain without precision B(E3) measurements in the interband cases; whether or not these states are a separate collective degree of freedom besides the traditional quadrupole/octupole vibration remains an open question.

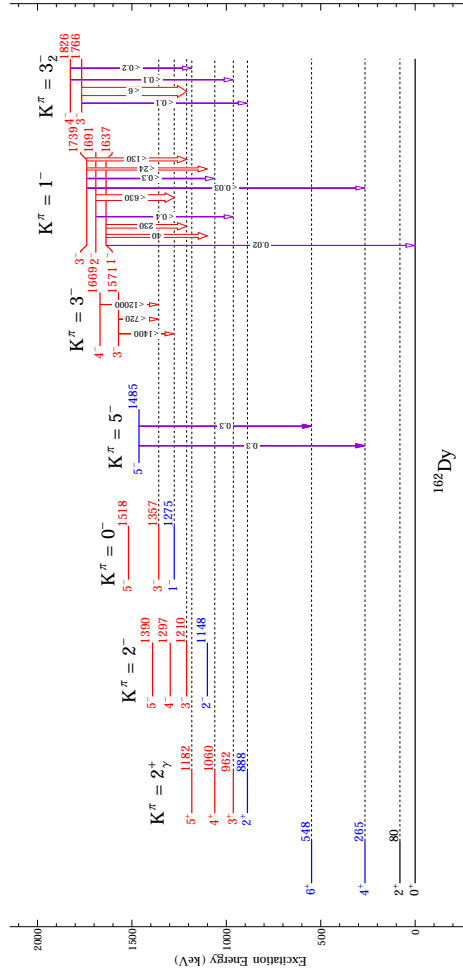


Figure 5.13. Observed γ -decays from higher lying $K^\pi=5^-, 3^-, 1^-, 3_2^-$ bands in ^{162}Dy . Transition strengths are proportional in width, with E2 transitions in red and E1 transitions in violet (color online). Hollow (white with colored border) transition arrows indicate that the resulting transition probability is tentatively from an unreliable lifetime measurement.

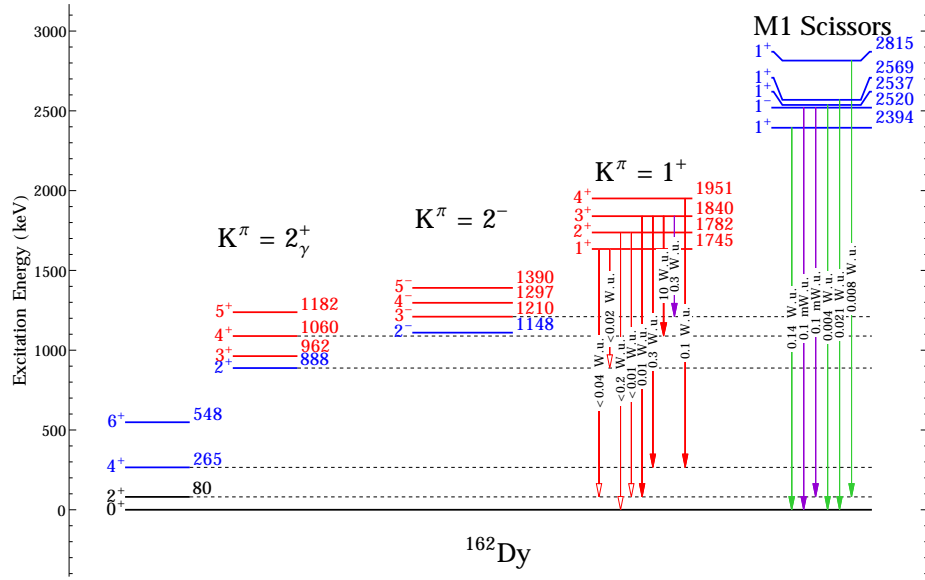


Figure 5.14. $K^\pi=1^+$ band and the 1^\pm -spin levels part of the isovector M1 scissors mode in ^{162}Dy . $B(E1)$ in violet and in mW.u., $B(M1)$ in green and W.u., and $B(E2)$ in red in W.u.



red and in W.u.

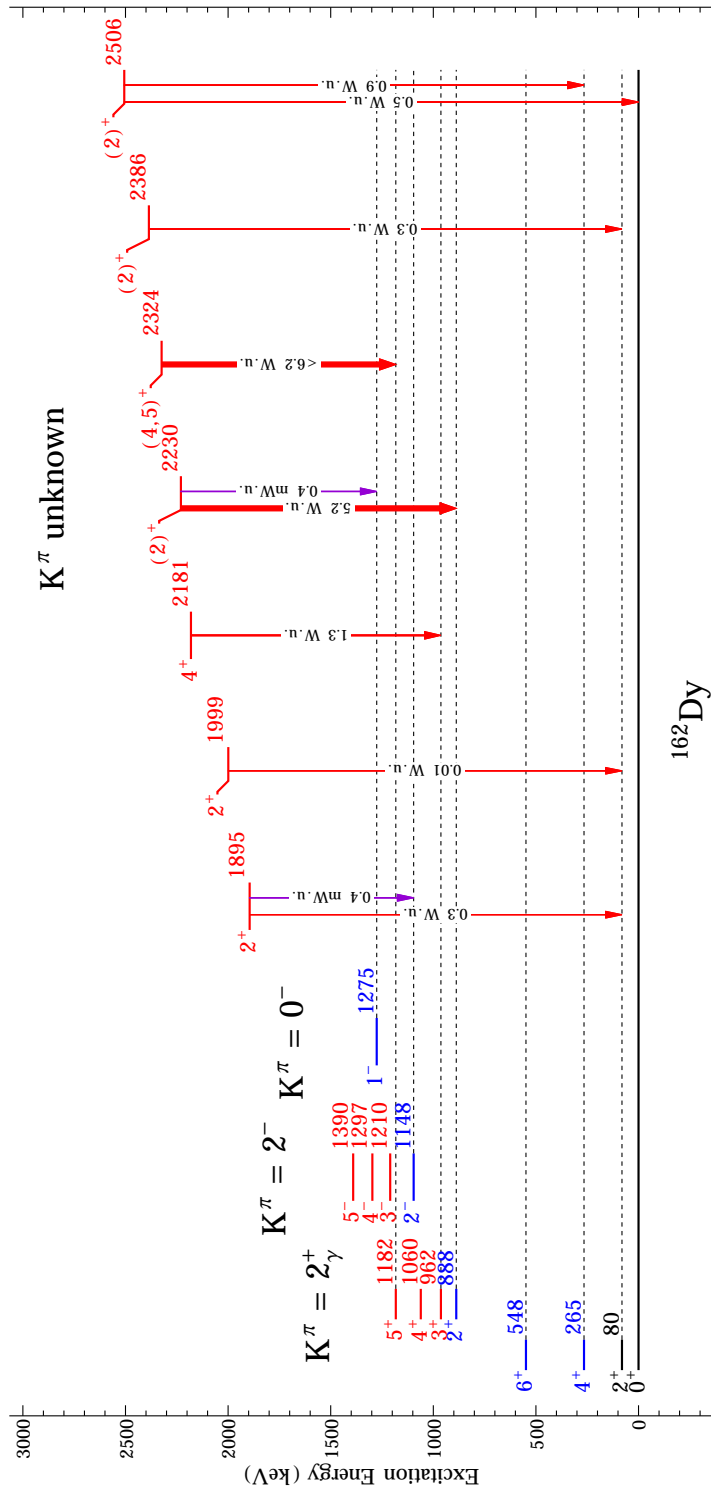


Figure 5.16. Levels in ^{162}Dy with no rotational band assignment above the pairing gap ($2\Delta_n=1720$ keV & $2\Delta_p=1914$ keV) (continued). $B(E1)$ in violet and in mW.u., and $B(E2)$ in red in W.u.

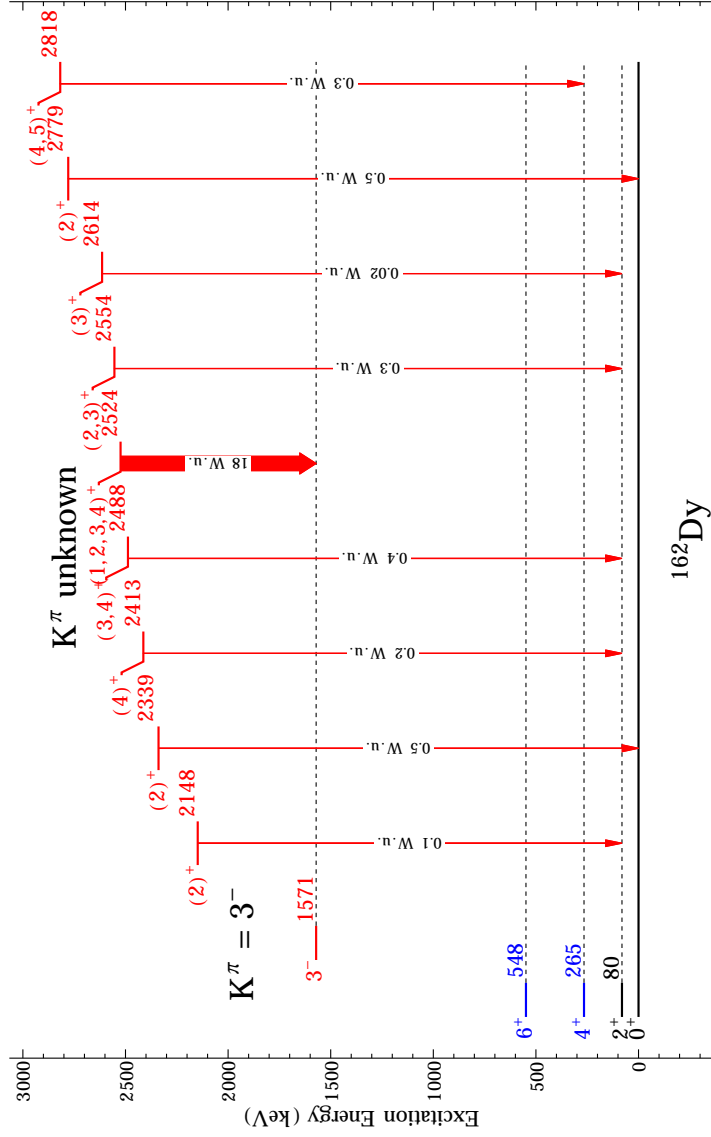


Figure 5.17. Levels in ^{162}Dy with no rotational band assignment above the pairing gap ($2\Delta_n=1720$ keV & $2\Delta_p=1914$ keV) (continued). $B(E1)$ in violet and in mW.u., and $B(E2)$ in red in W.u.

CHAPTER 6

FINAL REMARKS AND FUTURE OUTLOOK

6.1 Impact of Presented Lifetime Measurements

Aside from the overall contribution of the lifetimes presented in this work in the global systematics of rare-earth structure, each isotope has local, isotopic significance and impetus for the measurement of nuclear lifetimes. Our measurement of level lifetimes and corresponding reduced transition probabilities has been imperative in understanding the structure of these nuclei in this geometric model.

6.1.1 ^{160}Gd

Gadolinium-160 lies at the end of the road (figuratively) of decades long research on the structure of Gd isotopes; following the pioneering and continuing experimental works by Lesher, Aprahamian, de Haan, and others in $^{154-158}\text{Gd}$ [42, 48, 55], ^{160}Gd lifetimes act as a capstone to understanding nuclear structure at the edges of the valley of stability, as well as structure at the limits of stable prolate deformation. Careful examination of our data has narrowed the focus of the systematic and ongoing study of 0^+ excitations in the region, as we ruled out two possible states and measured key lifetimes for the remaining two $K^\pi=0^+$ bands. Invaluable knowledge on the characteristics of low-lying negative parity bands and $K^\pi=4^+$ bands was also gathered from our data, which opened the possibility of octupole and hexadecapole vibrations in deformed nuclei.

6.1.2 ^{162}Dy

The astounding fact that the 47 new ^{162}Dy lifetimes presented makes is that these measurements account for a $\sim 0.2\%$ increase for *all* literature lifetimes across *all* 3000+ nuclei in existence. Putting this figure into even greater context, the 84 literature lifetimes for ^{168}Er were gathered from extremely high resolution and efficiency detector arrays and spread across decades of experiments around the globe. With a single detector and a modestly discriminating spin population ($J^\pi \leq 5^\pm$), we are able to provide a comparable number of lifetimes in ^{162}Dy , putting it near the top of the list of experimentally measured lifetimes of excited states, not only in the rare-earth region, but across the entire Chart of Nuclides. In addition, if we compare the overall complexity of DSAM-INS experiments and data analysis at UKAL to other lifetime measurements around the globe, we notice an *extremely* cost-efficient process and low barrier of entry to the experimentalist. The efficiency of cost stems from the single-detector setup with modest electronics required for signal processing, in comparison to the robust coincidence measurements needed elsewhere, and the straightforward analysis routines lend a veritable swiftness to the time required to publish results.

6.2 What Lies Ahead for Rare-Earth Nuclei?

To reiterate the concerns of [38] on the nature of any possible quadrupole vibrations in deformed nuclei, the successful measurement of two-nucleon transfer reaction cross sections, absolute $B(E2)$ values (of which we have substantially added with this work), and the $\rho^2(E0)$ strengths is imperative. The spearheaded efforts by [55] and this work cover the first two criteria, with the most elusive and experimentally exhaustive work remaining to measure $E0$ transitions. Fortunately, measurement of these crucial internal conversion electrons is possible at the Nuclear Science Laboratory at

the University of Notre Dame du Lac, with the Internal Conversion Electron BALL array (ICEBALL). Using coincidence measurements of multiple Germanium detectors and charged particle Lithium-drifted Silicon detectors (SiLi), conversion electron strengths can be measured through careful electronics gates. The preferred mode of excitation at the NSL is via a $(\alpha, 2n)$ reaction for its preferential selection of positive parity, $L=0$ and $L=2$ states. The $(\alpha, 2n)$ reaction also provides a secondary particle gate for proper event discrimination, with the implementation of triple-coincidence measurements being open (*e.g.* one can trigger on a Germanium detector, a SiLi detector, *and* a neutron detector, if desired).

In the specific case of ^{160}Gd , this α implantation reaction proves difficult, as the preferred target required must be stable, and no suitable candidates apply (^{158}Sm is unstable). The feasibility of using other reaction channels is discouraging from a cross-section standpoint; the (n, α) reaction cross section is well below a few microbarns (μb) for MeV-range incident neutrons that would be extracted from the on-site Tandem accelerator at the NSL. Complicate this problem further with the current lack of neutron production capabilities at the NSL, and the successful measurement of E0 transitions begins to seem less realistic.

For ^{162}Dy , however, measurement of E0 transitions is readily possible at the NSL via the $(\alpha, 2n)$ reaction; incidentally and ironically, the backed targets used in ICEBALL experiments require a modest natural abundance of the particular isotope, in this case ironically, ^{160}Gd . Looking forward, E0 measurements could be a feasible experiment at Notre Dame in the very near future, and is worthwhile to carry out experiments of this type to continue research on the structurally rich ^{162}Dy .

To complete the picture of the evolution of nuclear structure in the rare-earth region, the measurement of absolute $B(E2)$ transition probabilities for other nuclei would be ideal. This can be done for a modest number of the even-even Gd, Er, and Yb isotopes, yet distinct challenges arise in the feasibility of acquiring enough target

material to perform DSAM measurements for other Dysprosium nuclei. A very large portion of the natural abundances of Dy nuclei is split between the odd-A isotopes; this poses a problem that would force either an (n,γ) reaction (not ideal because of the inherent neutron backgrounds) to be used, and that target production could become increasingly expensive. Piled on top of this, target purity greatly affects the reliability of lifetimes measured with DSAM, where we utilize very large quantities of $>95\%$ enriched oxide powders, but in lower quality targets, this enrichment would be severely impacted by the lack of natural abundances in certain isotopes.

As a supplement, refinement of lifetimes in the ^{160}Gd and ^{162}Dy is entirely possible and more than welcome in the cases where we can only measure lower limits for the lifetime. Luckily, methods to measure lifetimes in the super-picosecond range is achievable with the techniques mentioned in §2.1 such as GRID or Coulomb Excitation. Along the same lines in terms of the refinement of spectroscopy of the nuclei studied in this work, five (5) tentative and confirmed 0^+ excitations by [55] were not observed in our $(n,n'\gamma)$ experiments; these states could be probed further at the University of Notre Dame via $(\alpha, \alpha'\gamma)$ reactions with high-efficiency detectors in regular use in the lab (GEORGINA). Doing this removes certain, unfortunate, backgrounds (namely the (n,γ) humps that prevent the detection of the tentative 0^+ at 774.2 keV), and allows a much higher detection probability for much lower intensity γ rays. The precise coincidence measurements of γ rays stressed in §?? can also be done at the Nuclear Science Laboratory with multi-detector arrays like GEORGINA, further aiding the campaign to fully understand the nature of 0^+ excitations.

Since many rare-earth nuclei exist at the limits of a rotational, deformed shape, and that we have such a variation in the interpretation of the lowest-lying 0^+ states in the region, there may be latent trends hidden in the systematics of the states to further investigate. Figure 6.1 shows the energy of the 0_2^+ states in deformed rare-earth nuclei as a function of A (and N). Of note, we notice the sharp drop in

energy for Samarium nuclei as deformation rapidly takes hold, with a somewhat local peak in energy around the $^{166,168}\text{Er}$ isotopes, followed by another downward trend for Ytterbium and Hafnium nuclei. Experimentally, the lifetimes of 0^+ bands in this local area are far from complete, as we only have concrete evidence for $\gamma\gamma$ -type vibrations existing in the Erbium nuclei (as the second and fifth 0^+). One question we want to ask is: does this local peaking of energy correlate to a different interpretation of the lowest-lying 0^+ state? There may *not* be a connection between the energy of the state and its makeup, however, without proper spectroscopy (including absolute $B(E2)$ measurements), the question remains open, and perhaps this sparks a new interest in some targeted areas of rare-earth nuclei. On the same subject, Figure 6.2 shows the current status of absolute $B(E2)$ measurements for the $0_2^+ \rightarrow 2_{gs}^+$ transitions as a function of A , which is not only a sparsely populated figure, but also scattered across orders of magnitude of $B(E2)$ strength.

Finally, the stage is set for more lifetime measurements to be made (especially for the excited 0^+ states found in [55]) for the vast set of rare-earth nuclei. Recall the systematic pictures shown in §1.6, where we notice a complete paucity of lifetime information for these 0^+ excitations (namely $^{166,168}\text{Er}$ and $^{154,156}\text{Gd}$). These lifetimes have furthered the elucidation of single & double phonon vibrations in deformed nuclei, but “there is always work to do” in the rare-earth region of nuclei, as the mystery of many structure phenomena is far from clear or well understood.

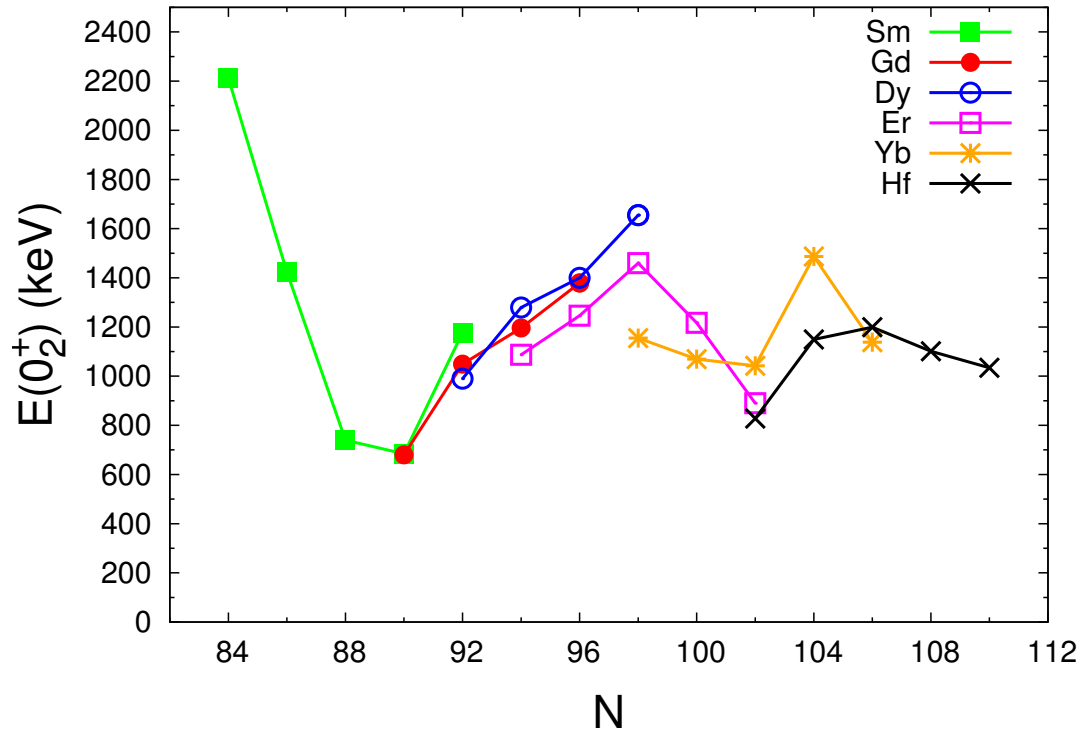
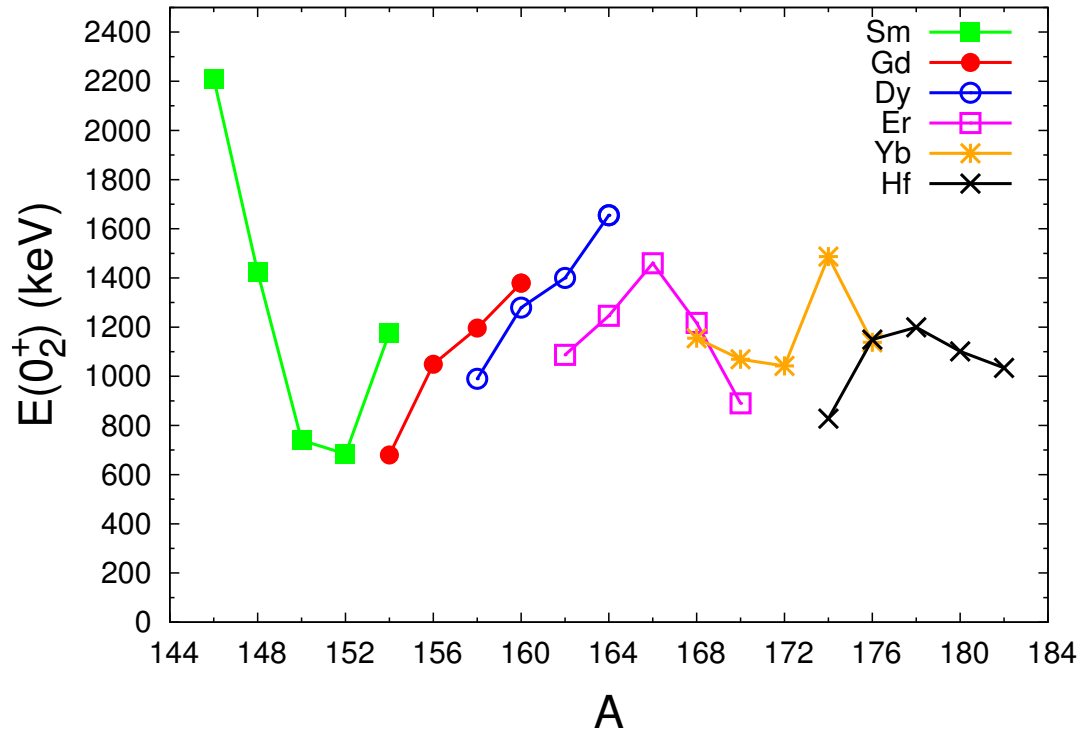


Figure 6.1. Energies of the lowest-lying 0_2^+ state as a function of A (top) and N (bottom) for rare earth Sm, Gd, Dy, Er, Yb and Hf isotopes.

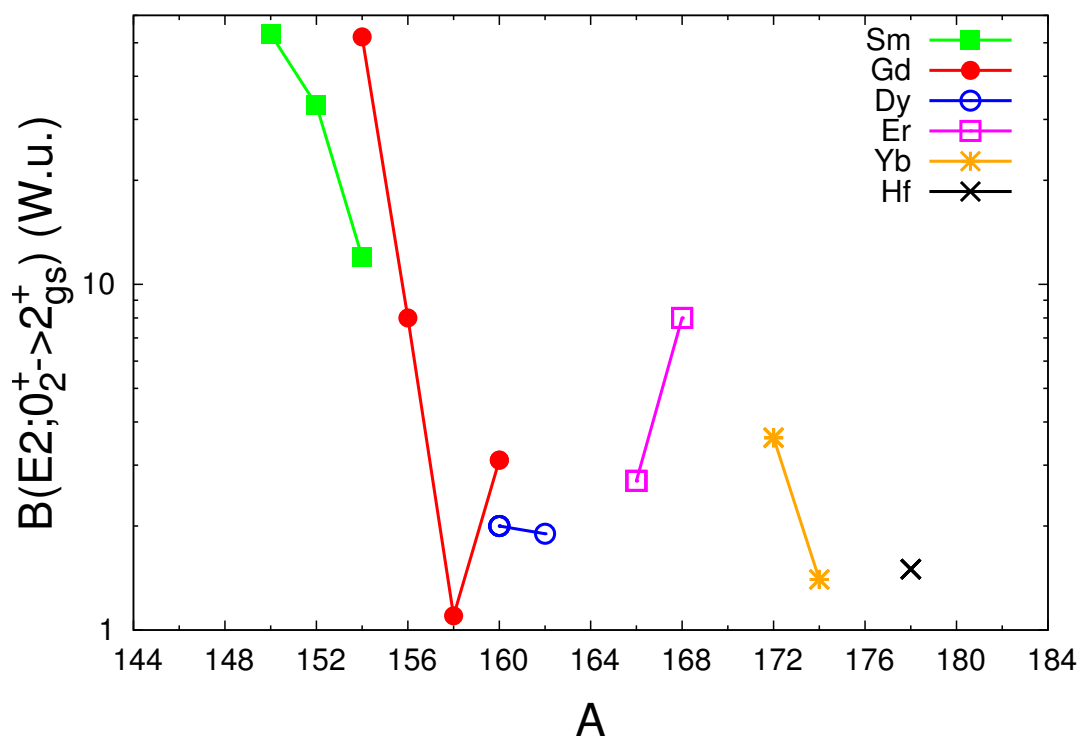


Figure 6.2. Known experimental $B(E2)$ strengths of the lowest-lying 0^+ state as a function of A for rare earth Sm, Gd, Dy, Er, Yb and Hf isotopes.

BIBLIOGRAPHY

1. A. Aprahamian. From ripples to tidal waves: Low lying vibrational motion in nuclei. *Nuclear Physics A*, 731:291 – 298, 2004.
2. A. Aprahamian, R. C. de Haan, H. G. Börner, H. Lehmann, C. Doll, M. Jentschel, A. M. Bruce, and R. Piepenbring. Lifetime measurements of excited $K^\pi = 0^+$ bands in ^{178}Hf . *Phys. Rev. C*, 65:031301, Feb 2002.
3. A. Aprahamian, X. Wu, S. Leshner, D. Warner, W. Gelletly, H. Börner, F. Hoyler, K. Schreckenbach, R. Casten, Z. Shi, D. Kusnezov, M. Ibrahim, A. Macchiavelli, M. Brinkman, and J. Becker. Complete spectroscopy of the ^{162}Dy nucleus. *Nuclear Physics A*, 764:42 – 78, 2006. ISSN 0375-9474.
4. Aprahamian, A. and Brenner, D. S. and Casten, R. F. and Gill, R. L. and Piotrowski, A. First observation of a near-harmonic vibrational nucleus. *Phys. Rev. Lett.*, 59:535–538, Aug 1987.
5. T. Belgia, G. Molnar, and S. W. Yates. Analysis of Doppler-shift attenuation measurements performed with accelerator-produced monoenergetic neutrons. *Nuclear Physics A*, 607:43 – 61, 1996.
6. M. Bender, K. Rutz, P. G. Reinhard, and J. A. Maruhn. Pairing Gaps from Nuclear Mean-Field Models. *EPJ manuscript CHECK*, 731:291 – 298, 2004.
7. Y. Y. Berzin, E. P. Grigorev, T. V. Guseva, and Y. Y. Tamberg. The Levels of ^{160}Gd Nucleus. *Izv.Akad.Nauk, SSSR:Ser.Fiz.* 53, 901, 1989.
8. J. Berzins, P. Prokofjevs, R. Georgii, R. Huckle, T. von Egidy, G. Hlawatsch, J. Klora, H. Lindner, U. Mayerhofer, H. Schmidt, A. Walter, V. Soloviev, N. Shirikova, and A. Sushkov. ^{162}dy studied with (n, γ) , $(n, n'\gamma)$, (d, p) and (d, t) reactions. *Nuclear Physics A*, 584(3):413 – 448, 1995.
9. P. R. Bevington and D. K. Robinson. *Data Reduction and Error Analysis for the Physical Sciences*. McGraw-Hill, 2003.
10. J. Blatt and V. Weisskopf. *Theoretical Nuclear Physics*. Wiley, 1952.
11. A. Bohr and B. R. Mottelson. *Nuclear Structure*, volume II. World Scientific Publishing Co., First edition, 1975.

12. Bohr, A. and B. R. Mottelson and D. Pines. Possible Analogy between the Excitation Spectra of Nuclei and Those of the Superconducting Metallic State. *Physical Review*, 110:936–938, May 1958.
13. Bonatsos, Dennis and E. A. McCutchan and Casten, R. F. Casperson, R. J. and Werner, V. and Williams, E. Regularities and symmetries of subsets of collective 0^+ states. *Phys. Rev. C*, 80:034311, Sep 2009.
14. J. Boring. *Gamma-ray ABSorption Correction (ABSCOR)*. PhD thesis, University of Kentucky, 1960.
15. H. G. Börner, M. Jentschel, N. V. Zamfir, R. F. Casten, M. Krticka, and W. Andrijschew. Ultrahigh resolution study of collective modes in ^{158}Gd . *Phys. Rev. C*, 59:2432–2439, May 1999.
16. B. Bucher, S. Zhu, C. Y. Wu, R. V. F. Janssens, D. Cline, A. B. Hayes, M. Albers, A. D. Ayangeakaa, P. A. Butler, C. M. Campbell, M. P. Carpenter, C. J. Chiara, J. A. Clark, H. L. Crawford, M. Cromaz, H. M. David, C. Dickerson, E. T. Gregor, J. Harker, C. R. Hoffman, B. P. Kay, F. G. Kondev, A. Korichi, T. Lauritsen, A. O. Macchiavelli, R. C. Pardo, A. Richard, M. A. Riley, G. Savard, M. Scheck, D. Seweryniak, M. K. Smith, R. Vondrasek, and A. Wiens. Direct evidence of octupole deformation in neutron-rich ^{144}Ba . *Phys. Rev. Lett.*, 116:112503, Mar 2016.
17. D. Burke. Hexadecapole-Phonon versus Double- γ -Phonon Interpretation for $K^\pi=4^+$ Bands in Deformed Even-Even Nuclei. *Phys. Rev. Lett.*, 73, Oct 1994.
18. M. Caprio. Levelscheme: A level scheme drawing and scientific figure preparation system for mathematica. *Computer Physics Communications*, 171(2):107 – 118, 2005.
19. R. F. Casten. *Nuclear Structure from a Simple Perspective*. Oxford University Press, Second edition, 1990.
20. Casten, R. F. and Hasegawa, M. and Mizusaki, T. Jing-ye, Zhang and E. A. McCutchan and N. V. Zamfir and Krücken, R. Anomalous behavior of the first excited 0^+ state in $N \approx Z$ nuclei. *Phys. Rev. C*, 71:014319, Jan 2005.
21. A. Chakraborty, F. M. Prados-Estévez, S. Choudry, B. Crider, P. Garrett, W. D. Kulp, A. Kumar, M. T. McEllistrem, S. Mukhopadhyay, M. Mynk, J. Orce, E. E. Peters, J. L. Wood, and S. W. Yates. New decay pattern of negative-parity states at $N = 90$. *Phys. Rev. C*, 86:064314, Dec 2012.
22. A. Charvet, R. Chry, R. Duffait, M. Morgue, and J. Sau. Lifetimes and structures of some levels above 1.5 mev in ^{168}Yb , ^{164}Er and $^{158,160,162}\text{Dy}$. *Nuclear Physics A*, 213(1):117 – 124, 1973.

23. R. Clark, R. Casten, L. Bettermann, and R. Winkler. Unified framework for understanding pair transfer between collective states in atomic nuclei. *Phys. Rev. C*, 80:011303, Jul 2009.
24. Crider, B. P. and Peters, E. E. and Allmond, J. M. and McEllistrem, M. T. and Prados-Estévez, F. M. and Ross, T. J. and Vanhoy, J. R. and Yates, S. W. Inelastic neutron scattering cross sections for ^{76}Ge relevant to background in neutrinoless double- β decay experiments. *Phys. Rev. C*, 92:034310, Sep 2015.
25. C. Engelbrecht. Multiple scattering correction for inelastic scattering from cylindrical targets. *Nuclear Instruments and Methods*, 80(2):187 – 191, 1970.
26. G. Løvholden and T. F. Thorsteinsen and D. G. Burke. States in $^{160,162}\text{Gd}$ Studied with the (t, p) Reaction. *Physica Scripta*, 34(6A):691, 1986.
27. Gabriela Ilie and Richard F. Casten. $E0$ transitions in deformed nuclei. *Phys. Rev. C*, 84:064320, Dec 2011.
28. P. Garrett. Characterization of the β vibration and 0_2^+ states in deformed nuclei. *Journal of Physics G: Nuclear and Particle Physics*, 27(1):R1, 2001.
29. P. E. Garrett. Characterization of the β vibration and 0_2^+ states in deformed nuclei. *Journal of Physics G: Nuclear and Particle Physics*, 27(1):R1, 2001.
30. P. E. Garrett, M. Kadi, M. Li, C. A. McGrath, V. Sorokin, M. Yeh, and S. W. Yates. $K^\pi = 0^+$ and 4^+ Two-Phonon γ -Vibrational States in ^{166}Er . *Phys. Rev. Lett.*, 78:4545–4548, Jun 1997.
31. Garrett, P. E. and Kulp, W. D. and Wood, J. L. and Bandyopadhyay, D. and Choudry, S. and Dashdorj, D. and Leshner, S. R. and McEllistrem, M. T. and Mynk, M. and Orce, J. N. and Yates, S. W. New Features of Shape Coexistence in ^{152}Sm . *Phys. Rev. Lett.*, 103:062501, Aug 2009.
32. L. I. Govor, A. M. Demidov, and V. A. Kurkin. Multipole mixtures in γ transitions accompanying the (n, n' γ) reaction on ^{162}Dy . *Physics of Atomic Nuclei*, 65(5):785–794, 2002.
33. L. I. Govor, A. M. Demidov, V. A. Kurkin, and I. V. Mikhailov. Multipole mixtures in gamma transitions in the (n, n' γ) reaction on ^{160}Gd . *Physics of Atomic Nuclei*, 72(11):1799–1811, 2009.
34. E. P. Grigoriev. Structure of levels of the ^{160}Gd nucleus. *Physics of Atomic Nuclei*, 75(12):1427–1431, 2012.
35. T. Grottdal, K. Nyb, T. Thorsteinsen, and B. Elbek. Collective vibrational states in even dysprosium nuclei. *Nuclear Physics A*, 110(2):385 – 399, 1968.

36. C. Günther, S. Boehmsdorff, K. Freitag, J. Manns, and U. Müller. Is there experimental evidence for an interpretation of the lowest $K=0$ collective excitation of deformed nuclei as a phonon excitation of the γ band? *Phys. Rev. C*, 54:679–683, Aug 1996.
37. K. Heyde. *Basic Ideas and Concepts in Nuclear Physics*. Institute of Physics Publishing, Second edition, 1999.
38. Heyde, Kris and Wood, John L. Shape coexistence in atomic nuclei. *Rev. Mod. Phys.*, 83:1467–1521, Nov 2011.
39. V. Hönig. Messung von Halbertszeiten K-berbotener Übergänge in gg-Kernen der Seltenen Erden. *Z. Physik*, 225:327 – 335, 1969.
40. F. Iachello and A. Arima. *The Interacting Boson Model*. Cambridge University Press, Cambridge, 1987.
41. M. Jammari and R. Piepenbring. Anharmonicities of γ -vibrations in deformed nuclei. *Nuclear Physics A*, 487(1):77 – 91, 1988.
42. M. Jentschel, L. Sengele, D. Curien, J. Dudek, and F. Haas. The negative parity bands in ^{156}Gd . *Physica Scripta*, 89(5):054017, 2014. URL <http://stacks.iop.org/1402-4896/89/i=5/a=054017>.
43. E. L. Johnson, E. M. Baum, D. P. DiPrete, R. A. Gatenby, T. Belgia, D. Wang, J. R. Vanhoy, M. T. McEllistrem, and S. W. Yates. Lifetime measurements of scissors mode excitations in $^{162,164}\text{Dy}$. *Phys. Rev. C*, 52:2382–2386, Nov 1995.
44. G. F. Knoll. *Radiation Detection and Measurement*. John Wiley & Sons, Third edition, 2000.
45. W. Korten, T. Hrtlein, J. Gerl, D. Habs, and D. Schwalm. Observation of a harmonic two-phonon vibration in a deformed nucleus. *Physics Letters B*, 317(1):19 – 24, 1993.
46. H. Lehmann, J. Jolie, F. Corminboeuf, H. G. Börner, C. Doll, M. Jentschel, R. F. Casten, and N. V. Zamfir. Lifetimes of the lowest $2^+_{K\pi=0^+}$ levels in ^{168}Er and ^{164}Dy . *Phys. Rev. C*, 57:569–576, Feb 1998.
47. S. R. Leshner, A. Aprahamian, L. Trache, A. Oros-Peusquens, S. Deyliz, A. Gollwitzer, R. Hertenberger, and B. D. New 0^+ excitations in ^{158}Gd . *Phys. Rev. C*, 66:051305, Nov 2002.
48. S. R. Leshner, J. N. Orce, Z. Ammar, C. D. Hannant, M. Merrick, N. Warr, T. B. Brown, N. Boukharouba, C. Fransen, M. Scheck, M. T. McEllistrem, and S. W. Yates. Study of 0^+ excitations in ^{158}Gd with the $(n, n'\gamma)$ reaction. *Phys. Rev. C*, 76:034318, Sep 2007.

49. S. R. Leshner, C. Casarella, A. Aprahamian, B. P. Crider, R. Ikeyama, I. R. Marsh, M. T. McEllistrem, E. E. Peters, F. M. Prados-Estévez, M. K. Smith, Z. R. Tully, J. R. Vanhoy, and S. W. Yates. Collectivity of 0^+ states in ^{160}Gd . *Phys. Rev. C*, 91:054317, May 2015.
50. H. Mang, J. Poggenburg, and J. Rasmussen. Nuclear structure and pairing correlations for the heavy elements. *Nuclear Physics*, 64(3):353 – 378, 1965.
51. J. Margraf, T. Eckert, M. Rittner, I. Bauske, O. Beck, U. Kneissl, H. Maser, H. H. Pitz, A. Schiller, P. v. Brentano, R. Fischer, R.-D. Herzberg, N. Pietralla, A. Zilges, and H. Friedrichs. Systematics of low-lying dipole strengths in odd and even Dy and Gd isotopes. *Phys. Rev. C*, 52:2429–2443, Nov 1995.
52. F. McGowan, W. Milner, R. Robinson, P. Stelson, and Z. Grabowski. Coulomb excitation of vibrational-like states in $^{166170}\text{Er}$. *Nuclear Physics A*, 297(1):51 – 60, 1978.
53. F. K. McGowan and W. T. Milner. Reduced $M1$, $E1$, $E2$, and $E3$ transition probabilities for transitions in $^{156-160}\text{Gd}$ and $^{160-164}\text{Dy}$. *Phys. Rev. C*, 23:1926–1937, May 1981.
54. D. Meyer. *Nuclear Structure Studies in the Rare Earth and Trans-lead Regions*. PhD thesis, Yale University, 2006.
55. D. A. Meyer, V. Wood, R. F. Casten, C. R. Fitzpatrick, G. Graw, D. Bucurescu, J. Jolie, P. v. Brentano, R. Hertzenberger, H.-F. Wirth, N. Braun, T. Faestermann, S. Heinze, J. L. Jerke, R. Krücken, M. Mahgoub, O. Möller, D. Mücher, and C. Scholl. Extensive investigation of 0^+ states in rare earth region nuclei. *Phys. Rev. C*, 74:044309, Oct 2006.
56. R. Oehlberg, L. Riedinger, A. Rainis, A. Schmidt, E. Funk, and J. Mihelich. Coulomb excitation studies of ^{160}dy , ^{162}dy and ^{164}dy . *Nuclear Physics A*, 219(3): 543 – 562, 1974.
57. P. E. Garrett, Mar 2007. URL <http://www.physics.uoguelph.ca/~pgarrett/Collective-ex-def.htm>.
58. S. Pascu, D. Bucurescu, et al. Detailed spectroscopy of quadrupole and octupole states in ^{168}Yb . *Phys. Rev. C*, 91:034321, Mar 2015.
59. P.E. Garrett and others. Octupole and hexadecapole bands in ^{152}Sm . *Journal of Physics G: Nuclear and Particle Physics*, 31(10):S1855, 2005.
60. D. Pelte and D. Schwalm. *Heavy Ion Collisions*, volume 3.
61. E. E. Peters, A. Chakraborty, B. P. Crider, B. H. Davis, M. K. Gnanamani, M. T. McEllistrem, F. M. Prados-Estévez, J. R. Vanhoy, and S. W. Yates. Level lifetimes in the stable Zr nuclei: Effects of chemical properties in Doppler-shift measurements. *Physical Review C*, 88:024316, Aug 2013.

62. Peters, E.E. and others. E0 transitions in ^{106}Pd : Implications for shape coexistence. *The European Physical Journal A*, 52(4):1–5, 2016.
63. N. Pietralla and O. M. Gorbachenko. Evolution of the “ β excitation” in axially symmetric transitional nuclei. *Phys. Rev. C*, 70:011304, Jul 2004.
64. D. N. Poenaru and W. Greiner. *Experimental Techniques in Nuclear Physics*. Walter de Gruyter, 1997.
65. S. D. Conte and C. de Boor. *Elementary Numerical Methods of Analysis: An Algorithmic Approach*.
66. B. Sethi and S. K. Mukherjee. Half-lives of the excited states of ^{46}Ti , ^{84}Rb , ^{99}Tc , ^{162}Dy , ^{164}Er , and ^{196}Au . *Phys. Rev.*, 166:1227–1233, Feb 1968.
67. J. F. Sharpey-Schafer, T. E. Madiba, S. P. Bvumbi, E. A. Lawrie, J. J. Lawrie, A. Minkova, S. M. Mullins, P. Papka, D. G. Roux, and J. Timár. Blocking of coupling to the 0_2^+ excitation in ^{154}Gd by the $[505]11/2^-$ neutron in ^{155}Gd . *The European Physical Journal A*, 47(1):1–4, 2011.
68. Sharpey-Schafer, J.F., Mullins, S.M., Bark, R.A., Kau, J., Komati, F., Lawrie, E.A., Lawrie, J.J., Madiba, T.E., Maine, P., Minkova, A., Murray, S.H.T., Ncapayi, N.J., and Vymers, P.A. Congruent band structures in ^{154}Gd : Configuration-dependent pairing, a double vacuum and lack of β -vibrations. *Eur. Phys. J. A*, 47(1):5, Jan 2011.
69. E. Sheldon and V. Rogers. Computation of total and differential cross section for compound nuclear reactions of the type (a,a) , (a,a') , (a,b) , (a,γ) , $(a,\gamma-\gamma)$, $(a,b\gamma)$ and $(a,b\gamma-\gamma)$. *Computer Physics Communications*, 6(3):99 – 131, 1973.
70. V. G. Soloviev, A. V. Sushkov, and N. Y. Shirikova. Low-lying nonrotational states in strongly deformed even-even nuclei of the rare-earth region. *Fiz.Elem.Chastits At.Yadra*, 27:1643, 1996.
71. M. Spieker, S. Pascu, A. Zilges, and F. Iachello. Origin of Low-Lying Enhanced E1 Strength in Rare-Earth Nuclei. *Phys. Rev. Lett.*, 114:192504, May 2015.
72. Y. Sun, A. Aprahamian, J.-y. Zhang, and C.-T. Lee. Nature of excited 0^+ states in ^{158}Gd described by the projected shell model. *Phys. Rev. C*, 68:061301, Dec 2003.
73. University of Fribourg Nuclear Structure Group, Fribourg, Switzerland. FiTPiC spectra fitting program, version 5.1-8, (1996).
74. V. G. Soloviev. Quadrupole and Hexadecapole Vibrational Excitations in Deformed Nuclei. *International Journal of Modern Physics E, Nuclear Physics*, 06: 437–473, 1997.

75. C. Wesselborg, P. V. Brentano, K. Zell, R. Heil, H. Pitz, U. Berg, U. Kneissl, S. Lindenstruth, U. Seemann, and R. Stock. Photoexcitation of dipole modes in $^{160,162,164}\text{Dy}$. *Physics Letters B*, 207(1):22 – 26, 1988.
76. K. Winterbon. An analytic theory of Doppler-shift attenuation. *Nuclear Physics A*, 246(2):293 – 316, 1975.
77. S. S. Wong. *Introductory Nuclear Physics*. Wiley-VCH, Second edition, 1998.
78. C. Y. Wu, D. Cline, M. W. Simon, G. A. Davis, R. Teng, A. O. Macchiavelli, and K. Vetter. Electromagnetic properties of the rotationally aligned band in ^{162}Dy . *Phys. Rev. C*, 64:064317, Nov 2001.
79. X. Wu, A. Aprahamian, S. M. Fischer, W. Reviol, G. Liu, and J. X. Saladin. Multiphonon vibrational states in deformed nuclei. *Phys. Rev. C*, 49:1837–1844, Apr 1994.
80. W. Younes, D. E. Archer, J. A. Becker, L. A. Bernstein, P. E. Garrett, N. Warr, M. Kadi, A. Martin, S. W. Yates, G. D. Johns, R. O. Nelson, and W. S. Wilburn. Two-phonon excitations in ^{170}Er . *AIP Conference Proceedings*, 481(1):464–472, 1999. doi: <http://dx.doi.org/10.1063/1.59530>. URL <http://scitation.aip.org/content/aip/proceeding/aipcp/10.1063/1.59530>.
81. N. V. Zamfir, R. F. Casten, B. Liu, D. S. Brenner, C. J. Barton, R. Krücken, C. W. Beausang, J. R. Novak, J. R. Cooper, G. Cata-Danil, R. L. Gill, and D. D. Warner. Status of the $K^\pi=0_2^+$ band in ^{162}Dy . *Phys. Rev. C*, 60:054319, Oct 1999.
82. N. V. Zamfir, J.-y. Zhang, and R. F. Casten. Interpreting recent measurements of 0^+ states in ^{158}Gd . *Phys. Rev. C*, 66:057303, Nov 2002.
83. A. Zilges, P. von Brentano, H. Friedrichs, R. Heil, U. Kneissl, S. Lindenstruth, H. Pitz, and C. Wesselborg. A survey of $\Delta K=0$ dipole transitions from low lying $J=1$ states in rare earth nuclei. *Z Phys. A - Hadrons and Nuclei*, 340:155 – 158, Apr 1991.